Optical properties of gold nanostructures

Submitted by Baptiste Auguié

to the University of Exeter
as a thesis for the degree of

Doctor of Philosophy in Physics.

July 2009

I certify that all material in this thesis which is not my own work has been identified and that no material has previously been submitted and approved for the award of a degree by this or any other University.

"In particular, she had a wonderful sense of humor, and I learned from her that the highest forms of understanding we can achieve are laughter and human compassion."

Richard Feynman

to Simina,

Acknowledgements

In the Summer of 2005, I was offered the chance to visit Exeter for an interview with Prof. Bill Barnes, and at the same occasion I met a few members of the Thin Film Photonics group. It is my pleasure to have now this opportunity to say a few words about this group of people whom I got to know better in the past few years.

Bill is a very tactful person, and this quality combined with a constant search for different perspectives makes him a special physicist. Enthusiasm for research and a talent for seeing the bigger picture are the main qualities one could ask from a supervisor, Bill has never shown a lack of any of these skills. I must also acknowledge the fortunate interaction I have had with Roy Sambles, head of the research group. Roy's boundless curiosity and always insightful questioning are not only very stimulating for a PhD student, but they also undoubtedly influence our own scientific approach long after the PhD by pursuing his exemplary attitude towards the scientific method.

Before acknowledging the numerous members of the group, I would like to express my gratitude to a few other physicists from the department, Peter Petrov for his most friendly mentoring; Tim Naylor, now Head of School, Alex Savchenko for always very cordial discussions, Matthew Bate, and Charles Williams for the enjoyable experience of attending a few lectures in a UK university.

There have been a few people who have helped me a lot in matters of science and experimentation during these three years, and the first names that I should like to acknowledge are Andy Murray and George Zorinyants. It is my great pleasure to thank both of them for excellent and very complementary advice throughout my wanderings and mistakes. Andy has great skills in physics — perhaps too easily overlooked in reason of his quiet modesty, but he never misses a chance to help out. George is also one of the most talented physicists I have worked with, and he has provided invaluable advice during these three years in areas ranging from technical difficulties to enjoyable mathematical discussions. Ian Hooper has also managed to endure most of my routine question-times each morning for almost three years without complaining too much (although I finally had to chase him down to the point of sharing his office). This move may have decreased our productivity somewhat, but I enjoyed the relentless discussions about physics and stuff.

As far as help goes, I am indebted to Stephen Cornford, our unique guru in matters of computer science and theoretical considerations. Thank you Steph, for advice I've come to appreciate to its full value only very recently.

It is with regret that I now realise I've had too little interaction with Euan Hendry and Tim Atherton, but something in the few exchanges we've had has always been very enjoyable and memorable. It is the feeling of sharing a common interest in what fascinates me about physics, and also the excitement of talking to very smart people.

Lucy and Steve I met only too briefly, same goes for Tim Taphouse and John Birkett, and I've often regretted since then the particular atmosphere this group had, as at the time I was hardly able to join the lunchtime conversation. I also thank Alastair, Gemma, Ciarán, Joe, Sharon, Celia, Ed, Helen and all the members of the Thin Film Photonics group.

Chris and James deserve a special thank you note, for balancing out the french attitude I may have occasionally displayed. You two have proven that dark-field spectroscopy can be done with perhaps a more cheerful exterior attitude — what goes inside James' mind though, I dare not wonder!

I would like to thank Pete Cann for his excellent help in technical matters and many friendly walks and dinner invitations. I am also very grateful to Dave, John and the guys from the mechanical workshop; Denise and Natasha, and the school office for bearing with my incapability of keeping track of papers and time.

I am grateful to the different members of the Attogram project for providing the funding for this work, and also for some enjoyable presentations in vastly different areas of science.

I had the great opportunity to visit the group of Javier García de Abajo in Madrid for a week of enjoyable collaboration, and I would like to thank him and his students Alejandro, Viktor, and Xesùs for their hospitality and many interesting discussions. I am looking forward to further interaction in the future.

I must acknowledge the wonderful support I received from the R community [1], in particular of Hadley Wikham who developed the package I used for most of the graphics presented in this thesis [2].

Thomas Wriedt, Maxim Yurkin, and Alexander Moroz have also helped me substantially in using their respective modelling codes and deserve a grateful thank you.

One of the most exciting opportunities in conferences is to meet new interesting people, and I had the chance to make the acquaintance of a few nice persons whom I would like to mention. Felicia and Heidi at a Summer school in Corsica; Paul Mulvaney, Elena Eremina, and Vince Loke at a workshop in Bremen.

I met a few special professors during my undergraduate years whom I would like to thank for their early contribution to this work through their teaching of physics. From Montréal I want to acknowledge the excellent courses of David Ménard, Raman Kashyap, Nicolas Godbout. By displaying an invaluable enthusiasm for teaching physics and a profound insight characteristic of the sharpest minds, their lectures have been a very decisive experience in my education.

[1] http://cran.r-project.org/

[2] http://had.co.nz/ggplot2/

I am very glad I also had the chance to attend the lectures of Olivier Guillou, who made me understand his passion for chemistry. I also wish to thank Loïc Hervé for his most interesting teaching of algebra.

I must include in my acknowledgements Thibaut Sylvestre and Eric Lantz from the Optics laboratory of Besançon, as they have always been very encouraging for my PhD and I spent a great time working in their company. Mika, Armand, Ludo and Jean-Charles also participated in making this a nice experience, and I learnt a lot about the grad student life from interacting with them and feeling part of the group for a few months.

Finally, I would like to mention the names of all the interesting persons I have lived with in the past few years, spending many enjoyable hours in their company: Kim, Tina, Nikki, Lisa, Darren, Khalid, Stephanie, Sophie, Charlotte, Ellena, Annabelle, Sami, David, Lisa, Oslem. However difficult to keep in touch, it is always a pleasure to remember the good times we have spent together. Thank you.

I also gratefully thank my family for coping with the distance.

Abstract

The optical properties of gold in the visible are dominated by the response of the free conduction electrons to light. In gold nanostructures, the surface charge density adopts a configuration that is constrained by the shape of the nanoparticles. As a result, the scattering of light by gold nanoparticles exhibits a resonant response characterised by a strong scattering and absorption in a narrow range of frequencies. The spectral range of this *localised surface plasmon resonance* (LSPR) can be tuned by varying the size and shape of the gold nanoparticle — the nanoparticles act as nanoscale antennas for the visible light. Confirmation of this scaling rule is obtained by conducting experiments with nanoparticles of varying size and aspect ratio. Such particles are fabricated by electron-beam lithography, and characterised by dark-field spectroscopy. Not only does the LSPR shift in frequency with a change of particle size, but its spectral lineshape is also modified. The intensity and width of the LSPR are dictated by a variety of factors that are related to the intrinsic material properties (the complex dielectric function of gold), and to the particle geometry and environment.

The optical response of small gold nanorods is well described by a simple oscillating dipole model — the incident electromagnetic field induces a current in the particle that re-radiates light (scattering). A series of refinements can be made to model more accurately the optical response of realistic particles. If the dipole moment characterising the particle is allowed to vary in phase across the particle, retardation effects provide a correction for the effective dipole moment of the particle. As the particle size approaches the wave length in the surrounding medium, the dipolar approximation breaks down and higher order multipoles need to be considered. The Mie theory provides a very accurate description of the response of spheres of arbitrary size. Further, the T-matrix and other numerical techniques can be employed to accurately reproduce the scattering properties of particles of arbitrary shapes.

When the scattering sample consists of a collection of gold nanoparticles, the collective optical response is affected by two key factors. First, the measured LSPR is a convolution of the distribution of particle sizes with the individual response of a single particle. This leads to an inhomogeneous broadening of the LSPR lineshape. Second, the light that is scattered by one such particle near resonance can strongly affect its neighbours which scatter light in proportion to the net field they experience, that is the sum of the incident field plus the perturbation arising from the neighbouring particles. The onset of such multiple scattering events is observed even for particle separations that are several times larger than the particle size.

Several regimes of interaction can be distinguished according to the ratio separation / wavelength. First, when the particles are in close proximity (separation $\ll$ wavelength), near-field interactions dominate and result in a spectral shift of the LSPR accompanied with a spectral broadening. Second, when the separation is commensurate with the wavelength, a coherent interaction can develop that couples a large number of particles. In ordered arrays, such coupling gives rise to a geometrical resonance that can strongly affect the LSPR of the particles. In particular a sharp spectral feature is observed that depends on both the single particle response and the geometrical arrangement of the particles in the array.

The coherence of such multiple scattering in diffractive arrays of gold nanoparticles can be broken by introducing disorder in the distribution of particle sizes, or in the particle positions. The optical properties of an irregular array reflect the departure from a periodic system and the spectral lineshape evolves as the level of disorder is increased. In the limit of uncorrelated positions, the diffractive coupling is suppressed and the response of the collection of the particles rejoins the response of isolated particles.

Contents

List of Figures

Glossary

DDA Discrete Dipole Approximation.

DF Dark-field (spectroscopy).

EBL Electron-beam lithography.

FDTD Finite Differences in Time Domain.

FEM Finite Elements Method.

KK Kramers-Kronig.

LSPR Localised Surface Plasmon Resonance.

MLWA Modified Long Wavelength Approximation.

NSL Nanosphere lithography.

RTE Radiative Transfer Equation.

SEM Scanning electron micrograph.

SPP Surface Plasmon-Polariton.

TE, TM Transverse Electric, Magnetic.

VSWFs Vector Spherical Wave Functions.

Symbols

$\mathbf{E}_{\mathrm{tot}}$, $\mathbf{E}_{\mathrm{loc}}$, $\mathbf{E}_{\mathrm{scat}}$, $\mathbf{E}_{\mathrm{inc}}$, $\mathbf{E}_{\mathrm{ext}}$, $\mathbf{E}_{\mathrm{subs}}$, $\mathbf{E}_{\mathrm{refl}}$ Electric fields (total, local, scattered, incident, external, substrate, reflected).

α Polarizability.

$\mathbf{A}$ Vector potential.

$\mathbf{E}$, $\mathbf{B}$, $\mathbf{D}$, $\mathbf{H}$, $\mathbf{J}$, $\mathbf{P}$ Field vectors in frequency domain.

$\mathbb{F}$ Scattering amplitude matrix.

$\mathbb{I}$ Unit matrix.

$\mathbf{M}$, $\mathbf{N}$ Vector spherical wave functions.

$\mathbf{\Pi}$ Electric Hertz vector.

$\mathbf{k}$ Wave vector in a medium.

$\mathbf{k}_0$ Wave vector in a vacuum.

$\hat{\mathbf{n}}$ Unit normal vector.

$\mathscr{E}$, $\mathscr{B}$, $\mathscr{D}$, $\mathscr{H}$, $\mathscr{J}$, $\mathscr{P}$, $\mathscr{M}$ Field vectors in time domain.

χ Susceptibility.

δ Dirac distribution.

$\bar{\mathrm{G}}$, $\bar{\mathrm{I}}$ Green's and unit dyadics.

$\mathbf{L}$ Shape factor.

μ_0, ε_0 Permeability and permittivity of a vacuum.

$\otimes$ Tensor product.

ρ Charge density.

σ Conductivity.

ε Dielectric function.

σ_{sca}, σ_{abs}, σ_{ext} Scattering, absorption, extinction cross-sections.

c Speed of light in a vacuum.

Would you tell me, please, which way I ought to go from here?'
'That depends a good deal on where you want to get to,' said the Cat.
'I don't much care where–' said Alice.
'Then it doesn't matter which way you go,' said the Cat.
'–so long as I get somewhere,' Alice added as an explanation.
'Oh, you're sure to do that,' said the Cat,
'if you only walk long enough.'

Lewis Carroll

1 Introduction

The work presented in this thesis has as its objective the study of the interesting optical properties of gold nanoparticles. The interaction of light with gold nanostructures is part of a rich field of optics called *plasmonics* which comprises the study of the interaction of light with planar metal-dielectric interfaces, and with sub-wavelength metallic structures [1, 2]. This thesis was motivated by the recent development of applications of such gold nanostructures as optical biosensors [3, 4].

This introduction will first outline the principle of a plasmonic-based sensing technique. Second, I will present a brief historical review of the study of metallic particles. Lastly, I will give an outline of the material discussed in the chapters of this thesis.

1.1 Sensing using surface plasmons

This work was part of a wider collaborative project to exploit surface plasmons for biosensing. The results in this thesis arose from a need to better understand the optical response of arrays of gold nanoparticles.

Real-time analysis of biochemical reactions is of great practical interest and is the subject of ever-growing activity [4, 5]. Amongst all sensing and characterisation techniques, non-intrusive optical sensors are markedly attractive. Using light as a probe of a chemical reaction in a biological sample offers the advantage of a non-invasive detection technique (visible or infra-red light does not damage the tissues for sufficiently low intensities). The use of an electromagnetic wave confined near the surface of the sample provides an efficient probe for the sample that is to be investigated optically [6–15]. Surface-plasmons —which are defined as a collective oscillation of the free electrons at the interface between a metal and a dielectric [2, 16], provide just such an electromagnetic wave bound to the surface. Figure 1.1 illustrates the principle of optical sensing assisted by surface-plasmons.

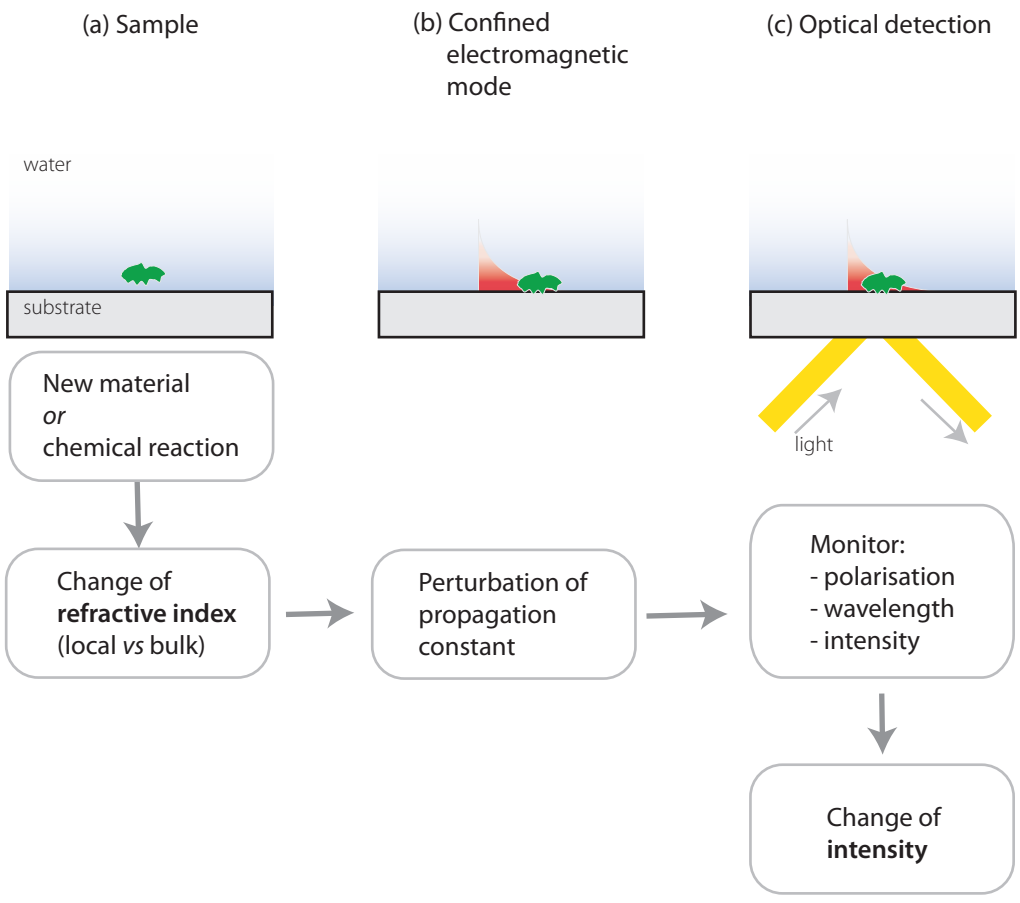

Figure 1.1: Schematic principle of optical sensing using surface-plasmons. (a) The sample consists of a substrate (typically glass), covered with a material to be characterised (typically, a buffer solution with a range of analytes in different concentrations). (b) The substrate is manufactured so as to support an electromagnetic mode bound to the surface. For example, the glass substrate can be coated with a thin gold film that supports a propagating surface-plasmon at the interface with the buffer solution. Another example is an array of gold nanoparticles deposited on the substrate. (c) An incident light beam is coupled to the surface mode. A detector is used to collect the reflected or transmitted light that has interacted with the surface mode.

The substrate is treated so as to offer an adapted platform for the chemical reactions that are to be monitored. A variety of surface treatments and surface chemistry have been developed for both glass and gold interfaces [4]. In biosensing, the molecules of interest are usually delivered in a buffer solution that defines a bulk refractive index environment above the sensing platform. For a given optical sampling area (typically a beam spot of several microns square), the sensing volume is only a small part of the actual liquid sample. An important issue is to provide an adapted fluidics system ensuring that the target molecules are efficiently into contact with the sensing area. Further, in a biological environment hundreds of different molecules are generally present in the solution even after purification. A high-throughput sensor array would present a collection of specific binding agents arranged on a single chip, different chemical spots monitoring the competition of binding of different components [12, 17].

The event that is monitored in time can be of two forms. (i) A new component is introduced in the buffer and binds to the surface. In optical terms, this added mass results in a change of refractive index. (ii) A chemical reaction occurs near the surface that causes a change of refractive index.

The local change of refractive index will lead to a perturbation of the propagation constant of the surface-plasmon mode that propagates along the interface. This perturbation is related to the overlap of the modal field with the perturbation of the refractive index profile, it is therefore desirable to obtain the highest possible field confinement of the mode near the interface [4].

The change of propagation constant of the surface mode needs to be monitored by external light. An incident beam couples to the surface mode, which in turn couples back to free-radiation monitored by a detector. The efficiency of coupling light in and out of the bound surface mode is an important issue to consider to optimise the efficiency of the sensor [3, 9, 11].

The perturbation of the propagation constant of the surface mode can be probed by light in several ways. In general, three categories may be considered. (i) The intensity of the light is directly monitored as a function of time. This is the situation of a planar Kretschmann geometry [18] where the incident light of fixed polarisation and fixed angle of incidence couples to the surface plasmon. A change of the dispersion of the surface-plasmon mode due to the perturbation of the local index causes an alteration in the coupling of the light with the surface mode. (ii) The polarisation of the incident light can be modulated, thereby affecting the coupling of the incident light to the surface-plasmon. A crossed-analyser situated in the path of the collection optics can allow for an accurate measure of the change of the polarisation state of the light that is re-radiated by the surface-plasmon due to the perturbation of refractive index. (iii) Finally, the incident light can be from a broadband source, and the dispersion of the surface-plasmon mode is monitored by a spectrometer during the change of refractive index. Monitoring spectral changes is the approach discussed in this thesis.

The use of gold nanostructures in such applications is justified by the combination of two characteristics [4]. (i) Gold is chemically inert and does not interfere with the biological samples. (ii) The interface between gold and a surrounding dielectric medium can support surface-plasmon modes, which are characterised by a strong confinement of the electromagnetic field near the interface. This field confinement offers two advantages. First, the interaction between the probing light and the medium of interest (analyte) is enhanced. Second, the localisation of the field in a sub-wavelength sampling volume makes it possible to distinguish between bulk refractive index changes of the environment and local refractive index changes. The bulk medium may be subject to perturbative effects such as temperature or pressure fluctuations. The effect of such environmental sources of noise on the detection of surface events is reduced by confining the electromagnetic field to the surface in a subwavelength sampling region [19–21].

The planar surface-plasmon geometry has been successfully used since the past two decades to probe interfacial changes [22], and has now reached a detection sensitivity that is close to the intrinsic limitations of the technique due to the environmental fluctuations of the bulk refractive index [23].

In an idealised experiment as depicted in figure 1.1, sensing a refractive index change requires having a light beam incident on the active region of the sample, and a change in the output signal corresponds to the presence of a given quantity of known material. The sensitivity can be unam-

biguously defined as the quantity of matter corresponding to the smallest change in signal one can detect (above the noise level).

Several complications arise in a practical implementation. First, experiments take place in an aqueous environment, where the change of refractive index of water due to thermal fluctuations, pressure, or pH variation lowers the detection limit. The dominant noise is the ultimate limitation: thermal and pressure fluctuations can be partially accounted for by using a reference channel.

The use of nanoparticles has been proposed to replace the planar geometry [24, 25], as it provides further spatial confinement of the surface-plasmon mode near the interface where the chemical reactions are to be monitored, and is therefore more sensitive to the local index change and comparatively less sensitive to spurious bulk index change [10, 26].

Another source of noise in optical measurements arises when the light intensity is low. The shot noise of the detector imposes constraints on the required signal level. For example, the size and shape of nanoparticles may result in a trade-off between the sensitivity of the surface-plasmon dispersion to a change of index, and the low signal intensity as observed in scattering [27]. The measurement of reaction kinetics may further push the compromise between the intrinsic sensitivity of the technique and the photon budget.

For a given active surface, planar techniques and particle plasmons have a very different sensing volume as a result of their different characteristic decay length. A comparative study of the intrinsic sensitivity and related merits of both techniques was recently given by the Van Duyne group [9].

In this thesis, I will present experiments that were performed on gold nanoparticles, either isolated or arranged in a 2-dimensional array. These experiments aim at a better understanding of the optical properties of such gold nanostructures, which may provide a basis for the future design of an optimised sensing nanostructure [10, 14, 28–30].

1.2 Optical response of gold nanoparticles: historical perspective

The study of planar surface-plasmons originates from the peculiar optical response of metallic gratings observed by Wood in 1902 [31]. The work of Rayleigh [32] tentatively explained the observed 'Wood's anomalies' in terms of a surface wave excited on the grating. The work of Fano [33] further clarified the existence and characteristics of this electromagnetic mode. The experimental observation and interpretation of surface-plasmons on planar surfaces was first made by Ritchie [34] in 1957, further discussed by Stern and Ferrell [35]. In those experiments, the charge density of the metal was perturbed by an electron-beam. The energy spectrum of the electrons after passing through a metallic film displayed characteristic absorption bands corresponding to the excitation of the collective bulk and surface-plasmon modes. The optical excitation of surface-plasmons was soon realised by Turbadar in 1959 [36], Otto [37], shortly followed by Kretschmann and Raether [18].

The study of the surface-plasmon modes supported by small gold nanoparticles can also be traced back to the beginning of the 20th century. The works of Lorenz [38], Maxwell-Garnett [39], Mie [40], and Debye [41] considered the mathematical problem of the interaction of light with a metallic sphere. In particular, what is now known as the Mie theory was a (greatly) successful

attempt at explaining the particular colouration of colloidal suspensions of sub-wavelength metallic particles.

Interestingly, the same year Wood discovered the 'anomalous' band in the transmission of metallic gratings he also made a pioneering observation on the scattering response of sub-wavelength gold particles [42, 43],

> *"In the case of the gold films, the particles are too small to be seen under the microscope, with the facilities at my disposal; and I am inclined to the opinion that, in the case of the sodium and potassium films, particles which were actually seen with the microscope were only the moderately large ones, and may not have been instrumental in producing the colour. In continuing the work, I plan to make more exhaustive examinations with the microscope, using higher powers if possible, employing photography, and ultra-violet light if necessary, for I believe that only in this way can the nature of the resonator be determined. There will be no great difficulty in determining the dispersion, since the gold films are permanent, and can be examined with the interferometer, or they may easily be given a prismatic form. I feel confident that they will show anomalous dispersion, a phenomenon which, if observed, would be almost proof positive that the absorption-band was due to resonance." — Wood, 1902.*

The link between planar surface-plasmons and the electromagnetic response of gold nanoparticles is discussed at length in the monographs of Kreibig [44], and Bohren and Huffman [45].

Recently, the field of plasmonics has seen a resurgence of interest with the work of Pendry [46]. The concept of *metamaterials* has emerged to describe artificial structures that make use of a sub-wavelength structure to tailor the electromagnetic properties of a material [1, 47].

The wide range of practical applications of plasmonics and metamaterials across the visible, IR, THz, and micro-wave regimes has led to a large number of publications as illustrated in figure 1.2. The data were collected manually from Web of Science[1] using different key-words.

Both surface plasmons and particle plasmons have led to a rising number of publications in the past decade, with an increasing growth of the number of publications. This trend has to be compared to the more linear growth for a more generic keyword such as 'optics' to account for the recent widespread of electronic referencing systems and the general increase of scientific research. The very recent field of 'plasmonics' (data start in the past decade) is comparatively growing at a much higher rate than optics, and this attraction is partly due to the emergence of a new range of applications such as metamaterials [48].

1.3 Outline of this thesis

This thesis is organised as follows.

In chapter 2, a microscopic description of the optical response of matter to an electromagnetic wave is reviewed, and leads to the Drude model expression that describes the optical properties of gold in the visible and infra-red region. This description of the macroscopic dielectric function is complemented by the derivation of the Lorentz-Lorenz formula that relates the refractive index of a material to the polarisability of the atomic constituents. This derivation provides a direct link to

[1] `http://www.isiknowledge.com/`

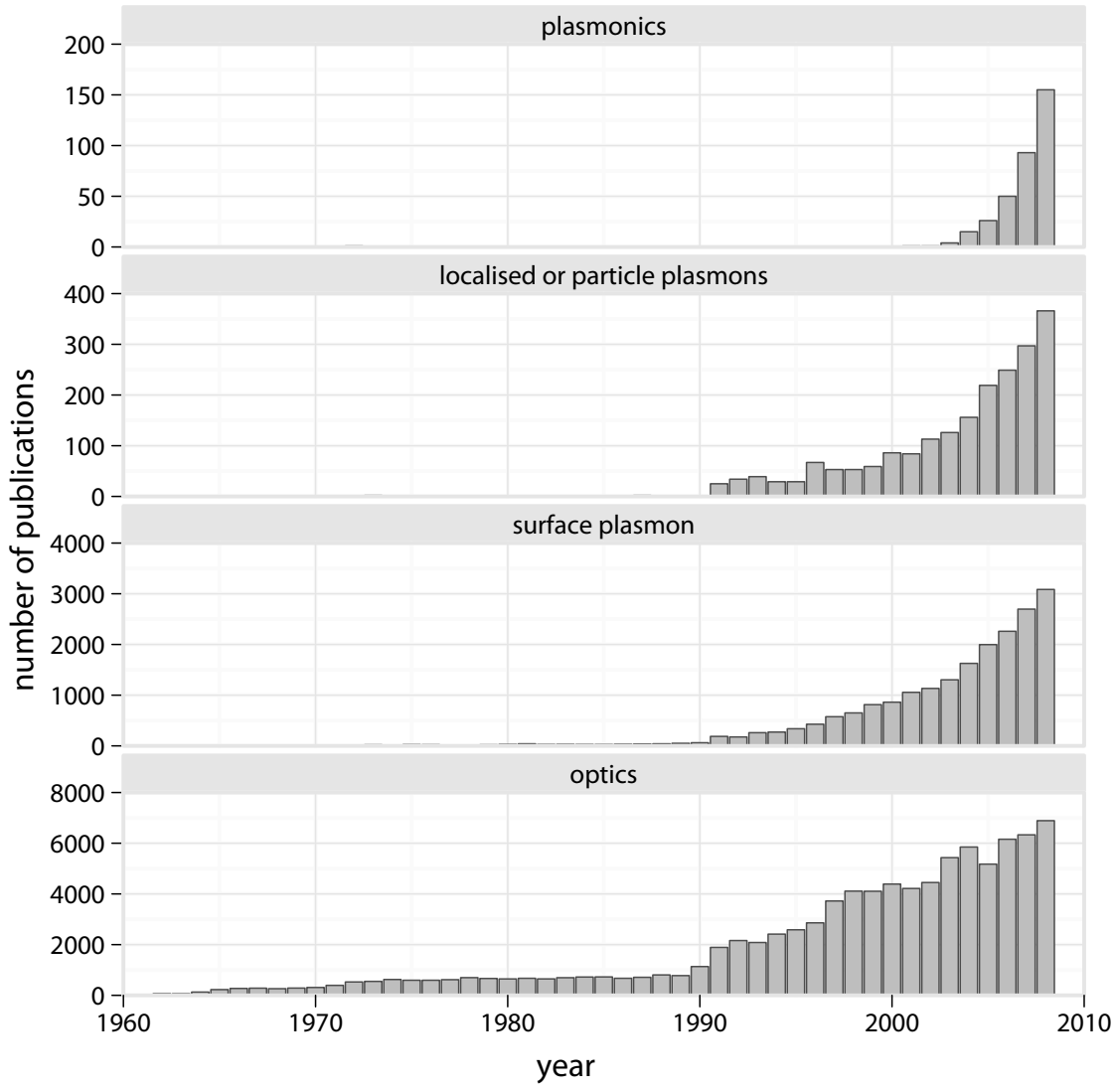

Figure 1.2: Histogram of the publications reported in Web of Knowledge (as of January, 12th, 2009) corresponding to different keywords.

the emerging field of metamaterials and to the more common effective medium theory. Surface-plasmon polaritons are introduced in the context of the optical response of thin films. The optical excitation of surface-plasmons using the Kretschman configuration is discussed, with a comparison of the experimental data and modelling based on the Fresnel coefficients.

The description of surface-plasmons on planar surfaces leads to the introduction of *localised plasmons* that are electromagnetic modes that can be supported by gold nanoparticles. Because the shape and size of the particle strongly affects the distribution of the free surface charge on the particle and its coupling to incident light, the modelling of the optical properties of gold nanoparticles requires a treatment in the framework of scattering theory which is introduced in chapter 3. A review of the current modelling techniques available to describe the interaction of light with gold nanoparticles is also given. The Mie theory provides an analytical solution for the scattering prob-

lem by a spherical particle that is used to illustrate several general features of the interaction of light with gold nanoparticles. A dipolar approximation with retardation corrections is introduced to describe the effect of a departure from a spherical shape to an elongated particle. Further, the T-matrix formulation and the discrete dipole approximation are presented as techniques that provide an accurate description of the scattering of light by particles of arbitrary shape. The interaction between particles is considered in the simple form of a coupled dipole model that is used in chapters 5—8.

Experiments on isolated single gold nanoparticles are discussed in chapter 4. The fabrication technique of electron-beam lithography is described, and the optical characterisation of single particles by dark-field spectroscopy is presented. The experiments performed on single particles aim at a better understanding of the influence of the particle size and shape on its scattering properties. Gold nanorods of varying size and aspect ratio are studied and reveal a correlation between the wavelength of excitation of a localised surface plasmon resonance and the geometry of the particle in accordance with the modelling presented in chapter 3. Further, the LSPR linewidth is characterised by separating the contributions of the material intrinsic properties, the size-dependent effect of surface scattering, and the radiative damping that affects large nanoparticles.

The interaction between closely packed particles is considered in chapter 5 where experiments are performed on collections of gold nanoparticles. The fabrication technique of nanosphere lithography is presented that allows one to fabricate large domains of particles in an hexagonal pattern. The arrays of particles are characterised by their extinction properties probed in bright field transmission spectroscopy. The effect of inhomogeneous broadening that affects the measurement of the LSPR linewidth in collections of particles is assessed by experiments and a coupled dipole model. Further, the interaction between particles is considered with arrays of different density and configuration — from a regular square lattice to a random distribution of particles with constant occupancy. The sensitivity of each configuration to a change in the bulk surrounding index is investigated experimentally.

Another regime of inter-particle interactions is observed in chapter 6, where the particles are placed on a regular array of periodicity commensurate with the excitation of the LSPR supported by the nanoparticles. In this regime I demonstrate experimentally the evidence of a sharp spectral feature that results from an interplay between the LSPR and a geometric resonance associated with the diffraction condition. The effect of introducing an asymmetry in the refractive index environment of the particles is discussed, as experiments suggest the disappearance of the feature in asymmetric configurations. The observed spectral features are explained by a simple coupled dipole model that reveals the main physical principles of the multiple scattering process in the plane of the particles.

In chapter 7 the influence of the particle size and aspect ratio on the optical response of arrays presenting such diffractive coupling is investigated. In particular, it is found that the integrated extinction per particle verifies a sum rule that relates the static (zero frequency) response of the scatterers to the integrated extinction over all frequencies. This verification is performed on the data from several nanoparticle arrays of varying sizes and periodicities, and is complemented by numerical simulations for gold ellipsoids.

The influence of disorder on the diffractive coupling of gold nanoparticle arrays is studied in chapter 8 where the periodicity is altered in two ways. First, the particles are displaced from their

regular location by an increasing amount. It is seen that the sharp and intense spectral feature resulting from the coherent multiple scattering in the plane of the particles is progressively weakened. In the limit of uncorrelated positions, the extinction spectrum is the result of an inhomogeneously broadened collection of non-interacting single particles. A coupled dipole model is used to investigate this effect numerically and the results confirm the experimental observation. Second, the particles are placed on a regular array, with a distribution of particle sizes. Here the diffractive coupling is observed, but the main resonance features associated with the excitation of LSPRs on the particles is broadened and weakened by the distribution of localised resonances.

"What traitors books can be! You think they're backing you up, and they turn on you. Others can use them, too, and there you are, lost in the middle of the moor, in a great welter of nouns and verbs and adjectives."

Ray Bradbury

2

Background physics

Gold's appeal to the eye is undoubtedly linked to its lustre and particular colouration. Other noble metals such as silver share its high reflectivity that results from the interaction of light with conduction electrons. The characteristic golden tint is however related to the interaction of light with bound electrons — silver and aluminium for example exhibit a more neutral reflectivity in the visible owing to a plasma frequency situated further in the UV regime. Understanding the optical properties of gold in the visible and infra-red therefore requires a description of the free electrons response to light, and of an additional contribution from the bound electrons. The first part of this chapter is devoted to the description of the optical properties of dielectrics and noble metals. The dielectric function is linked to a microscopic description of matter through the formulation of the Lorentz-Lorenz equation and the more general statement of the Ewald-Oseen theorem. Second, the optics of thin films offer an introduction to surface plasmons as a particular electromagnetic mode that can be supported at metal/dielectric interfaces. The description of particle plasmons is finally introduced and leads to the presentation of scattering by nanoparticles that will be discussed in detail in chapter 3.

2.1 Electrodynamics of continuous media

As an incident wave impinges on a material, the electromagnetic field exercises a force on the free and bound charges which are displaced in addition to their random thermal motion. These charges, in turn, re-radiate light in proportion to their acceleration. In a solid material, because the charges are extremely close to each other, the light that is scattered contributes substantially to the local field experienced by the other charges. As a very large number of elementary charges is present even in a nanometre-sized particle, a detailed treatment of the response of every elementary charges is not attainable. The total field at any instant in time is the sum of a multitude of partial waves emitted by a dynamical system of coupled oscillators. When the wavelength is much larger than the separation

between atoms we can, instead, choose to solve the problem in terms of a macroscopic field, treating in effect the material as a continuous distribution of polarisation. This field obeys the macroscopic Maxwell equations that describe the optical properties of matter in a continuous distribution of material large in comparison to inter-atomic distances [1].

2.1.1 The Maxwell equations

In this context, the scattering of light by nanoparticles, and optics in general can be accurately treated in the framework of the macroscopic Maxwell equations [2],

$$\boldsymbol{\nabla}\cdot\mathscr{D}=\rho \tag{2.1a}$$

$$\boldsymbol{\nabla}\times\mathscr{E}=-\frac{\partial\mathscr{B}}{\partial t} \tag{2.1b}$$

$$\boldsymbol{\nabla}\cdot\mathscr{B}=0 \tag{2.1c}$$

$$\boldsymbol{\nabla}\times\mathscr{H}=\mathscr{J}+\frac{\partial\mathscr{D}}{\partial t}, \tag{2.1d}$$

where $\mathscr{D}$, $\mathscr{E}$, $\mathscr{B}$, $\mathscr{H}$, are respectively the displacement field, the electric field, magnetic field, induction field. The current $\mathscr{J}$ and charge density ρ satisfy the charge conservation law,

$$\boldsymbol{\nabla}\cdot\mathscr{J}=-\frac{\partial\rho}{\partial t}. \tag{2.2}$$

The charge density ρ comprises the *external* charge ρ_{f} that could be added to the bulk material (it vanishes if the material is neutral), and a *polarisation-induced* charge ρ_{pol} that results from the response of the material to an applied field. A set of constitutive relations links the macroscopic fields to the electromagnetic response of matter,

$$\mathscr{D}=\varepsilon_0\mathscr{E}+\mathscr{P} \tag{2.3}$$

$$\mathscr{B}=\mu_0(\mathscr{H}+\mathscr{M}), \tag{2.4}$$

where the polarisation $\mathscr{P}$ and magnetisation $\mathscr{M}$ describe the reaction of the material to an external electromagnetic field and vanish in vacuum. The polarisation charge density is linked to the polarisation by $\nabla\cdot\mathscr{P}=-\rho_{\mathrm{pol}}$. We will consider only the linear response of materials in this work, which allows us to write,

$$\mathscr{P}=\chi^e\mathscr{E} \tag{2.5}$$

$$\mathscr{J}=\sigma\mathscr{E} \tag{2.6}$$

$$\mathscr{M}=\chi^m\mathscr{B}, \tag{2.7}$$

where the magnetic susceptibility χ^m is very close to zero for gold at optical and infra-red frequencies, χ^e is the electric susceptibility, and σ the conductivity. Combining 2.3 and 2.7 yields $\mathscr{D} = \varepsilon_0 \varepsilon \mathscr{E}$, where we define the relative permittivity of the material as $\varepsilon = 1 + \chi^e$.

In most materials with non-zero conductivity, and metals in particular, the free charge density ρ_f can be considered to be zero in most cases, as shown in the following derivation. We start with the conservation of charge and equation 2.1,

$$\nabla \cdot (\sigma \mathbf{E}) = -\frac{\partial \rho_\mathrm{f}}{\partial t} \tag{2.8}$$

$$\nabla \cdot (\varepsilon \mathbf{E}) = \rho_\mathrm{f}. \tag{2.9}$$

Equating $\nabla \cdot \mathbf{E}$ from both equations yields an equation for the time evolution of the charge density,

$$\frac{\partial \rho_\mathrm{f}}{\partial t} + \frac{\sigma}{\varepsilon} \rho_\mathrm{f} = 0, \tag{2.10}$$

which has the solution,

$$\rho_\mathrm{f}(t) = \rho_{\mathrm{f}0} \exp(-t/\tau), \tag{2.11}$$

where $\tau = \varepsilon/\sigma$ is the characteristic relaxation time for the a fluctuation in the charge density to diffuse in the bulk, which is much shorter than the light cycle of an incident wave at optical frequencies. The relevant charge density entering the Maxwell equations in the case of metals is therefore due to polarisation (the reaction of the material to an external perturbation). Adding an external charge to a metallic particle will however modify the charge density [3], and therefore the plasma frequency (see section 2.3.1).

Equations 2.1 form a local description of the average, macroscopic fields inside a continuous distribution of matter. At the interface between two different media 1 and 2, with unit normal vector $\hat{\mathbf{n}}$, the fields obey the following boundary conditions,

$$(\mathscr{D}_2 - \mathscr{D}_1).\hat{\mathbf{n}} = \rho_s \qquad \text{discontinuity yields a surface charge} \tag{2.12}$$

$$(\mathscr{E}_2 - \mathscr{E}_1) \times \hat{\mathbf{n}} = 0 \qquad \text{continuity of the tangential component} \tag{2.13}$$

$$(\mathscr{H}_2 - \mathscr{H}_1) \times \hat{\mathbf{n}} = -\mathscr{J}_s \qquad \text{discontinuity yields a surface current} \tag{2.14}$$

$$(\mathscr{B}_2 - \mathscr{B}_1) \times \hat{\mathbf{n}} = 0 \qquad \text{continuity of the normal component.} \tag{2.15}$$

Because of the necessity for the fields to obey these boundary conditions at the interface between different media, the shape of a scattering object imposes constraints on the possible solutions to the Maxwell equations in all space. In fact, the electromagnetic response of an object can be completely characterised by a set of electromagnetic eigenmodes (or *normal modes*) that can be supported by the object that depend on its constitution (refractive index) and geometry. An incident wave, that we will consider to be described as a plane wave (or, more generally, a combination of plane waves) will excite a combination of these modes, with a particular weight that is proportional to the overlap integral of the modal field with a plane wave of that frequency and polarization state.

It is often convenient to convert the Maxwell equations from the time domain to the frequency domain by invoking a time-harmonic excitation in equations 2.1,

$$\boldsymbol{\nabla}.[\varepsilon\mathbf{E}] = 0 \tag{2.16a}$$

$$\boldsymbol{\nabla} \times \mathbf{E} = i\omega\mu\mu_0\mathbf{H} \tag{2.16b}$$

$$\boldsymbol{\nabla}.[\mu\mathbf{H}] = 0 \tag{2.16c}$$

$$\boldsymbol{\nabla} \times \mathbf{H} = -i\omega\varepsilon\varepsilon_0\mathbf{E}, \tag{2.16d}$$

where the DC conductivity is included in the expression of the permittivity $\varepsilon = \varepsilon_0(1+\chi)+i\frac{\sigma}{\omega}$. The material parameters ε, μ and σ are complex quantities that depend on frequency, their arguments express the eventual dephasing between the different field quantities. In what follows we concentrate on non-magnetic, linear, and isotropic materials where we set $\mu = 1$, and ε is a (complex) scalar. The electromagnetic field will be described in terms of the electric field only — the Maxwell equations 2.16 can be used to retrieve the magnetic component if necessary.

2.1.2 The wave equation

The set of differential equations 2.16 can be regarded as a description of the electromagnetic field in terms of its structure (divergence free) and its relation to sources (the two curl equations). By taking the curl of equation 2.16b, we obtain the Helmholtz vector wave equation describing the structure of the field in homogeneous space [4, 5],

$$\nabla^2\mathbf{E} + k^2\mathbf{E} = \mathbf{0}, \tag{2.17}$$

where we define the wavenumber $k = \sqrt{\varepsilon\mu}\omega/c$, and $c = \sqrt{\varepsilon_0\mu_0}$ is the speed of light in vacuum. The analogous time-domain equation describes the propagation of an electromagnetic wave at a speed $v = \frac{c}{n}$ where $n = \sqrt{\varepsilon\mu}$ is the refractive index of the medium.

The macroscopic response of the material to an electric field can be characterised by either the complex dielectric function $\varepsilon = \varepsilon' + i\varepsilon''$ or alternatively the complex refractive index $n = n' + in''$. The real and imaginary parts of ε and n are linked by the following relations,

$$\varepsilon' = n'^2 - n''^2 \tag{2.18a}$$

$$\varepsilon'' = 2n'n'' \tag{2.18b}$$

$$n' = \sqrt{\frac{\sqrt{\varepsilon'^2 + \varepsilon''^2} - \varepsilon'}{2}} \tag{2.18c}$$

$$n'' = \sqrt{\frac{\sqrt{\varepsilon'^2 + \varepsilon''^2} + \varepsilon'}{2}}. \tag{2.18d}$$

It is often convenient to use n in describing the propagation of a wave in a medium, n' is related to the phase change and n'' to the attenuation of a wave during the propagation. The dielectric func-

tion ε is used to describe the response of the material with respect to an applied electric field. The displacement field is a measure of the effective field experienced by a charge inside the material [6].

Plane wave solution

The simplest solution to the Helmholtz equation in unbounded, homogeneous media is a transverse plane wave of the form $\mathbf{E} = \mathbf{E}_0 \exp(i\mathbf{k}\cdot\mathbf{r} - i\omega t)$, where $\mathbf{E}_0$ is a vector of constant amplitude characterising the polarisation of the wave, and $\mathbf{k}$ is the wavevector of modulus $n\omega/c$.

2.2 From microscopic to macroscopic optical properties

The description of the electromagnetic response of a material to light may span three different length-scales: (i) At the molecular level, the interaction of electrons and photons can be described in a semi-classical picture of a harmonic oscillator characterised by a dipole moment. (ii) The Maxwell equations of continuous media describe the average electromagnetic field over a portion of matter much larger than the inter-atomic distance. (iii) Agglomerates of nanoparticles may be treated as an effective medium for the incident light provided their size and separation are relatively small compared to the wavelength. This last level of averaging has led to the concept of *metamaterials*: the electromagnetic characteristics of a material can be artificially tuned by designing a suitable combination of sub-wavelength components of different electromagnetic properties (see for example [7] and references therein). At each of these three levels of observation, the Maxwell equations are valid, but necessitate the introduction of an appropriate set of material parameters. In this section I will discuss the link between the molecular, *intrinsic* properties of matter and the macroscopic refractive index of a homogeneous medium. In chapter 3, a similar link will be discussed between the scattering properties of individual nanoparticles, and the material parameters of an effective medium consisting of an agglomeration of such particles.

2.2.1 Microscopic origin of the refractive index

The refractive index of a material as described in the framework of the macroscopic Maxwell equations does not reveal the link to its microscopic origin. The phenomena of reflection and refraction at an interface find the simple mathematical interpretation of a boundary problem of matching the fields at the interface between adjacent media. Yet, the microscopic, physical origin of the refractive index is present in the macroscopic Maxwell equations, and results from the insertion of the material response into the constitutive relation for $\mathbf{J}$, $\mathbf{P}$, and $\mathbf{M}$. A more direct approach that aims to describe the refractive index from basic principles of molecular optics was initiated by Lorentz, Clausius and Mossotti [6], and given a formal and general description in the Ewald-Oseen extinction theorem [2]. This formulation provides a physical insight into the deceptively simple form of the Fresnel formulas, and a rigourous derivation of the Lorentz-Lorenz formula that relates the molecular material properties to the averaged dielectric function entering the constitutive relation 2.3.

2.2.1.1 The Ewald-Oseen theorem

The microscopic theory of polarisation can be rigourously treated in the form of the Ewald Oseen extinction theorem [2, 8–12]. This theorem provides a physical insight into the origin of the laws

of classical optics from a microscopic perspective. The laws of refraction, reflection, the Brewster angle, the Lorentz-Lorenz formula can all be derived from this powerful approach [13]. It also plays a central role in the null-field method [14] which is a powerful formulation of the scattering of light by arbitrarily shaped particles (see chapter 3). The derivation of the extinction theorem is rather lengthy and purely mathematical (see [2] for a rigourous presentation) but its conclusion may be readily summarised in physical terms. An electromagnetic wave incident on a material excites its atoms which in turn re-radiate light; this re-radiation originates not only from the geometrical boundary but from both adjacent media. The summation over all partial waves has two underlying contributions: (i) the radiation of each molecular unit, and (ii) the influence of a structure factor that depends on the spatial arrangement of the material [12]. The net resulting field vanishes in almost every direction due to the rapid variation of the relative phase between the different scattered wavelets, except for three particular directions. These three waves are the reflected wave, the refracted wave whose phase velocity is altered from the incident wave, and a wave with velocity c which exactly cancels the incident wave in the medium.

This result can also be understood by a purely macroscopic consideration, as shown in the following derivation. For simplicity, the discussion is restricted to a wave impinging on an interface between two semi-infinite, homogeneous media, at normal incidence. We consider the (artificial) division of the EM field $\mathbf{E}_{\text{tot}}$ inside a dielectric into two components: the incident wave, travelling as it would in a vacuum at a speed c, $\mathrm{E}_{\text{vac}} = \exp(-i k_0 z)$, and the wave created due to the response of the material, $\mathbf{E}_{\text{rad}}$. By linearity of the Maxwell equations, each of these components satisfies a Helmholtz equation. Further, the total field satisfies the Helmholtz equation in the medium,

$$\nabla^2 \mathbf{E}_{\text{tot}} - k^2 \mathbf{E}_{\text{tot}} = 0, \tag{2.19}$$

where $k = n k_0$. We can split equation 2.19 in the two field components,

$$\nabla^2 \mathbf{E}_{\text{vac}} + \nabla^2 \mathbf{E}_{\text{rad}} - k^2 \mathbf{E}_{\text{vac}} - k^2 \mathbf{E}_{\text{rad}} = 0, \tag{2.20}$$

and using the fact that $\mathbf{E}_{\text{vac}}$ satisfies the Helmholtz equation in a vacuum, we substitute $\nabla^2 \mathbf{E}_{\text{vac}} = k_0^2 \mathbf{E}_{\text{vac}}$. This leads to the following inhomogeneous equation, after rearranging the terms,

$$\nabla^2 \mathbf{E}_{\text{rad}} - k^2 \mathbf{E}_{\text{rad}} = (k^2 - k_0^2)\mathbf{E}_{\text{vac}} = k_0^2 (n-1)\mathbf{E}_{\text{vac}}, \tag{2.21}$$

where the right hand side can be seen as a source for the radiated wave. The general solution to equation 2.21 is the sum of a particular solution, $\mathbf{E}_{\text{part}}$, and a general solution $\mathbf{E}_{\text{hom}}$ to the homogeneous equation for $\mathbf{E}_{\text{rad}}$. We first note that $\mathrm{E}_{\text{part}} = -\mathrm{E}_{\text{vac}}$ is a solution to equation 2.21. Indeed, we have, $\nabla^2(-\mathbf{E}_{\text{vac}}) = -\nabla^2 \mathbf{E}_{\text{vac}}$, $k^2(-\mathrm{E}_{\text{vac}}) = -k^2 \mathrm{E}_{\text{vac}}$, hence:

$$\nabla^2(-\mathbf{E}_{\text{vac}}) - k^2(-\mathbf{E}_{\text{vac}}) - (k^2 - k_0^2)\mathbf{E}_{\text{vac}} = -\nabla^2 \mathbf{E}_{\text{vac}} + k^2 \mathbf{E}_{\text{vac}} - k^2 \mathbf{E}_{\text{vac}} + k_0^2 \mathbf{E}_{\text{vac}} = 0. \tag{2.22}$$

Physically, this solution corresponds to the exact cancellation of the incident wave by the re-radiation of the charges everywhere in the medium. A solution to the homogeneous equation can be found

in the following trial function, $\mathrm{E_{hom}} = \exp(ikz)$, which physically represents the refracted wave propagating in the medium at a speed c/n. The field inside the material can therefore be expressed as a sum of two waves, one that extinguishes the incident wave everywhere in the material ; one that propagates in the material with a modified velocity. Outside the medium, all waves propagate with the same velocity c, and the reflected wave that arises from the re-radiation of the charges can be found by the requirement to match the fields at the boundary: the net resultant field in the medium is the refracted wave, while the field outside is the sum of two terms. Assuming an incident field of unit amplitude, two continuity equations at the boundary are required in order to obtain the ratio of amplitudes between the reflected and refracted waves. One of these equations is the continuity of the magnetic field,

$$\mathrm{B_1} = \frac{\mathrm{B_2}}{\mu}.$$

For the electric field, the continuity equation reads,

$$\mathrm{E_1} = \mathrm{E_2}.$$

Moreover, from Faraday's law of induction, we have in each medium, $\mathbf{k} \times \mathbf{E} = -\omega \mathbf{B}$, *i.e.* $\mathrm{B} = \pm \frac{n}{c} \mathrm{E}$ where the sign is taken positive for waves propagating in the direction of the incident field and negative for contra-propagating waves. For the total field on each side of the interface, we therefore obtain,

$$\mathrm{E_{vac}} - \mathrm{E_{rad}} = \frac{n \mathrm{E_{tot}}}{\mu}.$$

the amplitude of the reflected wave satisfies the following system of equations,

$$\begin{cases} \mathrm{E_{vac}} + \mathrm{E_{rad}} = \mathrm{E_{tot}} \\ \mathrm{E_{vac}} - \mathrm{E_{rad}} = \mathrm{E_{tot}} \sqrt{\dfrac{\varepsilon}{\mu}}. \end{cases}$$

The substitution $n = \sqrt{\varepsilon \mu}$ has been made in order to symmetrize the notations. We therefore recognise the physical interpretation of the wave impedance as a measure of the ratio of amplitudes on both sides of an interface,

$$Z = \sqrt{\frac{\mu}{\varepsilon}}.$$

with inverse the admittance $Y = 1/Z$. The reflection and transmission coefficients are now readily expressed in terms of the admittance by solving the system,

$$r = \frac{\mathrm{E_{rad}}}{\mathrm{E_{vac}}} = \frac{Y-1}{Y+1} \tag{2.23}$$

$$t = \frac{\mathrm{E_{tot}}}{\mathrm{E_{vac}}} = \frac{2}{1+Y}. \tag{2.24}$$

These formulas can be generalised to arbitrary incidence [2], and are given in equation 2.35.

2.2.1.2 The Lorentz-Lorenz formula

This formula relating the microscopic polarizability of a material to its dielectric function can be rigourously obtained from the Ewald-Oseen theorem, but a simpler heuristic derivation was initially proposed by Lorentz-Lorenz and is illustrated in figure 2.1. We consider a block of material for which the optical response is characterised by a homogeneous dielectric function ε. The local field $\mathbf{E}_{\text{loc}}$ experienced by the atoms in the material is different from an applied external field $\mathbf{E}_{\text{ext}}$ due to the polarisation of the material in response to this perturbation (a 'screening effect'). The

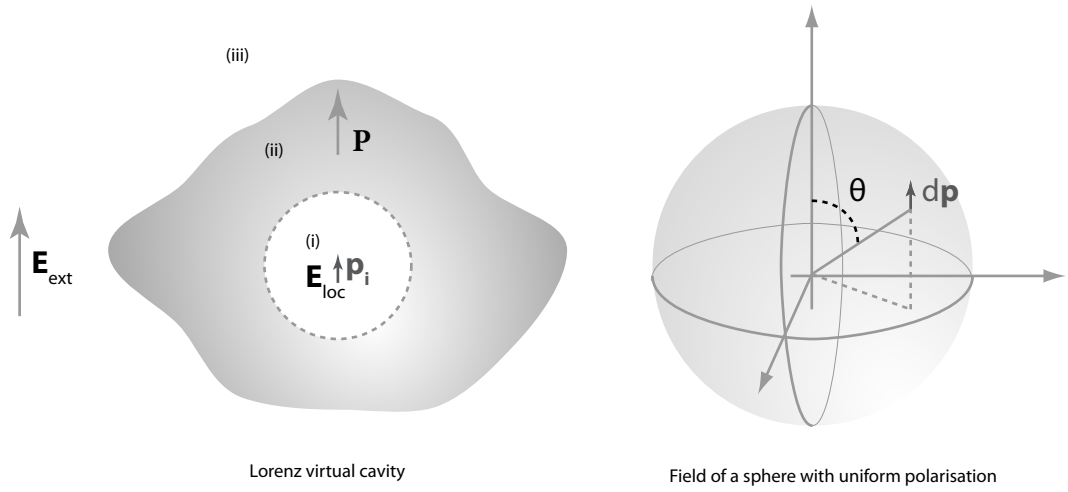

Figure 2.1: Derivation of the Lorentz-Lorenz formula with the aid of a virtual cavity.

atomic response of the material can be described by a molecular polarizability α, an intrinsic characteristic of the material. Each 'atom', or volume element (the atom is foreign to the framework of continuous electrodynamics) reacts to this local field, that is the sum of the applied field plus a *depolarisation field* that expresses the reaction of all the surrounding matter. To find the depolarisation field, we create an artificial separation of space into two regions by introducing the virtual Lorenz cavity centred about the location at which we wish to evaluate the effective field. The atoms present inside the cavity are assumed to be near neighbours of our region of interest. The contribution of these dipole elements vanishes for two particular configurations of importance: (a) a cubic lattice, (b) a random medium (*e.g.* a gas). This is because the dipolar field has a particular symmetry and for each dipole in the cavity there is a combination of dipoles that leads to a cancellation of the field at the centre [6].

The contribution of the polarised material outside the Lorenz cavity is described as a continuous distribution of polarised matter. It is equivalent to calculating the electric field created by a sphere with opposite homogeneous polarisation $\mathbf{P}$ (figure 2.1, right). We can consider the contribution of an infinitesimal volume element of dipole moment $d\mathbf{p}$ which is to be integrated over the volume of the sphere, or alternatively consider the field created by an equivalent surface charge. From $\boldsymbol{\nabla} \cdot \mathscr{P} = -\rho_{\text{pol}}$, a uniform polarisation is equivalent to a surface charge density $\sigma_{\text{pol}} = -\text{P}\cos\theta$. Because of the symmetry of the problem, it is sufficient to calculate the integral for the total field

over the polar angle θ according to Coulomb's law,

$$\mathrm{E} = \frac{-1}{4\pi\varepsilon_0}\int_{\text{sphere}} \sigma_{\text{pol}}\frac{\cos\theta}{a^2}\mathrm{d}S = \frac{\mathrm{P}}{2\varepsilon_0}\int_0^{\pi}\cos^2\theta\sin\theta\,\mathrm{d}\theta = \frac{\mathrm{P}}{3\varepsilon_0}. \tag{2.25}$$

This depolarisation field is added to the applied field $\mathbf{E}_{\text{ext}}$ to define the local field $\mathbf{E}_{\text{loc}}$ experienced by the charges inside the material,

$$\mathrm{E}_{\text{loc}} = \mathrm{E}_{\text{ext}} + \frac{\mathrm{P}}{3\varepsilon_0}. \tag{2.26}$$

From the definition of the dielectric function, we can write,

$$\mathbf{P} = (\varepsilon - 1)\mathbf{E}_{\text{ext}}, \tag{2.27}$$

and we also know that the dipole moment p is linked to the polarisation by,

$$\mathrm{P} = Np, \tag{2.28}$$

where N is the volume density of the material. Combining equation 2.27 and equation 2.28 yields the Lorentz-Lorenz formula,

$$\alpha = \frac{1}{3N}\cdot\frac{\varepsilon - 1}{\varepsilon + 2}.$$

2.2.2 The Lorentz model for dielectrics

The response of a dielectric material to light can be understood by a simple analogy with a harmonic oscillator under the influence of a sinusoidal excitation. Incident light in the form of a harmonic wave causes the electrons of the material to move in response to the electromagnetic field. The deformation of the electron density around the ionic core of the atoms forms a dipole with two opposite charges slightly displaced. The applied electric field is varying in time, and as a result the separation between the two centres of charges evolves at the same frequency. For fields with sufficiently low intensity, the displacement is linear with the field and the system behaves as a simple harmonic oscillator where the restoring force is the coulomb attraction between the electron and the ion core. Because of the proximity of neighbouring charges, there may be a frictional term in the effective motion of the charges that describes the possible collisions between charges (electron-electron, electron-defect, electron-phonon, *etc.*).

The equation of motion for an electron of mass m can be written [2, 15],

$$m\frac{\partial^2 r}{\partial t^2} + m\gamma\frac{\partial r}{\partial t} + m\beta r = -eE_0\exp(-i\omega t), \tag{2.29}$$

where the coefficient γ describes the damping mechanisms, β accounts for a restoring force due to the coulomb interaction between the electron and the nucleus, and the right hand side is the force imposed by the applied field on an electron of charge $-e$.

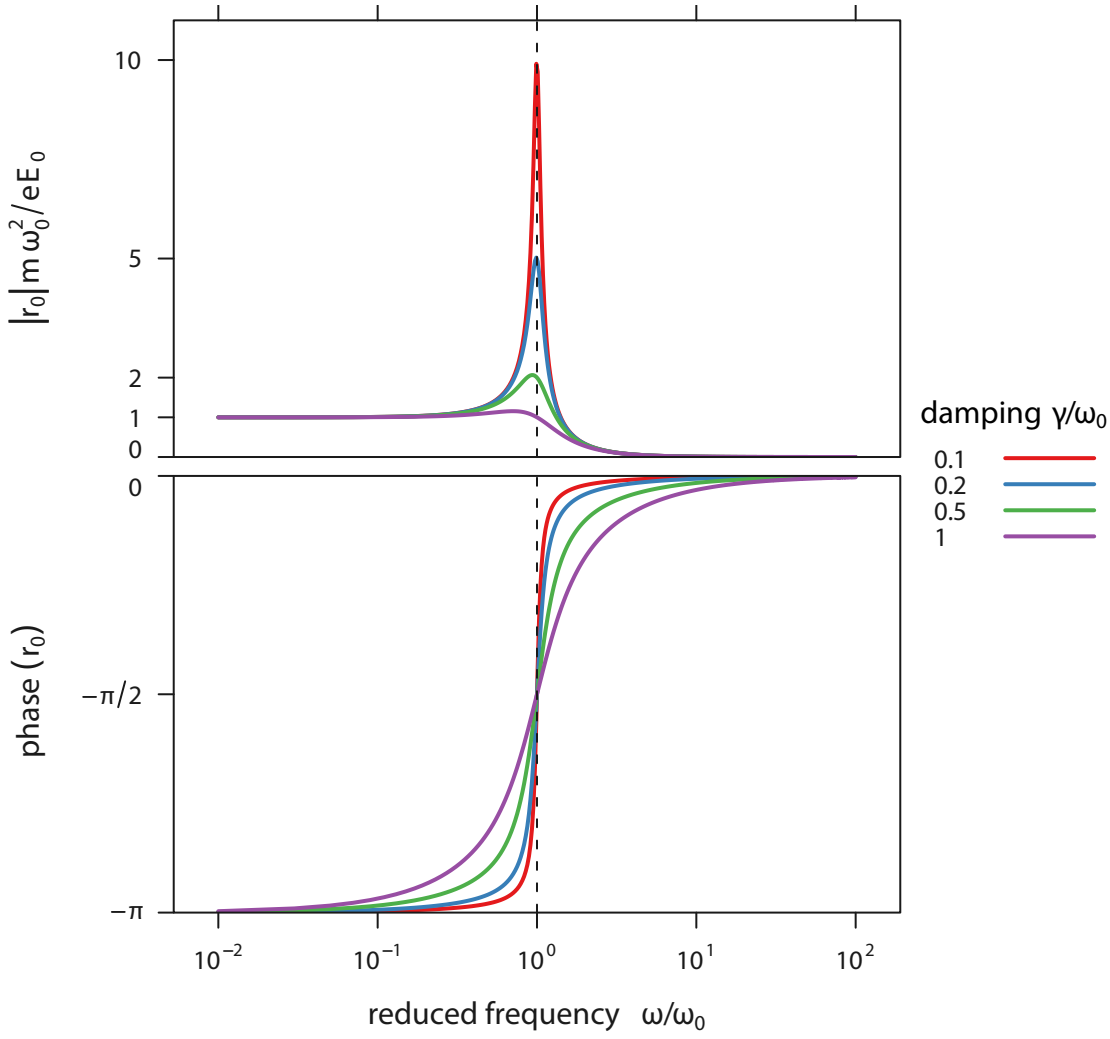

Figure 2.2: Displacement of an harmonic oscillator in the Lorentz model as a function of normalised frequency.

Because the excitation is at a frequency ω we seek a solution at the same frequency in the form $r(t) = r_0 \exp(-i\omega t)$, for which equation 2.29 becomes,

$$r_0 = \frac{eE_0/m}{(\omega^2 - \beta + i\gamma\omega)}. \tag{2.30}$$

We recognise $\sqrt{\beta}$ as being a characteristic frequency noted ω_0 for which the displacement reaches a maximum, only limited by the damping parameter γ. The real and imaginary part of the displacement according to equation 2.30 are shown in figure 2.2 for several values of the damping parameter. At low frequencies, the charges respond instantly to the perturbation, the displacement follows the applied force (opposes the field) without any phase lag. The amplitude of the oscillations is identical for all damping parameters and is simply proportional to the amplitude of the applied field. As the frequency of the light rises, the inertia of the charges leads to a decreasing phase lag between the displacement and the applied field for each light cycle. Additionally, the amplitude of

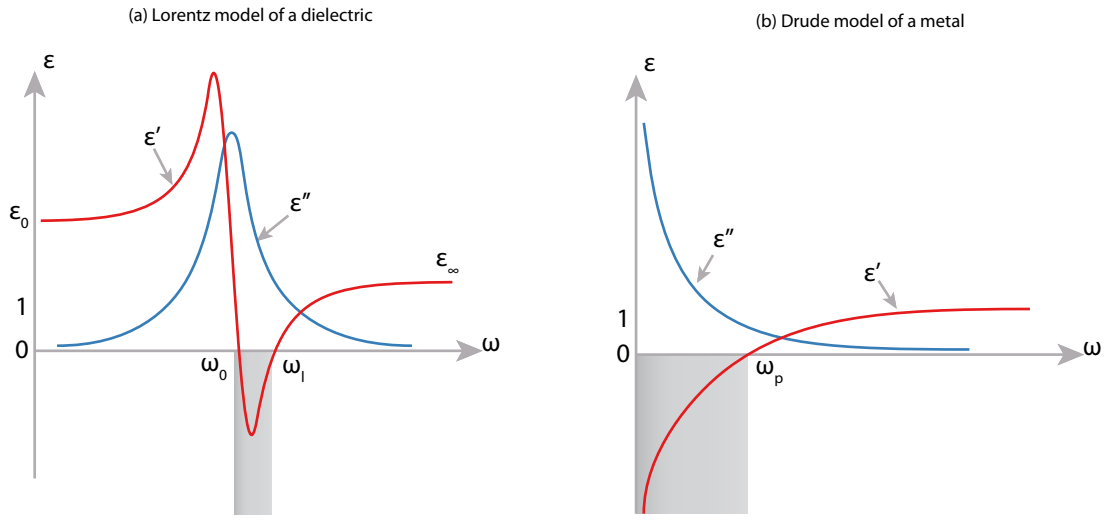

Figure 2.3: Schematic dielectric function of a dielectric and a metal according to the Lorentz and Drude models. The greyed zones correspond to negative values of the dielectric function where waves cannot propagate in the medium.

the oscillations of the charges increases in magnitude and reaches a maximum when the excitation frequency corresponds to the natural frequency of the free oscillator. The phase-lag is −90°, and the transfer of energy to the oscillator is maximum: the work done on the charges per light cycle is most efficient when the maximum field occurs at the minimum velocity of the charged particle. At $\omega = \omega_0$, the harmonic oscillator is in resonance with the incident field: the driving force excites an eigen-frequency of the system, *i.e.* the natural frequency of oscillation which is the solution to the source-free, homogeneous equation of motion. The *quality factor* $Q = \omega_0/\gamma$ measures the peak intensity at resonance.

For frequencies higher than the resonant frequency of the oscillator, the phase lag increases and tends toward 0° at large frequencies: the electrons cannot follow the force applied by the incident field. The work done by the field on the charges and the amplitude of the oscillations tend towards zero and the material become transparent to radiation for all values of the damping parameter.

The displacement of the charges corresponds to a microscopic dipole moment $p = e^2 r_0$. The macroscopic average of the microscopic dipole moments is described by the polarisation $P = Np = \varepsilon_0 \chi E_0$, where N is the volume density of the electrons in the material and χ the susceptibility. Using $\chi = \varepsilon - 1$ we obtain,

$$\varepsilon = 1 - \frac{\omega_p^2}{(\omega^2 - \omega_0^2) + i\gamma\omega}, \tag{2.31}$$

where we define the *plasma frequency* $\omega_p = \sqrt{Ne^2/(m\varepsilon_0)}$. Figure 2.3 presents the frequency dependence of the dielectric function for dielectrics according to the Lorentz model of equation 2.31 (left panel). For comparison the right panel describes the dielectric function of metals according to the Drude model as a limiting case where $\omega_0 \to 0$.

The plasma frequency delimits the spectral region below which electromagnetic cannot propagate in the material [16]. A negative real part of the dielectric function implies that the material will

prevent penetration of electromagnetic radiation, resulting in a strong reflectivity. Physically, the polarization $P = \varepsilon_0 \chi E$ is of opposite sign with respect to the incident field so the scattered field cancels out the incident field inside the material. From equation 2.18, a large and negative value of ε' corresponds to a large imaginary part of the refractive index. A small portion of the incident wave may enter the bulk material as a decaying exponential, the *skin depth* effect, this field is responsible for absorption and does not propagate inside the material. The Maxwell equation $\nabla \cdot \mathbf{D} = 0$ yields two possible solutions: $\nabla \cdot \mathbf{E} = 0$ which describes the possible existence of a transverse electromagnetic mode in the material, or $\varepsilon' = 0$ which is the condition for longitudinal, collective oscillations of the charges in the material. A zero of the dielectric function therefore describes collective, longitudinal oscillations of the Fermi sea at the frequency ω_p. These oscillations define the bulk plasmon resonance of the material [15, 16], which cannot be excited by light due to the transverse nature of electromagnetic waves. A beam of electrons can however be used to probe this bulk mode of the charge density, and led to the first experimental observation of bulk and surface plasmons by Ritchie [17]. Similar collective oscillations can occur at an interface, the frequency of these *surface plasmon modes* is lower than ω_p due to the additional depolarisation field arising from the accumulation of charges at the boundary. The surface plasmon dispersion and its relation to the boundary of the material will be discussed in section 2.3.1.

2.2.3 Lorentz-Drude model

A metal is characterised by the presence of conduction electrons that move freely in the bulk material. These free charges will respond strongly to an applied EM field, but in contrast to the Lorentz model the restoring force is absent. The incident light may also excite bound electrons if the excitation energy is sufficient, resulting in *interband transitions*.

The equation of motion for the free electrons in a conductor subject to an applied field can be written [18],

$$m\frac{\partial^2 r}{\partial t^2} + m\gamma\frac{\partial r}{\partial t} = -eE_0\exp(-i\omega t), \tag{2.32}$$

where the restoring force entering equation 2.29 has been removed. The damping parameter γ expresses a frictional force arising from collisions between electrons and defects or phonons. This frictional force is related to the mean free path of the electrons, and can be expressed in terms of the average time between collisions τ. The average change of velocity acquired by an electron after a number of collisions proportional to $1/\tau$ (or, equivalently[1], the average over a number of electrons at a given instant) reads,

$$\frac{d\bar{v}}{dt} = \gamma\bar{v}, \tag{2.33}$$

with $\gamma = 1/\tau$ defined as the frequency of collisions. The average change of momentum $m\,d\bar{v}/dt$ is homogeneous to a force that is inversely proportional to the velocity of the charges and the time between collisions. The damping of the Drude model is therefore a measure of the inverse scattering rate of the electrons moving in the crystal. γ is related to the mean free path l_{eff} of the electrons inside the material by $\gamma = v_F/l_{\text{eff}}$ with v_F the Fermi velocity.

[1] considering the collisions as a Markov process, where the motion of charges is a random path with no memory of the previous state after each collision

The dielectric function describing the response of the free electrons can be obtained directly from equation 2.31 by setting $\omega_0 \to 0$ (vanishing restoring force),

$$\varepsilon = 1 - \frac{\omega_p^2}{\omega^2 + i\gamma\omega}. \tag{2.34}$$

A comparison of equation 2.34 and the experimental dielectric function of gold in the visible is shown in figure 2.5. The values of ω_p and γ for gold can be estimated from their definitions ($\hbar\omega_p = 8.95eV$, $\hbar\gamma = 65.8meV$), however the influence of the bound electrons leads to a poor agreement. An alternative approach is considered here by treating ω_p and γ as free phenomenological parameters that are retrieved from an optimization procedure using equation 2.34 and the measured values for ε in the visible range. We note that the plasma frequency in the Drude model

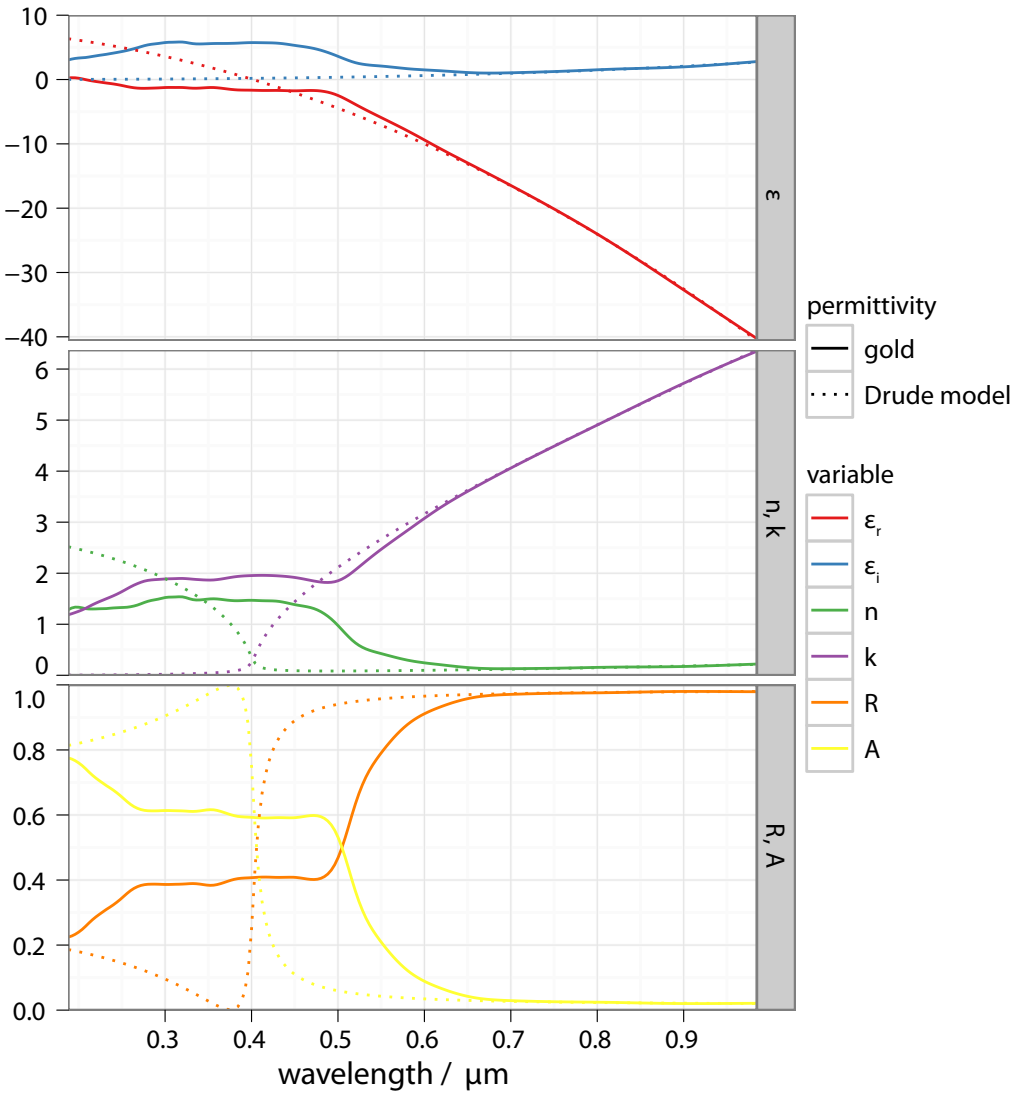

Figure 2.4: Reflection, absorption, and optical constants of gold in the visible. The dielectric function for the solid lines is taken from Johnson and Christy [19]. The dotted lines are for a Drude model with parameters fitted to the data in the range 0.6 µm–1 µm.

corresponds to the condition $n' = n''$ as expected from equation 2.18.

Because the free electrons are able to screen an incident electromagnetic field very efficiently, the fields cannot propagate inside the bulk metal. The bottom panel of figure 2.4 displays the reflectance and absorbance properties of gold in the visible, and of the Drude model for comparison. The reflectivity is approaching 1 for the low-energy region of the visible and IR spectrum. The absorption manifests itself as a sharp edge on the high-energy regime (below 500 nm) for gold, while the Drude model exhibits a similar behaviour at shorter wavelengths due to the different plasma frequency.

Within the frequency range of negative ε', the fields decay exponentially in a typical *skin depth* of less than a wavelength. This spatial confinement is associated with the existence of an inhomogeneous evanescent wave at the surface which, when bound to the surface, yields an exponentially decaying field on the dielectric side of the interface. The spatial confinement of the fields in gold structures is in fact a consequence of the strong attenuation of the fields by the surface charge that screens the field inside the material.

A good metal is sought to make efficient radio-wave antennas because the efficiency of radiation depends on the Joule loss due to the finite conductivity of the material. Similarly, gold at visible and infra-red frequencies is able to support currents with much less Joule loss than copper for instance, and is therefore a good *plasmonic material*.

When the displacement vanishes ($E + P = 0$), the only electromagnetic mode that can be supported by the bulk material is a longitudinal wave, the *bulk plasmon*. Similarly, the presence of an interface allows the possibility of additional surface modes that depend on the depolarisation field created by the charges accumulating at the boundary. These *surface plasmon* modes may be excited by light under appropriate conditions (section 2.3.1).

A good agreement between a Drude model and the measured dielectric function can be obtained in the wavelength range 0.65 µm–1.2 µm with an optimisation procedure considering the constants γ and ω_p as free parameters. The best fit over this range of wavelength for both the real and imaginary parts is shown in red in figure 2.5 with the parameters $\omega_p = 1.36 \times 10^{16}$ rad/s, $\gamma = 1.45 \times 10^{14}$ rad/s. A large discrepancy is however observed in the high energy side of the visible range and in the UV regime. The cause for this resides in the contribution of the bound electrons that undergo interband transitions when the incident light has an energy corresponding to this gap. The response of the bound electrons is not described in the Drude model. Two possible routes have been envisaged in this thesis to obtain a more realistic model for the properties of gold used in the calculations as illustrated in figure 2.5. (i) The experimental data from Johnson and Christy [19] can be interpolated by a smooth curve (cubic spline) which can provide a good estimate of the dielectric function at any given frequency in the range of interest. Unless explicitly stated otherwise, I have used this approach in the calculations shown in this thesis. Although the experimental values of the permittivity have the advantage of providing an accurate description of the dielectric function, the Drude model employed above exposes some physical insight into the functional form of the dispersion of the dielectric function that is missing from an *ad hoc.* interpolation procedure. To remedy this, Etchegoin *et al.* [20] proposed an accurate analytical formulation for the optical properties of gold that complements the Drude model with an adequate description of interband

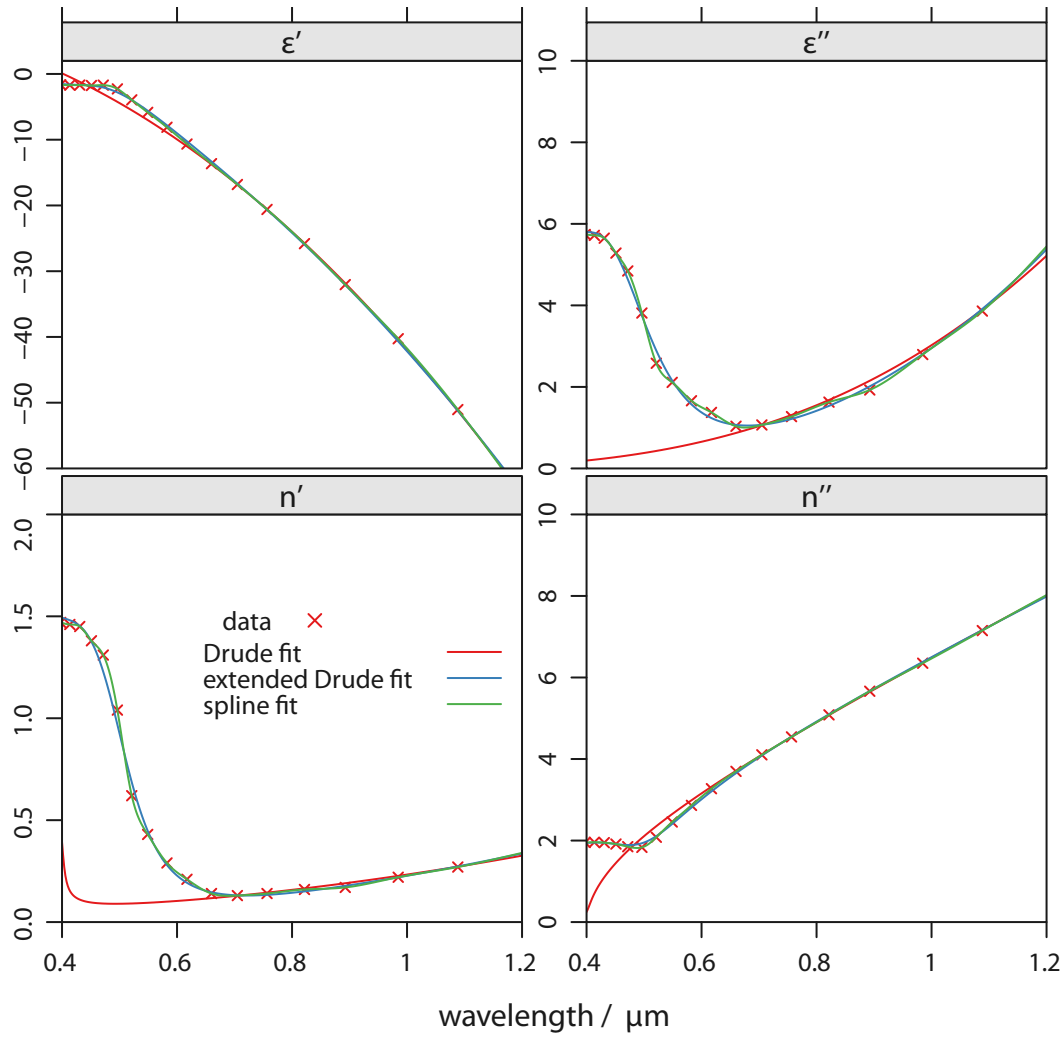

Figure 2.5: Dielectric function of gold, from Johnson and Christy [19] (points), a Drude model fit, and a spline fit.

transitions The result of their approach is a model with several parameters that can be adjusted through comparison to the experimental data by an optimization procedure. The best fit result in our range of interest is shown in blue in figure 2.5, and provides a remarkable good description of the dielectric function of gold. The advantage of this approach is that dielectric function is described in terms of a few parameters that have a physical interpretation. In particular, the damping parameter from the Drude model can be modified to account for increased scattering rate in small nanoparticles as I will discuss in chapter 4.

2.3 Optics of thin films

Because the electromagnetic field can penetrate only to a small distance in bulk gold, the design of interesting plasmonic components relies on the use of sub-wavelength structures, where the dimensions can be tuned to modify the optical response of the bulk material. The simplest example of such a system is a subwavelength gold film supported by a dielectric medium. I will discuss

in this section how the optical properties of thin films of dielectric and metallic materials can be understood from a generalisation of the Fresnel equations. Surface plasmon-polaritons will be naturally introduced as a particular electromagnetic mode supported by such structures.

The boundary conditions for the electric and magnetic fields can be summarised in the Fresnel coefficients that describe the reflection and transmission of electromagnetic waves at the interface between two media. The waves may not be homogeneous — when the dielectric function is negative, or simply in the case of total internal reflection, the electromagnetic field takes the form of an evanescent wave on one or two sides of the interface. The Fresnel coefficients are still valid, but involve complex angles that have a less intuitive physical interpretation. A convenient formulation of the Fresnel coefficients uses the in-plane wave-number on both sides of the interface as the invariant of propagation. For a single interface from 1 to 2 with normal along the z direction, the Fresnel coefficients read [2, 18],

$$\begin{aligned} r_{01}^{p} &= \frac{\varepsilon_2 k_{z1} - \varepsilon_1 k_{z2}}{\varepsilon_2 k_{z1} + \varepsilon_1 k_{z2}}, & r_{01}^{s} &= \frac{\mu_2 k_{z1} - \mu_1 k_{z2}}{\mu_2 k_{z1} + \mu_1 k_{z2}} \\ t_{01}^{p} &= \frac{2\varepsilon_2 k_{z1}}{\varepsilon_2 k_{z1} + \varepsilon_1 k_{z2}} \sqrt{\frac{\mu_2 \varepsilon_1}{\mu_1 \varepsilon_2}}, & t_{01}^{s} &= \frac{2\mu_2 k_{z1}}{\mu_2 k_{z1} + \mu_1 k_{z2}}. \end{aligned} \tag{2.35}$$

Note that,

$$r_{ij} = -r_{ji}, \tag{2.36}$$

and, for either polarisation,

$$t_{ij} t_{ji} = 1 - (r_{ij})^2. \tag{2.37}$$

From the discussion of the Ewald-Oseen theorem, we understand the Fresnel coefficients to express the response of the bulk material to an incident wave, even though they appear to relate the fields only at the boundary between two media. The refracted wave and reflected wave are the result of a coherent response of the material in the depth of the sample. A straight-forward verification of this is obvious in the optical response of thin films. A multi-layered structure as shown in figure 2.3 will generally modify the reflection that would be expected for the first interface alone (between two semi-infinite media). In fact, the reflection and transmission can be modulated from 0 to 1 by tuning the underlying structure. If the material participating to the generation of the reflected and transmitted waves has a thickness commensurate with half the wavelength inside the medium, the net effect of the structure on the incident light can be a constructive or destructive interference. Further, a multi-layered structure with a periodic repetition of the index variation will result in a modulation of the effective reflectance and transmittance with a direct correspondence to the spatial frequency [21]. This is the basis of the fabrication of anti-reflection coatings (also known as Bragg stacks) widely used in optics. In the next section I will discuss the optical properties of such structures, with a particular attention to subwavelength, metallic films.

Reflectivity of a layer

From the viewpoint of ray optics, a thin layer will support an infinite number of internal reflections (absorption and irregularities will however reduce the intensity in a physical situation). The infinite series of reflected orders can be expressed in the form a geometric sum, leading to a

closed form formula as shown below. An incident plane wave with amplitude A impinges on the

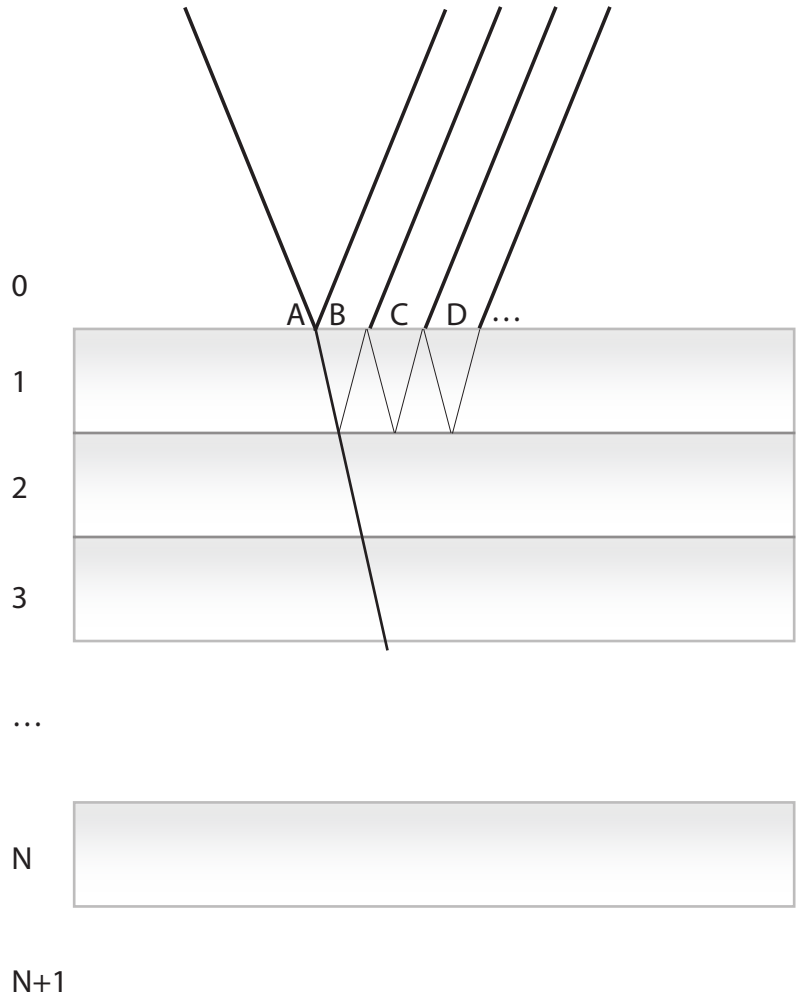

Figure 2.6: Schematic of reflection and transmission by a multilayer slab. A few reflected orders are noted 'A', 'B', 'C' and 'D' for the first interface.

first interface. It can be reflected, $B = r_{01}A$, or transmitted. The total response of the slab can be obtained by following each order of reflection inside the slab ('C', 'D', …).

Upon transmission, the wave amplitude is $t_{01}A$. Application of Fermat's principle yields a phase change $\Delta\phi = k_{z1}d$ when the wave hits the second interface. The reflection coefficient at this interface is r_{12}. The partial wave reflected from this path, noted 'C', is therefore $C = t_{10}t_{01}r_{12}\exp(2ik_{z1}d)A$.

Similarly, in 'D',

$$D = t_{10}t_{01}r_{10}r_{12}^2\exp(4ik_{z1}d)A.$$

And, for the j^{th} partial wave,

$$t_{10}t_{01}r_{12}^j r_{10}^{j-1}\exp(2ijk_{z1}d)A.$$

The wave reflected by the slab is the sum of these contributions,

$$r_{\text{slab}}A = B + C + D + \cdots = \left[r_{01} + t_{10}t_{01}r_{12}\sum_{j=0}^{\infty} r_{12}^{j} r_{10}^{j} \exp(2j\,i\,k_{z1}d) \right] A.$$

For clarity, I introduce $\beta = r_{12}r_{10}\exp(2i\,k_{z1}d)$. The summation of all partial waves is thereby expressed as a geometrical sum,

$$r_{\text{slab}} = r_{01} + \left(t_{10}t_{01}r_{12}\exp(2i\,k_{z1}d)\right)\sum_{j=0}^{\infty}\beta^{j}.$$

Recalling that the sum of a geometric series of common ratio q is $\frac{1}{1-q}$, we can write,

$$r_{\text{slab}} = r_{01} + \frac{t_{10}t_{01}r_{12}\exp(2i\,k_{z1}d)}{1 + r_{12}r_{10}\exp(2i\,k_{z1}d)}.$$

Using the relation 2.37 and the substitution $r_{10} = -r_{01}$ we finally obtain,

$$r_{\text{slab}} = \frac{r_{01} + r_{12}\exp(2i\,k_{z1}d)}{1 + r_{01}r_{12}\exp(2i\,k_{z1}d)}. \tag{2.38}$$

For the transmission, one obtains,

$$t_{\text{slab}} = \frac{t_{01}t_{12}\exp(i\,k_{z1}d)}{1 + r_{01}r_{12}\exp(2i\,k_{z1}d)}. \tag{2.39}$$

When `N` layers are stacked together, the reflection coefficient of the structure can be found by applying recursively the preceding formula for a single layer. This amounts to considering one of the reflection coefficients to be the effective reflection accounting for all the layers behind.

The optical response of a subwavelength gold film is presented in figure 2.7 for measured values of the gold dielectric function, and for a best-fit Drude model (equation 2.34). In contrast to figure 2.4, the transmittance is non-zero even though the dielectric function of gold is negative over this frequency range. This is because the very thin layer of metal cannot completely screen the incident field, which acts as a tunnel barrier for the incident light [22]. The transmittance peaks at around 500 nm — thin gold films appear blue in transmission, and the intensity of this peak decreases as a function of film thickness. The absorbance and reflectance of gold are only mildly modified by the thickness (ignoring the change in dielectric function for very thin films below 10 nm typically). The Drude model however exhibits a strongly oscillating spectrum in the near-UV regime, with a frequency of beats that increases with film thickness. These (here artificial) modes are a result of the multiple interference of the light inside the film that forms a Fabry-Perot etalon. Because the dielectric function of our Drude model is almost purely real and positive in this region, little loss occurs that would dramatically damp the beating between multiple orders of reflections.

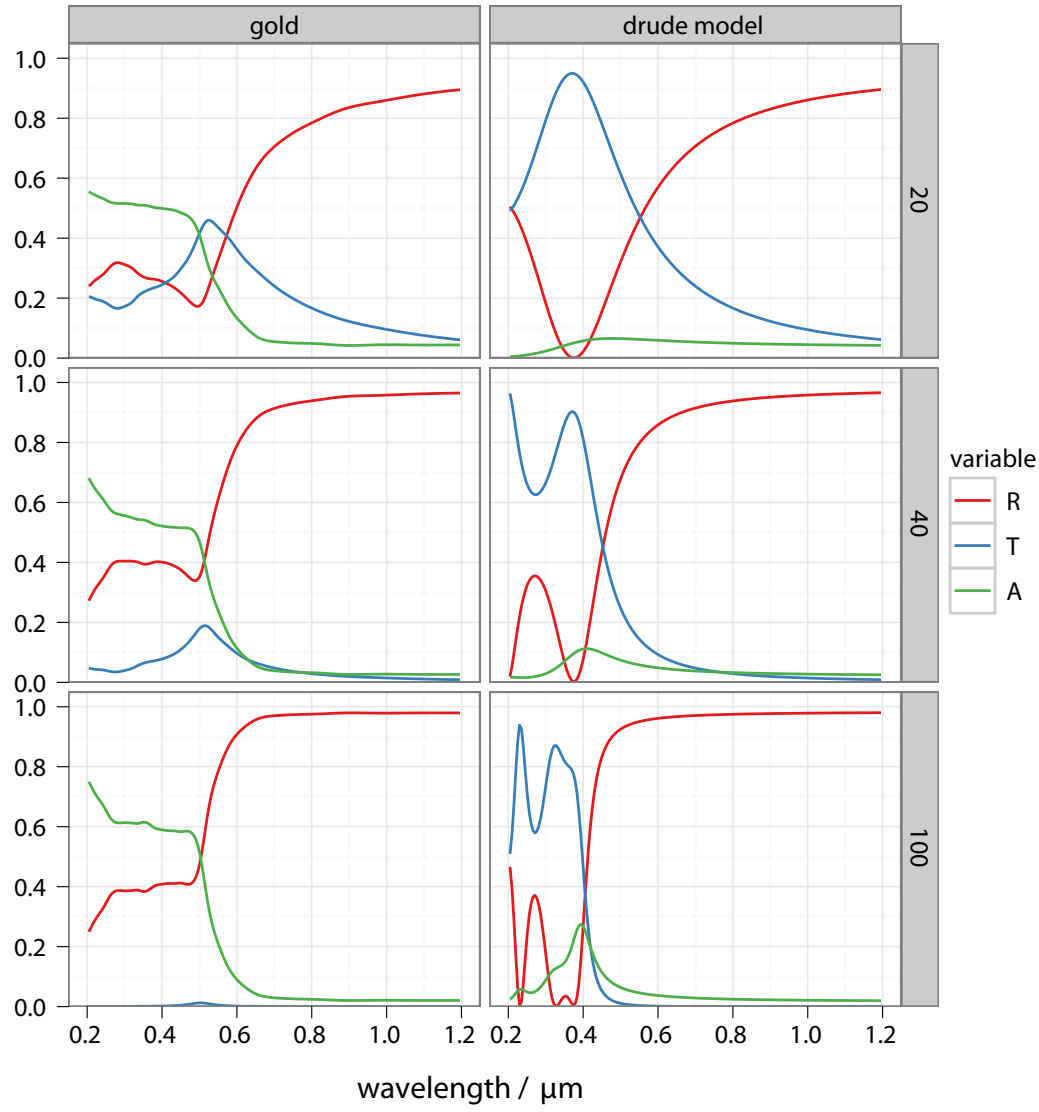

Figure 2.7: Modelled reflectance, transmittance and absorbance of a thin film for several film thicknesses (20 nm, 40 nm, 100 nm) for gold and a Drude model fitted to the data in the visible (parameters $\omega_p = 1.34 \times 10^{16}$ rad/s, $\gamma = 1.12 \times 10^{14}$ rad/s, $\varepsilon_{\mathrm{DC}} = 8.1$).

2.3.1 Surface plasmons

The interface between a dielectric and a metal introduces an abrupt change of the polarisation that may lead to a confinement of the charge density associated with a surface electromagnetic mode known as *surface plasmon*. The coupling between an electromagnetic field and the collective oscillation of the charge density forms a surface plasmon-polariton. This particular electromagnetic mode arises at the zero of the complex reflectivity (equation 2.35),

$$\varepsilon_2 k_{z1} - \varepsilon_1 k_{z2} = 0. \tag{2.40}$$

At the interface between two dielectrics, this condition describes the Brewster angle, where p-polarised light is not reflected at the interface. With a metal of negative permittivity on one side, the condition of equation 2.40 occurs for a complex wave-number (or complex angle), which means that no free incident light can directly couple to this surface mode. The conservation of the total wavenumber across the interface reads,

$$k_{\parallel}^2 + k_z^2 = \varepsilon k^2. \tag{2.41}$$

This equation combined with equation 2.40 provides the dispersion relation for the surface plasmon polariton,

$$k_{\mathrm{SPP}} = k_0 \sqrt{\frac{\varepsilon_m \varepsilon_d}{\varepsilon_m + \varepsilon_d}}. \tag{2.42}$$

Because of the opposite sign of the dielectric functions $\varepsilon_m < 0$ (metal) and $\varepsilon_d > 0$ (dielectric), free charges are trapped at the interface (figure 2.8) [23], and the normal component of the wave-vector is purely imaginary. The solution to equation 2.40 is therefore a true surface mode [18].

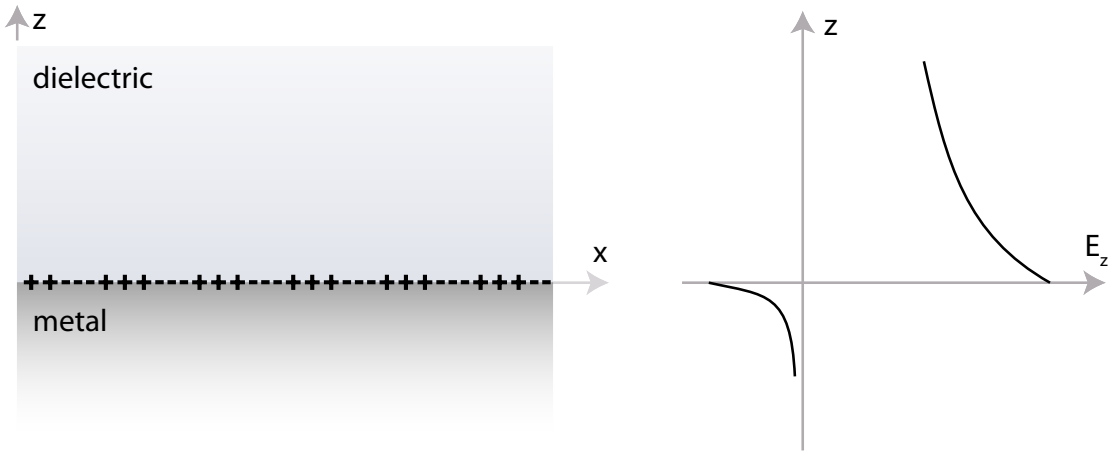

Figure 2.8: Schematic representation of SPPs at a metal dielectric interface.

A schematic of this dispersion relation is plotted in figure 2.9. The low-energy part of the curve lies very close to the light line $\omega = k_0 c$ that describes a grazing photon, uncoupled to the material. As the in-plane wave-number increases (optical regime), the dispersion of the SPP departs from uncoupled photons — the polariton character of the mode becomes clearer as the interaction with the material augments. Because of the high index contrast at long wavelengths only a small portion of the field can penetrate the metal, while at optical wavelengths the index mismatch decreases and allows for a larger penetration in the metal. Surface plasmon-polaritons are characterised by an exponential decay of the field away from the interface,

$$E_z \sim \exp(i k_z z). \tag{2.43}$$

where k_z stands for the (purely imaginary) component of the wavevector in the medium (metal or dielectric).

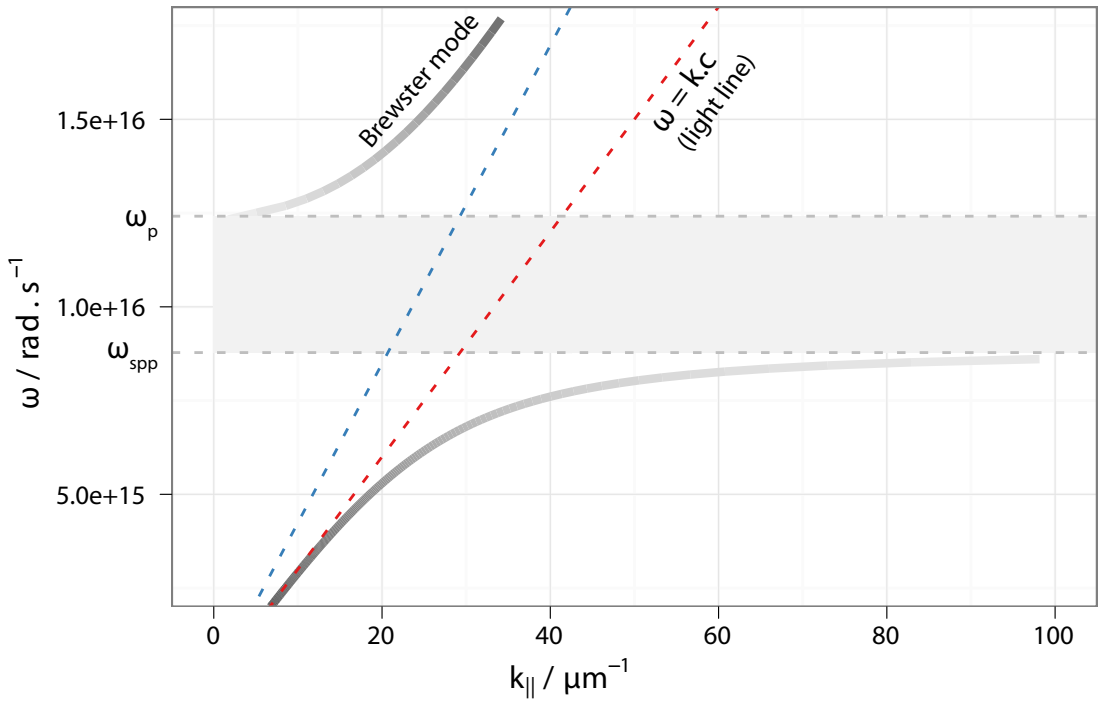

Figure 2.9: Dispersion of planar SPPs at a metal / dielectric interface. The dashed red line represents the light line (free propagating light at grazing incidence). The grey curve is the dispersion of the surface mode. The grey scale (black to white) indicates the imaginary part of the SPP wave-number (dark represents a purely real wave-number, white indicates strong damping in the propagation). The dashed blue line indicates the asymptote to the Brewster mode (upper branch of the dispersion curve).

Figure 2.8 depicts the character of the surface plasmon polariton at the interface between a metal and a dielectric. A collective oscillation of the charges trapped at the interface is associated with an electromagnetic mode confined to the interface.

In figure 2.9 the SPP never crosses the light-line, it is therefore impossible for free-propagating light to couple directly with SPPs. The momentum mismatch can be overcome by the use of prism coupling (discussed below), grating coupling, or scattering coupling [24]. The asymptotic limit ω_{SPP} corresponds to a standing wave — the dispersion of the mode flattens at high in-plane wavenumber, indicating a low group velocity.

SPPs can propagate along the interface, the decay length characterising their decay along the interface is related to the imaginary part of the in-plane wave-vector that arises from the imaginary part of the dielectric function of the metal (Joule heating) and the radiative damping due to possible out-coupling to free space radiation.

An experimental scheme was proposed by Kretschmann to allow for optical excitation of the surface plasmon polariton on thin metallic films, and is described in figure 2.10. The physical mechanism describing the excitation of surface plasmons on a thin metallic film is well understood, as detailed in the monograph of Raether [24], but the physical explanation can be subtle [25]. A deceptively simple and rigourous description of the optical response of the system can be done using the Fresnel coefficients, as shown above. It is however rather difficult to extract the physical mean-

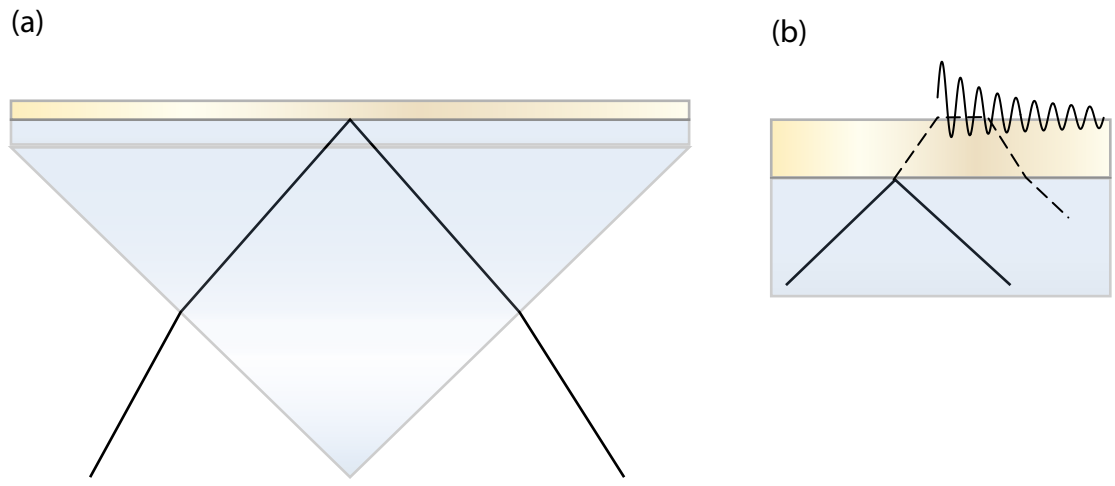

Figure 2.10: Excitation of SPPs at a metal dielectric interface using the Kretschmann configuration.

ing of the surface plasmon polariton solution from this formulation — it is a pole in the reflectance of the system that describes the existence of electromagnetic eigenmodes of the system. In physical terms, the excitation of SPPs by the incident light will occur when the in-plane momentum of the light inside the prism matches the momentum of the SPP mode of the same energy,

$$n.\sin\theta_{\text{int}} = \sqrt{\frac{\varepsilon_m \varepsilon_d}{\varepsilon_m + \varepsilon_d}}. \tag{2.44}$$

The incident light is converted into the surface mode when the conservation of energy and momentum are both satisfied. The coupling condition in the Kretschmann geometry is perturbed from equation 2.44 as the dispersion of the mode is modified by the presence of the second interface of the thin metallic film. In figure 2.11 the calculated reflectivity of a 50 nm gold film on a prism, using the recursive Fresnel coefficients presented above. The dispersion of the surface plasmon mode calculated from equation 2.42 using the permittivity from Johnson and Christy is displayed as a dotted line, and follows a marked minimum in the reflectivity of the system corresponding to the excitation of the surface plasmon by the incident light. The light-line (dashed-red line) is also visible as a maximum of reflectivity. In the high frequency regime (wavelengths below 500 nm) the reflectivity uniformly drops and the plasmonic feature disappears: the presence of interband transitions leads to a large absorption, and a large damping of the SPP.

The drop in reflectivity at the condition of excitation of the SPPs can be understood by the following argument. The incident light gains momentum inside the prism ($k = n k_0$). The reflected light that is detected outside the prism can come from two reflection channels,

1. Upon total internal reflection (for angles above the critical edge), part of the incident light is reflected at the metal/prism interface

2. As in frustrated total internal reflection, there is a probability that the incident light couples to the surface plasmon polariton on the other side of the thin metallic film. The light converted into this surface mode can decay in two forms: non-radiative (Joule heating of the film), or

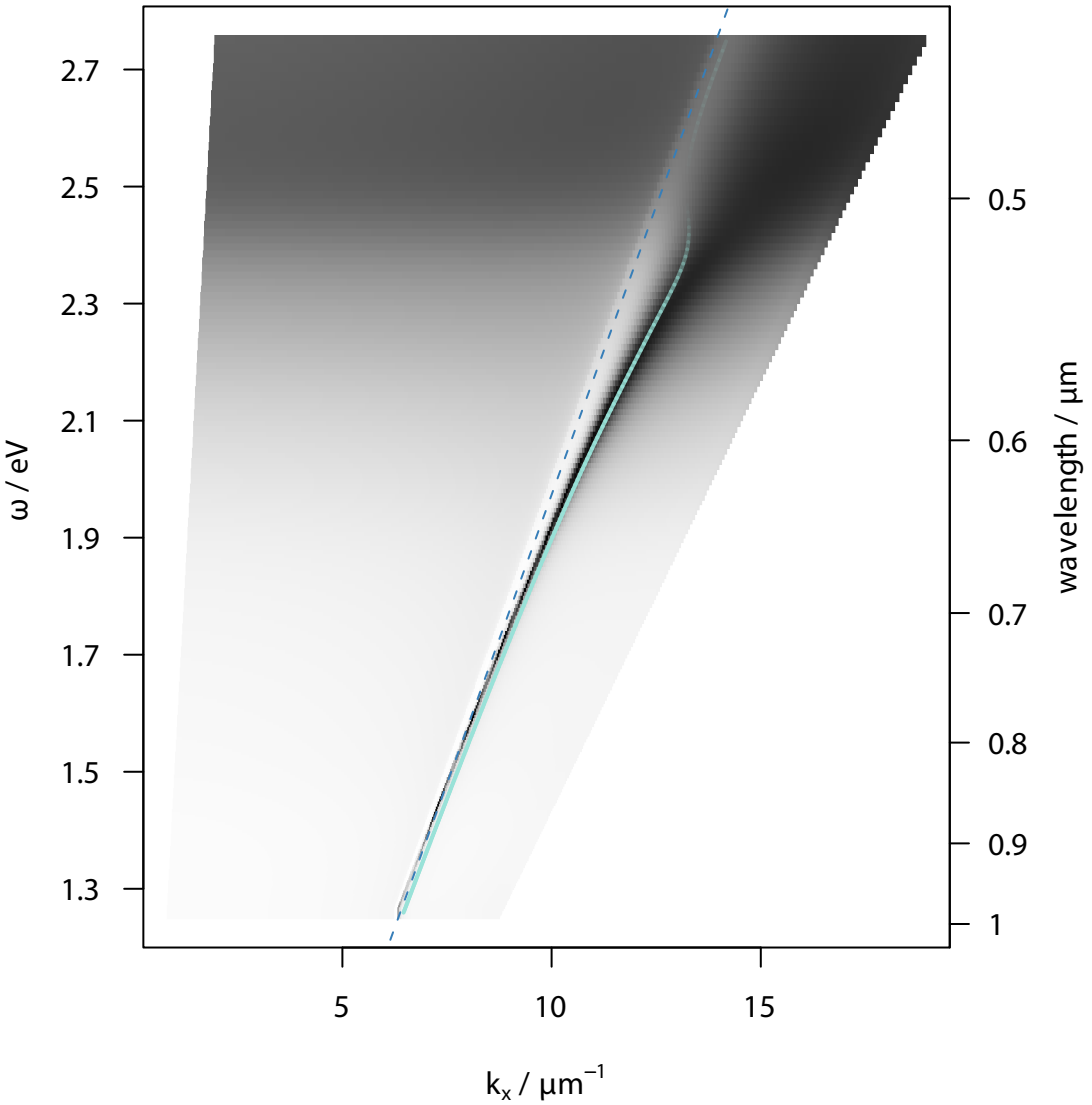

Figure 2.11: Calculated dispersion of the reflectivity of a thin gold film (permittivity from Johnson and Christy). The dark regions correspond to low reflectivity (black is 0, white is 1). The blue dashed line is the light-line in the surrounding medium. The green curve is the solution to the dispersion relation 2.44 for a semi-infinite gold film.

radiative. It is clear that if the light inside the prism had a momentum commensurate with the SPP mode, the reverse conversion from SPP to light can occur: the surface plasmon mode re-radiates light in the prism.

It is the interference of these two channels that is measured by the detector (therefore, their relative phase and amplitude matter). When the thickness of the film is such that the radiative and non-radiative losses are equal, 100% absorption can occur. The energy is then completely converted into heat inside the film. The existence of an optimum thickness stems from the balance of two opposite constraints: a thick film will allow very little overlap between the incident field and the SPP mode; a film too thin will see a higher amplitude of the second channel (SPP over-damped, re-radiating light). Figure 2.12 presents the experimental observation of the surface plasmon po-

lariton in a Kretschmann geometry using a silver film at a wavelength of 632.8 nm. This angle scan

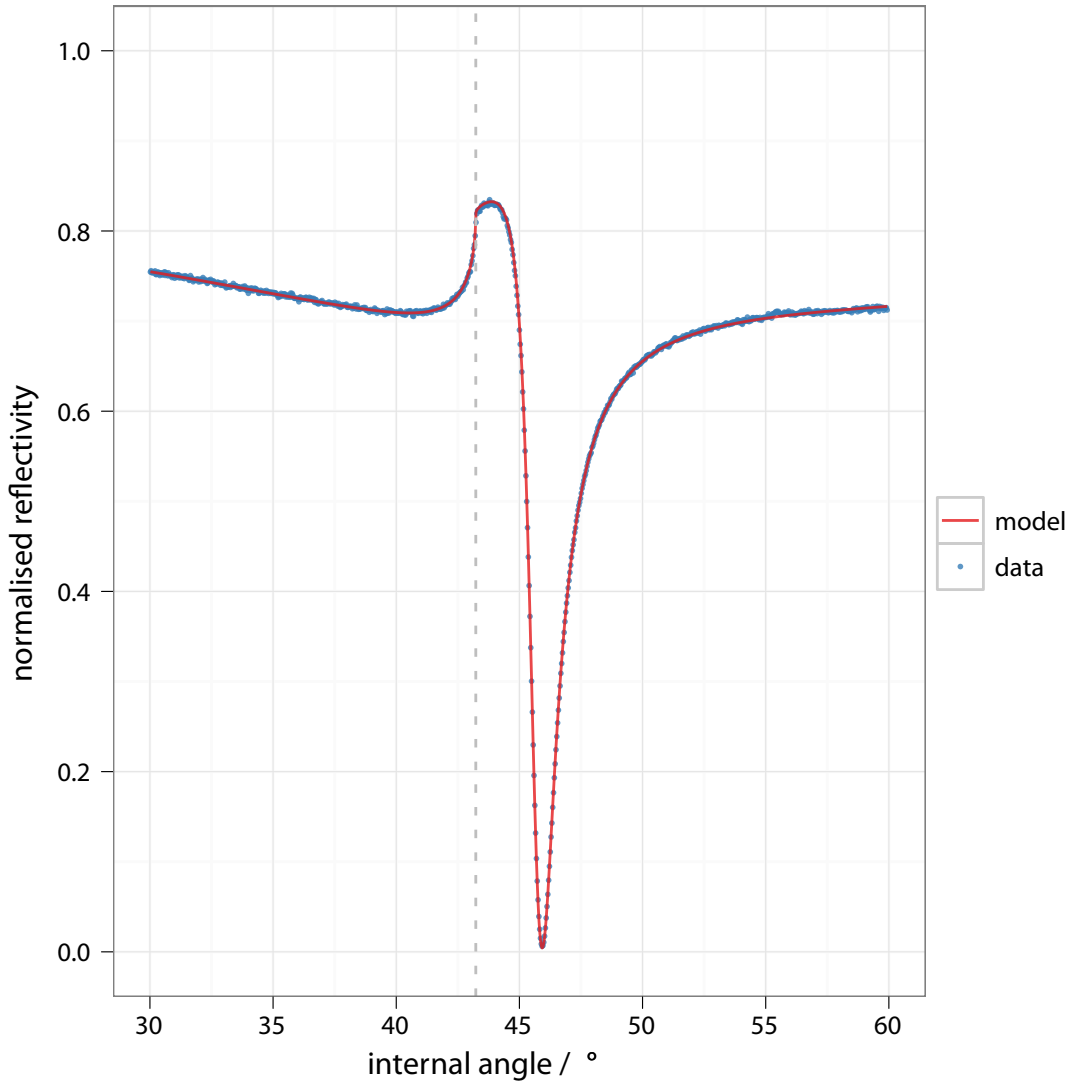

Figure 2.12: Excitation of SPPs at a metal dielectric interface using the Kretschmann configuration (60° silica prism $n = 1.46$, $\lambda = 632.8\,\text{nm}$). The fitted parameters for this silver film are $\varepsilon = -11.9 + 1.3i$, thickness 45.3 nm.

corresponds to a horizontal cross-section of the dispersion diagram of figure 2.9 (constant energy). When the incident angle in the prism is larger than the critical angle for total internal reflection, the reflectivity of the silver film increases to unity (the scaling of the experimental data comes from the reflectivity at the interface air/prism). At the angle where equation 2.44 is satisfied, the reflectivity drops sharply as the incident light is converted into the surface plasmon mode. The width of this mode is related to the radiative and non-radiative decay routes for the surface plasmon. An optimization routine based on the use of the recursive Fresnel coefficients can be used to extract the parameters of the film, namely the film thickness and the complex permittivity. The best-fit result is shown in figure 2.12, in very good agreement with the data.

2.4 Nanoparticles

Surface plasmons were introduced in the preceding section as a solution for the Maxwell equations when the presence of an interface adds a restoring force acting on the free electrons of a metal [26, 27]. The depolarisation field resulting from the accumulation of charges at the boundary between the metal and a dielectric will therefore be modified if a curvature is introduced. The influence of the curvature on the surface charge is the gist of the link between planar surface plasmon polaritons and the *particle plasmons* that are at the centre of the work presented in this thesis.

By changing the dimensionality of the system (from a 2-dimensional, infinite interface to a 3-dimensional scatterer), the charge is now subject to a different constraint that is tied with the shape and size of the particle. In particular, the depolarisation field is linked to the shape of the particle — the precise expression will be treated in chapter 3. Instead of searching for a pole in the reflectance — a concept that was applicable to an infinite surface but not to a subwavelength particle, the localised plasmon resonance occurs at a pole in the *polarizability* of the scatterer (equation 3.25) with an appropriate factor accounting for the influence of the shape. A very elegant illustration of the nature of the modes supported by the charge density confined in a nanoparticle was discussed by Hohenester *et. al.* [28]. They considered the equation of motion for the charge density when

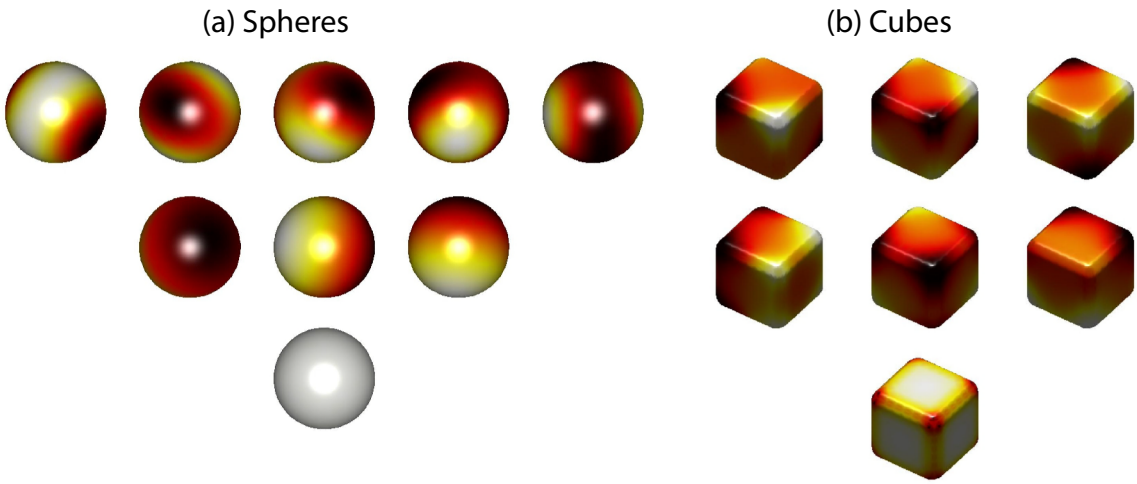

Figure 2.13: Illustration of the normal modes adopted by the charge density on spherical and cubic nanoparticles. (From [28], reprinted with permission).

constrained by the boundary of a nanoparticle much smaller than the wavelength of the incident light. In this approximation, the charge density is found to obey a quantization constraint in the form of a discrete set of eigenmodes: the charge density adopts a configuration around the particle that depends on the shape and size of the particle. An incident electromagnetic wave will excite a combination of these modes that in turn re-radiate resonantly in the visible, leading to a strong scattering and absorption of such particle-plasmon supporting particles.

A direct experimental observation of such oscillations of the charge density in nanometre sized particles was recently achieved in a comparison between experiment and theory by Abajo *et al.* [29]. Figure 2.14 (reprinted with permission) is a map of the energy loss from an electron-beam passing

near a gold nanoparticle. The electron-beam has a very narrow width that provides the extremely high resolution required to image the fields beyond the realm of conventional optics. The energy loss of the electron beam is found to coincide with the probability of excitation of a localised surface plasmon mode in the particles. This is similar to the early experiments of Ritchie [17] who first discovered the bulk and surface plasmon on a planar geometry by analysing the energy loss of electrons passing through a sample. Here, the 2-d map of the particle is obtained by a raster scan of the plane with the fine electron beam.

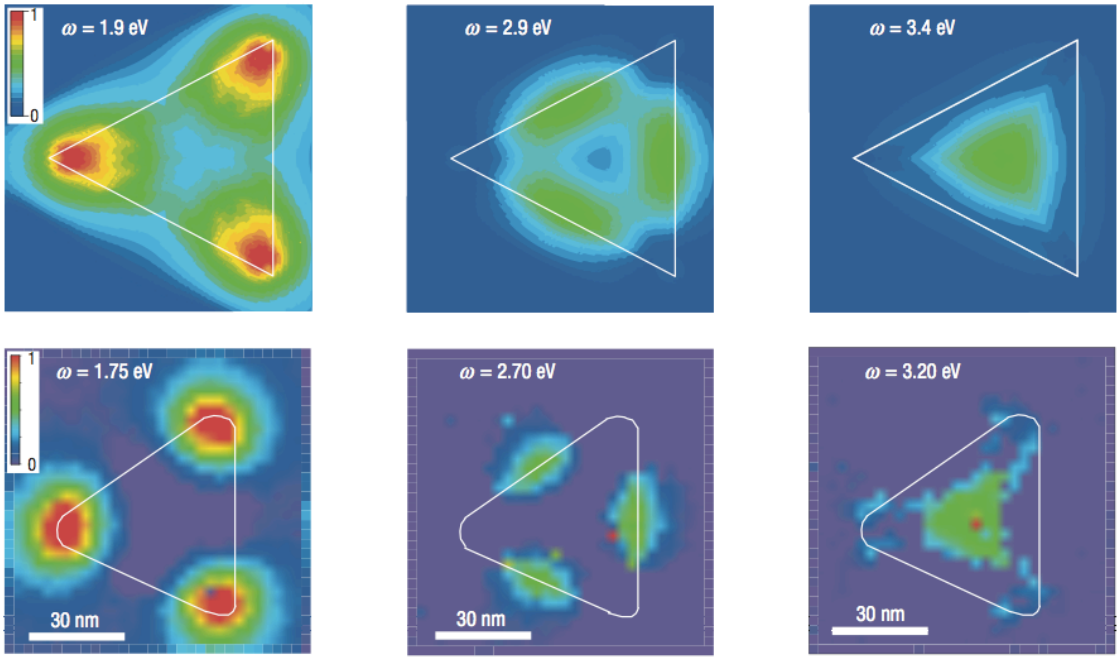

Figure 2.14: Direct observation of the particle plasmon modes supported by a nanoprism. Top: numerical modelling of the modes supported by the nanoparticle at three different energies. Bottom: map of the electron loss after numerical deconvolution. (From [29], reprinted with permission).

2.5 Conclusion

In this chapter were presented the basic concepts that are required to study the particular optical properties of gold. Two approaches were discussed: (a) the electrodynamics of continuous media as described by the Maxwell equations complemented by a set of *ad hoc* constituents relations for **P**, and **J**. (b) The microscopic origin of the polarisation of matter as described in the Drude-Lorentz model. The link between the two viewpoints was discussed in relation to the extinction theorem and the derivation of the Clausius-Mossotti equation.

The optical properties of bulk gold can be described by a dielectric function that can be obtained experimentally, or approximated using a Drude model for the response of the free conduction electrons to an applied electromagnetic field. Several possible prescriptions for the dielectric function of gold have been discussed, and their repercussion on the reflection and absorption properties of gold have been shown for the visible range.

The dielectric function for gold is negative at optical frequencies, which allows the existence of a bound surface wave at the interface between a gold sample and a surrounding dielectric. The electromagnetic mode supported by such a structure is known as a surface plasmon-polariton. The properties of the SPP were described for the Kretschmann configuration by using a model for the optical properties of thin films based on the use of generalised Fresnel coefficients. The conditions for a coupling of incident radiation to a surface plasmon were discussed in relation to the dispersion relation for SPPs at a planar interface.

The particle plasmons which are the object of this thesis were introduced as the result of the spatial confinement of the charge density when the interface between the metal supporting a surface plasmon mode and the surrounding medium takes the form of a particle smaller than the wavelength of the incident light. The geometrical shape of the particle dictates the possible conformation of the excitation of the surface charge density, and these patterns were illustrated by recent theoretical and experimental studies from the literature.

Bulk gold presents a strong interaction with light due to the response of the free electrons that can screen an incident electromagnetic wave. The dielectric function of any material obeys general sum rules that describe the integrated response over all frequencies as a characteristic of the material (quantum oscillator strength) and not of the particular arrangement of the atoms. By tailoring the geometry of the sample from bulk to a thin film or to a particle of a given shape, the electromagnetic response of the charge density can be restricted to a narrower range of resonance frequencies, for which the interaction with light is therefore intense, even for very small particles.

For particles that are smaller than the wavelength, the concept of reflection, absorption and transmission at a planar interface are of little practical use. It is therefore necessary to describe the optical response of nanoparticles to light within the more general framework of scattering theory, and this will be the subject of the next chapter.

"Chemin : bande de terre sur laquelle on marche à pied. La route se distingue du chemin non seulement parce qu'on la parcourt en voiture, mais en ce qu'elle est une simple ligne reliant un point à un autre. La route n'a par elle-même aucun sens ; seuls en ont un les deux points qu'elle relie. Le chemin est un hommage à l'espace. Chaque tronçon du chemin est en lui-même doté d'un sens et nous invite à la halte."

Milan Kundera

3

Modelling techniques

The theoretical study of light scattering by metallic particles has a long history that reflects a more general interest in light scattering. The original works of Lorenz [1], Maxwell-Garnett [2], Debye [3] and Mie [4] at the beginning of last century are generally regarded as pioneering the field. The seminal paper of Mie [4] in 1908 explained rigourously the intense red colouration observed in colloidal solutions of gold particles, and this understanding was achieved through a very general solution of the Maxwell equations for a sphere of arbitrary size illuminated by a plane wave. The Mie theory has since been extended and reformulated, and is a cornerstone of the study of light scattering [5, 6]. The monograph of van de Hulst [7] on light scattering by small particles stands as a reference amongst physics books, and a comprehensive historical review of the field.

From a different perspective — and indeed a vastly different frequency range, the electrical engineering community working on the design of antennas developed powerful methods to investigate the emission and scattering of microwave radiation by metallic structures in different configurations.

The scattering problem can be stated as follows: given the knowledge of an incident field from a distant source, and a scattering medium characterised by a spatial distribution of refractive index, what is the resulting electromagnetic field distribution in all space? Clearly, this broad definition embraces the whole area of optics. In fact, scattering theory can be considered the foundation of classical optics, as presented in the classic monographs of Stratton [8] and Born and Wolf [9]. The understanding of light scattering by subwavelength metallic particles therefore gains from the larger interest in scattering theory in areas such as climate research, remote sensing, and astronomy. In fact, the foundations of most of the numerical models discussed in this chapter originated from different fields of interest and were later applied to the case of metallic nanoparticles. A good example of this transfer is the Discrete Dipole Approximation developed by Purcell and Pennypacker [10] to study the extinction of light in interstellar dust clouds.

Similarly, the scattering of light by periodic structures benefits from the comprehensive set of tools developed in the field of solid state physics. An example of this is the KKR (Korringa Kohn Rostoker) method which originated in the study of electronic properties of solids and is now widely applied to the study of dielectric and metallic photonic crystals [11–14]. Newton [15] gives a general presentation of scattering that allows for a similar treatment of electrons and photons in a quantum mechanical framework.

Although scattering of light by particles has been a field of active research interest for over a century, it is only in the past few decades that a quantitative comparison between experiments and theory has been feasible for nanoscale particles [16, 17]. It has only been possible to implement powerful numerical techniques with the advance and widespread use of fast computers. In parallel, fabrication and characterisation techniques have also considerably improved in the past decades, allowing for a quantitative verification of the theories by experiment. It is worth noticing the fact that while this field has been extensively studied theoretically, and numerous numerical codes can be used to model the optical properties in a variety of situations, the very existence of many modelling approaches indicates that no single technique is ideal for all cases. It is therefore our task to ask the following questions when choosing a particular approach: i) What is the information we would like to obtain from modelling? This requirement can go further than the straight-forward objective of reproducing the experimental result — in many cases some field quantities calculated by the theory may not be accessible in the experiment but can help our physical understanding. ii) What are the different approaches, and more importantly which approaches are best suited for a particular type of problem? iii) What approximations can be made to reveal enough physical insight without losing too much accuracy?

The first part of this chapter is devoted to presenting the general equations of scattering theory and to giving an overview of the techniques used in this thesis. The exact Mie solution for scattering by spheres of arbitrary size is discussed, with an emphasis on the limiting case of Rayleigh-Gans approximation applicable to small particles. Finally, possible techniques to treat the scattering of light by a large collection of particles are discussed.

3.1 Context

Scattering of light by particles and systems of particles is reviewed in comprehensive monographs such as Kahnert [18], Mishchenko [5, 19], Barber [20] and Newton [15] to cite only a few major references. For the particular problem of modelling the optical properties of gold nanoparticles in the visible and infra-red Schatz [17, 21–23] and García de Abajo [16] recently gave reviews on the most commonly used techniques. The strong optical response of gold in this frequency range imposes particular constraints on the numerical scheme (large complex and dispersive permittivity, arbitrary shape). I will discuss in this chapter only a few of the techniques that adequately describe the optical response of metallic nanoparticles in the visible with moderate size to wavelength ratio.

3.1.1 General formulation of the scattering problem

The typical scattering problem can be summarised as follows: find the total field in all space that satisfies the Helmholtz equation (equivalently, the Maxwell equations) in the different constituents (for simplicity I note 1 for exterior, 2 for interior),

$$\begin{cases} \nabla^2\mathbf{E}_1 + k_1^2\mathbf{E}_1 = \mathbf{0}, \\ \nabla^2\mathbf{E}_2 + k_2^2\mathbf{E}_2 = \mathbf{0} \end{cases}, \tag{3.1}$$

with $\mathbf{k}_1 = n_1\mathbf{k}_0$, $\mathbf{k}_2 = n_2\mathbf{k}_0$ the wavevector in each medium. These two homogeneous equations can be combined by introducing an artificial current density $\mathbf{J} = k_1^2[m^2-1]\mathbf{E}$, where $m = n_1/n_2$ is the ratio of refractive index,

$$\nabla^2\mathbf{E} + k_1^2\mathbf{E} = \begin{cases} \mathbf{0} \text{ in medium 1} \\ \mathbf{J} \text{ in medium 2} \end{cases}. \tag{3.2}$$

In this inhomogeneous equation, the current $\mathbf{J}$ (therefore, the index contrast) is seen as the source of the scattered field: the associated homogeneous equation describes the propagation of a wave in the unbounded, source-free medium 1, which is our definition of the incident field.

The set of the Maxwell equations 2.16 or equation 3.2 is used directly in several modelling techniques, *e.g.* the Mie theory, the separation of variables method (SVM), and in a discretized form in the finite elements method (FEM) and the finite differences in time domain method (FDTD). An alternative route [18] is based on casting the set of partial differential equations into an integral formulation, this forms the basis of the discrete dipole approximation (DDA) and Null-Field method discussed in sections 3.4.1 and 3.4.2.

3.1.2 Boundary conditions

Equation 3.2 assumes a particularly simple form when all the characteristic dimensions of the problem are much smaller than the wavelength in the incident medium — the scattering problem reduces to finding a quasi-static electric field distribution in the vicinity of the particle. In this case we retrieve the source-free Laplace equation $\boldsymbol{\nabla}^2\mathbf{E} = 0$ whose solutions are the well-studied class of harmonic functions. The geometry of the system alone dictates the form of the electromagnetic field everywhere in space. The presence of the wave-vector in equation 3.2 introduces *retardation effects*: the electromagnetic field has the additional characteristic of having a phase varying in space.

An additional constraint on the electromagnetic field is provided by the so-called *radiation condition* which dictates that the field must decay away at large distance from the sources as a transverse spherical wave with amplitude inversely proportional to the distance. This condition ensures that energy is conserved, as the energy flux radiated per solid angle is constant. In the time domain, this condition describes the formation of out-going spherical waves in regions sufficiently far away that the scatterer can be considered a point-like source of radiation. Symmetrically, it also describes the possibility of *in-going* spherical waves converging to a point.

The distance at which the electromagnetic field is 'free' from its source and propagates in the form of a transverse spherical wave depends on the wavelength and size of the source as well as its constitution. The transition from a *near-field zone* to a *far-field zone* and its dependence on the different parameters is discussed by Mishchenko [24] and Wolf [25].

Figure 3.1 depicts the scattering process as treated in this chapter. The total electromagnetic field in all space can be artificially separated into two contributions: the external field that would exist everywhere in space if the particles were not present (in this case, simply a plane wave); the scattered field that is the difference between the incident and total fields. It should be noted that in the frequency domain, no causality relation can be expressed between the incident and scattered fields and it is not adequate to describe the scattering process as a chronological series of interactions in this framework [19, 26]. When considering scattering by a cluster of particles the field scattered by one particle can affect its neighbours. Such interactions can strongly affect the response of the individual components as will be discussed in section 3.5 on multiple scattering and in chapters 5–8. At large distances from the scattering medium, all scattering bodies can be seen as a point source of radiation and the scattered field takes the asymptotic form of a spherical wave as required by the radiation condition,

$$\mathbf{E}_{\text{scat}} \sim \frac{\exp(i\mathbf{k}\cdot\mathbf{r})}{r}\left(e_\phi\hat{\boldsymbol{\phi}} + e_\theta\hat{\boldsymbol{\theta}}\right). \tag{3.3}$$

The strength and angular pattern of the scattered field is influenced by the constitution of the cluster, the incident polarisation and direction. For instance, for single particles much smaller than the wavelength, the Rayleigh approximation treats the scatterer as point dipole which emits symmetrically in a typical $\cos^2\theta$ radiation pattern (no radiation along the dipole axis, symmetric pattern). Larger particles will exhibit a so-called *Mie focussing effect*: the forward scattering dominates over the backscattered radiation. Very large particles can display the opposite behaviour: a large metallic sphere appears as a mirror to visible light and back-scatters (*reflects*) a large proportion of the incident light (there is also a substantial amount of highly directional forward scattered light in the form of *diffraction* by the edges of the object). The scatterer can also take the form of a collection of smaller particles, in which case both the individual particles scattering properties and the geometrical conformation of the cluster will influence the scattering properties in the near- and far-field.

A simplified hierarchy of scattering problems is shown in figure 3.2. The Maxwell equations are the foundation of the classical theory of light scattering, and may be used directly or in their discretized form to solve some specific scattering problems (for example, with the FDTD method). However, in many practical situations the complexity of the scattering problem — even within this macroscopic framework, makes it difficult if not intractable to solve directly for the field in all space. For instance, a large cluster comprising thousands of particles of irregular shapes in arbitrary configurations is commonly encountered in experiments. The general problem of light scattering by systems of particles can be divided into sub-categories as shown in figure 3.2. The first division may be the distinction between *static* and *dynamic* scatterers. In the latter, the scattering medium is constantly evolving from one configuration to another. Time averaged or transient optical response

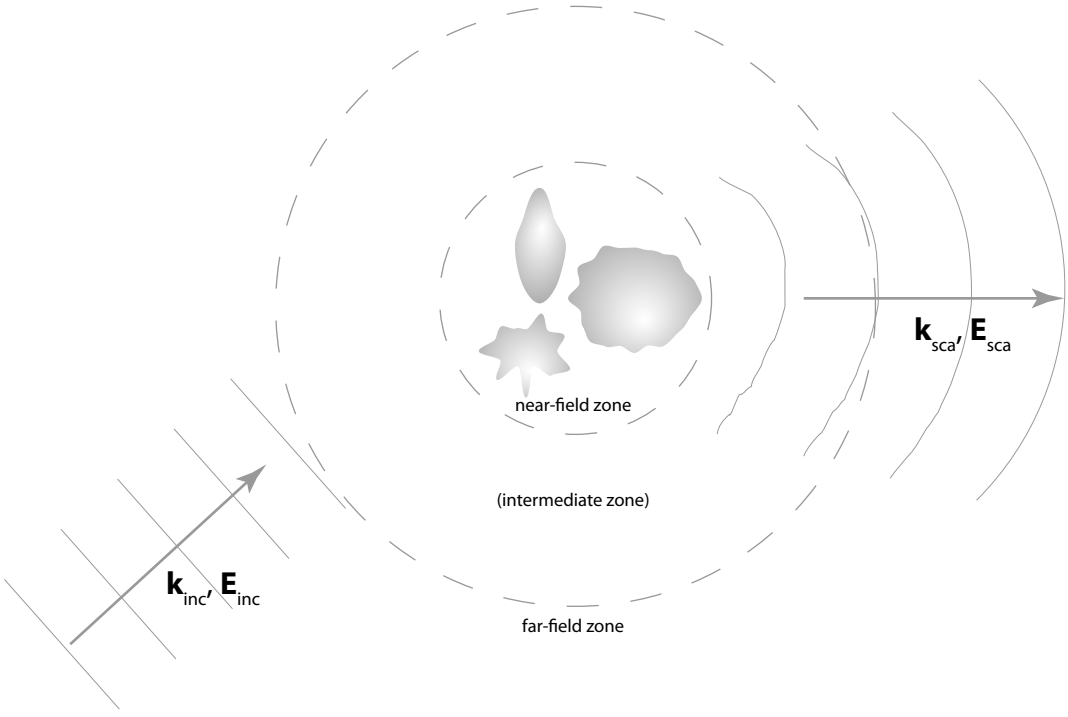

Figure 3.1: Schematic representation of scattering by a cluster of particles. A plane wave characterised by its wavevector **k** and electric vector **E** excites the charges in the particles which generate a scattered field in response. The total field is the superposition of the incident and re-radiated fields, and may be divided in two (in some cases, three) zones: near-field, (intermediate), and far-field.

of such systems will not be investigated here, we will restrict the discussion to *static* configurations. The second distinction is between a single scattering particle and a disjoint collection of particles in a *cluster*. The case of single particles will be discussed in relation to experiments in chapter 4. Clusters of particles may vary in number, from a pair to an infinite number of particles. While small clusters (up to a hundred particles) can be treated with direct methods, it is often necessary to introduce new simplifying assumptions when dealing with larger collections of particles. A notable exception is the case of *infinite periodic structures*, where the problem may be solved for a unit cell in a way that is very similar to the single particle case with appropriate periodic boundary conditions in the Finite Element Method, Finite Difference Time Domain method, or Discrete Dipole Approximation [27]. Another natural option for periodic structures is to expand the fields in a series of Fourier harmonics, which forms the basis of the Fourier modal expansion method.

If the particles are widely separated and scatter light weakly, it is sometimes possible to neglect the electromagnetic interaction between the particles, and the scattering properties of the medium are found to reflect the average distribution of the individual scattering properties of the particles in isolation. For dense media, however, this assumption is clearly invalid and a delicate task consists in defining the limit where *multiple scattering* becomes important [28].

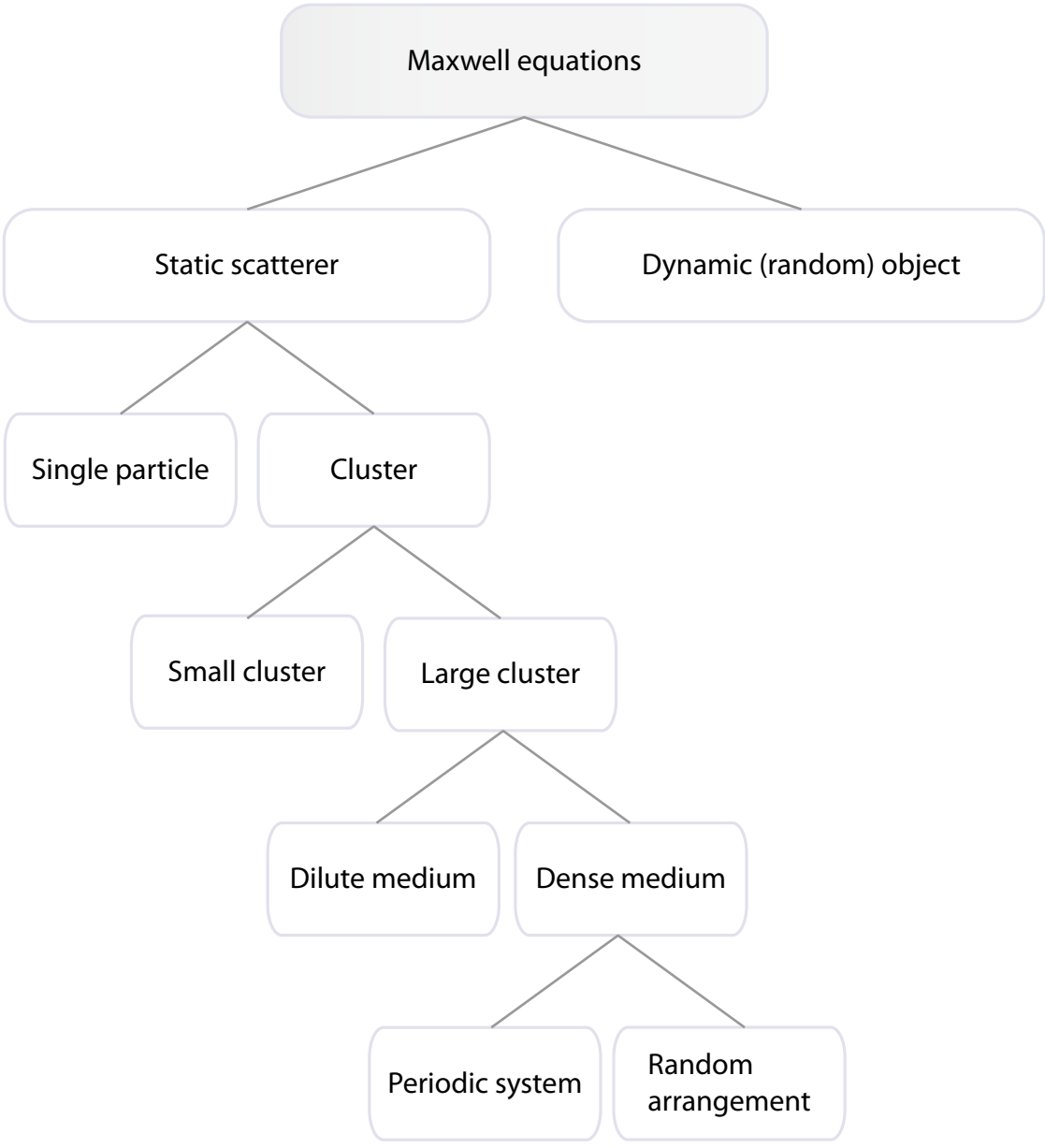

Figure 3.2: Simplified hierarchy of scattering systems. (Inspired from [19])

3.1.3 Volume integral formulation

The solution of equation 3.2 may be obtained formally using the formalism of Green's functions. In this approach, the solution is expressed as a convolution of the source with the response to a Dirac distribution,

$$\mathbf{E}_{\text{scat}} = i\omega\mu_0 \int_V \mathrm{d}\mathbf{r}' \bar{\mathrm{G}}(\mathbf{r}, \mathbf{r}')\mathbf{J}(\mathbf{r}'), \tag{3.4}$$

where the integral is taken over the the volume V of the scattering body, and the Green's dyadic $\bar{\mathrm{G}}$ satisfies an associated equation with a unit source term,

$$(\boldsymbol{\nabla}^2 + \mathbf{k}_1^2)\bar{\mathrm{G}}(\mathbf{r}, \mathbf{r}') = \bar{\mathrm{I}}\delta(\mathbf{r} - \mathbf{r}'). \tag{3.5}$$

The physical interpretation of the Green dyadic is the expression for the electric field radiated at a location r in space by three orthogonal dipoles located at r'. It represents the propagator for the electromagnetic field in a quantum mechanical description of the scattering process. Introducing new elements in the scattering problem, such as a substrate, can be elegantly achieved in this integral formulation through the introduction of an adequate Green function[29]. In free homogeneous space, the Green's dyadic takes the form [18, 30, 31],

$$\bar{\mathrm{G}} = \left[\bar{\mathrm{I}} + \frac{1}{k^2}\nabla\nabla\right]\mathrm{G}_0, \qquad \mathrm{G}_0 = \frac{e^{\pm ik|r-r'|}}{|r-r'|}. \tag{3.6}$$

This expression for the Green dyadic can be obtained using the scalar and vector potentials, or using the alternative formalism of Hertz (polarisation) potentials. In a similar manner that one can describe electromagnetic waves as solutions to the Helmholtz equation for the potentials ϕ and A where charge and current densities are sources, one can derive a formalism where the sources are the polarization (and magnetisation) [9, 32],

$$\begin{gathered}\Pi = \int_{\text{volume}} \frac{\mathbf{P}(t - |r-r'|/c)}{|r-r'|}\mathrm{d}\mathbf{r}' \quad \Leftrightarrow \quad \mathbf{A} = \int_{\text{volume}} \frac{\mathbf{J}(t - |r-r'|/c)}{|r-r'|}\mathrm{d}\mathbf{r}' \\ (\boldsymbol{\nabla}^2 + \mathbf{k}_1^2)\boldsymbol{\Pi} = -\mathbf{P} \quad \Leftrightarrow \quad (\boldsymbol{\nabla}^2 + \mathbf{k}_1^2)\mathbf{A} = -\mathbf{J}.\end{gathered} \tag{3.7}$$

The Hertz vector is parallel to the source of polarisation, and is transferred in the form of a spherical wave which conserves this initial symmetry. The electric field $\mathbf{E}_{(\mathrm{d})}$ of a dipole is obtained by the following formula,

$$\mathbf{E}_{(\mathrm{d})} = \boldsymbol{\nabla} \times (\boldsymbol{\nabla} \times \boldsymbol{\Pi}). \tag{3.8}$$

The volume integral formulation is obtained by inserting equation 3.6 into equation 3.4, which expresses the summation of the applied field and the dipolar field radiated by all unit dipole elements inside the scatterer,

$$\mathbf{E} = \mathbf{E}_{\text{ext}} + i\omega\mu_0 \int_{\text{volume}} \left[\bar{\mathrm{I}} + \frac{1}{k^2}\nabla\nabla\right] \mathrm{G}_0(\mathbf{r}, \mathbf{r}') \cdot \mathbf{J}(\mathbf{r}')\mathrm{d}\mathbf{r}'. \tag{3.9}$$

The volume integral equation 3.9 expresses the field everywhere in space in terms of the incident field, provided the field inside the scattering body is known. Discretizing this integral equation and solving self consistently for the local field at any point inside the particle is the basis of the discrete dipole approximation, where the internal current sources are modelled as point dipoles located on the discrete mesh.

When the index contrast is small (*soft scatterer*) and the particle is small compared to the wavelength, this internal field may be considered to be uniform and equal to the incident field. This so-called *first Born approximation* forms the basis of the Rayleigh theory applicable to small particles. A more accurate approach consists in carrying out this first approximation, and then iteratively replacing the corrected internal field calculated from equation 3.9. This procedure is especially useful when the scattering body consists of several particles: the iteration reproduces the interaction of the particles via *partial waves* in an order-of-scattering numerical scheme.

3.1.4 Null-field equation

In equation 3.9 the internal current describes the polarization of the material in response to an external field. By applying Stokes' theorem, the volume integral may be converted into a surface integral over the particle boundary. The polarization can be expressed in terms of an equivalent surface charge (from equation 2.16b), which forms an appealing picture for the scattering of light by metallic particles where the excitation of eigenmodes for the surface charge density coincide with the existence of *localised plasmon* modes. The surface integral formulation forms the basis of the Null-Field method method discussed in sections 3.4.1 and 3.4.2.

$$\mathbf{E}_{\text{inc}} + \int_{\partial V} \left[\frac{i\omega\mu}{c} (\hat{\mathbf{n}} \times \mathbf{H}) \cdot \bar{\mathrm{G}} + (\hat{\mathbf{n}} \times \mathbf{E}) \cdot (\boldsymbol{\nabla} \times \bar{\mathrm{G}}) \right] \mathrm{d}\sigma(r') = \begin{cases} \mathbf{E} \text{ outside} \\ \mathbf{0} \text{ inside} \end{cases} . \tag{3.10}$$

Equation 3.10 is an expression of the Ewald-Oseen theorem: the surface integral represents the scattered field, which exactly cancels the incident field inside the particle.

3.1.5 Scattering in the far-field zone

In all experiments performed in this work, the scattering properties of the particles are investigated in the far-field: the intensity of the scattered light is collected at a distance that is very large compared to the wavelength and any dimension of the scattering medium. In this regime, the scattering process is described by a matrix $\mathbb{F}$ that links the asymptotic expression for the scattered wave to an incident plane wave,

$$\mathbf{E}_{\text{scat}} = \frac{\exp(i\mathbf{k}\cdot\mathbf{r})}{r} [\mathbb{F}] \, \mathbf{E}_{\text{inc}}. \tag{3.11}$$

The scattering amplitude matrix $\mathbb{F}$ describes the electromagnetic field scattered for a given incident field characterised by its frequency and polarisation, and depends on the refractive indices and on the angle between the incident and scattered beam. Actual measurements will however only measure an average power flux, proportional to the modulus squared of the fields. Further, to account for the possible change in polarisation of the beam, a full description of the scattering process requires the use of Stokes parameters that fully characterise any given light beam. The phase coherency matrix links the input and output Stokes vectors. Its elements are quadratic combinations of the elements of the scattering amplitude matrix. A remarkable property of the phase coherency matrix is that a fully linearly polarized wave remains fully polarized when scattered by a single particle [5]. In most experiments discussed in this thesis (e.g chapter 4) the incident light was fully polarised

along the axis of the particles and a single element of the scattering matrix is therefore sufficient to interpret the results.

To characterise the scattering properties of the particles we will consider *far-field cross sections*, namely absorption, scattering, and extinction cross-sections. These quantities are physical observables that allow for a direct comparison between experimental measurements and theoretical modelling [33]. Cross-sections express the probability of interaction of the incident light with the scatterer, and can be derived from the expression of the conservation of energy in the Poynting theorem (Appendix 1). The scattering cross-section is the area that the beam should intercept to provide the equivalent energy scattered by the particle; the absorption cross-section is the effective area taken from the incident beam that is converted into heat inside the particle; and the extinction cross-section describes the energy that is removed from the beam as a result of scattering and absorption,

$$\sigma_{\text{ext}} = \sigma_{\text{abs}} + \sigma_{\text{sca}}. \tag{3.12}$$

For convenience, the scattering, absorption and extinction cross-sections can be compared to the geometrical area intercepted by the incident beam G, this ratio is named *efficiency* and should only be strictly defined for scatterers with convex shapes.

The scattering cross-section can be obtained by integrating the scattered power in all directions and normalising to the incident flux: it also characterises the extent to which an incident beam can be said to interact with the particle in the sense that it expresses the field overlap between a plane wave and the normal modes of the scattering body. A metallic nanoparticle can display a resonant response to visible light and as a result its scattering cross-section may be much greater than the geometrical cross-section (a factor of 5 for gold spheres, even higher for gold ellipsoids). This makes it possible to observe the light that is scattered by subwavelength particles with the naked eye (figure 4.5).

The absorption cross section measures the loss of energy inside a scatterer: it vanishes for a non-absorbing material ($\text{Im}(n) = 0$), and more generally depends on the integrated internal field, times the imaginary part of the permittivity,

$$\sigma_{\text{abs}} = \frac{k}{|\mathbf{E}_0|^2} \int_V \varepsilon'' \mathbf{E} \cdot \mathbf{E}^* \mathrm{d}\mathbf{r}'. \tag{3.13}$$

The energy lost by scattering and absorption is one facet of extinction: another equivalent definition considers extinction as the destructive interference of the light that is scattered by the particle with the incident light. This standpoint can be expressed in a rigourous manner by considering the energy conservation for a detector placed in the exact forward direction. The result of this formulation is expressed in the *optical theorem* [33],

$$\sigma_{\text{ext}}(\omega) = \frac{4\pi}{k^2} \Im \left[\mathbb{F}(0°, \omega) \right], \tag{3.14}$$

which relates the far-field extinction to the forward scattering amplitude $\mathbb{F}(0°, \omega)$. In general, the extinction will depend on the polarization state of the incident light, an effect known as *dichroism*.

In a turbid medium such as a colloidal suspension, the propagation of light can be treated phenomenologically by the so-called *radiative transfer equation* (RTE) for which the rigourous derivation from first principles (the Maxwell equations) was only very recently achieved [19, 26, 28]. The radiative transfer equation describes the evolution of the light intensity as a result of (multiple) scattering and absorption. The ratio of scattering to absorption (*albedo*) and the phase matrix dictate the evolution of the light intensity as it passes through the medium. For a dilute solution and under very strong simplifying assumptions, the RTE can be reduced to the well-known *Beer-Lambert* law that expresses the exponential attenuation of the intensity of the light that traverses a colloidal solution as a result of scattering (the light is redirected in other directions) and absorption along the path,

$$I = I_0 \exp(-\sigma_{\text{ext}} N L), \tag{3.15}$$

where N is the volume density of particles in the medium, and L the path-length followed by the light inside the scattering medium.

The intuitive meaning of extinction can lead to erroneous conclusions with respect to experimental measurements: the true extinction in the far-field is subject to several stringent conditions as noted in [6, 33]. In practice, it may be impossible to meet all the required conditions and part of the scattered light in directions other than the exact forward direction may be collected, resulting in an effective extinction smaller than the ideal definition.

3.1.6 Scale invariance in scattering theory

An important property of light scattering is the *scale invariance rule*, which states that the scattering characteristics of a system depend only on the *size parameter* defined as the product ka where a is a linear dimension of the scatterer, k the wavenumber in the incident medium; and relative index contrast $m = n_1/n_2$. In particular, if the index contrast is kept constant, the scattering properties of the system are invariant upon the following transformation,

$$\begin{aligned} a &\rightarrow s \cdot a \\ k &\rightarrow k/s, \end{aligned} \tag{3.16}$$

where s is a scalar. The scale invariance property holds for most adimensional quantities such as the scattering amplitude matrix elements, the T-matrix elements, the product of the far-field cross sections times k^2, *etc*. This result forms the basis of the microwave analog technique that has been used extensively to test experimentally the scattering properties of single particles in the microwave regime where the fabrication and characterisation of samples is often easier than in the optical regime. It also permits one to understand the behaviour of gold nanoparticles in the visible domain in analogy with radio antennas [34–36]. A major difference in this case however is the different permittivity ratio (air/metal) as metals behave very much like perfect conductors at microwave frequencies. Nonetheless, this scale invariance often provides fruitful inspiration, as illustrated for instance in the recent design of *spoof plasmons* at microwave frequencies that mimic the optical surface plasmon by allowing a decay of the electromagnetic field into the metal through the use of a microstructure [37].

3.2 Rayleigh regime

For particles much smaller than the wavelength, a quasi-static approximation greatly simplifies the problem and leads to intuitive understanding of the optical response in terms of dipolar radiation. This is the regime of Rayleigh scattering, that conveniently describes the optical response of small, optically soft particles. This approximation can be deduced from exact theories such as Mie theory for spheres, or more generally as a result of the first Born approximation in the volume integral equation [5, 9, 15].

3.2.1 Dipolar approximation

In a small gold particle, an incident field will displace the free electrons that oscillate rapidly from one end of the particle to the opposite side. The ionic background provides a restoring force, and the system is therefore equivalent to a dipole with two opposite charges separated by a distance that depends on the particle geometry. Such a dipole radiates energy in proportion to its dipole moment, which is proportional to the number of charges and their displacement. This simple consideration led Rayleigh to the semi-quantitative description of the scattering of light by small air molecules (fluctuations of the average air permittivity, more precisely) that is responsible for the blue coloration of the sky.

The electric field incident on a small particle will induce a dipole moment proportional to the particle's volume (a^3),

$$\mathbf{p} \propto a^3 \mathbf{E}_{\text{inc}}, \tag{3.17}$$

this dipole will radiate a field proportional to the acceleration of the charges, that is the second derivative of the dipole moment with respect to time. Treating the incident field as a monochromatic wave, the scattered field in the frequency domain is proportional to,

$$\mathbf{E}_{\text{scat}} \propto \omega^2 a^3 \mathbf{E}_{\text{inc}}. \tag{3.18}$$

The intensity of the scattered light is therefore,

$$I_{\text{sca}} \propto I_{\text{inc}} \frac{a^6}{\lambda^4}, \tag{3.19}$$

where I_{inc} is the incident energy flux with units W/m^2.

The $1/\lambda^4$ dependence explains why blue light is more strongly scattered than red light for optically soft scatterers. From a dimensionality argument, it is clear that the proportionality between the incident energy flux and the scattered energy integrated over all solid angles must be equivalent to an area, defined as the scattering cross-section.

In this discussion, the importance of the scatterer composition has been ignored under the assumption of a soft scattering medium. This is not true for metallic particles in the visible and infra-red due to the strong Drude response of the free electrons that dictate their optical properties. Equation 3.17 needs generalising by replacing the particle volume with its shape and wavelength

dependent polarizability.

$$\mathbf{p} = \varepsilon_m \alpha \mathbf{E}_{\text{inc}}, \tag{3.20}$$

where the prefactor ε_m is the permittivity of the incident medium that can be different from that of a vacuum (but generally non-absorbing). The frequency dependence of the polarizability is described by the Lorentz-Lorenz formula, also known as Clausius-Mossotti formula when expressed in terms of the refractive index,

$$\alpha = \frac{a^3}{3} \cdot \frac{\varepsilon - \varepsilon_d}{\varepsilon + 2\varepsilon_d}, \tag{3.21}$$

The resonance in particles supporting localised plasmons is seen as the pole in equation 3.21: when the dielectric function of the metal verifies $\varepsilon + 2\varepsilon_d = 0$, the polarizability diverges, a condition known as *the Fröhlish frequency*. The presence of absorption prevents a purely real resonant frequency, therefore limiting the divergence to a Lorentzian lineshape with a width defined by the loss in the system. In this resonant regime, the strong dispersion in the dielectric function of gold introduces a large scattering peak that superimposes on the $1/\lambda^4$ trend. Similarly the absorption and extinction both peak at the excitation of the LSPR.

The Rayleigh-Gans theory is an extension of equation 3.21 which considers the scattering of light by particles of arbitrary shape, keeping the assumption that the particle size is much smaller the wavelength [6]. The effect of particle shape on the dipolar response is approximated by the introduction of a suitable *shape factor* that accounts for the depolarisation field of a particle in the quasi-static limit,

$$\alpha = \frac{abc}{3} \frac{\varepsilon - \varepsilon_d}{\varepsilon_d + \mathrm{L}(\varepsilon - \varepsilon_d)}. \tag{3.22}$$

Shifting the Fröhlish frequency from the position dictated by the intrinsic material properties can be achieved by changing the shape of the particle. The physical root of this depolarisation field stems from the screening of the external field by the surface charge that accumulates at the boundary of the particle. Equivalently, this surface charge can be described as an internal polarization that enters the displacement field. Each subvolume element of the scatterer experiences a field that comprises the external, applied field, and the field associated with the response of this surrounding, polarised material. Because the shape influences the distribution of charges at the boundary, the depolarization field is size and shape dependent where the Lorentz-Lorenz derivation (equation 3.38) assumed a spherical boundary. It is possible to evaluate the depolarization factors by integration of equation 2.25 which can be done analytically for simple shapes such as spheres, ellipsoids and infinite cylinders, or numerically for general shapes [6, 38]. For example, ellipsoids exhibit a depolarization field that can be expressed in the form,

$$\mathbf{E}^{\text{dep}} = \bar{\mathrm{L}}\mathbf{P}, \tag{3.23}$$

where $\bar{\mathrm{L}}$ is a tensor with principal components that are the geometrical factors associated with each axis,

$$\mathrm{L}_a = \frac{abc}{2} \int_0^\infty \frac{dq}{(a^2+q)\sqrt{(a^2+q)(b^2+q)(c^2+q)}}. \tag{3.24}$$

A sum rule constrains the trace of $\bar{\mathrm{L}}$: the three principal geometrical factors add up to unity, $\mathrm{L}_a + \mathrm{L}_b + \mathrm{L}_c = 1$. Closed form expressions can be obtained for the particular case of ellipsoids with rotational symmetry (oblate or prolate spheroids).

The effect of the aspect ratio of the particles in the frequency of the LSPR (in the quasi-static approximation) is shown in figure 3.3.

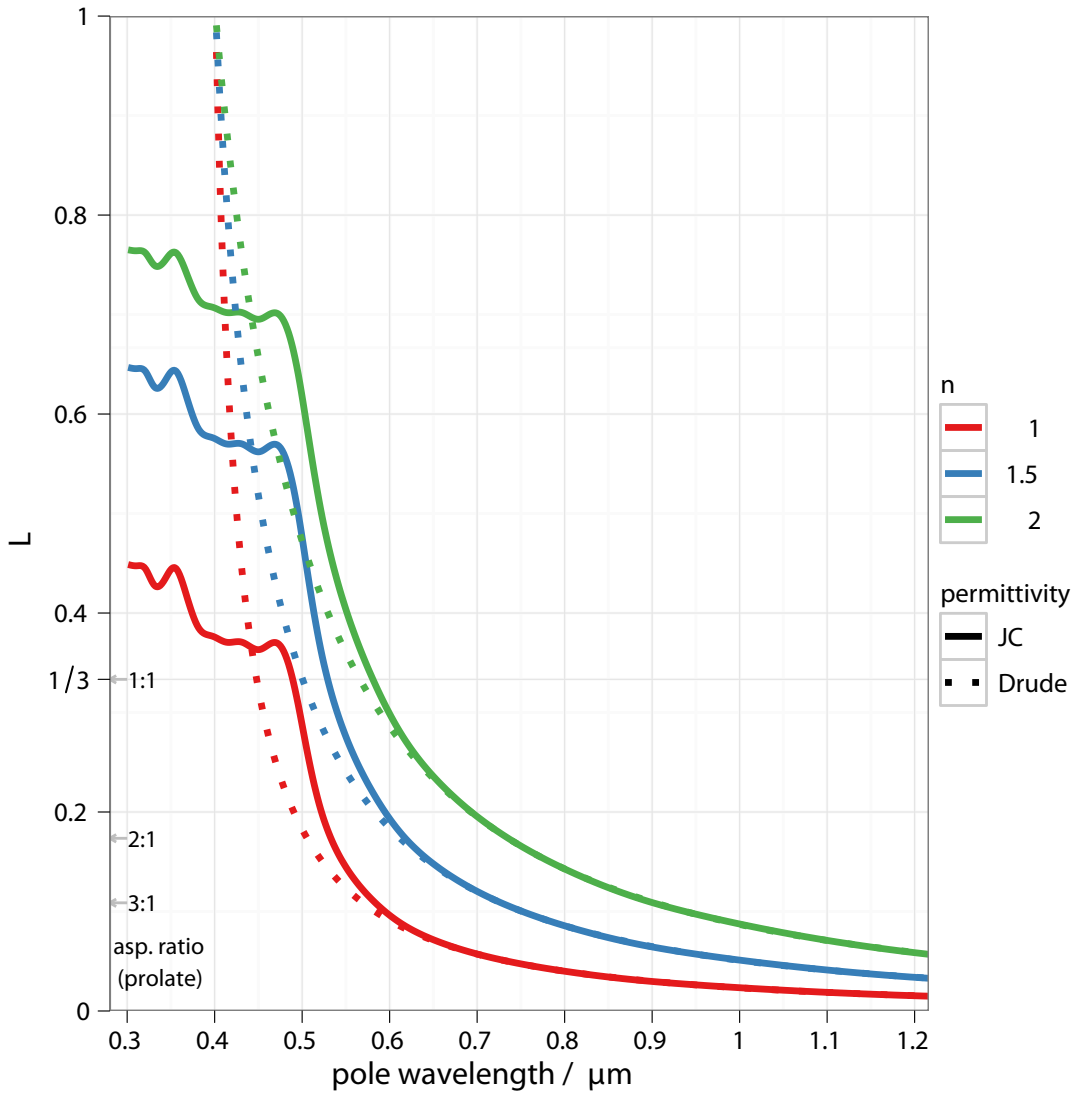

Figure 3.3: Variation of the Fröhlish frequency of ellipsoids as a function of aspect ratio.

A resonance is characterised by a pole in the polarizability (equation 3.22), which occurs when the frequency approaches,

$$\Re\left[\varepsilon_d + \mathrm{L}(\varepsilon - \varepsilon_d)\right] \approx 0. \tag{3.25}$$

This condition is satisfied for

$$\varepsilon' = \varepsilon_d\,(1 - 1/\mathrm{L}).$$

ω_s	$\varepsilon'(\omega_s)$	geometry
$\omega_p/\sqrt{3}$	-2	sphere
$\omega_p\sqrt{L}$	1-1/L	ellipsoid
$\omega_p/\sqrt{2}$	-1	planar surface
ω_p	0	bulk

Table 3.1: Resonance frequency of plasmon modes for different geometrical configurations.

Inserting a simple Drude model of the form $\varepsilon = 1 - \left(\omega_p/\omega\right)^2$ yields the resonance frequency of a surface mode ω_s,

$$\omega_\mathrm{s} = \omega_p/\sqrt{d}, \tag{3.26}$$

where $d = L/\left[\varepsilon_d - \mathrm{L}(\varepsilon_d - 1)\right]$. The pole of equation 3.22 is plotted in figure 3.3 for different values of the surrounding medium and a range of aspect ratios.

Using the permittivity from the Drude model, the surface modes have resonances that span the whole range from L=0 to L=1. The strong absorption of gold for wavelength below 500nm results in overdamping of the resonances where the pole of equation 3.22 does not correspond to a real resonance.

It is interesting to consider equation 3.26 with the surrounding medium set to vacuum ($\varepsilon_d = 1$). where we recognise a dimensionality argument that links the resonance frequency of the charge density to the geometry of the system [39, 40] (Table 3.1).

When the size of the particle becomes comparable to the wavelength of light in the surrounding medium and inside the particle, retardation effects not taken into account in this dipolar approximation start to play an important role.

3.2.2 Retardation effects

Modelling the dipolar response of a scatterer of finite size to an external field amounts to determining an equivalent dipole for the system. In fact, any collection of charges can be represented in the far-field as an equivalent point source of radiation with characteristics given by a multipolar expansion [30]. The dipolar term is dominant for the range of sizes we consider in this work. Another equivalent view is to divide the scatterer into smaller sub-volumes characterised by a dipole moment, the integral over this distribution of polarization gives the overall dipolar response.

In this dipolar approximation, two cases can be considered. 1) The object is negligibly small compared to the relevant wavelength (excitation in the incident medium, and in the particle). In this case, the problem of finding the polarization of the scatterer is equivalent to an electrostatic problem. This problem can be solved self-consistently by assuming the establishment of a uniform and isotropic polarization of the material, proportional to the applied field. With these restricting hypotheses, the interaction of the neighbouring polarizable sub-volumes is adequately modelled by a $1/r^3$ electrostatic contribution. The integration over the volume leads to the usual Lorentz-Lorenz formulation for the polarizability of a sphere, generalised to equation 3.22 for a more ar-

bitrary shape. 2) The size parameter is not negligibly small and/or the material of the scatterer is highly polarizable. In this case, the interaction of the sub-volumes is not only electrostatic, but also involves dynamic terms that are modulated with the phase of the wave inside and outside the scatterer. The interaction between subvolumes involves terms with longer range interaction than the quasi-static limit ($1/r^2$ and $1/r$) to describe more accurately the coupling of the different parts of the material. These contributions generate *retardation effects*, in that they describe the delayed radiation of a source from other points in the particle. This effect of retardation is clearly expressed in equation 3.7 that we used to formulate the scattering problem in terms of a volume integral equation. The wave equation for the retarded Hertz potential involves the summation of the field at a time $(t - r/c)$ in perfect analogy with the solution of the wave-equation for the electric and magnetic potential.

The meaning of *self-consistency* in the above discussion can be expressed as follows: the incident field induces a polarisation of the medium, which in turn causes further polarisation, *etc.* (or equivalently charges at the surface induce a field, *etc.*). When this polarisation is homogeneous in amplitude and phase and also isotropic, the problem falls into Rayleigh-Gans theory. When the polarisation is constant and isotropic but its phase varies over the particle, the dipolar term may still be predominant but the electromagnetic response is no longer quasi-static: the system dynamically evolves as the interaction between different sub-volumes of the scatterer depends on their relative phase. This is well accounted for in the modified long wavelength approximation, which considers the series expansion in terms of ka of the first Mie scattering term [16, 41, 42]. Finally, when the polarization cannot be considered constant in amplitude or isotropic, due to a significant size and/or field lines distortion by sharp edges, the higher order multipolar terms may become important. However, when considering the scattering system in a multipolar expansion (or looking at the Mie series), the different terms (multipoles) correspond to orthogonal vector solutions, which can hence be considered independently for the purpose of discussing the eigenmodes of the system.

Modified long wavelength approximation

When considering particles having a size comparable to the wavelength of light in the surrounding medium, dephasing effects come into play and the quasi-static approximation breaks down. The Mie theory includes such retardation effects, whereas the Rayleigh approximation truncates the Mie series to the first static dipole term and breaks down for particles with $2a \gtrsim \lambda/10$ where λ is the wavelength in the surrounding medium.

Non-spherical particles need further correction that account for the aspect ratio that affects the depolarisation field, therefore the position of the LSPR. A semi-analytical correction known as the modified long wavelength approximation can retrieve most of the physics, with the notable exception of multipolar resonances. In this approximation, the electric field inside the particle is represented as the sum of the incident field, plus a correction from the response of the medium [9, 41, 42],

$$\mathbf{E}_{\text{rad}} = \frac{2}{3} i k^3 \mathbf{P} + \frac{k^2}{a} \mathbf{P}, \tag{3.27}$$

a being the semi-major axis of the particle along the polarisation of the incident field. The first term describes *radiation damping*, *i.e.* the loss of energy in the form of radiation. In physical terms, this means that the field radiated by the moving charges does work on the particle (self-reaction, also described as radiation resistance in the antenna literature) [8, 43]. The second term represents a *dynamic depolarisation* — each point of the particle contributing to the effective field seen at another location, this field becomes more and more out of phase across the particle as the characteristic size of the particle increases.

Using equation 3.27 the dipolar response of a particle is formulated in terms of a corrected polarizability of the form,

$$\alpha^{\text{mlwa}} = \frac{\alpha^{\text{static}}}{1 - \frac{2}{3} i k^3 \alpha^{\text{static}} - \frac{k^2}{a} \alpha^{\text{static}}}. \tag{3.28}$$

The derivation presented in Appendix B may be invoked to realise how an effective polarizability of the form 3.28 can result in a red-shift and broadening of the LSPR.

In the realm of the Rayleigh-Gans theory the expression for the extinction cross-section simplifies to,

$$\sigma_{\text{ext}} = k \Im(\alpha), \tag{3.29}$$

which expresses the interference between the incident and scattered field. The scattering cross-section reads,

$$\sigma_{\text{sca}} = k^4 |\alpha|^2. \tag{3.30}$$

The modified long wavelength approximation has been introduced as a generalisation of the work of Meier and Wokaun for spheres [42]. An alternative route to describe the retardation effects in the dipolar approximation consists of truncating the Mie theory to its first terms and develops the solution in powers of ka. This procedure led Kuwata *et al.* [44] to a practical formulation of the retardation corrections for arbitrarily shaped particles [44]. Figure 3.4 compares the modelled response of two gold ellipsoids with different prescriptions for the polarizability : quasi-static (equation 3.22), MLWA (equation 3.28), Kuwata. A rigourous solution of the Maxwell equations obtained with a T-matrix code (described in section 3.4.2) is shown for comparison.

Using this model together with the polarizability of ellipsoids can provide a good approximation to the features observed, when no multipolar resonance is present.

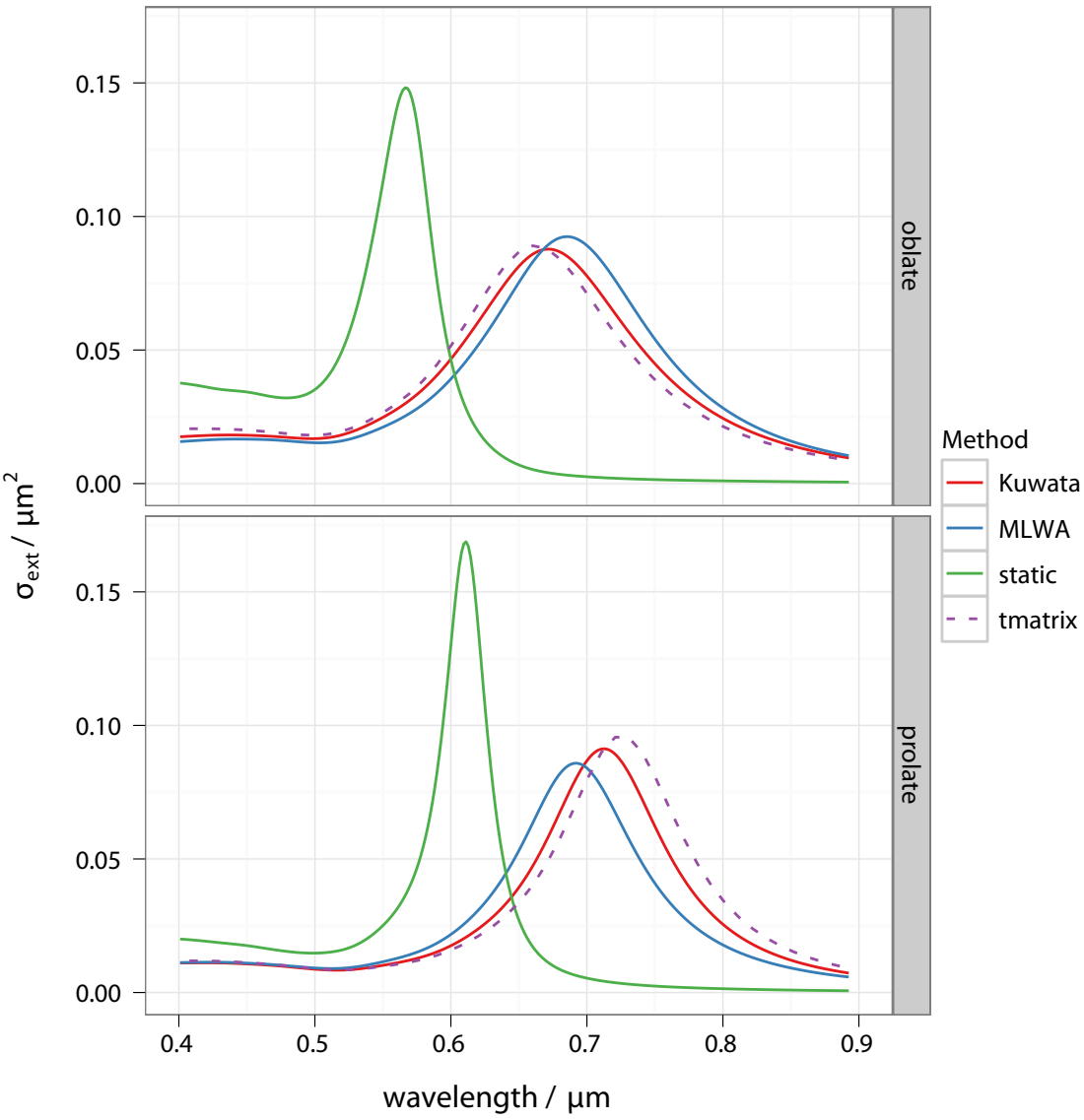

Figure 3.4: Comparison of approximate models: static, MLWA, Kuwata for a gold ellipsoid in a surrounding medium of index 1.46 (permittivity from Johnson and Christy). The comparison is made for a prolate and an oblate ellipsoid (long-axis 60 nm, short axis 30 nm). The dashed lines show the exact result obtained from the null-field method.

3.3 Mie scattering

Mie theory is one of the few examples of exact analytical solutions to the scattering problem. It belongs to the class of methods known as *separation of variables* (SVM) whereby a solution to the wave equation equation 2.17 is sought in spherical coordinates r, θ, ϕ, with the form,

$$E(r,\theta,\phi) = F(r)G(\theta)H(\phi). \tag{3.31}$$

Such solutions will exist only if the Laplace operator ∇^2 is separable in the particular geometry of the problem. There are only a few coordinate systems where this is the case, most notable of

which are the spherical and ellipsoidal coordinates. Mie theory is the application of the separation of variables to a spherical scatterer illuminated by a plane wave. The simplicity of the Mie solution and its analytical formulation have lead to the widespread use of Mie theory beyond its strict range of applicability. Because it provides a theoretically exact solution to the scattering of light by a spherical particle, with any size parameter and dielectric function, the Mie theory is often used as a benchmark to test the accuracy of other numerical techniques. Such analytical solutions can also be derived for ellipsoids [45], however the solutions are much more difficult to implement and result in numerical codes that behave very similarly to numerical methods such as the Null-Field method (NFM) discussed in section 3.4.2 (in fact, some tests not presented here showed that the NFM was generally faster than a code based on the SVM in ellipsoidal coordinates (Ref. [45]) for a comparable accuracy).

We begin by considering two orthogonal vector spherical wave functions $\mathbf{M}$ and $\mathbf{N} = \dfrac{\boldsymbol{\nabla} \times \mathbf{M}}{k}$ that satisfy the vector wave equation and are divergence free. It can be shown [8] that this is equivalent to solving the *scalar* wave equation for a potential ψ, with $\mathbf{M}$ and $\mathbf{N}$ retrieved from,

$$\mathbf{M} = \boldsymbol{\nabla} \times (\mathbf{r}\psi). \tag{3.32}$$

Solving the vector Helmholtz equation is therefore reduced to the problem of solving the scalar wave equation in spherical coordinates. Applying the method of separation of variables to this equation leads to a system of three decoupled differential equations in the variables r, θ and ϕ. The radial dependence satisfies a Bessel equation, the azimuthal dependence satisfies an associated Legendre equation, and the longitudinal coordinate is a simple harmonic function that describes the quantization of the eigen-modes around the sphere. The angular dependence of the electromagnetic field can therefore be expanded onto the basis of vector spherical harmonics $\mathrm{Y}_l^m(\theta, \phi)$, which represent normal modes of the electromagnetic field for a sphere. The scalar spherical harmonics have the following expression,

$$\mathrm{Y}_l^m(\theta, \phi) = \sqrt{\frac{(2l+1)(l-m)!}{4\pi(l+m)!}} \mathrm{P}_l^m(\cos\theta) \exp(i m \phi). \tag{3.33}$$

with P_l^m the associated Legendre polynomials. Figure 3.5 shows the real part of the first few spherical harmonics for $l = 1$ to $l = 5$. We recognise the increasing number of nodes and antinodes as the numbers l increase. Comparison of the first few spherical harmonics with figure 2.13 reveals the identity between the eigen-modes of the charge density on a spherical particle and the Mie solution. Higher order spherical harmonics describe the excitation of multipolar resonances.

The solution of the scattering problem is obtained by projecting the incident, internal, and scattered fields onto a suitable basis of vector spherical harmonics $\mathbf{M}$ and $\mathbf{N}$. The coefficients a_l, b_l, c_l, d_l of these expansions are linked using the continuity relations of the electric and magnetic fields at the boundary of the particle, in a similar fashion to the planar interface. In fact, the analogy can be extended to multilayered spheres [46] where recursive formulas link the fields in each successive layers (such an extension of the Mie theory is used in figure 3.9). The overlap integral of a plane wave with the normal modes over a sphere is non-zero only for $m = 1$, there-

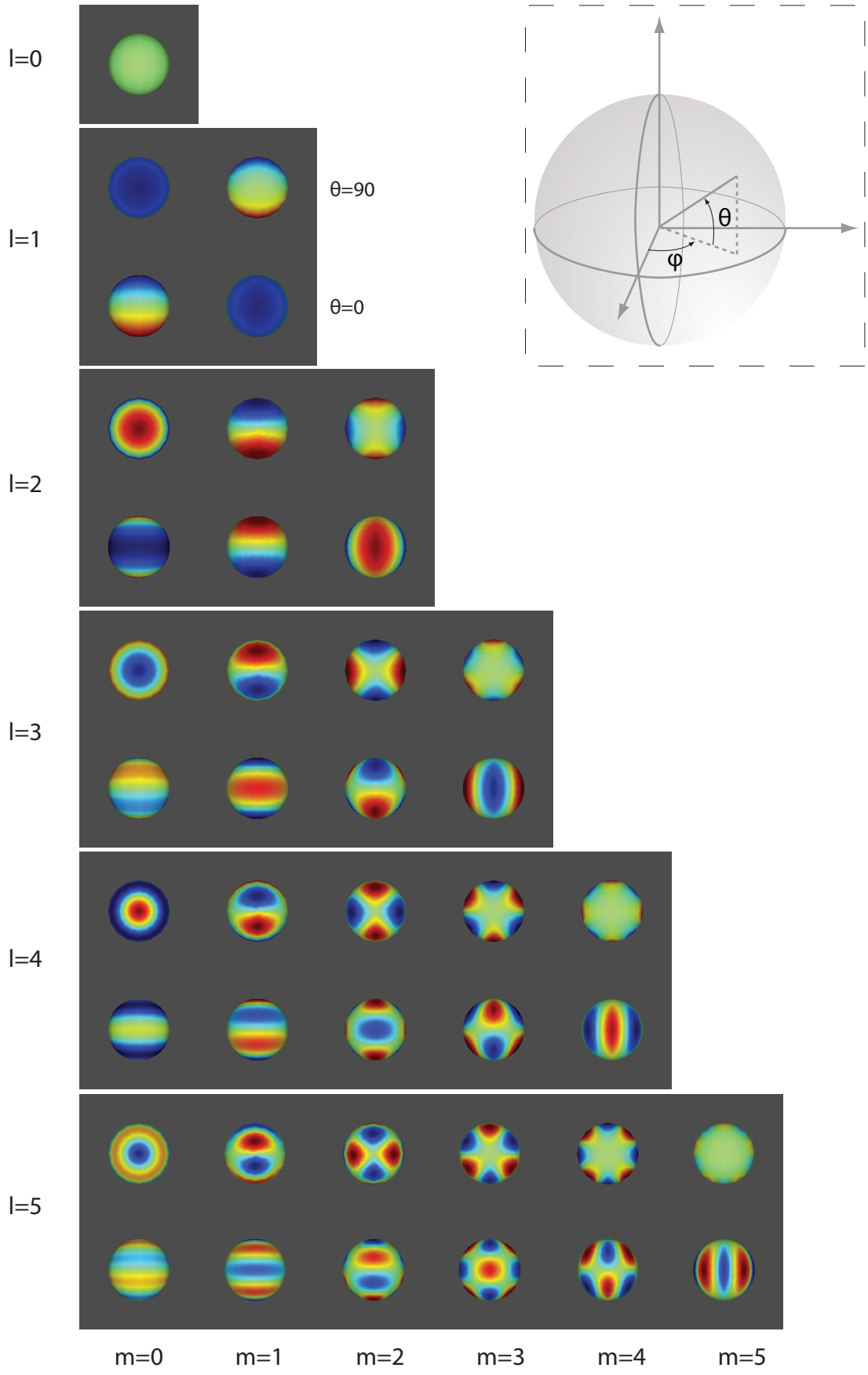

Figure 3.5: Spherical harmonics for $l = 1$ to $l = 5$ (Bottom view: $\phi = \theta = 0$, Top view: $\phi = 0$, $\theta = 90°$). Only positive values of $m = -l \cdots l$ are shown, the negative values are obtained by a simple rotation.

fore the Mie solution can be expressed as a series over only one index, l. The general form of the scattered field is formally written as an infinite sum of vector spherical harmonics, each of these can be considered as a normal mode of the scatterer, or *partial wave* [6],

$$\mathbf{E}_{\text{scat}} = \sum_{l=1}^{\infty} E_l \left(i a_l \mathbf{N} - b_l \mathbf{M} \right), \tag{3.34}$$

where the scattering coefficients have the form,

$$\begin{aligned} a_l &= \frac{m\psi_l(mx)\psi_l'(x) - \psi_l(x)\psi_l'(mx)}{m\psi_l(mx)\xi_l'(x) - \xi_l(x)\psi_l'(mx)} \\ b_l &= \frac{\psi_l(mx)\psi_l'(x) - m\psi_l(x)\psi_l'(mx)}{\psi_l(mx)\xi_l'(x) - m\xi_l(x)\psi_l'(mx)}, \end{aligned} \tag{3.35}$$

with ψ_l, ψ_l', ξ_l and ξ_l' the Riccati-Bessel functions and their derivatives, and m the relative refractive index. In any practical implementation of this theory we need to truncate this series expansion, the approximation requires more terms as the size parameter increases.

In figure 3.6 the scattering, absorption and extinction spectra of a gold sphere are presented for two values of the permittivity of the surrounding environment and three different sphere diameters. The smallest sphere exhibits a characteristic dipolar response: the scattering is much weaker than absorption and the interband transition leads to a clear absorption edge below 450 nm. The effect of increasing the refractive index of the surrounding medium is to enhance the cross-sections: the effective size parameter is increased as the wavelength in the medium is reduced. A slight redshift of the LSPR is observed as a result of dynamic depolarisation. As the sphere is made larger, the scattering becomes more important and in fact at 50 nm radius the scattering and absorption cross-sections are of equivalent magnitude. In a vacuum, a 80 nm radius sphere exhibits mainly a dipolar response, but changing the surrounding index to 1.5 introduces a quadrupolar feature at 450 nm. As the sphere size increases, the scattering dominates and higher order resonances appear that lead to a very broad scattering response that can span the whole visible range. A 500 nm radius sphere exhibits a scattering spectrum that resembles the reflection from a continuous gold film (figure 2.4, chapter 2.). We also note that the *efficiency* reaches a maximum of about 5 before decreasing towards 2 (the so-called *extinction paradox* discussed in Ref. [6]). This confirms that the interaction between light and particles is maximum for ratio size/wavelength of order unity [16]. The absorption cross-section also saturates to a sharp edge that resembles the absorption characteristics of planar gold (figure 2.4).

To further investigate the size-dependence of the scattering by gold nanoparticles, figure 3.7 presents a comparison of the relative strength of different partial waves in the multipolar expansion of the fields. This is done by truncating the Mie series to the first, second, and third coefficients for the TE and TM modes (a_l and b_l coefficients of equation 3.34). The definition of TE and TM is analogous to the planar case, where the local form of the electromagnetic field is characterised immediately outside the sphere: TE (resp. TM) modes correspond to the electric (magnetic) field tangential to the sphere.

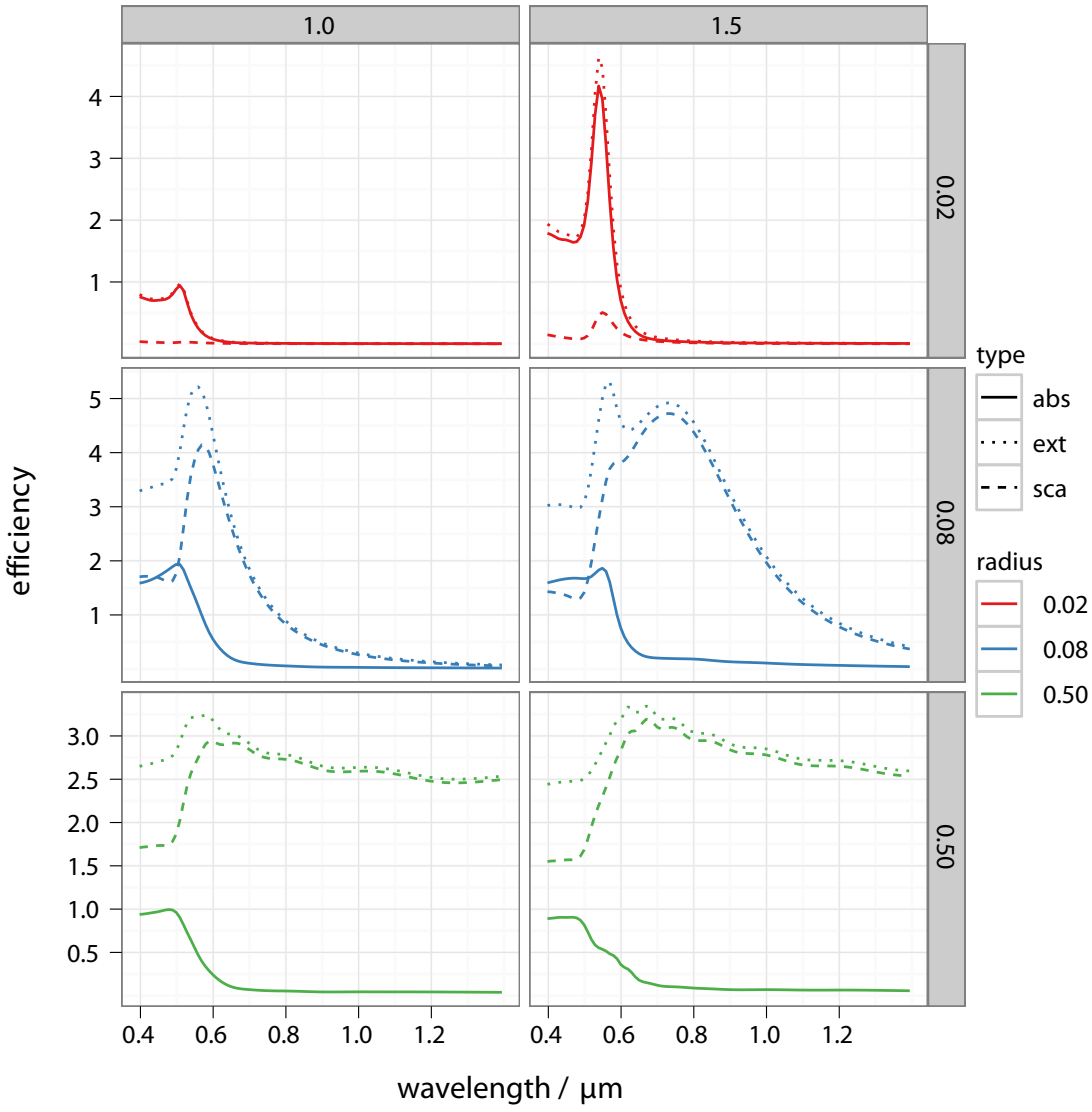

Figure 3.6: Scattering, absorption, and extinction efficiency spectra of gold spheres (permittivity from Johnson and Christy) in air (left panels) and in homogeneous surrounding index (1.5, right panels) for 3 values of the sphere radius: 20 nm (top), 80 nm (middle), 500 nm (lower).

The smaller particle exhibits a purely dipolar response with no magnetic contribution. At 80 nm, a shoulder on the high-energy side of the dipolar resonance reveals the presence of a weak electric quadrupole resonance. The magnetic dipole response is almost zero. For a large sphere of 100 nm radius (larger than any particles studied in this work), the quadrupolar response is of comparable intensity to the electric dipole [47]. The magnetic dipole response is weak, and does not exhibit a resonant behaviour. The magnetic response simply adds a slowly varying background contribution.

Figure 3.8 shows the calculated field profile around gold spheres at three particular frequencies corresponding to the resonant excitation of multipolar modes. The field intensity decays very rapidly in the dielectric surrounding the particles. The cross-sections describe the interaction between an incident plane wave and the particle and can be compared to experiments performed in the far-

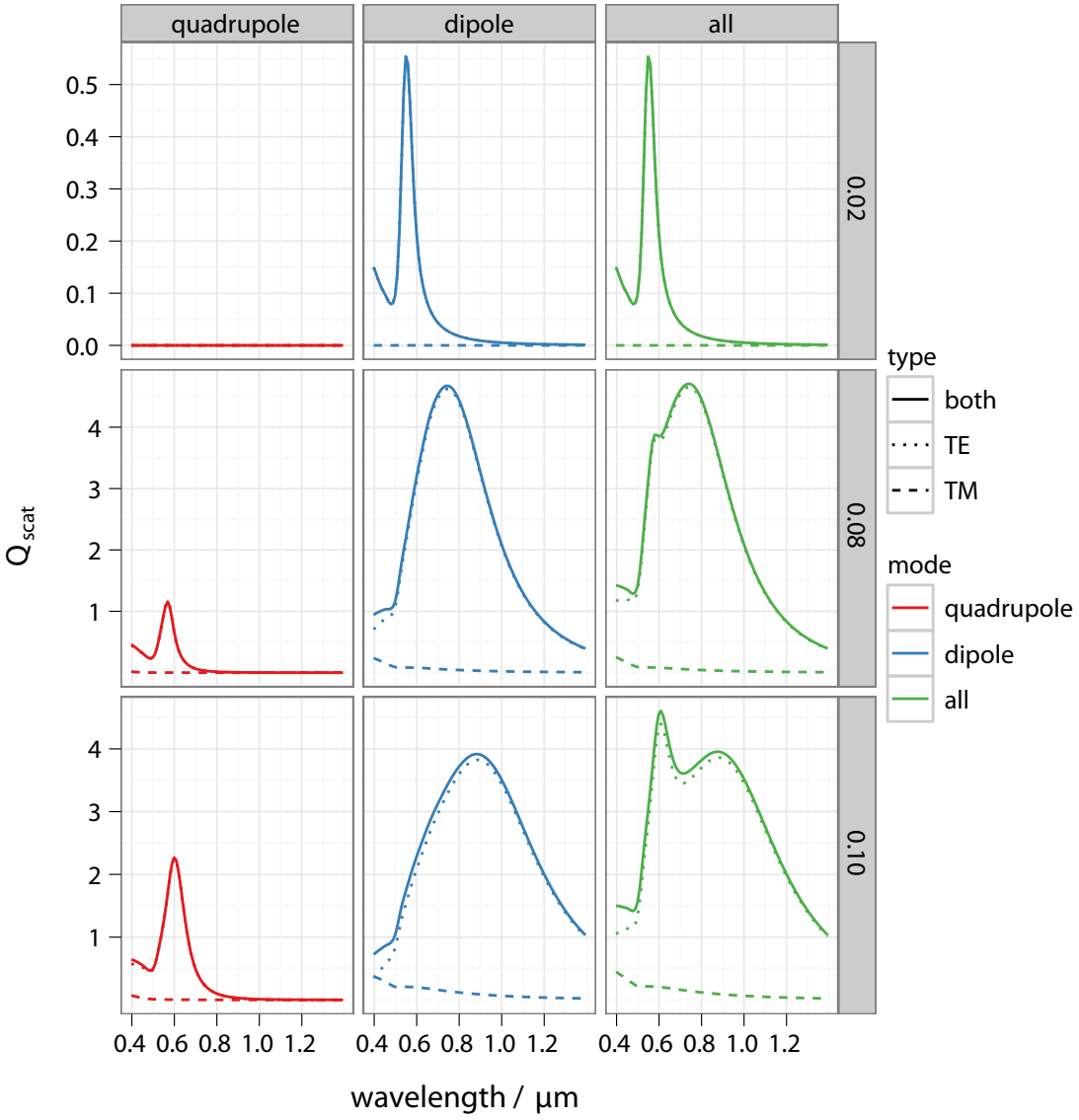

Figure 3.7: Comparison of the scattering cross section obtained from the first 2 coefficients and the fully converged series in the Mie theory for gold spheres of radius 20 nm, 80 nm, and 100 nm. The surrounding medium is of index 1.5.

field. It is also possible to infer some near-field properties of the scattering by a particle by comparing the response of the bare particle and the response of the particle with a thin dielectric coating. This is done by using a generalisation of the Mie theory for concentric layers. For sufficiently thin and soft coatings, the modification of the fields near the particle is small enough to be described as a perturbation of the modes of the bare particle. In planar systems the decay length of the SPP is much larger than the extent of a layer of target molecules in a typical biosensing experiment; it is therefore possible to reduce the effective sensing volume by using localised plasmons with a much shorter decay length [48]. This has the advantage of making the sensor less prone to background variations in index from the bulk solution such as temperature and pressure fluctuations. In figure 3.9 the influence of a thin coating on the far-field scattering response of gold nanoparticle is studied for a typical configuration: the bulk index of the surrounding medium is that of air (left

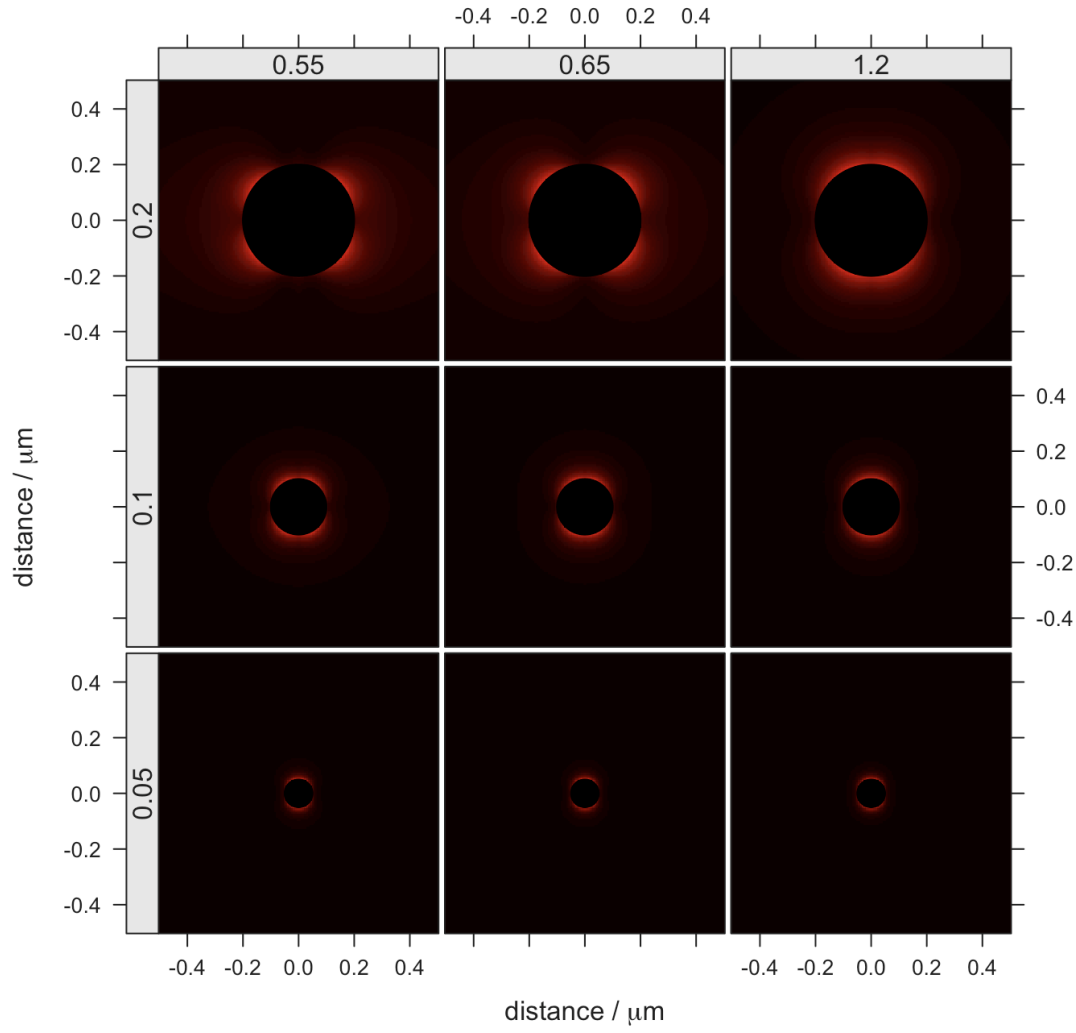

Figure 3.8: Mie calculation of the scattered electric field around gold spheres of different size parameter. The colour scale indicates the time-averaged magnitude of the electric field (modulus squared). The internal field is not represented in these plots.

panels), and water (1.33, right panels), and a coating of index 1.5 characteristic of most biological molecules [49] is added in increments of 1 nanometre. As the thickness of the overlayer is increased, the LSPR is seen to present a consistent red-shift from the position of the resonance of a bare particle in air (left) or water (right). The intensity of the scattering is also increased, and this can attributed to both the increase in diameter of the scattering body, and also in the variation of the permittivity across the visible range (gold is a 'better' Drude metal near the IR region). The dashed line represents the scattering response of a particle in a homogeneous index of 1.5. It is interesting to note that although the peak position of the LSPR of the coated particles tends towards this resonance frequency, the intensity is considerable weaker for the homogeneous case. This is because the limit of an infinite thickness of the coating is not a realistic physical situation for the far-field scattering response which considers the scatterer as a point source of radiation. To com-

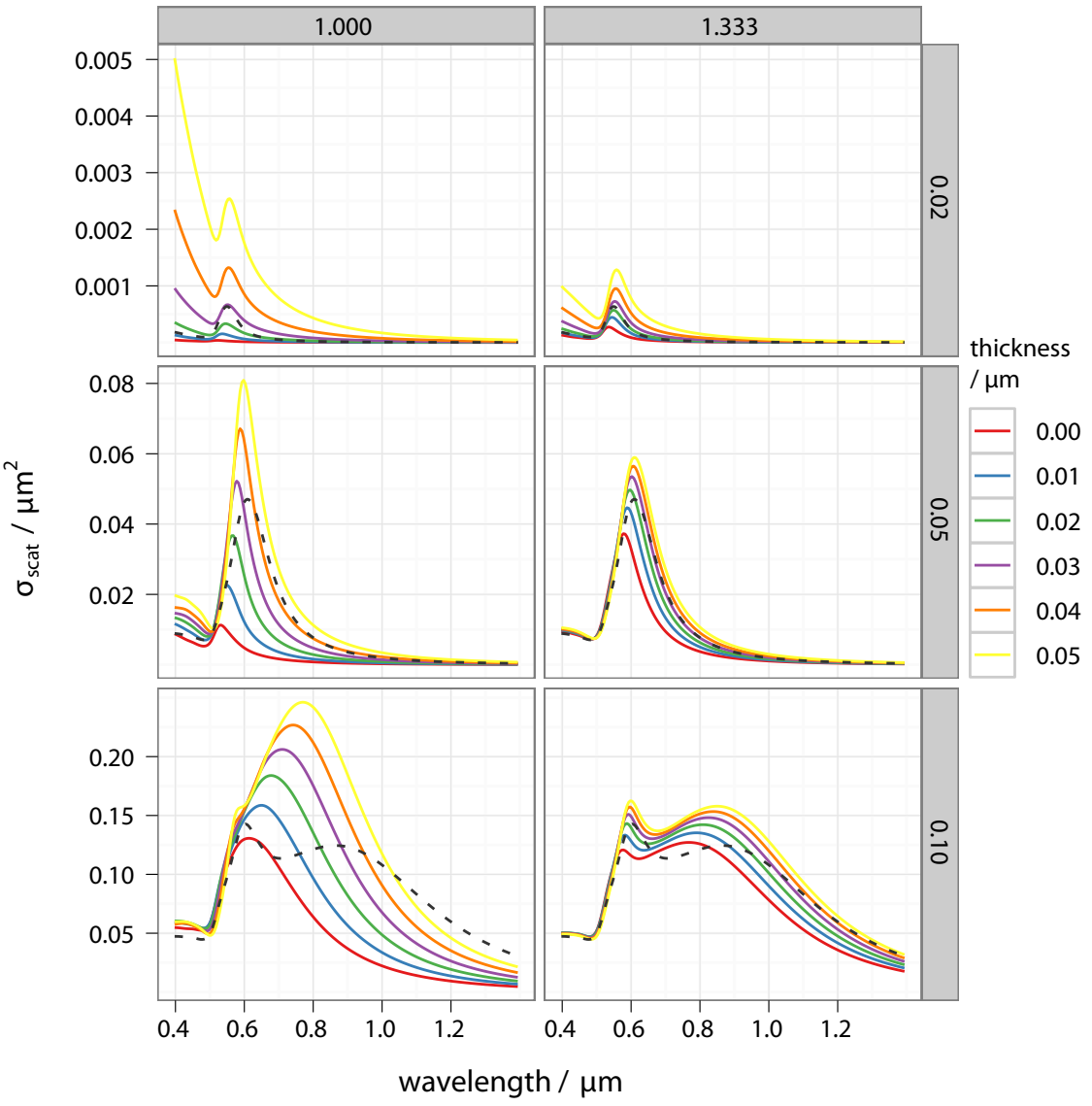

Figure 3.9: Scattering cross-section spectra of gold spheres in air (left panels) and in water (right panels) with an overlayer of increasing thickness and index 1.5 calculated with the Mie theory. Three radius of the core sphere are considered: 20 nm, 50 nm, 100 nm. The dashed lines consider the case of an homogeneous medium of index equal to that of the coating.

pare with the situation for a homogeneous medium, the detector would need to be placed *inside the coating*.

3.4 Numerical techniques for nanoparticles of arbitrary shape

The optical properties of non-spherical particles can differ considerably from the response of spherical particles [5, 46]. Unfortunately, analytical solutions to the scattering problem are limited to very particular shapes (*e.g.* infinite cylinder, spheroids, and spheres). A large range of numerical techniques are available to solve the Maxwell equations for a particle (or system of particles) of ar-

bitrary shape (possibly inhomogeneous). Kahnert [18] gives a comprehensive review of the most widely used techniques such as FDTD, FEM, DDA, and T-matrix techniques, each method having its advantages and drawbacks. Of particular interest for fast and accurate computations is the family of T-matrix methods [50].

3.4.1 T-matrix formulation

The T-matrix is a very general reformulation of the scattering problem which was first introduced by Waterman (1965) [50]. His initial formulation was linked to the null-field method [51] which is one of several techniques that can be employed to extract the T-matrix of a scatterer [52]. The T-matrix formalism was later recognised as a powerful tool to describe the scattering by single particles and clusters of particles including infinite periodic structures.

In this approach, the linearity of the Maxwell equations is used to postulate a linear relationship between the coefficients a_{mn} and b_{mn} of an expansion of the incident field onto a basis of vector spherical wave functions (VSWFs), and the coefficients of the scattered field p_{mn} and q_{mn},

$$\begin{bmatrix} p \\ q \end{bmatrix} = \begin{bmatrix} T \end{bmatrix} \begin{bmatrix} a \\ b \end{bmatrix}. \tag{3.36}$$

The fact that the VSWFs form a complete basis over a sphere surrounding the scatterer reveals one of the most appealing features of the T-matrix formulation in that it contains the full description of the scatterer independently of the orientation of the particle and of the incident field. This is particularly useful when one considers the scattering by a collection of particles in arbitrary configurations: one only needs to calculate the T-matrix of each individual element separately. The formalism lends itself to very efficient analytical formulas for the rotation and translation of the T-matrix that can be used to treat the scattering problem of a cluster in any direction and polarisation of the incident light, and for averaging over orientations. The treatment of multiple scattering in a cluster can make use of the translation theorem for vector spherical wave functions: the partial waves scattered by any individual component of the cluster can be expressed in a basis of VSWFs centred at any other particle location. The T-matrix elements can often be simplified for scatterers with a particular symmetry such as axially-symmetric particles. Spheres, for example, lead to drastic simplifications and the double infinite series reduce to the single series of the usual Mie formulation. In this sense the T-matrix provides a generalisation of the Mie theory to arbitrarily shaped particles and systems of particles.

Although a wide range of techniques are available to calculate the T-matrix of a particle, the most commonly used implementations are based on a variation of the null field method. The elements of the T-matrix are expressed in terms of vector products of VSWFs on the particle surface.

3.4.2 Null field method

The Null-Field method is based on equation 3.10 which is the surface-integral counterpart of the volume integral equation. The discretization of the scatterer is therefore done only at the boundary of the particle, which often results in a much reduced computational cost in terms of time and

storage. Axi-symmetrical particles can provide additional improvement in computation time as the costly element integration needs to be carried only in one dimension. The incident, internal, and scattered fields are represented using a basis of vector spherical wave functions. The coefficients of these expansions (incident and scattered) are related by the T-matrix, which describes completely the scattering system for a given incident wavelength.

To compute the T-matrix, the Null Field Method applies the following scheme [53]: (i) at the boundary of the particle domain, the null field equation 3.10 must be satisfied, which provides a relation between the internal field and the incident field. (ii) The scattered field is computed from the surface currents by applying the Huygens principle: each portion of the surface is a source which radiates a wavelet, the scattered field comprises the wave-front obtained by summing over these partial waves.

The convergence of the technique has been the object of extensive studies, and the T-matrix is generally used as a benchmark for other numerical techniques due to its excellent numerical accuracy in the far-field zone. Several improvements to the technique have been proposed, in this work I used the implementation by Eremin *et al.* [53, 54], known as the discrete sources method. Discrete current sources are located on the surface of the particle and the expansion is made over VSWFs located at these sources. The computation can be drastically shortened when the particle is axisymmetric: the sources are then placed on the axis of the particle and the summations involve line integrals rather than surface integrals.

3.4.3 Discrete Dipole Approximation

The Discrete Dipole Approximation is based on the volume integral formulation 3.9. The scattering volume is discretized (often in a cubic lattice) in a set of N polarizable elements (or 'dipoles'). Each of the dipoles is assigned a polarizability that describes its response to an electromagnetic excitation. The most commonly used prescription for α is a corrected version of the Clausius Mossotti equation that accounts for the radiation damping of the dipole element. The sub-elements are allowed to interact via the retarded expression for the field of a dipole.

Each dipole element radiates a field in proportion to the local field it experiences,

$$\mathbf{p}_{(\mathrm{d})} = \alpha \mathbf{E}_{\mathrm{loc}}, \tag{3.37}$$

where α is related to the optical constant of the material. In the first formulation of the DDA, the Clausius-Mossotti prescription was used,

$$\alpha_{\mathrm{CM}} = v \frac{\varepsilon - 1}{\varepsilon + 2}, \tag{3.38}$$

where v is the volume associated with a polarizable sub-unit. Because each dipole is surrounded by a large distribution of identical dipoles, the incident field it experiences is substantially different from the external field. In general, the local field may be divided in several contributions,

$$\mathbf{E}_{\mathrm{loc}} = \mathbf{E}_{\mathrm{inc}} + \sum_{\mathrm{dipoles}\setminus i} \mathbf{E}_{(\mathrm{d})} + (\mathbf{E}_{\mathrm{refl}} + \mathbf{E}_{\mathrm{subs}}), \tag{3.39}$$

where the sum represents the contribution of the dipolar field associated with the other dipoles in the scatterer volume, $\mathbf{E}_{\text{refl}}$ and $\mathbf{E}_{\text{subs}}$ are supplementary contributions that may arise when the particle is supported by a substrate. They represent respectively the additional excitation field resulting from the reflection of the incident field on the substrate, and the field resulting from the reflection of each dipole element on the substrate. $\mathbf{E}_{\text{subs}}$ has been approximated as the effect of dipole images [55], or more rigourously by replacing the free space Green's dyadic describing the coupling between dipoles by a Green's function in the presence of an interface [29].

The field radiated by a dipole is described by,

$$\mathbf{E}_{(\text{d})} = \frac{e^{i\omega r/c}}{4\pi\varepsilon_0}\left\{\frac{\omega^2}{c^2 r}\hat{\mathbf{r}}\times\mathbf{p}\times\hat{\mathbf{r}} + \left(\frac{1}{r^3} - \frac{i\omega}{cr^2}\right)\left[3(\hat{\mathbf{r}}\cdot\mathbf{p})\hat{\mathbf{r}} - \mathbf{p}\right]\right\}. \tag{3.40}$$

Ignoring the reflection terms for clarity, we can cast equation 3.39 in matrix form,

$$A\mathbf{P} = \mathbf{E}_{\text{inc}}, \tag{3.41}$$

where A is the *interaction matrix* that describes the radiative coupling between the polarizable units in the non-diagonal terms,

$$A_{ij} = \frac{e^{(ikr_{ij})}}{r_{ij}}\left\{k^2(\hat{\mathbf{r}}\otimes\hat{\mathbf{r}} - \mathbb{I}) + \frac{ikr_{ij} - 1}{r_{ij}^2}(3\hat{\mathbf{r}}\otimes\hat{\mathbf{r}} - \mathbb{I})\right\}, \tag{3.42}$$

and the self-reaction term $1/\alpha$ in the block diagonal.

Solving equation 3.41 for $\mathbf{P}$ can be a problem as the discretization of a particle will typically require 50 000 elements to obtain a good accuracy. Iterative methods for inversion can be used, but the most efficient technique to date is based on a fast Fourier transform taking advantage of the particular Block Toeplitz structure of A when the grid is chosen with cubic symmetry. This improvement arises because the radiative coupling depends only on the relative distance between two dipole elements and can therefore be written as a spatial convolution [56].

When the polarization is known at all points inside the discretized mesh, the scattered field and all optical properties are readily obtained. For example, the extinction cross-section is obtained by,

$$\sigma_{\text{ext}} = \frac{4\pi k}{|E_0|^2}\Im(\mathbf{E}_{\text{inc}}{}^{*}\cdot\mathbf{p}_{(\text{d})}). \tag{3.43}$$

Several numerical tests showed that the DDA has a large computational cost compared to the Null-Field method and offers little advantage for the simple shapes (ellipsoids) that I studied in this thesis. The coupled dipole model is however a useful concept to use when describing the interaction between small nanoparticles, with only a few modifications to the DDA equations as described in the next section.

3.5 Multiple scattering by collections of particles

Scattering is defined as the result of the interaction of the electromagnetic field with an obstacle without any restriction on the form of the material. In particular, the scatterer may comprise several unconnected bodies without altering the preceding formalism. For example a unit cell of the computational box in FDTD or FEM methods can contain several particles and we need to solve the Maxwell equations in all of the computational domain. With a large collection of scatterers such an approach can become difficult if not impossible to manage in a reasonable amount of time. This is where the concept of multiple scattering can be used as an alternative route to solve the Maxwell equations for a cluster of scattering objects when the individual scattering properties are known beforehand. There are two equivalent approaches to this multiple scattering formulation: the *successive scattering orders* method and the *self-consistent* approach [57]. In the successive scattering orders method the scattering by each particle is first evaluated in the single-scattering approximation where each particle is only excited by the incident field. The resulting partial waves scattered by each particle are then used to compute a second order of scattering by the neighbouring particles, *etc*. until convergence is attained. This approach is very general and is justified by the rigourous order-of-scattering expression of the volume integral equation 3.9. Some approximations can be introduced so as to simplify the problem, such as neglecting certain scattering paths [26]. The second approach seeks the unknown distribution of the field in all space in a self-consistent manner: the field scattered by each particle is expressed in terms of the unknown total field.

When considering the optical response of a collection of closely spaced particles, the question arises as to whether the light incident on each particle contains a non-negligible contribution from the light scattered by surrounding particles. If each scatterer experiences only the incident field, the response of the medium to light is said to be dominated by single scattering, and the far field intensity measurements are simply described by an average of the individual particle scattering response [58]. If, however, the scatterers are not very soft or very dilute, the interaction can become significant and one has to consider a multiple scattering picture. A general review of the different degrees of approximation is given by Mishchenko [26, 28, 58], and links the radiative transfer equation to its microscopic derivation from the Maxwell equations.

Perhaps the simplest approach to multiple scattering is the consideration of a set of dipoles that form a coupled system, the interaction between two dipoles can be exactly described in the explicit, closed form of an effective polarizability [57]. There exists a strong connection between the formulation of the multiple scattering problem by a system of interacting dipoles, and the Discrete Dipole Approximation introduced in 3.4.3. I present in the next section the gist of the coupled dipole model that will be used in 5–8 as the major modelling approach to investigate the interaction in a collection of gold nanoparticles.

3.5.1 Coupled dipole model

The coupled dipole model has been widely used for several decades[59–61], and despite its relative simplicity I will show in the experimental sections of this thesis that it can provide an accurate ap-

proximation to the behaviour of complex many body systems. I present here a simplified version of the CDA that captures the major assumptions and results. The literature offers many detailed studies, see for example [62, 63] for a more complete treatment. In the coupled dipole approximation, each particle is modelled as a dipole of polarizability α. The particles studied in this work are described as ellipsoids (semi-axes a, b, and c, volume V), for which the static polarizability can be written as [6],

$$\alpha^{\text{static}} = abc\frac{\varepsilon_m - \varepsilon_d}{3\varepsilon_d + 3\mathrm{L}(\varepsilon_m - \varepsilon_d)}, \tag{3.44}$$

with ε_d and ε_d the relative permittivities of the metal and surrounding medium respectively, L is a shape factor. When the particle size is of order 50 nm or more, this expression needs to be modified to account for dynamic depolarisation and radiative damping. We do so by introducing an effective polarizability of the form equation 3.28. When excited by an electromagnetic wave at frequency ω, a dipole re-radiates a scattered wave in proportion to its dipole moment. The net field on every dipole is therefore the sum of the incident field, plus the radiation from all other dipoles, which leads to a system of coupled equations similar to equation 3.41 to be solved self-consistently for the total field.

3.5.2 Other techniques

Effective medium approximation

When very small particles are embedded in a matrix with a low concentration, effective medium theories can be applied as a simple macroscopic model [64]. Maxwell-Garnett theory describes the effective permittivity of such composites, in a derivation similar to the one used in the Clausius Mossotti equation, with the inclusions being modelled as dipoles in a continuous background. It should however be noted that the Lorentz expression for the internal field was derived under the assumption of a cubic lattice or a random orientation of the dipoles. Clearly, transposing this model to a 2D ordered or disordered array can have consequences on the validity of the effective medium approach, in particular the effective dielectric function of a composite material can present a non-local form [65, 66]. In particular, coherent coupling in regular arrays require us to introduce *ad hoc* corrections which eventually break down when multipolar resonances are present in the medium.

Superposition T-matrix method

When the T-matrix of individual scatterers has been obtained from rigourous calculations, the multiple scattering technique may be obtained using the formalism of the superposition T-matrix method. The principle of this technique relies on the translation theorem for VSWFs: the partial waves scattered by each individual scatterer are expanded in the basis of VSWFs at the centre of each neighbouring particles. The coefficients for this translation and expansion of VSFWFs are known analytically, resulting in a very efficient formalism that can model hundreds of particles in arbitrary orientations and positions. The particular case of a periodic arrangement can lead to drastic simplifications that allow for an analytical closed-form formula for the response of the medium in terms of the individual particle response. This formalism was developed in the study of electron diffraction in solids (KKR method) and later applied to dielectric and metallic photonic crystals [11, 13, 67]. The essence of the formalism is to convert the infinite sum of the scattered field

from the periodic structure in the Fourier space where the series can be calculated more efficiently by the method of Ewald summation [14].

3.6 Challenges

This section would not be complete without mentioning the current limitations in our ability to reproduce and better understand the experimental results with the help of numerical modelling. To this aim, I would like to present some remarks regarding the limitations I have faced in modelling the scattering of light by gold nanostructures.

The first issue concerns the comparison between modelling and experiments. The modelling approaches mentioned in this chapter suffer two limitations. First, the practical implementation of the scattering codes can make the use of a powerful technique difficult without a deep understanding of the theory behind the model — this is the case for the T-matrix method and advanced multiple scattering codes. Second, the current numerical methods for arbitrary shaped particles and in particular large aggregates of such particles are relatively slow even on modern computers, which makes the optimization of a structure a difficult task.

Many powerful techniques are available, each with its own strengths and weaknesses. The most widely used techniques are Mie theory, T-matrix, `FDTD`, `DDA`, `FEM`, and approximate techniques (for instance, the Rayleigh-Gans theory of section 3.2). Improvements on these methods is an active field of research, particularly in the context of metallic nanoparticles where they face the following challenges: (i) Transition from *ab initio* calculations to a macroscopic index description in nanoscopic structures [17]; (ii) Ameliorate our knowledge of optical dielectric functions, possibly by designing new experiments on nanoscale samples. (iii) The extent to which a description of a material in terms of a macroscopic response function (ϵ, μ) can be valid (*e.g.* for metamaterials, the question arises as to whether this set of effective parameters is unique for a structure. Non-local effects are another limitation in this regard).

On the technical aspect, I should like to mention a few interesting challenges that I have not considered in this thesis. First, the influence of a substrate on the scattering properties of particles is of great importance with respect to the particle sensitivity to the surrounding index [68], and is also responsible for a strong modification of the coupling between particles investigated in chapter 6. The presence of a substrate has been successfully modelled in a variety of numerical codes such as the T-matrix method [69], and the `DDA` [22] but requires a large modification of the available codes.

Similarly, the accurate comparison of the optical measurements of the scattered light by single particles with numerical modelling requires a precise match of the description of the incident light beam with the experimental setup. In dark-field spectroscopy, the range of incident angles departs substantially from a collimated beam (plane wave). In addition, the objective lens only collect a portion of the scattered light and the angular distribution of the scattering pattern may vary as a function of wavelength for large particles or for particles placed on a substrate. The experiments should therefore be performed with a well-defined incident angle and polarisation state, and the modelling should consider the integration of the differential scattering cross-section $d\sigma_{\text{sca}}/d\Omega$ over the solid angle Ω defined by the numerical aperture of the collection optics [69].

Investigating large but not infinite clusters of particles can be very computationally intensive. A promising approach to deal with such problems is to treat separately the scattering at different length-scales. For example each particle can be discretized with a fine mesh to account for the abrupt change of dielectric function with the surrounding medium, but the interaction between particles can be modelled on a coarser grid. Such a scheme has been suggested within the DDA method where the polarisable points need only to describe the particles [27].

Finally, I should like to note that I restricted the discussion to linear optical processes: nonlinear and inelastic processes in relation to plasmonic components are still less studied although recent theoretical advances suggest prolific comparisons to be made [70–72].

"L'homme est capable de faire ce qu'il est incapable d'imaginer."

René Char

4

Experiments on single nanoparticles

This chapter introduces the fabrication technique of electron-beam lithography that was used to fabricate samples with a precise control over the shape and size of nanoparticles. The influence of the shape and size of the particles on their optical characteristics is investigated through an analysis of the correspondence between the geometry of the particles retrieved from scanning electron micrographs (SEMs) and the optical scattering spectrum of the same isolated particles using dark-field spectroscopy. The use of nanorods in particular allows us to better characterise and understand the dependence of the LSPR spectral position and width on the particle volume and aspect ratio. Numerical modelling based on the techniques presented in chapter 3 is used to improve our understanding of the scattering properties of individual gold nanoparticles.

4.1 Fabrication techniques

The use of gold (and silver) nanoparticles for their optical properties can be traced back centuries ago, when artisans empirically obtained the bright colours of certain stained glass windows (a typical bright red for gold inclusions). This motivated the work of Mie who solved the more general problem of scattering by a sphere of arbitrary dimension and refractive index, a theory still actively used and studied a hundred years later [1]. It is a very notable fact that Mie's original paper ranks amongst the most cited papers in physics despite its apparent specialised impact [2]. It is, in comparison, only in the past two decades that a precise study of gold nanoparticles started to develop. This situation stems from the difficulty in fabricating and characterising the precise morphology of objects that are smaller than the diffraction limit of conventional optics. In figure 4.1 we illustrate the advance in this field by juxtaposing two different samples from completely different periods in time. The bottom image presents the Lycurgus cup, a Roman work dated to the 4th century A.D. that can be found in the British museum. It is composed of gold and silver nanoparticles embedded in the glass, these particles present in minute concentration (1%) produce a

striking variation in taint [3]. Observing the vase in reflection yields a green colouration, while in transmission the vase appears red. The top picture is a set of four silver nanoparticles produced in 2007 using electron-beam lithography and characterised optically using dark-field spectroscopy. The bright colours observed in scattering illustrate the strong influence of the size and shape on the scattering response (true colours, this illustration is courtesy of W.A. Murray [4]). With silver, the coloration may span across the whole visible range by small variation in the particle sizes. The strong absorption in the high-energy side of the visible spectrum limits the range of observable colours for gold nanoparticles.

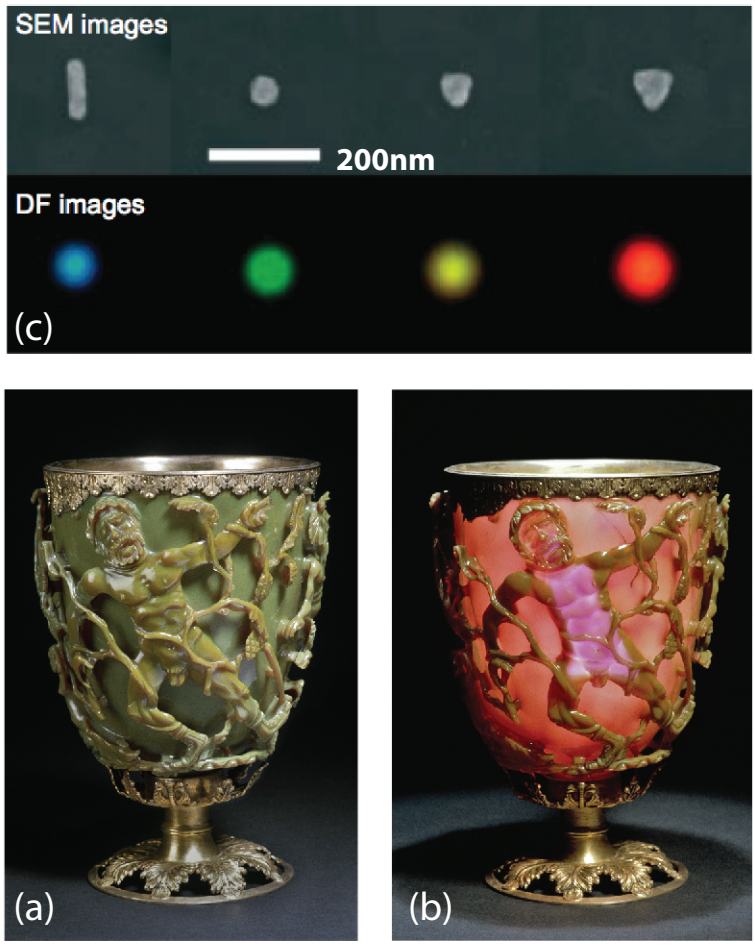

Figure 4.1: Illustration of the coloration due to plasmonic nanoparticles. (a) Lycurgus vase in reflection. (b) Transmission (from [3], © Trustees of the British Museum). (c) SEM and dark-field image of four silver nanoparticles (courtesy of W.A. Murray [4]).

4.1.1 Electron beam lithography

Several types of samples have been produced for this thesis, with two main purposes: (i) single particle characterisation, requiring a large spacing (typically 5 µm); (ii) observation of electromagnetic interaction between particles in a dense array of particles (this is the subject of chapters 5—8). The process of EBL is illustrated in figure 4.2, and involves the following steps:

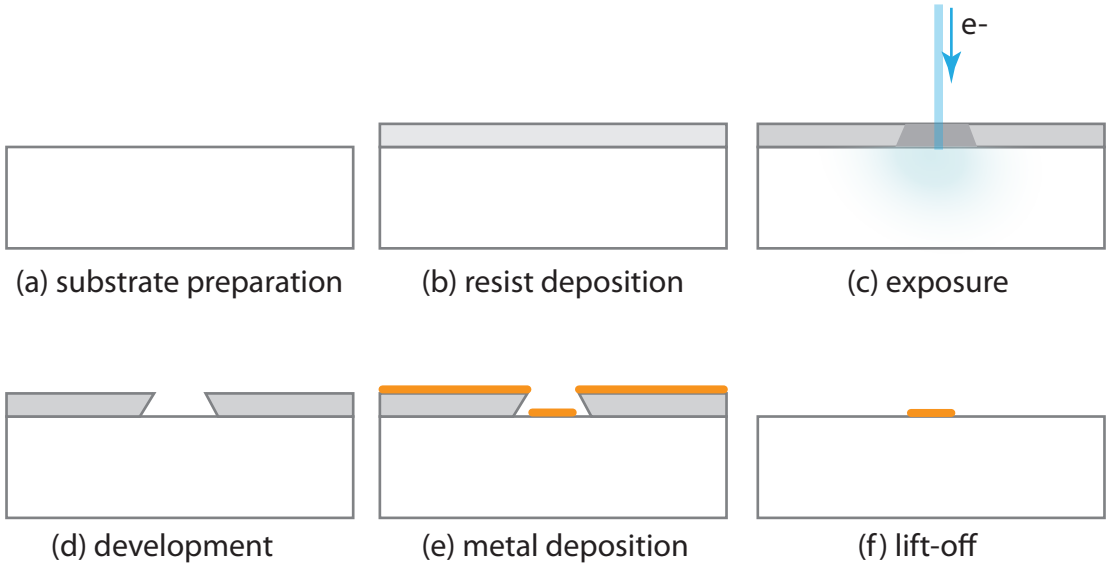

Figure 4.2: Schematic of the EBL process.

a. Cleaning of the substrate. First, the glass substrate is placed in nitric acid for 30 minutes, then rinsed in a sonicating bath of deionised water for 15 minutes. This is to remove the inorganic dust particles. Second, the substrate is placed in a sonicating bath with acetone, followed by isopropanol (IPA) (15 minutes each). The acetone is used to dissolve any organic contaminant, and the IPA further cleans the substrate from any residual chemical present with the acetone. The substrate is subsequently drag-cleaned on both sides with lens tissues and acetone followed by IPA. Dry nitrogen is finally used to remove any dust particles prior to the application of the resist coating.

b. Coating of the substrate with a sensitive resist. A mixture of a polymer (PMMA) diluted in a solvent (anisole) was used for all the samples reported here. The coating was done by spinning the substrate at 1500 rpm after depositing a drop of the liquid resist. This spinning rate was maintained for 90 s, resulting in an approximately 80 nm thick layer covering the substrate. The film uniformity across the substrate is of little importance for our application as the typical region occupied by the sample is less than half a millimetre in extent. The sample is then placed on a hot plate at 180 degrees for half an hour, to evaporate the solvent. A thin gold film (15 nm) is deposited for non-conducting substrates, following the procedure described in (e). This ensures that the substrate is conducting, a requirement for the electron-beam lithography process (the electron beam and the sample form a closed electrical circuit from the source to the ground).

c. The sample is placed under vacuum in the electron-beam system. After careful alignment and focussing procedures, the desired pattern is drawn by the collimated electron beam that passes through the resist layer, thereby exposing it with high energy electrons. The voltage and intensity of the beam can be adjusted to reach a good compromise between the exposure time (inversely proportional to the current passing through the sample), the available voltage

(directly controlling the energy of the electrons), and the required precision. Typical values for our available system were: V=30 kV, I=20 pA, dose 400 $\mu C/s^{-2}$. (see Appendix C for more details on the EBL process).

d. The sample is retrieved from the EBL system and the exposed resist is developed in a mixture of 90% isopropanol and 10% pure water for 1 minute, under constant agitation. In this process, the exposed areas of the positive resist are chemically dissolved and removed from the sample, leaving the underlying substrate free. The sample is immediately rinsed in deionised water for one minute. The development time is carefully monitored as the exposed area of the resist presents a gradual degree of exposure. Insufficient developing time may prevent the metal that is to be deposited to form the particles from being in contact with the substrate, and over-developing results in a loss of resolution in the particles. It is vital to maintain the sample in a very clean condition, as any contaminant would compromise the subsequent deposition of metal on the bare glass.

e. The sample is placed in a vacuum chamber, where gold is deposited by thermal evaporation. The thickness is monitored in real time by a calibrated quartz crystal situated in the chamber.

f. The remaining resist mask is dissolved in boiling acetone for several minutes to half an hour, until the sample appears clear from the thin gold coating covering the mask. The particles that were deposited on the bare glass are left in place, and the sample is cleaned in IPA and dry nitrogen from any chemical residue.

A set of different particle shapes is presented in figure 4.3. Each of the four duplicates of each shape (rod, triangle, square, disc) was produced on the same sample with the same nominal pattern. The variation from particle to particle is attributed to the limited resolution of the EBL process, and to the grain structure of the metal deposed by thermal evaporation.

Limitations

The electron beam can be deflected only over a limited area at a given resolution. This limits the spatial extent of the patterns that can be exposed in a single run. For larger areas, the stage holding the sample needs to be moved, and this mechanical displacement has less accuracy and leads to stitching problems. This limitation concerns large arrays of particles (chapter 5 to 8) and is not a problem for the single particles studies that are the object of this chapter.

The resolution (a few nanometres with the resist and lithography system available) is limited by a range of factors. First, the sensitivity and contrast of the resist lead to a limitation of the smallest features attainable, and to a blurring of the exposed pattern. Second, as the e-beam traverses the resist layer and the substrate, a widening of the beam occurs because of the scattering of the electrons by the material and the generation of secondary electrons that are emitted in all directions. The forward and backscattered secondary electrons induce an overexposing of the area around the pattern. In particular, the electrons backscattered from the substrate will expose a very large area of the resist layer. This can be a problematic issue in dense arrays and the dose must be carefully adjusted by using a range of doses and establishing an empirical chart of the optimal dose as a function of feature size and array density.

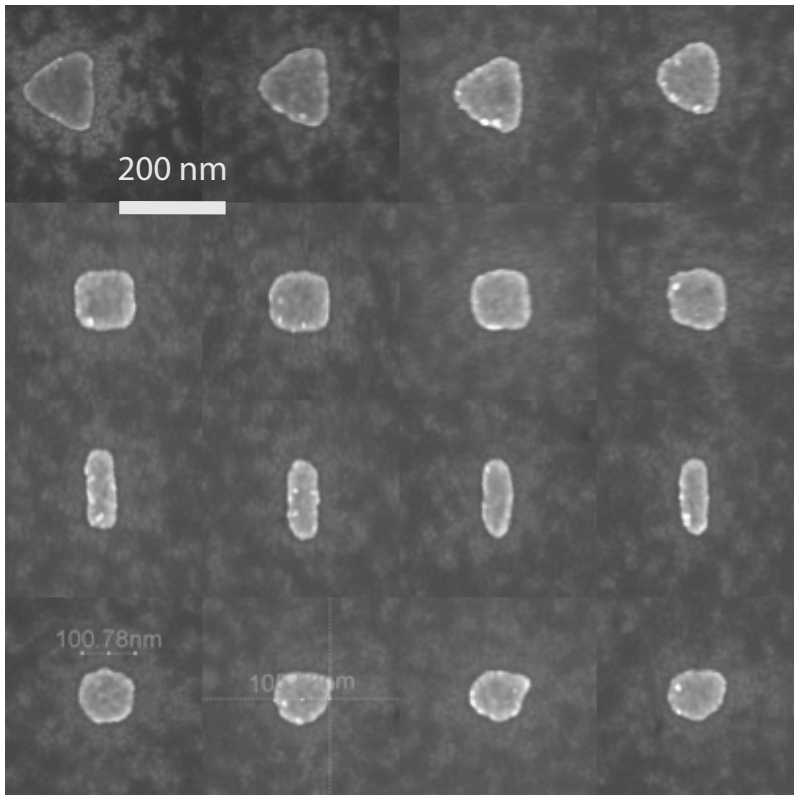

Figure 4.3: SEM of 16 gold nanoparticles of fixed thickness (30 nm) on an ITO coated glass substrate. The nominal shapes (triangles, squares, rods, disks) and dose were identical for each family of four particles.

4.2 Optical characterisation

Although metallic particles are responsible for very a pronounced optical response in colloidal solutions even in small concentrations, the spectroscopic characterisation of single nanoparticles is faced with the difficulty of locating the individual particle that is much smaller than the resolution attainable with conventional optics. The invention of the technique of dark-field microscopy is attributed to Zsigmondy who performed studies of metallic nanoparticles in colloidal solutions in the beginning of the 20th century [5]. The technique allows to observe single metallic particles of a size down to a few tens of nanometres, by simply adapting an ordinary microscope [6]. In the past few decades, the improvement of the fabrication techniques have triggered a renewed interest in the study of individual nanoparticles. The dark-field microscope was coupled to a spectrometer by Schulz [7] and Feldmann [8] (2000) which opened the way to quantitative comparison of the particle geometry and spectral response.

The single particle study provides information that cannot be obtained from a collection of particles. The dispersion of shapes and sizes (apparent in figure 4.3) leads to a convolution of optical properties such as inhomogeneous broadening of the resonance linewidth, and mixing of multiple resonances. Further, particle-to-particle interactions can modify the response of the sample in several ways as will be discussed in chapter 5. The ability to study an isolated nanoparticle is therefore a great advantage to unravel the physics of the excitation of LSPRs [8].

Alternative techniques

Several techniques have been developed to observe the optical response of objects at the microscopic scale. Among these techniques, the Scanning Near field Optical Microscopy (SNOM) uses a near field probe — typically a tip such as the sharpened end of an optical fibre, to retrieve information about the near field structure around the particle of interest [9, 10]. Confocal microscopy has been used [11, 12] to measure the extinction spectrum of a single nanoparticle. A variation of the dark-field microscopy experiment uses the evanescent illumination of the light in total internal reflection to excite a scatterer of interest deposited on a prism [13]. The light that is collected has been converted from evanescent wave to a propagating wave by the scattering object. The interpretation of the spectra obtained in this configuration is more difficult due to the excitation by inhomogeneous plane waves [14]. The need for total internal reflection also limits the range of applicability of the technique in terms of angles of incidence and environment of the particles under study (there needs to be a sufficient index contrast between substrate and superstrate). Finally, the use of fluorescent dyes [15], second-harmonic generation [16], and Raman spectroscopy [17] have been applied to the study of plasmonic nanoparticles.

In this thesis I used dark-field spectroscopy as a means to characterise the scattering response of single particles. The main advantage of the technique is the simplicity of the setup (described below). It also offers the advantage of being a non-intrusive probing technique that does not necessitate the introduction of a near-field probe that could modify the scattering properties of the particles.

4.2.1 Dark-field microscopy

Light from a white source is focussed down onto the sample with a dark-field condenser that blocks the light at small angles of incidence. The resulting hollow cone has a semi-angle ranging from $65 - 75°$. The collection objective has a smaller numerical aperture, therefore no direct light is transmitted from the illumination to the collection path. In the presence of a scattering object, the objective collects a portion of the scattered light, which is fed to a spectrometer. A typical dark-field image is shown in figure 4.5. The dark background is a most recognisable characteristic of the technique: in the absence of a sample, no light is collected. It is of primary importance to ensure an optimal cleaning of the substrate at every step of the lithography process. Any dust particle, on either side of the substrate, will result in a unusable part of the sample. Such problems are apparent in the figure: in (A) a gold flake of dimensions around a few microns landed near the region of interest and causes a very bright scattering in DF microscopy. If it were present on an array of particles, they would be unusable. Similarly, (B) illustrates the effect of a dust particle that remains in the opposite side of the substrate. It is out-of-focus, but as the sample thickness is only 100 μm, the diffraction pattern is clearly visible in the form of Airy rings. Again, such a defect near the particles under investigation would compromise any spectroscopic characterisation. In (C) we recognise large labels (arrows) that are drawn to easily locate the arrays. The disc is a so-called 'contamination spot' that remains from focussing the e-beam before exposing the arrays. (D) is a set of 5×3 arrays of 8×8 gold nanorods. Each array differs in the nominal sizes and dose, therefore an increase in scattering intensity is noticeable from right to left (smallest to largest nominal volume)

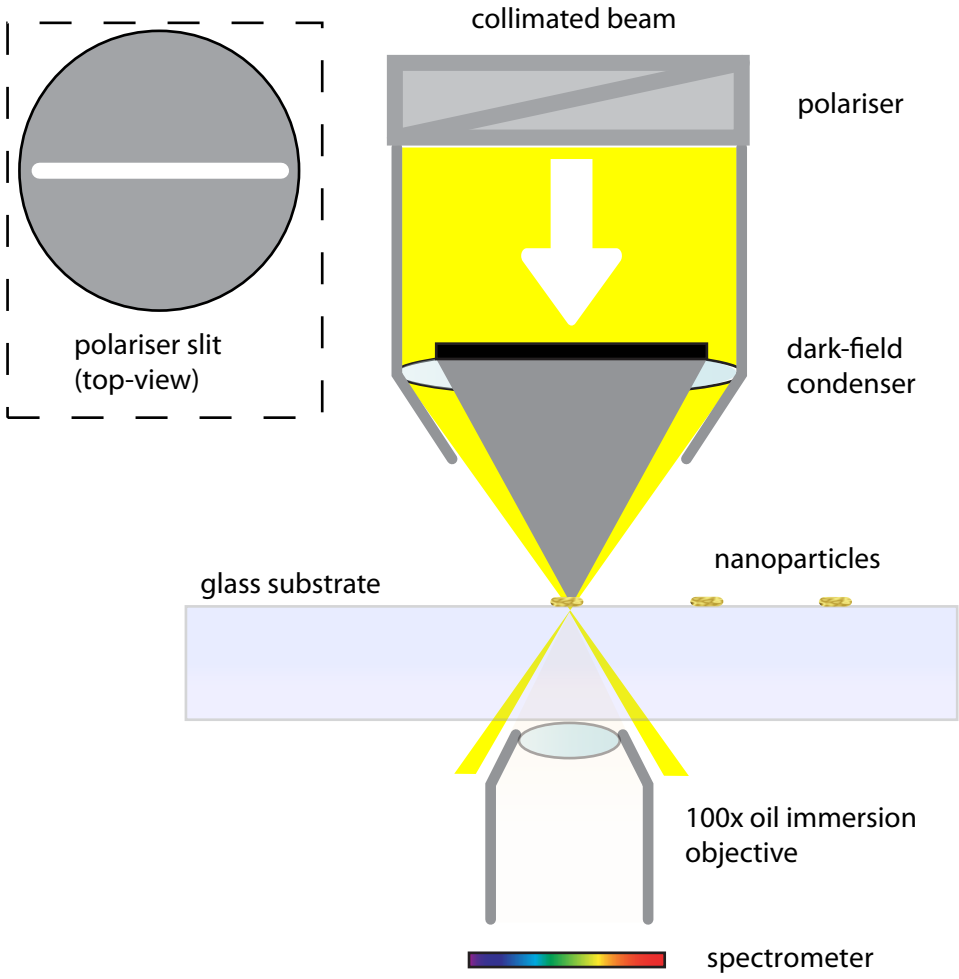

Figure 4.4: Schematic view of a dark-field spectroscopy setup. Inset: a cache with a narrow slit opening is used to restrict the incident light to two incident beams with s-polarisation. The dark-field condenser blocks a portion of the incident light and focusses the light onto the sample. The resulting hollow cone of light is focussed onto the region of interest of the sample. Any light that is collected by the objective must have undergone scattering by the sample. This scattered light is fed to a spectrometer.

and from top to bottom (smallest to highest dose). (E) is a set particle arrays with 2 µm separation used to study the effect of inhomogeneous broadening (subject of chapter 5). (F) is a set of 5 arrays of gold nanorods with periodicities ranging from 300 nm to 700 nm. These arrays have a periodicity commensurate with the wavelength of visible light and act as diffraction gratings for the incident light, producing a strongly coloured response in the limited collection angle of the objective. Such arrays will be studied in detail in chapters 6,7,8.

4.3 Results on gold nanorods

Two gold nanoparticles of different dimensions will support LSPRs that differ in frequency, intensity, and quality factor [7]. In analogy with a radio-antenna, the length of the particle will dictate the frequency of radiation, and the characteristic loss controls the efficiency of coupling to radiation.

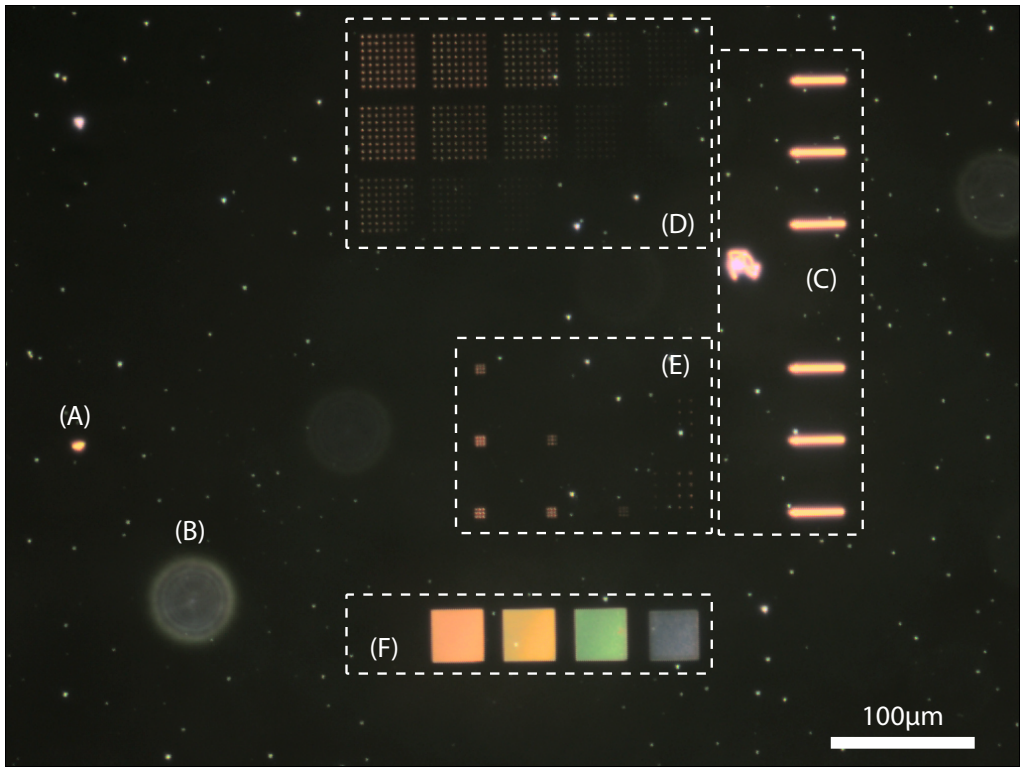

Figure 4.5: Dark-field image overview (real colours). (A): gold flake remaining after the lift-off process. (B): Airy rings due to the diffraction of light by a dust particle on the opposite side of the substrate. (C): contamination spot and markers. (D) arrays of isolated nanoparticles with varying sizes and dose. (E): small arrays of isolated particles. (F): diffractive arrays of varying periodicity.

An increase in the aspect ratio of nanorods leads to a red-shift of the LSPR associated with the long-axis of the particle (figure 3.3, chapter 3). Further, the intensity of the scattered light increases with decreasing frequency as the refractive index of gold offers a larger contrast with the surrounding environment (increased impedance). The resonance width has a more complicated dependence upon the aspect ratio and the volume of the particles as several physical effects contribute to the broadening of the resonance.

To better understand and characterise these phenomena, a large number of nanorods were fabricated, enabling us to find a correlation between the geometry of the particles and their scattering response. A set of 40 SEMs is shown in figure 4.6. Each row consists of nanorods with a constant nominal size of the short axis, while the long axis is increased, starting from a 1 : 1 to 1 : 3 aspect ratio. The height of the particles is held constant (at 35 nm), as these particles were fabricated on the same substrate with a small separation (5 µm between particles).

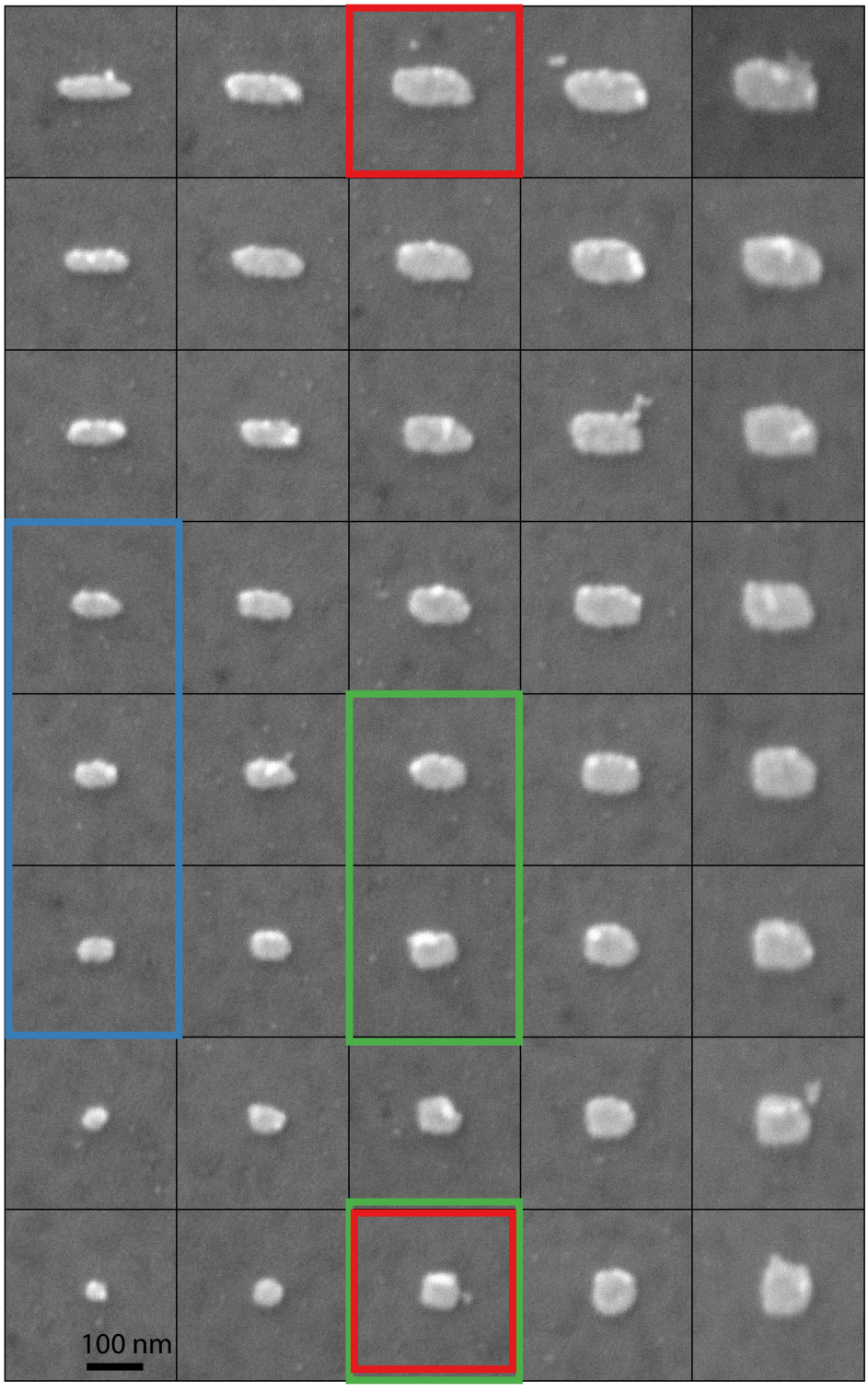

Figure 4.6: Scanning electron micrographs of 40 individual nanorods (the separation between particles has been trimmed for clarity). Each column of 8 nanorods was designed with a common nominal value of the short axis, and a long axis increasing up to an aspect ratio of 2:1. The colours identify 3 particular studies, namely: (i) in blue, three small nanorods illustrate the shift of the LSPR due to an increase in the long axis of individual nanorods (figure 4.7); (ii) in green, 3 larger nanorods demonstrate some difficulties in isolating the resonance associated with the short and long axis of these slightly irregular shapes (figure 4.8); (iii) in red two particles with a common value of the short axis but a very different volume are used to illustrate the effect of radiative damping in the quality factor of LSPRs (figure 4.15)

4.3.1 Tuning the resonance position of gold nanorods

Figure 4.7 illustrates the shift in resonance frequency as the length of a gold nanorod is increased. The experimental scattering spectra (lower panel) were obtained with a polariser set before the dark-field condenser, with a slit to restrict the incident light to a polarisation in the plane of the sample, along the long axis of the particles (inset of figure 4.4). A long acquisition time (∼ 5 mins) is

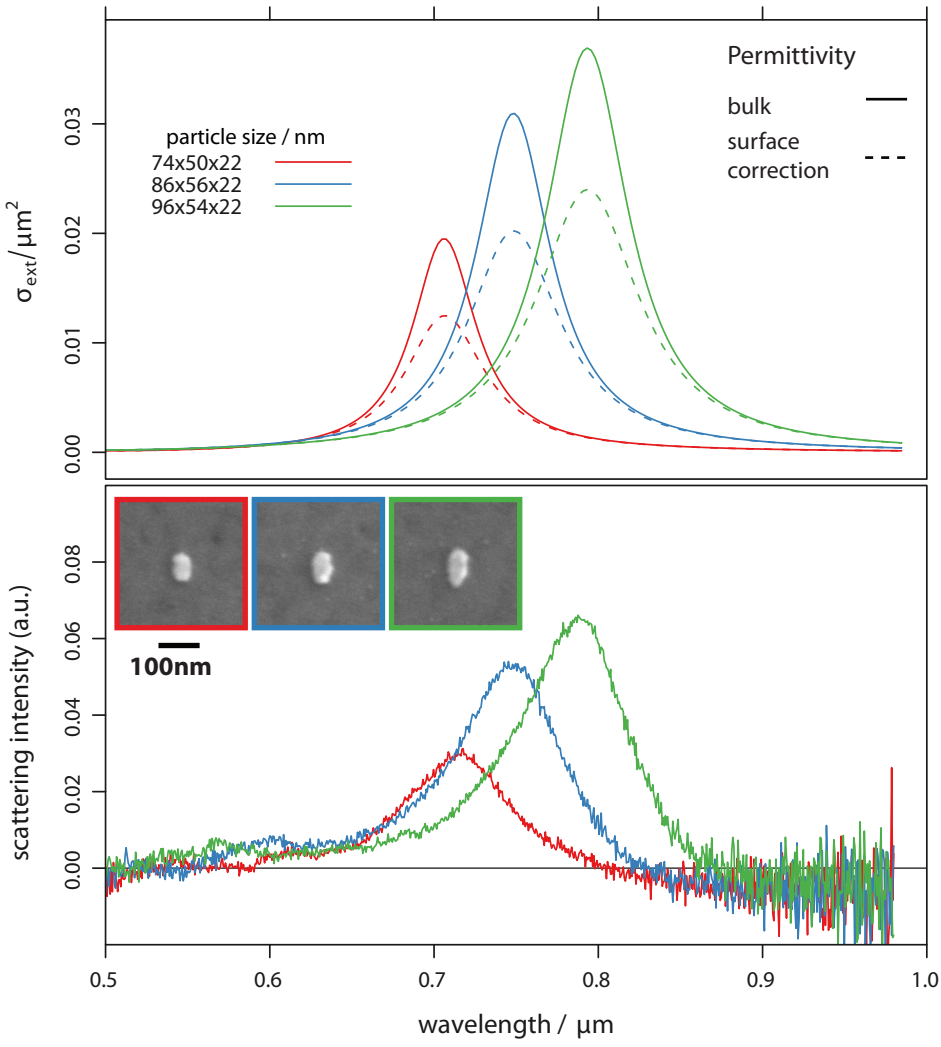

Figure 4.7: Dark-field scattering spectra of individual nanorods (approximate ellipsoids of semi-axes 74 nm×50 nm×22 nm, 86 nm×56 nm×22 nm, 96 nm×54 nm×22 nm) in oil immersion environment ($n = 1.5$). (Bottom) Experimental scattering spectra from three nanorods (SEMs shown in inset). (Top) Simulated scattering spectra (T-matrix method from [18]) for gold ellipsoids with the dimensions retrieved from the SEMs. The solid lines present the result with a bulk permittivity from [19], the dashed lines include a surface scattering correction discussed in 4.3.2.1.

necessary to collect sufficient light in these conditions. The noise level is still high, particularly at the edges of the spectral window where the light bulb has a low emission. For the three spectra shown in the bottom panel, the short axis of the particles is almost constant. The correlation between the LSPR position and the aspect ratio of the particles is clear: the LSPR is red-shifted by increasing the length of the long axis. This is in good agreement with the theory discussed in chapter 3 whereby

the aspect ratio of the particle dictates the depolarisation field acting on the charge density. A lower depolarisation field implies a lower restoring force, leading to a lower resonance frequency. As a comparison, the top panel presents the calculated spectra obtained with T-matrix modelling of ellipsoids whose dimensions were retrieved from the SEM measurements. The spectral position and relative height of the resonances is qualitatively well reproduced, and it is worth noticing that there is no free parameter that has been adjusted. The light intensity as measured in our dark-field configuration is arbitrary as the normalisation uses a diffuser to retrieve the spectral dependence of the lamp. The main difference between the model and the experimental data is the smoother spectral lineshape in the modelling, that assumes a perfectly ellipsoidal shape for the scatterer and an ideal state of polarisation for the incident light (plane wave with polarisation along the main axis). A small peak may be observed at a wavelength of about 600 nm, although the data are noisy, and could be attributed to the excitation of a resonance along the short axis of the particles. In addition to this marginal discrepancy, the resonance width is narrower in the model. A plausible cause for this discrepancy is the inadequate dielectric function that does not account for size-related damping mechanisms such as surface scattering (see section 4.3.2.1). In dashed lines in figure 4.7 the same model was run with a dielectric function modified to account for this additional damping mechanism. The main effect is to reduce the quality factor of the LSPR, introducing a ~ 20 nm broadening of the resonance, in better agreement with the experimental data.

The situation depicted in figure 4.7 is somewhat simpler than the typical spectrum retrieved from LSPR-supporting nanoparticles, however, where the spectral overlap of multiple resonances complicates the interpretation of the scattering response [20]. In figure 4.8 a similar study is made for larger gold nanorods. Both long axis (blue curves) and short axis (red curves) resonances are probed for particles of increasing aspect ratio (SEMs as insets). We observe that as the long axis becomes longer than the short axis, the two LSPR initially occurring at a similar wavelength become separated. However, the presence of the LSPR associated with the other axis is always present and results in a more irregular lineshape. Such polarisation conversion may occur because of the shape irregularity, and the lack of precise control on the illumination conditions. This mixture of resonances is almost always observed and hinders the interpretation of the spectral response in correlation to the particle morphology [20]. An additional complication arises when the particle size approaches 200 nm, as higher order multipolar modes can substantially contribute to the scattering response. It has also been demonstrated in the literature [21] that more irregular shapes such as triangular nanoprisms can exhibit high order resonances at smaller aspect ratios, due to the distortion of the field lines increased around sharp corners. In figure 4.9 I illustrate this effect with the scattering spectra of four individual gold nanoprisms. We can see that the precise morphology of the triangular cross section can affect the relative intensity of the two main resonances observed.

4.3.2 Understanding the damping of LSPRs

In figure 4.7, it can be observed that the width of the LSPR is sensitive to the precise shape of the particles. The effect of surface scattering was included to try to obtain a better agreement between the numerical modelling and the experimental data. I will now discuss the different mechanisms that contribute to the width of the LSPR in isolated particles.

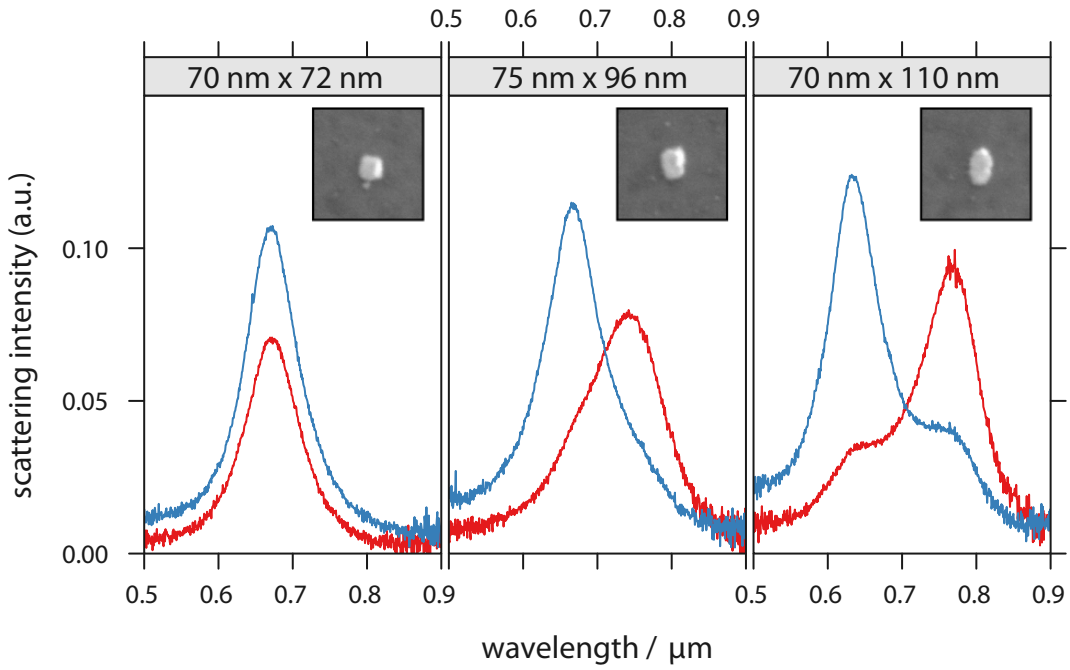

Figure 4.8: Dark-field scattering spectra of individual nanorods in oil immersion environment ($n = 1.5$). A polariser was used in the illumination path to selectively probe the short axis (blue) and long axis (red) of the nanorods.

The linewidth of the LSPR has generally received less attention than the position of the resonance [8]. This is because a comprehensive survey of the LSPR linewidth is affected by the following difficulties: (i) inhomogeneous broadening in a collection of particles affects the width of the spectral features ; (ii) individual, small particles scatter little light and are difficult to observe in dark-field; (iii) the linewidth is affected by a combination of factors that are of similar magnitude for particles in the range of sizes 10 nm–100 nm; (iv) to be easily interpreted, the scattering spectrum needs to present only well-defined resonances, whereas most particles display a combination of resonances when no special attention is paid to the polarisation of the incident light and the aspect ratio of the particles (figure 4.9).

A single particle such as a gold nanorod excited with light polarised along one axis can present a well defined LSPR lorentzian lineshape in its scattering response (figure 4.7). For such a case, the dependence of the spectral linewidth on the particle composition and geometry can be decomposed into three contributions. (i) The bulk material properties — the plasmon population suffers a loss mechanism that is described in the phenomenological dielectric function, it is linked to the scattering rate in the Drude model and interband transitions. (ii) The surface of the particle can increase the dephasing of the plasmon population, this effect is especially important for small particles where the ratio volume / surface is comparable to the mean free path of the Fermi electrons. (iii) The radiation of light from the moving electrons in the particle causes a reaction force that dampens the electrons — this is the radiative damping, which is an important contribution for large particles.

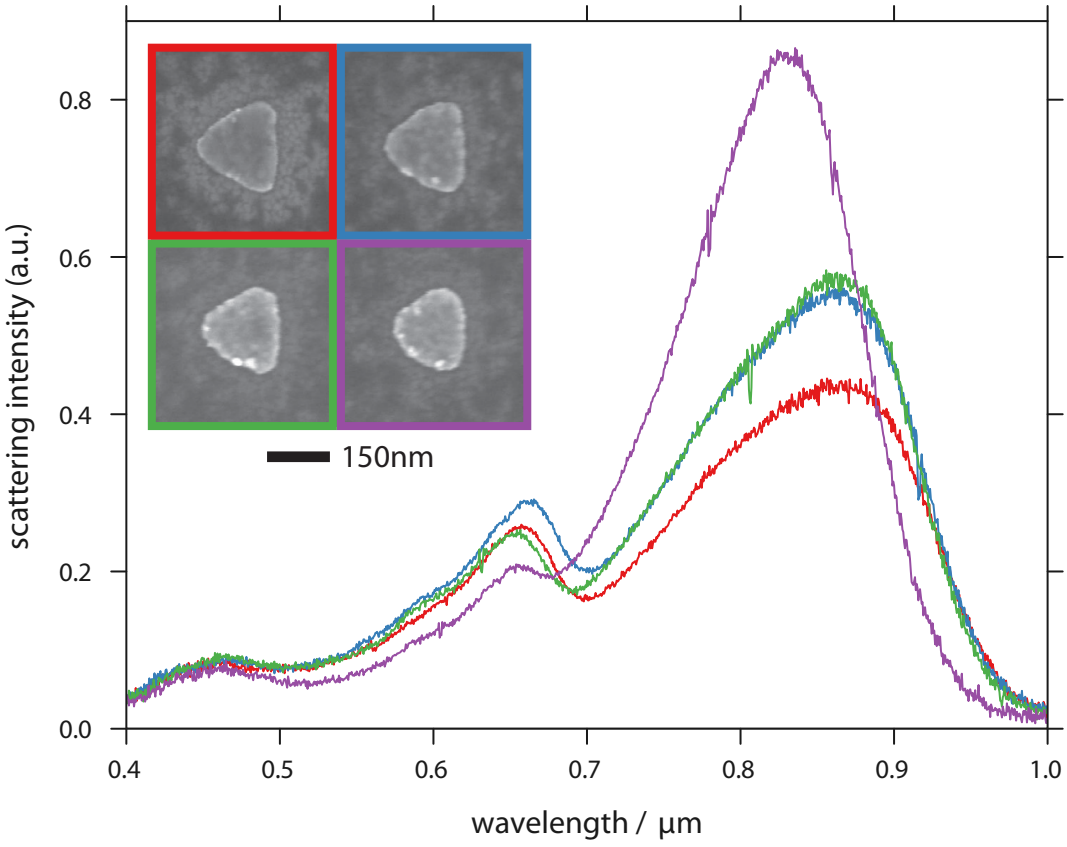

Figure 4.9: Dark-field spectra from four individual nanoprisms. The nominal in-plane shapes were identical triangles. The resulting SEMs are shown in the inset.

4.3.2.1 Intrinsic damping

In this section I will discuss how the material properties of gold affect the width of the LSPR. When considering small particles (below ~ 40 nm), radiative damping can be neglected, and experimental results from Sönnichsen *et al.* [8] suggest the relative independence of the width for gold nanorods of varying aspect ratio, as shown in figure 4.10. The open squares show the observed dependence of the LSPR width as a function of the resonance peak energy. These data were obtained by measuring the scattering spectrum of small gold nanorods of increasing length, and fitting a lorentzian lineshape to extract the LSPR position and width. The LSPR is red-shifted for nanorods of increasing aspect ratio, and the width is seen to decrease for the more elongated rods. The open circles were obtained in the same study for gold spheres. The resonance width of the small gold nanorods is noticeably narrower than for the spheres. Such an improvement in the quality factor of LSPRs is of great practical importance in applications such as non-linear surface enhanced processes (SERS, fluorescence) [22, 23], lasing [24], and plasmon-mediated propagation of light [25, 26].

Ignoring for now the influence of surface scattering, the resonance width of small nanoparticles is dictated by the material properties of gold, expressed in the dielectric function. The resonance width corresponds to a spread of energies for the plasmon population. For simplicity I will consider the case of small nanorods that can be adequately modelled as dipoles according to the formulas

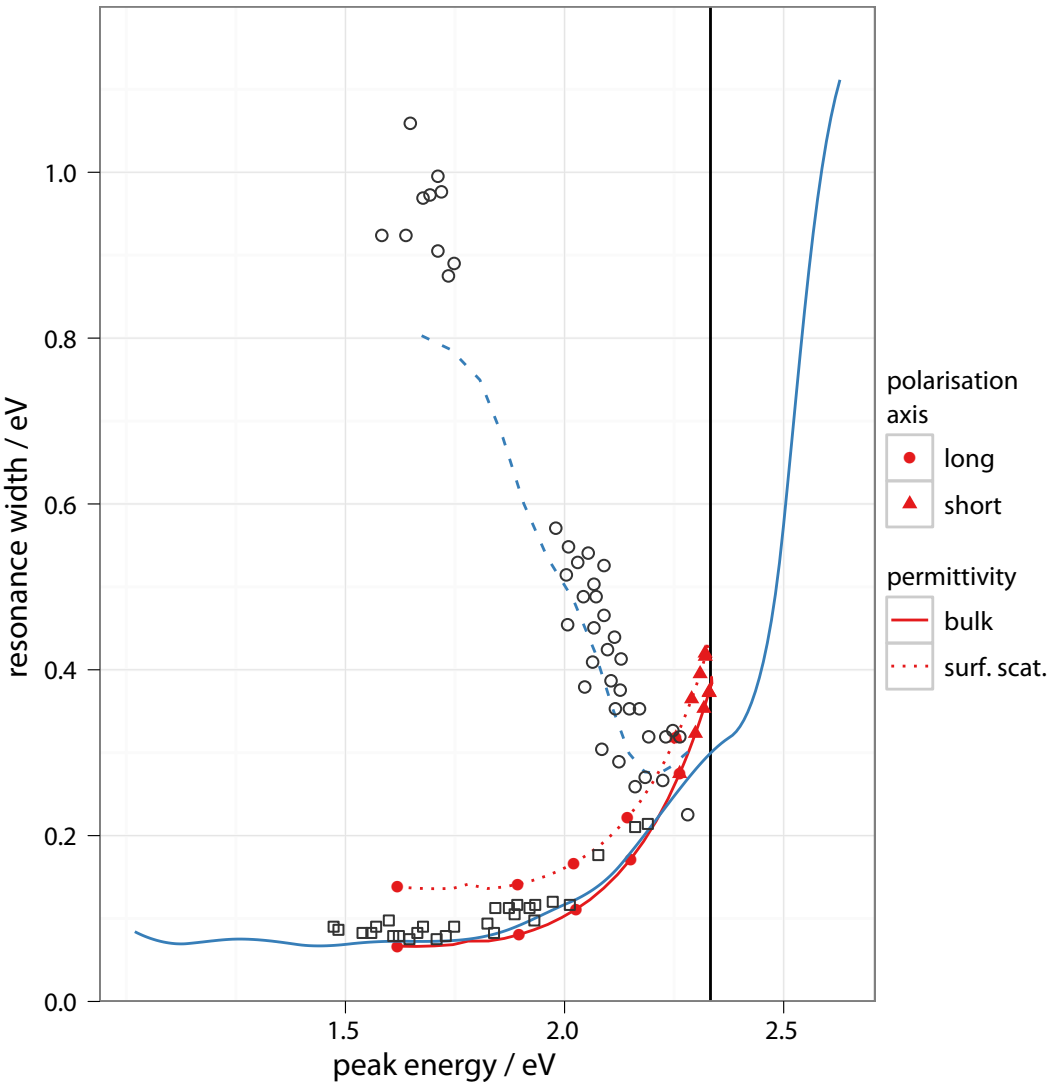

Figure 4.10: Damping in dipolar resonances. The solid line shows the damping calculated from equation 4.3 for gold (permittivity values from Johnson and Christy). The dashed line is the result obtained from Mie theory for gold spheres (surrounding index 1.52). Open symbols are single particle measurements on colloidal nanorods and spheres from [8]. The two red lines are the calculated width of LSPRs obtained by modelling scattering by small prolate ellipsoids (equivalent-volume radius: 10 nm) of increasing aspect ratio, using two different permittivity values: a modified Drude model with and without a correction for the shape-dependent effect of surface scattering (solid and dashed lines respectively).

presented in chapter 3. From equation 3.22, the polarizability of such a particle reads,

$$\alpha = \frac{abc}{3} \frac{\varepsilon - \varepsilon_d}{\varepsilon_d + \mathrm{L}(\varepsilon - \varepsilon_d)}. \tag{4.1}$$

The Fröhlish resonance frequency is obtained as a pole in the polarizability — the frequency for which the system may undergo natural oscillations independently of an external perturbation. The frequency corresponding to this pole is complex, the system will have a resonance when the real

frequency approaches the condition,

$$\varepsilon = \frac{\mathrm{L}\varepsilon_d}{1+\mathrm{L}}. \tag{4.2}$$

It is clear from equation 4.2 that a flatter dispersion of the dielectric function ε around the condition $\varepsilon = \mathrm{L}\varepsilon_d/(1+\mathrm{L})$ will result in a broader range of frequencies for which equation 4.1 diverges: the resonance width therefore depends on the slope of the dielectric function around the Fröhlish frequency.

The loss of energy in the form of Joule heating is also responsible for the intrinsic broadening of the LSPR: it is a general property of oscillators such as an optical cavity that the width of the resonant mode increases with the energy loss. The Joule heating is proportional to the imaginary part of the dielectric function (equation A.7). The resonance width due to this intrinsic property of the material is expressed as,

$$\Gamma = \frac{2\varepsilon''}{\sqrt{\left(\frac{d(\varepsilon')}{d\omega}\right)^2 + \left(\frac{d(\varepsilon'')}{d\omega}\right)^2}}. \tag{4.3}$$

Equation 4.3 was first derived for spheres in the quasi-static regime by Kreibig [27]. Wang and Shen derived a similar expression for general metal/dielectric nanostructures [28] in the quasi-static limit. A similar expression has not yet be obtained for general LSPR-supporting particles beyond the quasi-static approximation [29], and this may lead to novel ways to overcome the intrinsic broadening of the LSPR [30]. In equation 4.3 we recognise the ratio of the energy loss in the form of Joule heating (imaginary part of the permittivity) to the energy stored in a metal/dielectric system. The strongly dispersive nature of gold at optical frequencies must be considered in the expression for the energy density u [31, 32],

$$u = \frac{d\,\omega\varepsilon}{d\,\omega}|\mathbf{E}|^2. \tag{4.4}$$

As a further physical insight into equation 4.3, we note that the dispersion of the real part of the dielectric function is naturally linked to the imaginary part through the Kramers-Kronig relations, that is the absorption of a material is correlated to the dispersion at other frequencies.

The resonance width corresponds to a characteristic *dephasing time* in the time domain. The 'particle plasmon' mode is formed of a coherent oscillation of the charges in the particle, and the spectral broadening can be attributed to a loss of coherence in the electron population. Insofar as only the intrinsic damping contribution is considered, two main processes can contribute to the loss of coherence of the LSPR. First, the electrons can suffer collisions with phonons as they travel in the particle, which accounts for the collision with impurities, grain boundaries, *etc.*. This effect is temperature dependent [33]. Second, the plasmon population may suffer intraband and interband transitions in the form of exciton states. This contribution is known as Landau damping, for Landau first gave the mathematical description of the loss of energy of a wave in a system with multiple charges in relative motion. The result of this analysis is that the wave (here, the EM field associated with the surface plasmon mode) loses energy to the charged particles that have a velocity comparable to the group velocity of the wave. Because the localised plasmons have a low group velocity, this process is an important cause of dephasing in gold nanoparticles.

The variation of equation 4.3 with respect to the resonance energy is plotted as a blue line in figure 4.10. This material limit describes very accurately the damping in small particles, where the radiative damping is found to be negligible. The small discrepancy between the width obtained by numerical modelling of small nanorods and from equation 4.3 can be attributed to several factors: the half-width of the resonances is not always accurately retrieved from a lorentzian fit; the permittivity of the evaporated gold is not accurately known (in place of experimental values for the dielectric function, an extended Drude model has been used in the numerical modelling to be able to introduce the additional damping mechanism of surface scattering).

Equation 4.3 describes the influence of the real and imaginary part of the dielectric function on the width of the LSPR. Because gold presents a strong departure from an ideal Drude metal in the high energy side of the optical range, it is interesting to study the simpler case of a Drude material (section 2.2.3), which we describe by the approximate formulae ($\gamma \ll \omega, \omega_p$),

$$\varepsilon' = 1 - \frac{\omega_p^2}{\omega^2}, \qquad \varepsilon'' = \frac{\omega_p^2 \gamma}{\omega^3}, \tag{4.5}$$

with $\omega_p = 1.35 \times 10^{16}$ rad/s, $\gamma = 1.25 \times 10^{14}$ Hz as a best fit for gold in the visible.

Inserting these expressions in equation 4.3 yields $\Gamma = \gamma$, as expected: the intrinsic width of the LSPR is inversely proportional to the scattering time of the electrons in the Drude model. In figure 4.11 we assess the influence of the damping constant γ in the Drude model: increasing values of γ give broader resonances that are mostly independent of the resonance energy. A small departure from this constant value is seen in the highest value of γ, the resonance width slightly decreases in the near infra-red. This effect is due to the larger curvature in the imaginary part than in the real part of the dielectric function with the parameters used for this simulation. The value $\gamma = 1.128 \times 10^{14}$ Hz gives a very good approximation of the width for gold particles having a resonance away from interband transitions.

Surface scattering

The parameter γ can be altered in a variety of ways. On a microscopic scale, γ is the inverse of the scattering rate that describes the dephasing of the electrons due to interactions with phonons, and with impurities. In particular, a thin metal film will present a higher value of γ due to the modification of the bulk permittivity by the presence of the interface, when the thickness becomes commensurate with the mean free path of the electrons in the bulk L_∞. This mean free path can be evaluated from the Drude damping parameter γ as $L_\infty = A\frac{v_F}{\gamma} \approx 11\,\text{nm}$, where $A \approx 1$ is a phenomenological constant characterising the detail of the scattering process of the electrons, and $v_F = 1.4 \times 10^6$ m/s is the velocity of the Fermi electrons in gold. The effect of surface scattering on the mean free path is particularly important in small metal particles, where this time the entire shape may be smaller than the mean free path in all directions. A simple way to account for this increased intrinsic loss is to characterise the modification of γ in terms of the shape of the particle. Schatz *et al.* [34] derived a simple general expression for this effective mean free path by considering the average cord length in arbitrary geometries, the result of which is very simply summarised

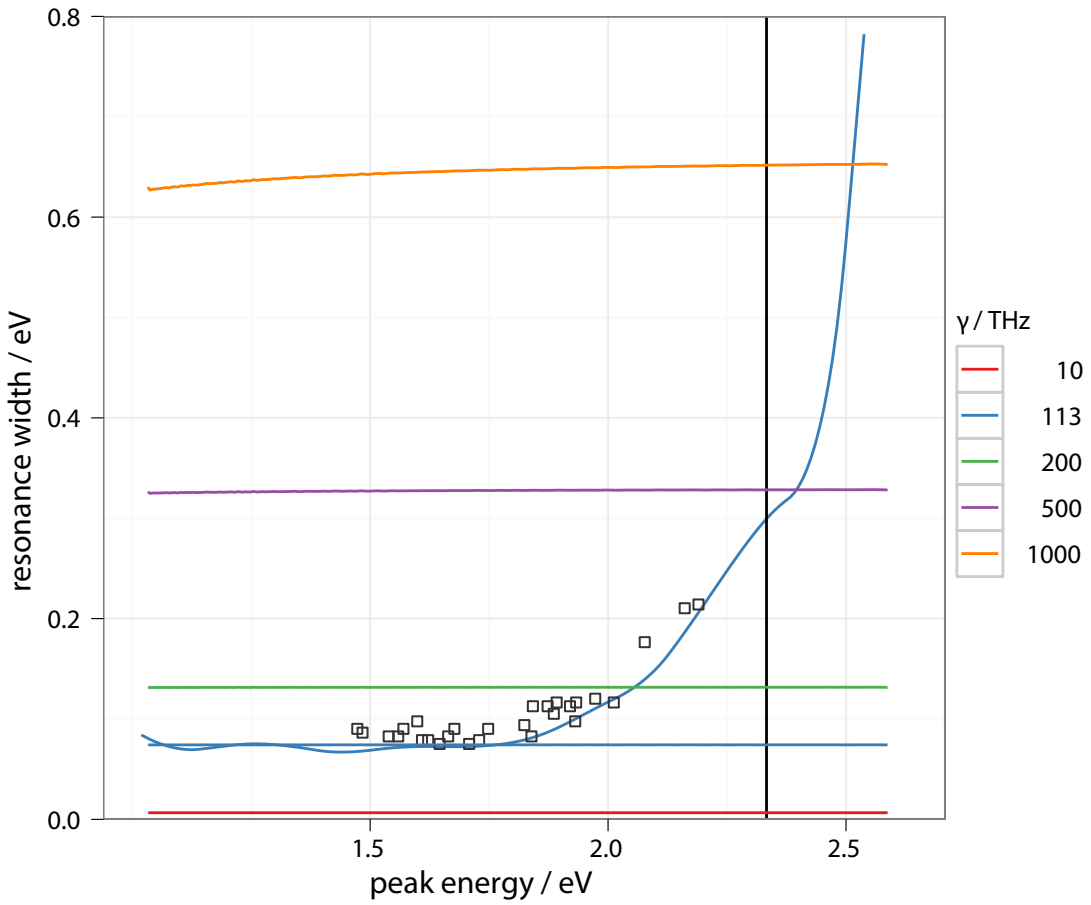

Figure 4.11: Intrinsic damping in gold and in the Drude model. Four different values of the damping parameter γ are considered, with $\gamma = 1.128 \times 10^{14}$ Hz ($= 74$ meV) being the best fit of the Drude model to the permittivity values of gold from the literature in the wavelength range 0.7–1.2 µm.

as the ratio volume/surface of the particle,

$$L_{\text{eff}} = 4\frac{V}{S}. \tag{4.6}$$

This geometrical parameter is shown in figure 4.12 for oblate and prolate ellipsoids of varying volume and aspect ratio. In the limit of extreme aspect ratio, $L_{\text{eff}} \to 0$, and for a given volume the smallest modification to the mean free path is obtained for a sphere that minimises the ratio surface/volume. We note that the smaller particles are the most sensitive to this effect for small aspect ratio as we consider in nanorods. In ellipsoids, the increase of surface area is almost linear in the increase of volume (the curves have almost a constant spacing for all aspect ratios). It should be noted, however, that the description of the shape as an idealised ellipsoid is likely to be inaccurate as the fabrication technique used here (EBL) leads to a grain structure with appreciable roughness (see figure 4.6).

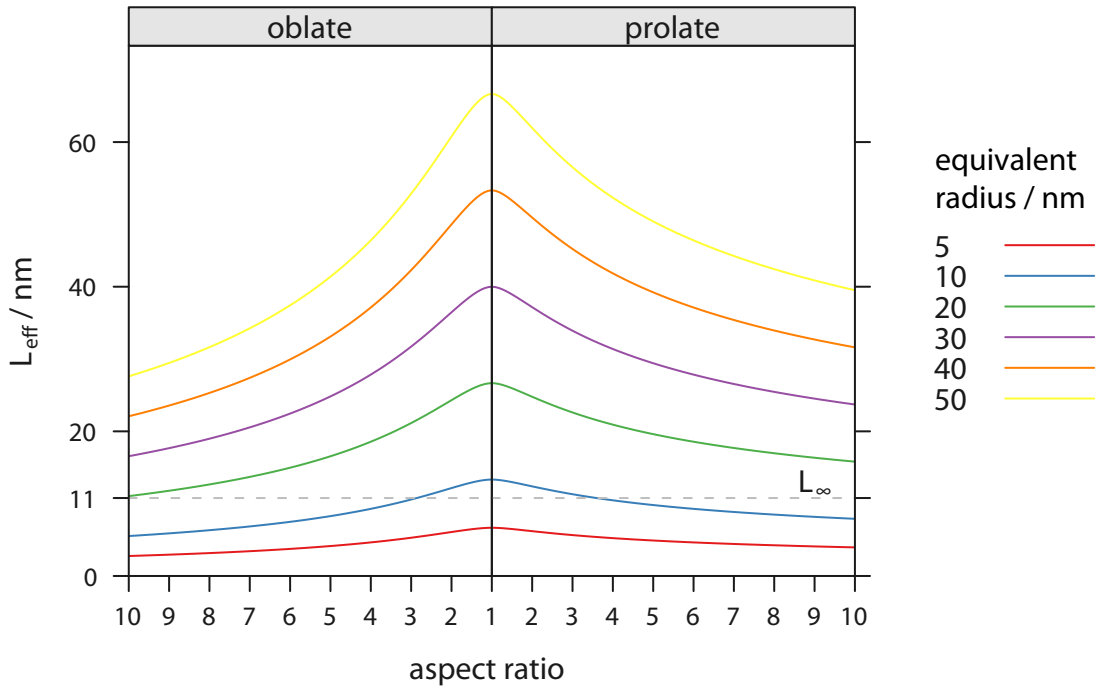

Figure 4.12: Effective mean free path parameter for oblate (left) and prolate (right) ellipsoids as a function of the aspect ratio.

As a result of this reduced mean free path, the dielectric function suffers an increase in its imaginary part,

$$\gamma = \gamma_0 + \frac{A v_F}{L_{eff}}, \tag{4.7}$$

where γ_0 is the damping parameter of the bulk material, A is a phenomenological constant of the order of unity, and v_F is the Fermi velocity. An illustration of the effect of finite size on the dielectric function is shown in figure 4.13 for $L_{eff} = 25$ nm, a typical value of the small nanorods considered in this work. We note that the main effect of the limitation in the mean free path due to the restricted size of the particle is to increase the imaginary part of the dielectric function (causing an increased absorption) and the real part of the refractive index (reducing the index contrast, therefore allowing a larger portion of the EM field to penetrate in the metal). The real part of the dielectric function and the imaginary part of the refractive index are largely unaffected.

In order to maintain a correct description of gold throughout the visible, a modified Drude model has been used, following the study by Etchegoin *et al.* [35]. The effect of increasing γ is straight-forwardly included in this model, and can be compared to the measured values tabulated in the literature (Johnson and Christy). We see the effect of surface scattering in the scattering spectra of gold nanorods in figure 4.14. Three families of prolate ellipsoids are shown for comparison, the particles differ in volume (top, middle, and bottom panels) and aspect ratio (colours). The bulk dielectric function was used to calculate the scattering cross-section shown by the dotted lines, while the solid lines are the result of the calculations with a shape-dependent correction to the

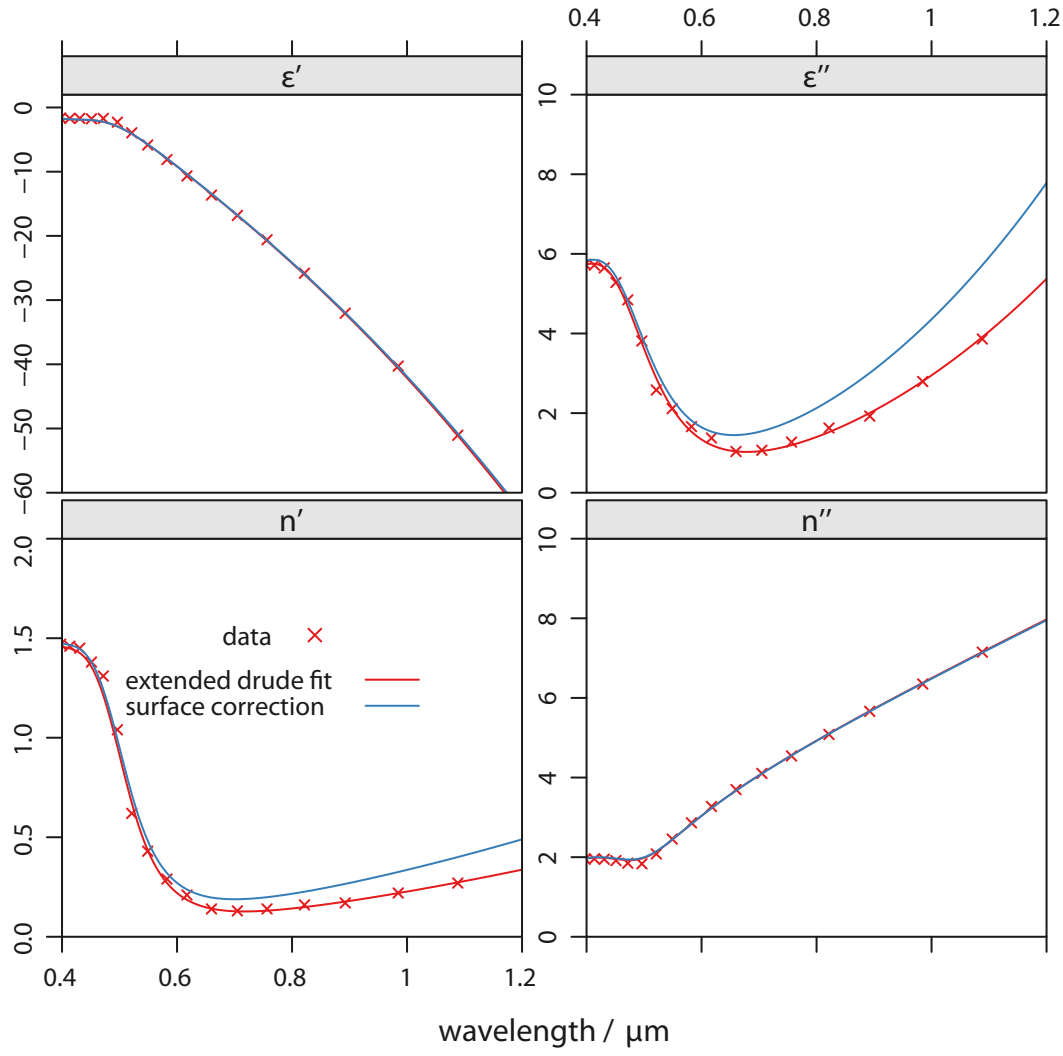

Figure 4.13: Dielectric function of gold with a contribution from surface scattering (equation 4.7, with $L_{\text{eff}} = 25\,\text{nm}$).

dielectric function obtained from equation 4.7. The main effect of the surface scattering correction is that the resonance is weakened and broadened by the increased loss in the metal. We note that this effect is more pronounced in the smaller particles, and the particles with higher aspect ratio.

In addition to modifying the dielectric function through the mechanism of surface scattering, the shape and size of a scatterer modifies the *radiative damping* contribution to the LSPR linewidth: in figure 4.14 the linewidth increases as a function of volume and aspect ratio of the particles. This is the subject of the next section.

4.3.2.2 Radiative damping

The electrons moving inside the particle radiate light, and this forms an additional loss channel for the plasmon mode that is proportional to the number of accelerated charges, *i.e.*, the volume of the

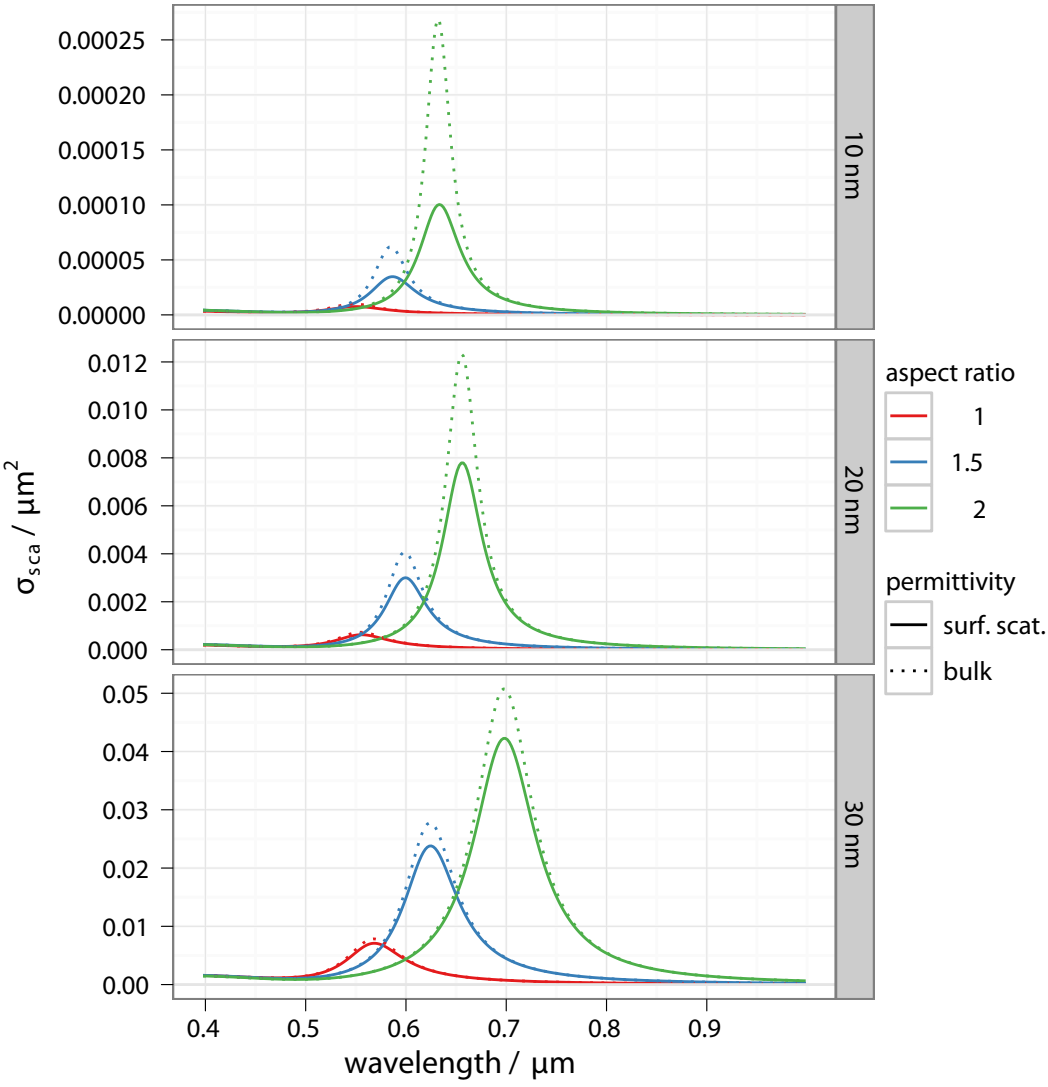

Figure 4.14: Simulated scattering spectra of gold nanorods of different volume and aspect ratio. The equivalent volume sphere is of radius 10 nm, 20 nm, 30 nm. For each family three aspect ratio are considered: 1 (sphere), 1.5, and 2 (polarisation along the long axis). The solid line uses the bulk permittivity values, and the dashed lines consider a size-dependent surface scattering correction (equation 4.7).

particle when the skin depth is larger than the particle size. In gold nanoshells, the reduced volume of metal compared to a solid sphere has been shown to substantially reduce the effect of radiative damping [36]. The effect of radiation damping on the resonance can be seen in the modified long wavelength approximation for dipolar resonances (equation 3.28),

$$\alpha^{\text{mlwa}} = \frac{\alpha^{\text{static}}}{1 - \frac{2}{3} i k^3 \alpha^{\text{static}} - \frac{k^2}{a} \alpha^{\text{static}}}, \tag{4.8}$$

The static polarizability of the particle is corrected by the term $\frac{2}{3} i k^3 \alpha^{\text{static}}$ that describes the radiation of light.

The volume and aspect ratio of the particle can therefore influence the resonance width by changing the resonance frequency (k^3 factor), and the value of the static polarizability (a function of the volume, shape factor, and surrounding environment). Appendix B describes the modification of the scattering spectrum for an effective polarizability of the form equation 4.8 and predicts a red-shift and broadening of the LSPR. This dependence was investigated for gold nanorods, as

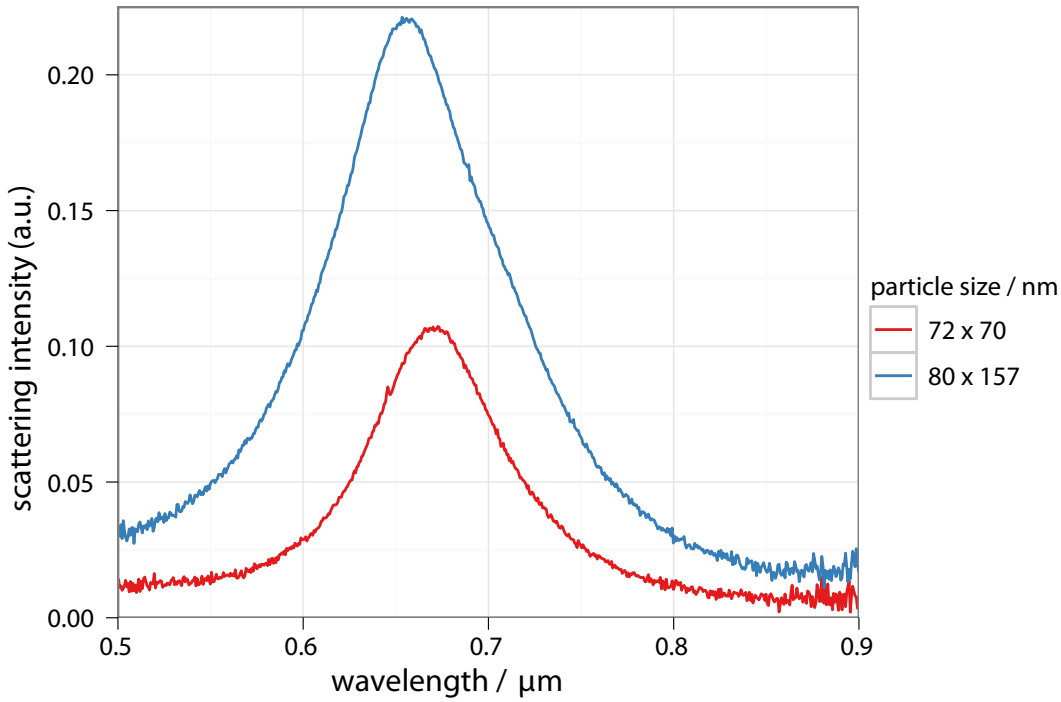

Figure 4.15: Dark-field scattering spectra of 2 individual gold nanorods in 1.52 surrounding index. The two nanorods have the same height (30 nm) but different in-plane axes as indicated in the legend. The polarisation of the incident light is along the short axis.

illustrated in figure 4.15 which presents the dark-field spectra of two nanorods with incident polarisation along the short axis of the particles. The observed resonance occurs at a similar wavelength (slightly blue shifted for the particle with a longer long axis, as expected from the consideration of the depolarisation factor associated with the short axis), but the intensity and quality factor are very different. The larger particle (longer long axis) exhibits a more intense ($\sim \times 2$) and broader resonance (120 nm against $\sim$ 100 nm). In general, the resonance intensity and width will also vary as the resonance position is modified by the size and shape.

Radiative damping is proportional to the total dipole moment of the particle — therefore proportional to the particle volume, and inversely proportional to the cube of the wavelength. As a result it is clear that gold spheres present a much broader resonance than elongated nanorods (ignoring the effect of surface scattering), as the Mie resonance suffers a much smaller shift with increased diameter than a rod stretched along one axis to the same linear dimension. It is difficult to assess the effect of radiative damping alone by seeing the effect of particle size, as the resonance shifts to the red for larger and more elongated particles.

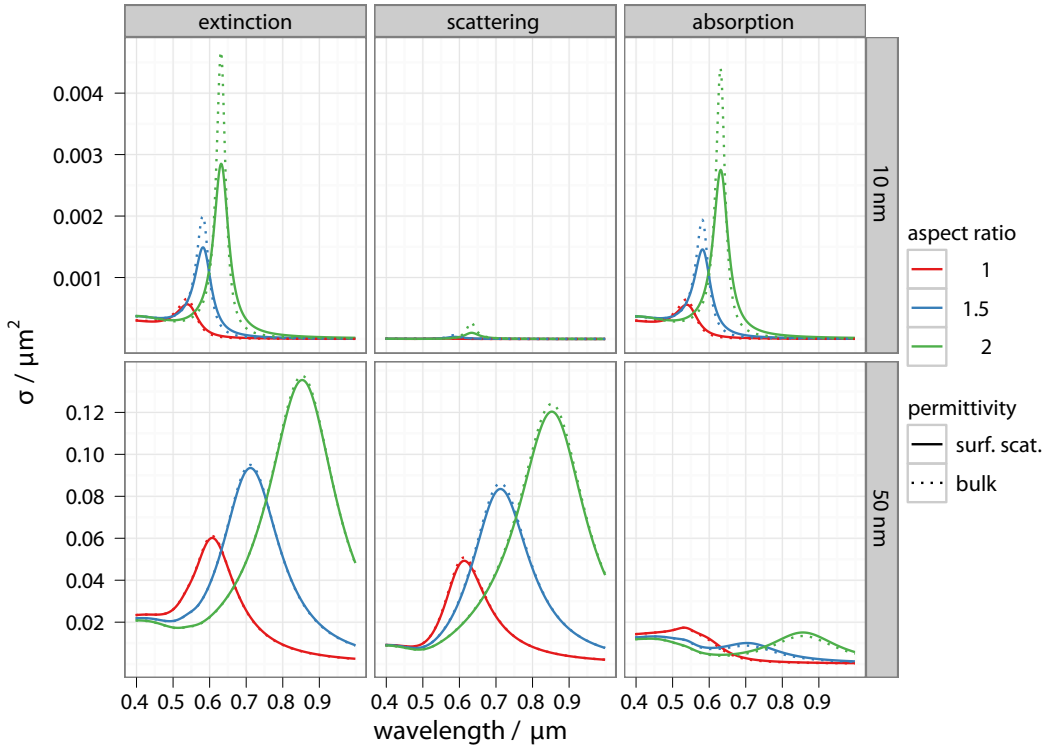

Figure 4.16: T-matrix model of gold ellipsoids with a constant volume and a range of aspect ratios, in surrounding medium of index 1.5. The equivalent-volume spheres have for radius 10 nm (top panels) and 50 nm (bottom panels). The extinction, scattering and absorption cross-section are shown for the calculation using bulk permittivity and a size-dependent surface scattering correction.

To investigate the effect of radiative damping on the resonance width, several simulations have been run for prolate ellipsoids of constant volume and increasing aspect ratio. The result of these simulations is a set of scattering and absorption spectra, a few of which are shown in figure 4.16. The effect of increasing the volume of a gold nanoparticle in the form of a prolate ellipsoid is investigated for different aspect ratios (colours) and two different volumes (top *vs* bottom panels). The clear effect of increasing the volume of the particle from a 10 nm equivalent radius sphere to 50 nm is a large increase in the cross-sections (note that the scale is very different). A larger aspect ratio also leads to an increase in the cross-sections, and to a larger red-shift of the LSPR associated with the long axis of the rod. The 10 nm-volume particles have an optical response dominated by absorption: the scattering albedo $\sigma_{\mathrm{sca}}/\sigma_{\mathrm{abs}}$ is much smaller than unity, while it is much greater than one for the 50 nm-equivalent volume particles. The transition from a regime where absorption dominates to the regime where scattering dominates lies in the range of sizes considered in this thesis (about 50 nm, depending on the surrounding environment). It is interesting to note that the absorption edge feature observed in thin films (chapter 2, 2.7) is mostly unaffected by the shape and size of a particle, as it is an intrinsic (bulk) loss mechanism. Because the scattering and absorption are linked by the relation [33]

$$\sigma_{\mathrm{sca}} = \frac{\gamma_{\mathrm{rad}}}{\gamma_{\mathrm{nr}}}\sigma_{\mathrm{sca}}, \tag{4.9}$$

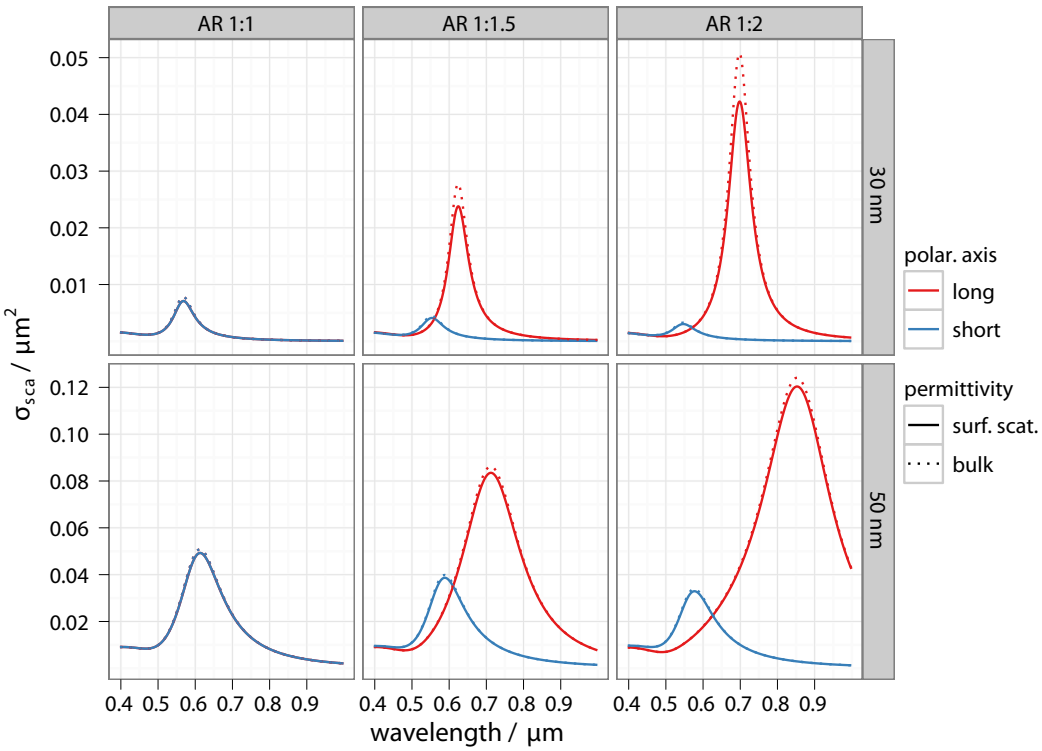

Figure 4.17: Scattering cross-sections calculated from a T-matrix model of gold ellipsoids in 1.5 surrounding index. The particles have a constant volume and a range of aspect ratios (1:1, 1:1.5, 1:2). Two orthogonal polarisations of the incident light are shown in different colours (light polarised along the long axis in red, blue for the short axis). Two sets of permittivity values have been considered (bulk: dashed lines, surface scattering correction: solid lines).

the shape of the absorption edge strongly constrains the scattering response for particles with a small aspect ratio.

An alternate view of the simulated data is presented in figure 4.17 where only the scattering spectra are displayed for two orthogonal polarisation states. Here it is clearly observed that the volume of the particle affects the resonance width and intensity. The short axis resonance is blue-shifted and weakens with increasing aspect ratio as the volume of the particles is held constant in this simulation.

From these families of simulated spectra with constant volume, the half-width can be extracted by a Lorentzian fit and the result is reported on figure 4.18 which summarises this study of the resonance width of dipolar localised surface plasmon resonances.

The dipolar resonance extracted from the Mie solution is plotted as a dot-dashed line and shows a strong increase of the LSPR linewidth with increasing diameter. This conclusion is verified by the experimental data (open circles). In contrast, small nano-rods (open squares) show a narrowing of the LSPR with increased aspect ratio — this is due to the strong red-shift of the LSPR away from the absorption edge of gold (gold is a better Drude metal in the near-IR). The linewidth for these small particles is limited by the intrinsic properties of the material (Landau damping). Very small particles suffer an increased loss mechanism in the form of surface scattering, which is volume

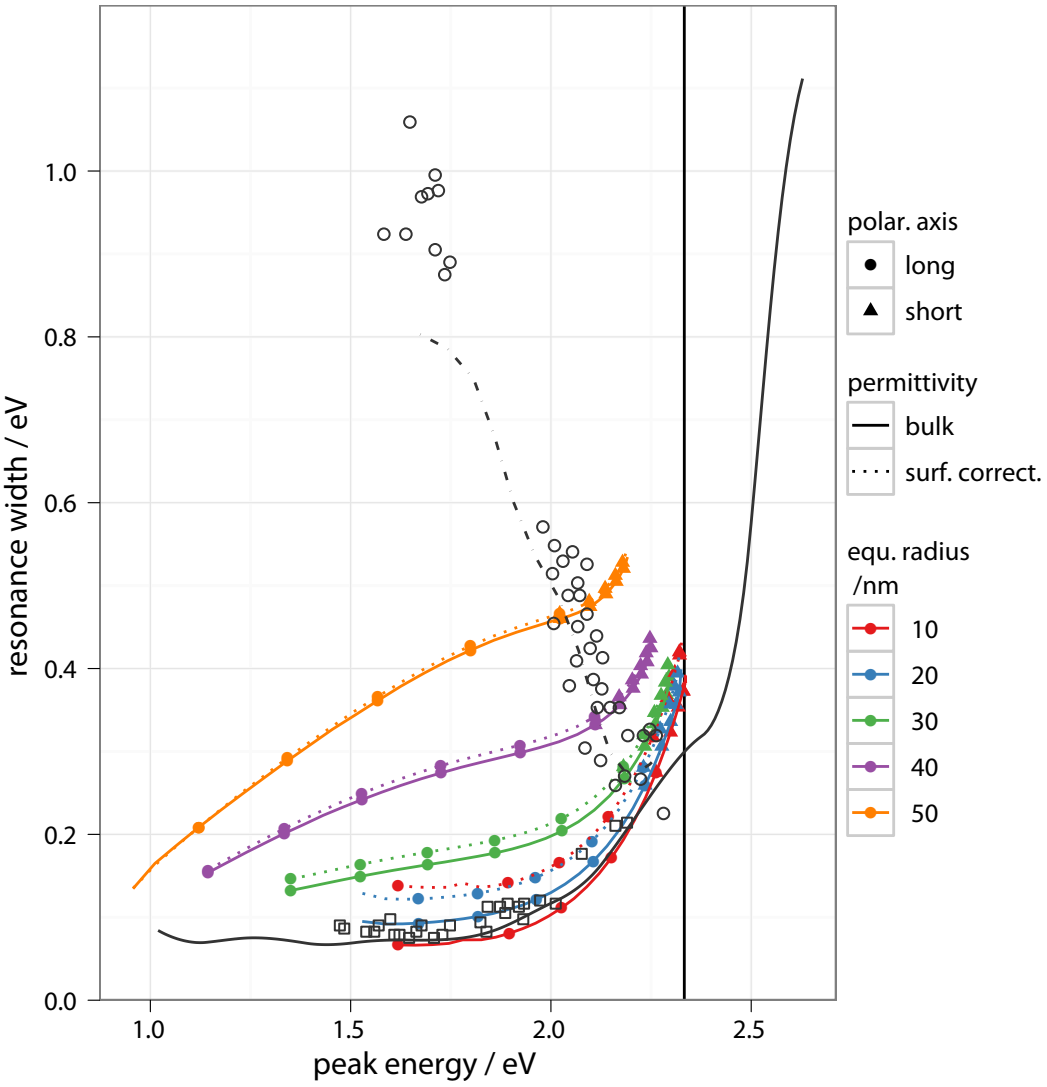

Figure 4.18: Width of dipolar resonances: summary of results for small gold nanorods. The dot-dashed line is from the Mie theory (dipolar mode only). The vertical solid line indicates the Fröhlish frequency $\varepsilon = -2\varepsilon_d$. The coloured curves correspond to the numerical simulations of prolate ellipsoids of different volumes (colours), for two polarisations (solid symbols) and two prescriptions for the dielectric function (bulk — solid lines, surface scattering correction — dashed lines). The open symbols are experimental data from [8].

and shape dependent. For nanorods of intermediate geometry between very small rods and large spheres, there is an optimum region where the effect of surface scattering is almost negligible, and the radiative damping is also reduced by a red-shift of the LSPR [20]. In this regime the radiative damping leads to a general increase of the resonance width with respect to the smaller particles, but the effect of the surface scattering becomes less important (compare the dashed lines with the solid lines for different colours). The short-axis resonance of the prolate nanoparticles is however always blue-shifted and broadened by increasing the aspect ratio of the particles. In the limit of a very narrow rod (very large aspect ratio) the short-axis LSPR tends towards the limit $\varepsilon = -2\varepsilon_d$ which is the minimum possible Fröhlish frequency for particles of this geometry in a dielectric medium of permittivity ε_d.

4.4 Conclusions

In this chapter the fabrication technique of electron-beam lithography was used to fabricate gold nanoparticles of various shapes and sizes. The optical response of individual particles was characterised by dark-field spectroscopy. A study of the influence of the precise particle morphology was performed by comparing the scanning electron micrographs of several particles and the scattering spectra obtained from the same particles. The study of gold nanorods revealed a number of characteristics of the dipolar response of gold nanoparticles. First, the size and aspect ratio of the particle dictates the spectral position of the LSPR. This tunability can be used to red-shift the LSPR from the static Fröhlish frequency for spheres where gold presents a strong absorption. The resonance gains in strength as it is shifted towards the infra-red. Second, the rough composition of the particles fabricated by thermal deposition of gold leads to the excitation of a mixture of resonances for particles larger than $\sim 50\,\mathrm{nm}$. The lineshape presents a combination of resonances that reveals a polarisation conversion. In this respect a study of individual nanoparticles obtained by colloidal growth would provide a useful comparison as these particles present a perfectly regular shape and a mono-crystalline structure [20]. The importance of surface roughness and end-cap geometry in the precise description of the LSPR was studied by Mulvaney *et al.* using the Discrete Dipole Approximation [37]. Last, the resonance width was studied for different ranges of particle sizes. The smaller nanoparticles are shown to exhibit an intrinsic limit for the width of the LSPR that is due to the material properties. The experimental data from Sönnichsen *et al.* was found in good agreement with the analytical formula for the material contribution to the damping. Using the Drude model we found that the LSPR width is equal to the damping parameter of the Drude model, which provides a good approximation for the observed resonance width away from the region of interband transitions. The shape and size-dependent effect of surface scattering was assessed with an evaluation of the effective mean free path in ellipsoidal particles. The resulting size-dependent dielectric function was used in simulations for nanorods of varying sizes and resulted in weaker and broader resonances in better agreement with the experimental observations. For smaller particles, the effective mean free path reduction due to the finite size of the particle is not sufficient to describe the optical response of gold nanoparticles. A non-local description of the dielectric function may be necessary [38] to provide a more accurate description of the material response. This limitation also applies to the case of strongly interacting particles.

Finally, it should be noted that the single particle studies in this thesis have been focussed on particles supporting only dipolar resonances. Larger nanoparticles [30], nano-stars [39] and nano-rings [40] have been shown to display interesting optical properties that result from the excitation of higher order resonances.

The study of the dipolar response of small gold nanorods has given us an insight into the optical properties of isolated LSPR-supporting particles. In the next chapters I will present experiments where the optical response of such particles is modified by the arrangement of the particles in a two-dimensional array.

"Il faut souffler sur quelques lueurs pour faire de la bonne lumière."

René Char

5

Extinction measurements in a collection of particles

Where two or more plasmon-supporting metallic nanostructures are in close proximity the possibility exists for interaction between the modes of the individual nanostructures to form new hybrid modes [1–3]. In chapter 4 we observed that gold nanoparticles present a very strong scattering response in the visible, it is therefore expected that particle interactions will play an important role in a dense collection of particles. The case of two interacting particles with varying separation has been extensively studied (for example see [4]). For multiple nanostructures there is also the possibility of long-range coherent interaction arising from multiple scattering, something that may find application in energy transport [5, 6], slow light [7–9], and sensing [10, 11]. This situation will be investigated in chapters 6,7,8.

The optical response of a collection of particles can be understood with different approaches that depend on the geometrical arrangement, density, and individual particle properties. In the limit of very tenuous collection of particles (large separation), the optical observables such as cross-sections are a linear superposition of the individual particle responses. When the average distance decreases, however, interactions between particles can lead to dramatic changes in the overall scattering and extinction properties of the cluster because each particle responds to an electromagnetic field that comprises the contribution of the light scattered by the neighbouring particles. Such interactions between particles are particularly important to consider when at least one of the following conditions is met: (i) the field incident on each particle has a non-negligible component arising from light that was scattered by another particle; (ii) the arrangement of the particles has a periodicity that encourages the build-up of such multiple scattering events. In this chapter I will present the experimental study of the transition between a disordered and ordered collection of

particles in a 2-dimensional configuration in the regime where the particles can have a relatively strong near-field interaction.

First, a review of fabrication techniques is given, with a description of nanosphere lithography and the formation of islandised films by thermal evaporation. The observation and interpretation of inhomogeneous broadening of the LSPR in collections of particles is discussed in the study of EBL samples. Second, a coupled dipole model is introduced that describes the essence of the electromagnetic interaction for neighbouring particles. Last, this study is followed by an investigation of the effect of particle proximity, overlap, orientation, and density on the transmission spectrum of the sample. The experiments that are presented also compare the bulk index sensitivity for the different geometrical configurations.

5.1 Fabrication techniques

In addition to the procedure of electron-beam lithography presented in chapter 4, several complementary techniques have been used and will be introduced in this section.

5.1.1 Islandised films

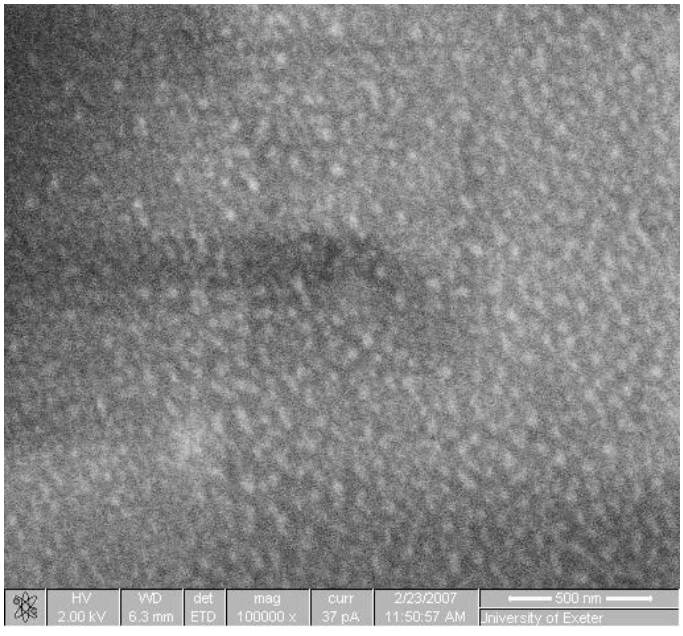

Figure 5.1: Scanning electron micrograph of an islandised film. The substrate is glass, and gold (purity 99.99%) was evaporated at a rate of ~ 1 Å/s to an effective mass-thickness of ~ 5 nm under vacuum ($P = 2 \times 10^{-6}$ T.) The gold appears as light areas on a dark background (substrate).

Perhaps the simplest fabrication technique to produce a collection of nanometre-sized metallic particles supported on a substrate is the formation of islandised films by thermal evaporation [12]. The nucleation kinetics of thin metallic films involve a process of diffusion of the deposited material at the surface of the sample. While thermalising at the surface, the deposited clusters of gold seek a state of minimum energy. Surface tension between the clusters and the substrate yields a partial wetting of the glass by the gold. When two clusters in close proximity merge, their shape rearranges

to minimise the global surface tension. Such shape transformations require sufficient thermal energy: the final configuration of the clusters therefore depends on the balance of the thermal diffusion of the evaporated material, the rate of deposition, and the surface tension between the deposited material and the substrate. When depositing thin films (~ 5 nm) of gold and silver on a glass substrate at a pressure of 1×10^{-6} Torr, the deposited material forms disjoint clusters that thermalise as separate islands. If the deposition was continued, these fixed islands would act as seeds for the new material to join and eventually merge into a continuous layer where grains of different orientations meet and coalesce. If, however, the deposition process is stopped, the sample consists of a random clustering of metallic islands of typical dimensions 50 nm. Because of the absence of freedom in the design of such samples, the lack of reproducibility and the intrinsic variability of particle sizes using this fabrication technique, the optical studies of gold nanoparticles presented in this thesis were performed on samples fabricated by electron-beam lithography and nanosphere lithography.

5.1.2 Nanosphere lithography

Nanosphere lithography (NSL) is a large scale and inexpensive technique that can be used to fabricate arrays of nanoparticles over large regions [13, 14]. The fabrication of nanoparticles by NSL requires several steps, illustrated in figure 5.2.

i. Deposition of a solution of microspheres onto a substrate. Polystyrene spheres of diameter 390 nm are dispersed into a water solution with additional surfactant that prevents agglomeration of the spheres, and 50% of ethanol used as a solvent. The deposition is carefully made by hand with a pipette as illustrated in figure 5.2(a). A glass slide prepared with a surfactant is placed on a PTFE trough containing pure dionised water and the clean substrate immersed at mid-height. All components have been thoroughly cleaned with a cycle of solvents (IPA, chloroform, pure water) so as to avoid any contamination of the bath. The spheres are carefully introduced on the slide and reach the interface with the water where they form a thin layer at the surface. The surface treatment of the slide with a surfactant (STS) is extremely important for the surface tension to produce a meniscus that allows the spheres to migrate to the surface of the water and not sink. A slow deposition rate is maintained so as to form a homogeneous film over several linear centimetres of the water surface. The spheres must be free to rearrange at the surface and not impose stress on the film. At the same time the solvent evaporates and the film becomes less ductile. A careful compromise is reached only after many experiments and the process is generally prone to sample-to-sample variation. This situation could be overcome by automating the deposition process with a larger control over environmental variables such as temperature, vapour pressure, vibrations, *etc.*

ii. The water is carefully drained with the free-standing film of nanospheres floating at the surface. The spheres are constrained laterally with two PTFE bars so as to maintain the integrity of the film during the removal of the water. When the water level reaches the substrate, the spheres deposit on the glass surface. As the solvent evaporates, capillary forces draw the spheres together in a close-packed array.

iii. When the sample is dry, the nanospheres form an hexagonal mask over the substrate (see figure 5.2(b) which presents a SEM of the nanospheres arranged onto a glass substrate). Once the solvent has dried out, the crystalline structure of the arrangement of spheres is clearly visible by eye. The periodicity of $\sim 400\,\text{nm}$ makes the array diffractive for visible light. The boundaries of domains with monocrystalline order present different iridescent colours (figure 5.2(c)). The best samples present mono-domains of several centimetres. The ordering of spheres can be broken by stress during the deposition process, and the presence of defects arising from a distribution of sizes in the solution of spheres (figure 5.2(b)). The sample is placed in under vacuum in an evaporator where gold can be deposited by thermal evaporation (figure 5.2(d)).

iv. The spheres can be removed by sonication of the substrate in ethanol for a few seconds. A SEM of a resulting sample is presented in figure 5.2(e).

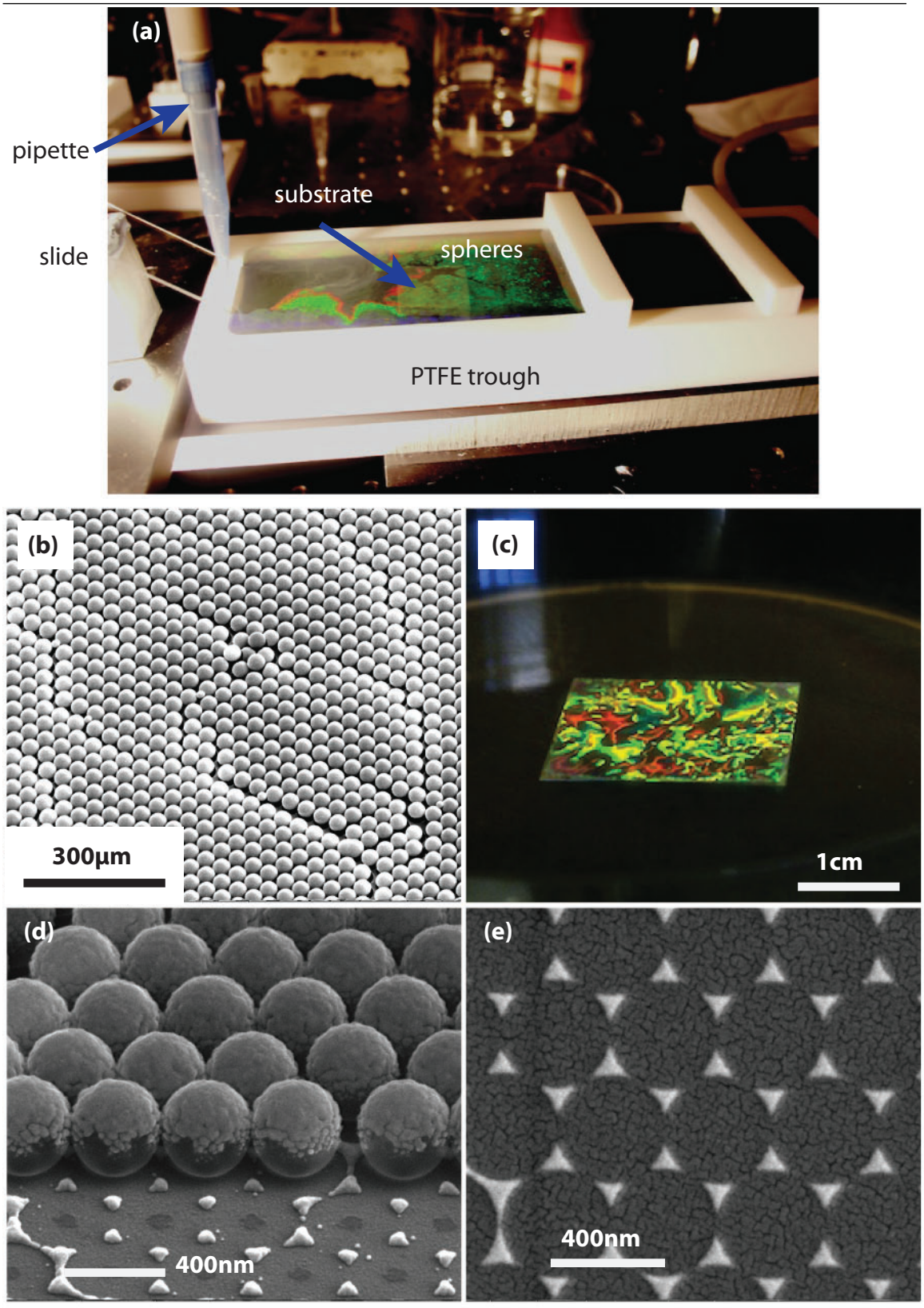

Figure 5.2: Nanosphere lithography. (a): PTFE trough for the deposition of nanospheres on the substrate. The spheres are injected from the pipette onto a glass slide. The bath contains the substrate immersed in pure water. A monolayer of spheres is standing on the surface of the water. (b): SEM of a glass substrate coated with polystyrene spheres. Several defects are apparent, due to the presence of stress or inhomogeneities in the sphere sizes. (c): Real colours photograph of a glass substrate coated with polystyrene spheres. The iridescence arises from diffraction by the regularly spaced spheres. (d): SEM the sample after the metal deposition (silver in this picture). (e): SEM of a NSL sample after removal of the spheres.

The typical mono-crystalline domains obtained by this semi-empirical technique are wide enough for optical studies. The local defects in the packing of the spheres, however, have a strong influence on the optical properties of the final sample as they lead to a dispersion of gold particle sizes. The resulting NSL samples present three different defects: the grain boundaries where two regions of different crystalline order meet; line defects associated with the disparity in the sizes of spheres; shape imperfections in the final particles. The triangular particles obtained by NSL have sharper corners than similar particles fabricated using electron beam lithography, as the mask formed by the spheres does not suffer from the limitations of resolution due to the exposure of the PMMA resist. This effect is illustrated in figure 5.3 which presents two SEMs of a NSL sample (a) and an EBL sample (b). Sample (a) consists of an array of nanoparticles produced by nanosphere litho-

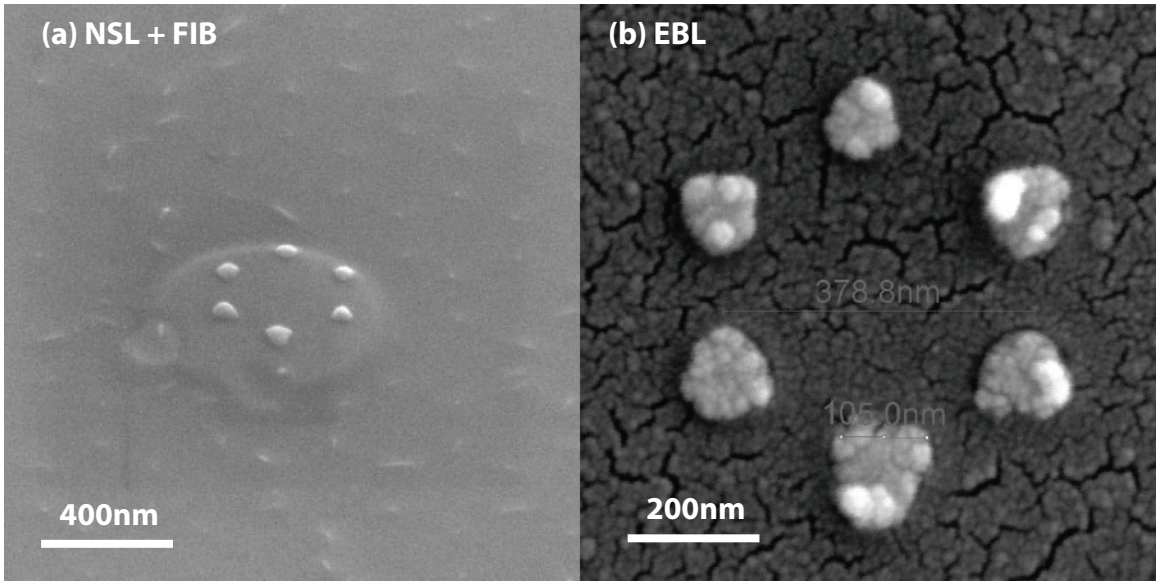

Figure 5.3: Hexagonal structures fabricated by NSL and FIB (a), and by EBL (b). The apparent roughness in (b) is the result of a thin chromium layer (5 nm) that was deposited for imaging purposes.

graphy. Focussed ion beam (FIB) milling was subsequently used to isolate an hexagonal structure comprising six silver nanoprisms. The milling by the ion beam is an intrusive process that damages the optical quality of the particles. First, the ion beam introduces impurities that are embedded in the substrate and the particles. These contaminants modify the optical properties of the substrate and of the particles. Second, the milling process leads to a rough surface around the particles of interest that will scatter light and compromise any spectroscopic characterisation of the particles. Further, the milled material is scattered with high energy and affects the neighbouring particles (partial etching leads to a rounding of the particles, and re-deposition of material on the particles leads to further contamination). For these reasons, it was not possible to characterise the scattering response of this sample.

Sample (b) presents an hexagonal structure fabricated by electron-beam lithography. The pattern was drawn to mimic the arrangement that results from the process of nanosphere lithography (the dimensions of the nanoprisms were retrieved from SEM and drawn onto the resist mask by the e-beam). The comparison with figure 5.2(e) clearly demonstrates the higher quality of the triangles

produced by NSL over EBL. The closed-packed spheres provide a very well-defined mask for the metal deposited by thermal evaporation, while the resist suffers a lack of resolution discussed in chapter 4.

NSL-fabricated samples offer the advantage of a cost-effective fabrication technique for covering large areas of a sample. The particles have a well-defined shape with sharp corners. For the purpose of characterising the optical properties of gold nanoparticles, the technique of electron-beam lithography was however preferable as it provides more control over the particle shape, size, and on the relative position of surrounding particles. Further, the presence of defects in NSL samples can lead to a large variation of optical properties (see figure 5.8).

5.1.3 Other techniques

Colloidal growth is a widely used technique to produce metallic nanoparticles in solution [15–18]. Seed gold nanoparticles of typical diameter a few nanometres are introduced in a solution containing Au^{3+} ions and a surfactant (CTAB, cetyltrimethylammonium bromide). This surfactant acts as capping agent and allows a control over the shape of the particles, whose growth follows preferential crystalline directions such as {001} planes in gold [17]. The concentration of ions can

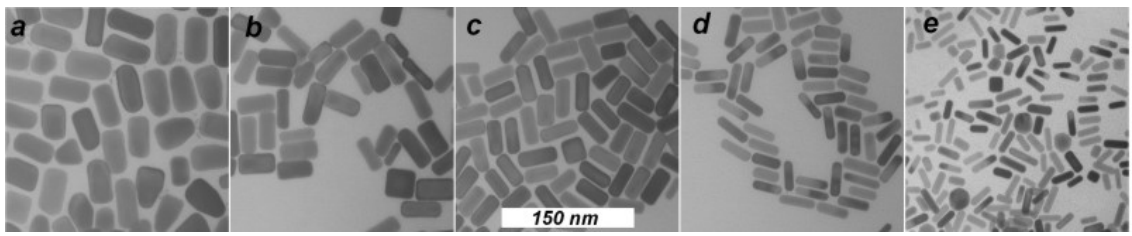

Figure 5.4: TEM of gold nanorods of varying aspect ratio produced by wet chemistry (from [19]).

be used to tune the aspect ratio of the nanorods. Additionally it has been demonstrated that the excitation of LSPR by a laser beam can be used to tune the morphology of the particles during their growth [19]. The particles can be deposited on a substrate, however the difficulty remains of how to control their relative positions and orientations [20].

I chose to fabricate disordered arrays using electron-beam lithography, so as to retain optimum control and freedom over the particle sizes and particle positions. A program was developed to produce the position lists used to expose arrays of arbitrary design. A sample shape (polygon) is repeated and arbitrarily distorted, rotated, and positioned at specific locations across the write-field, as illustrated in 5.5. In this chapter the nominal size of the particles is held constant, but the position and orientation of the particles is varied from a regular lattice of aligned nanorods to a disordered collection of nanorods with random in-plane orientation.

Disorder can be defined as a breaking of symmetry from a periodic system. This departure from the crystalline state can occur in two forms [21]. (i) The unit cell of the lattice is altered at several locations that have no spatial correlation with the lattice. This type of disorder is termed cellular disorder. The alteration to the motif may be a vacancy (the particle is missing); a particle of a different size or shape, or orientation; a particle of a different material; a motif containing more than one particle. (ii) A different kind of disorder is positional disorder where the motif is

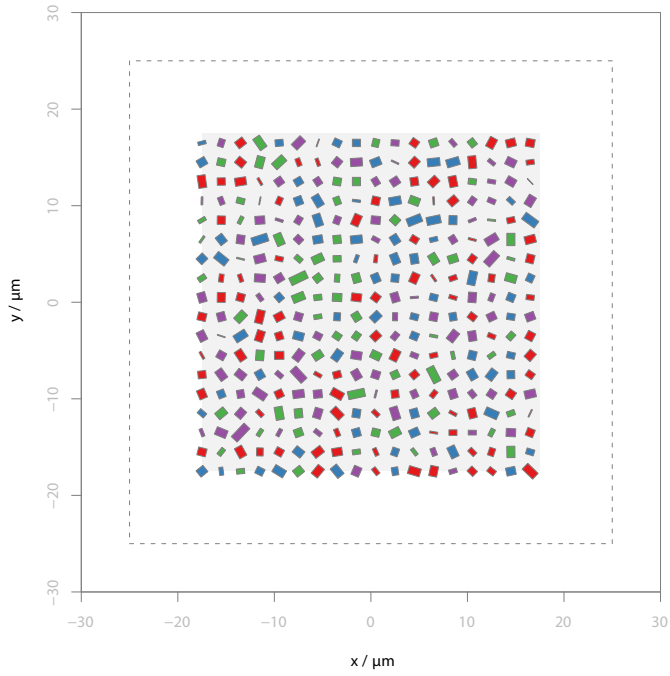

Figure 5.5: Illustration of a position-list with a custom specification of the shape (rectangle), orientation, scaling, and positions. The polygons are scaled for clarity in this figure. The colours illustrate the dose factor that will be applied during the exposure.

consistent across the sample, but the position of the scatterers is displaced from the lattice in a non-periodic manner. The displacement may vary in amplitude and range of correlation (distinction between long-range and short-range disorder).

In chapter 8, the effect of cellular and positional disorder will be investigated in diffractive arrays of gold nanorods with a periodicity of order the wavelength of resonant excitation of the LSPR. In this chapter, attention will be focussed on denser arrays, that are non-diffracting in the visible. The comparison is made between arrays that have a strict periodicity, and arrays for which the particles are displaced from their regular locations by an increasing amount. Figure 5.6 sketches

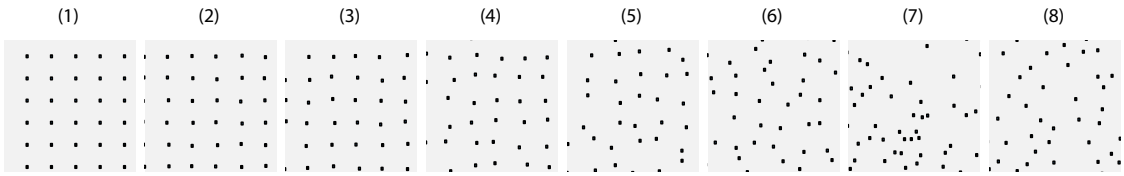

Figure 5.6: Images of 8 designs of particle arrays with increasing levels of disorder. Array 1 is a regular square array ; arrays 2–6 have an additional jitter to the x-y positions (respectively 5%, 10%, 20%, 30%, 40%) ; array 7 is an array with random x-y positions ; array 8 is a pseudo-random configuration drawn from a Strauss point process [22] (no overlap).

a few realisations of positional disorder in arrays of particles, with a fixed occupancy. The pattern drawn by electron-beam on the resist mask can be designed to present a varying degree of disorder in the particle positions. For a sufficiently large number of particles in the array, the assumption of ergodicity can be made and the properties of one realisation of disorder should reflect the general

response of many such realisations. Figure 5.6(7) and (8) are two examples of arrays where the positions were *random* and *pseudo-random*. The distinction arises because in order to study the positional disorder independently of the cellular disorder, careful attention must be taken so that the particles—which have a finite extent, are not overlapping. This constraint of introducing an exclusion zone around each particle while maintaining a low correlation in the positions of the scatterers was achieved by using a *hard core* spatial point process [22, 23]. The problem of designing a point pattern that does not exhibit a regular structure and avoids clustering has been studied extensively in a broad range of areas such as digital half-toning (the process of mimicking grey levels in black and white images using only black spots with varying density); Monte-Carlo integration; the search for a state of minimum energy for a set of charges constrained in a finite domain with a short-range coulomb repulsion between the charges, and between the charges and the border [24].

The samples fabricated by electron beam lithography consisted of arrays of nanoparticles with a spatial extent of $35\,\mu m \times 35\,\mu m$.

5.2 Optical characterisation

Unlike the optical characterisation performed on single particles that provides a signal of low intensity, the measurement of the optical response of a collection of metallic particles can be done with an ordinary microscope. The strong interaction of light with the particles makes it possible to obtain a strong extinction of the light through a sample even with a low density of particles. The measurement of transmittance through a sample is a common characterisation technique for particle in solutions. The linear extinction coefficient obeys the Beer-Lambert law (equation 3.15) that describes the exponential attenuation of the beam upon propagation in a dilute solution of scatterers. The extinction coefficient is directly proportional to the extinction cross-section per particle and the density of scatterers in solution.

The experimental measurements of the optical response of the 2-dimensional samples discussed in this chapter were performed using the setup presented in figure 5.7. A collimated beam of white light from a tungsten filament is passed through the sample, at normal incidence. A polariser may be placed in the path of the beam to selectively probe the extinction for a given polarisation of the incident light relative to the particles. A flow cell can also be adapted on the illumination side of the sample so as to monitor the response of the particles to a change of the refractive index of the superstrate medium (section 5.5).

In comparing the measured extinction with theoretical predictions, particular attention must be taken in the precise experimental conditions for the incident light and the collection optics. In particular, the definition of extinction from the optical theorem (equation 3.14) expresses the interference of the scattered light and the incident light in the exact forward direction. Because a real measurement always involves a spread of incident and collection angles, a portion of the scattered light that is not exactly in the forward direction may be collected by the detector. This leads to an apparent extinction cross-section that is smaller than the expected value from the theory. The conditions for a true measurement of extinction are detailed by Mishchenko [25, 26] and Bohren and Huffman [27]. The spurious effect of scattering at small angles is particularly important for scat-

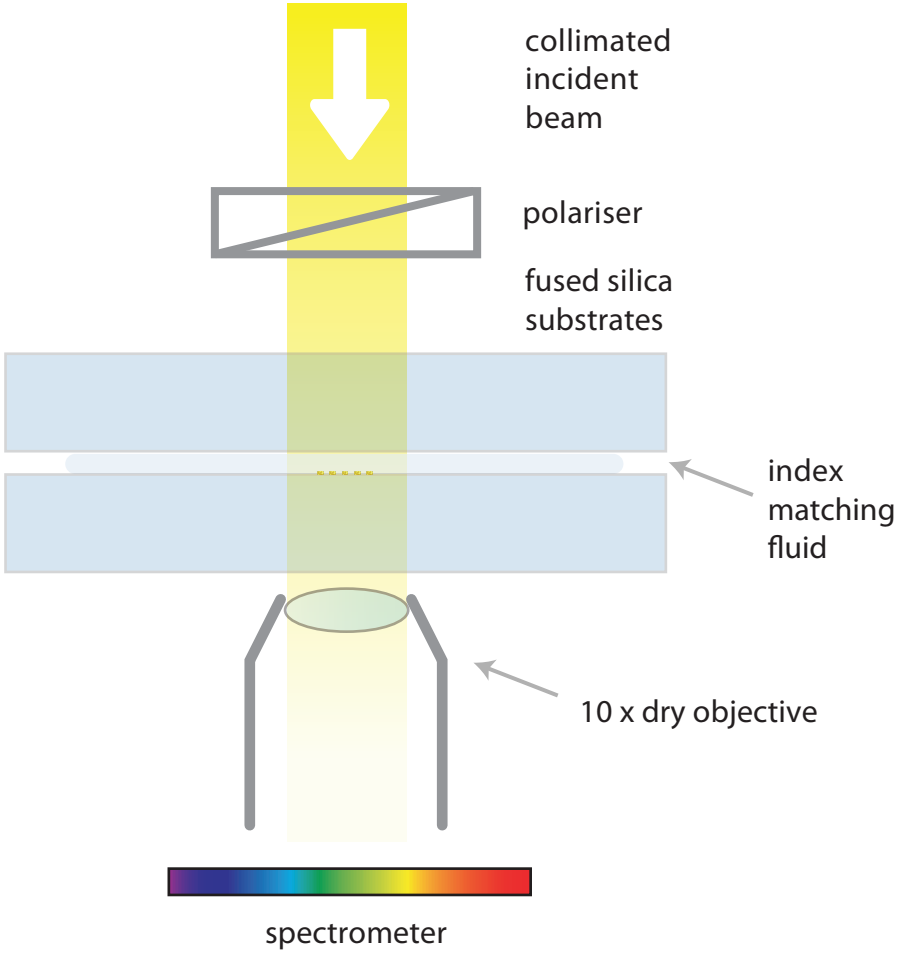

Figure 5.7: Schematic of the experimental setup for measurements of optical transmittance. The collimated beam has a divergence of less than 0.1°.

tering structures that are large compared to the wavelength (the foward scattered light is a sharply peaked lobe associated with diffraction). One should also ensure that the incident light is well collimated and forms a beam of light much wider than the scattering sample, and that the detector has a sensitive area much larger than the scattering sample under consideration. In the experiments detailed in this chapter, the focus is made on the general transmission properties of samples with diverse geometrical configurations but not on the absolute intensities. Although careful attention was paid to observe the conditions for a true measurement of extinction, the general intensity scale is always weaker than the extinction obtained by theoretical modelling. This spurious scaling is independent of the study of inhomogeneous broadening that is presented in the following section.

5.3 Inhomogeneous broadening

Samples prepared by nanosphere lithography have defects intrinsic to the fabrication procedure, and present themselves as a close-packed collection of particles. An optical measurement performed on such samples therefore always involves a distribution of particle shapes and sizes whose

optical response will contribute unequally to the average response of the ensemble. In figure 5.8 typical optical extinction and scattering spectra are presented that were obtained from a sample prepared by NSL.

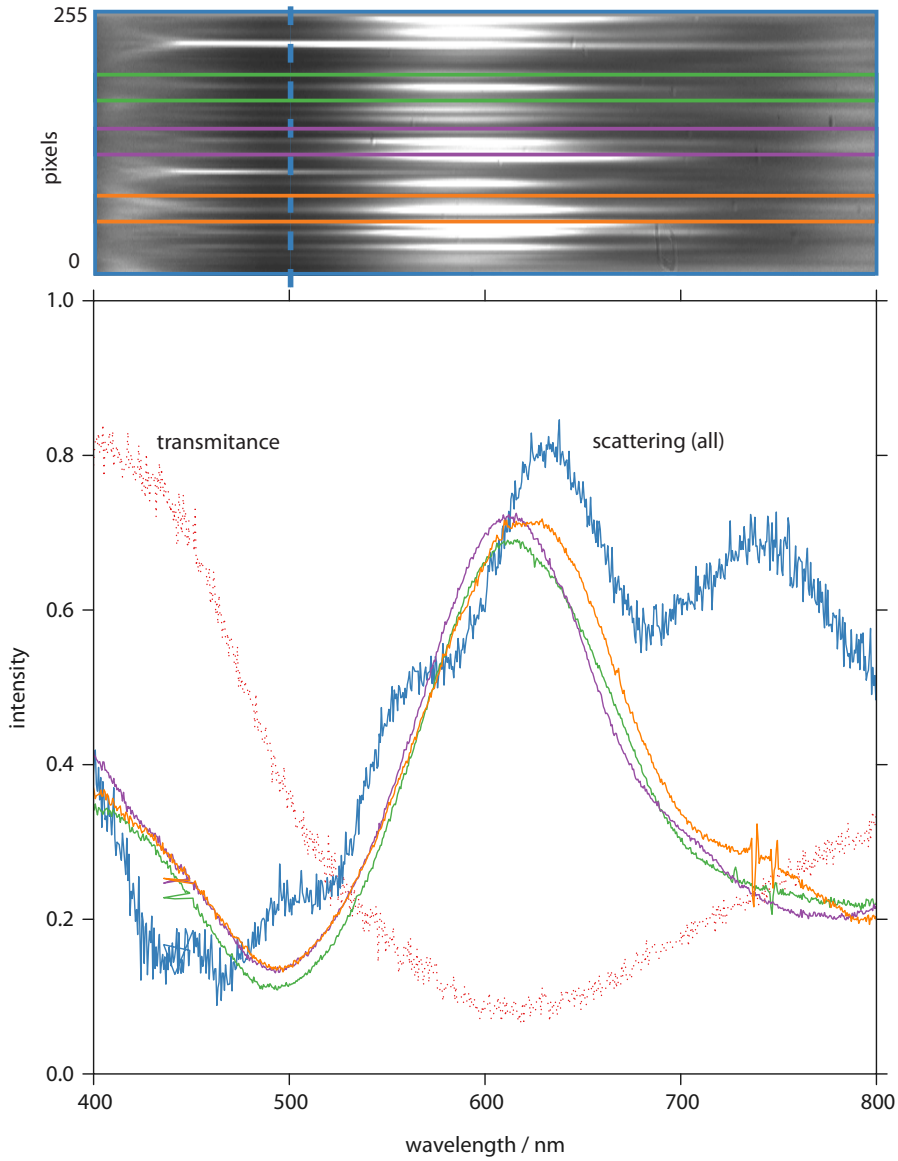

Figure 5.8: Spectroscopy measurements from NSL sample. (Top) spectrometer image of a 5 µm wide, ∼ 400 µm long region of a NSL sample in dark-field scattering (not normalised by the lamp spectral response). Note the dispersion in scattering responses across the sampled area. The vertical dashed line indicates the approximate position of the diffraction condition for the array illuminated at an angle of 65°. (Bottom) Bright-field transmittance (dashed-line) and dark-field scattering spectra across different regions of the scanned area.

The top image is the scattering spectrum of a region of a typical NSL sample for a range of 256 pixels on the camera that is attached to the spectrometer. The scattering spectrum averaged over the full observation window of the spectrometer is reported in blue in the bottom plot. The characteristic feature of this spectrum is a resonant scattering response centred around 600 nm. This spectral feature is recognised as the excitation of a dipolar LSPR supported by the prismatic particles (fig-

ure 4.9). On the high energy side of this resonance peak, we observe an increase of scattering owing to the presence of diffraction by the regular lattice formed by the particles. The light that is diffracted by this array results in an increased intensity when the first diffracted order enters the collection optics. We also note the broadening of the scattered light in the vertical direction below the diffraction limit, indicating the spreading of the scattered light onto the grating of the spectrometer. On the low energy side of the resonance, the multiple peak structure arises from the occasional presence of a larger particle or particle cluster that supports a LSPR at a longer wavelength. In addition, the grating of the spectrometer introduces an artefact in this spectral region if no high-pass filter is used (as was the case for this experiment). The observation of a distribution of resonances in such a sample is emphasised when comparing the overall scattering spectrum with the spectra from smaller regions of the sample (seen as white bands of unequal brightness in the image from the spectrometer). Three such traces are reported in the graph of figure 5.8, and clearly coincide with the expected LSPR resonance from triangular particles (figure 4.9).

In a sample comprising several defects and closely spaced particles, it is difficult to assess the relative influence of the dispersion in particle sizes and the interaction between particles on the average spectrum. To separate out these two contributions, a specific study of inhomogeneous broadening was made on nanorods fabricated by electron beam lithography.

Figure 5.9 presents the morphology of three particles fabricated for this study, which had the same nominal dimensions and were fabricated on the same sample with a spacing of two microns. This distance was chosen as a trade off between several constraints. (i) The particles should reveal as little electromagnetic interaction as possible. (ii) A spacing too large would compromise the spectroscopy of the ensemble, in terms of spectral resolution and signal-to-noise ratio. (iii) The available collection optics do not allow to distinguish particles that are less than a micron apart.

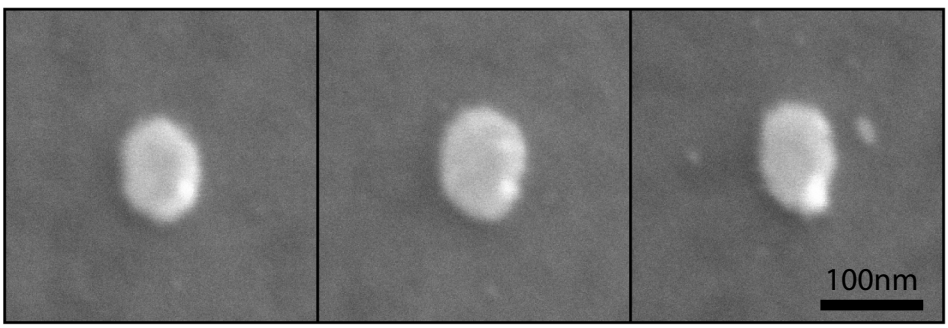

Figure 5.9: Scanning electron micrographs of 3 gold nanorods on a glass substrate (approximate dimensions 100 nm×80 nm×40 nm). The actual separation between particles is 2 µm.

These three particles were characterised by dark-field spectroscopy in two steps: first, a scattering spectrum from each individual rod was collected. Second, the spectrometer slit was adjusted to allow the measurement of the scattering by the three particles. These spectra are shown in figure 5.10 for the polarisation of the incident light along the short axis of the particles. The trace in red is added for comparison, and represents the average of the three individual spectra.

We observe a good resemblance between the ensemble response and the average of the individual spectra. It is however noticeable that the agreement is not perfect, and was indeed worse for

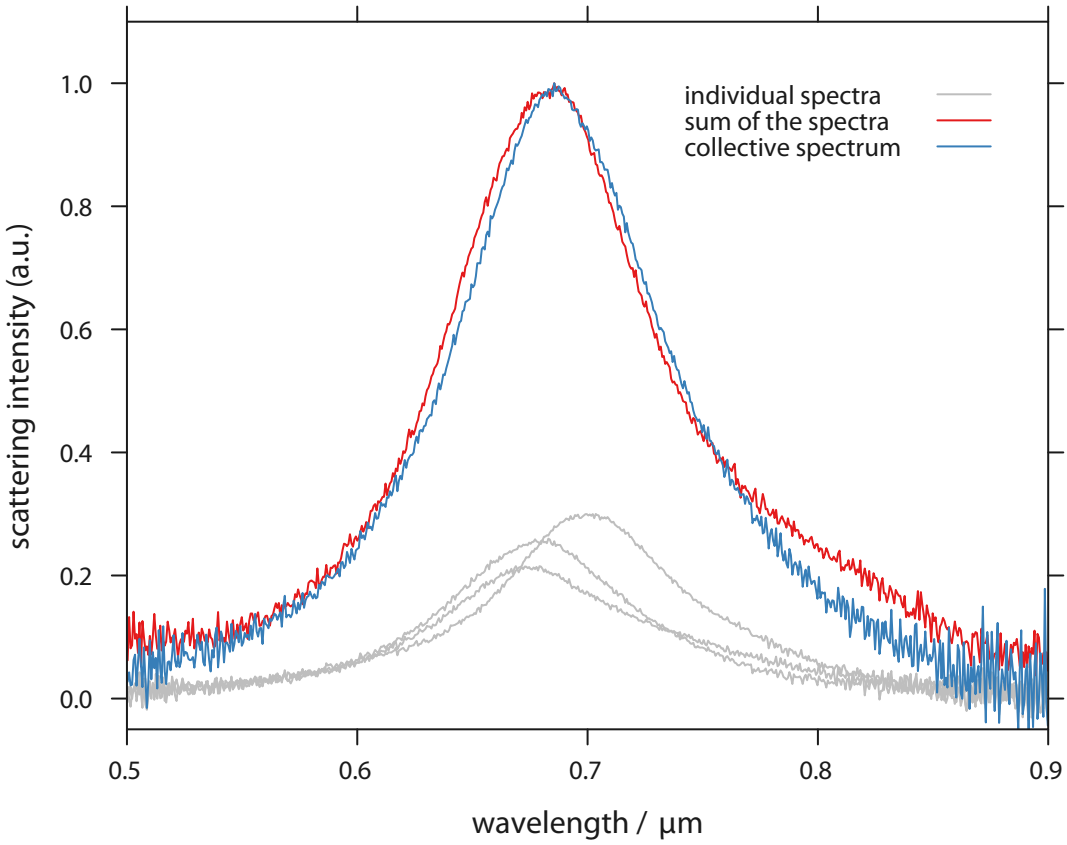

Figure 5.10: Dark-field spectra of three individual nanorods (approximate dimensions 100 nm×80 nm×40 nm), and the collection of them. The particles are immersed in index-matching fluid (refractive index 1.46). The incident light is polarised along the short-axis, in the plane of the sample.

the polarisation along the long axis of the particles. Amongst possible causes for this discrepancy is the high sensitivity of the scattering response with respect to the precise conditions of illumination. As the sample is slightly moved to characterise each individual particle, the illumination condition is altered and results in a similar problem to that faced in chapter 4 where the scattering response of the larger nanorods was shown to display a mixture of resonances even with careful attention being paid to the polarisation of the incident light.

A simple dipole model was used to further investigate the effect of inhomogeneous broadening and to provide some insight on the influence of the particle size distribution in the ensemble spectrum when no electromagnetic interaction between particles is considered. In figure 5.11, the dipolar approximation is used to model the optical extinction of gold nanoparticles with a normal and uniform size distribution. The average of the spectra corresponds to the optical response of a dilute collection of such particles, where no interaction is considered (single-scattering).

A notable feature of the average spectra for the highest value of disorder is the asymmetry (and multiple peaks) in the spectral lineshape, skewed towards the long wavelengths. This skew

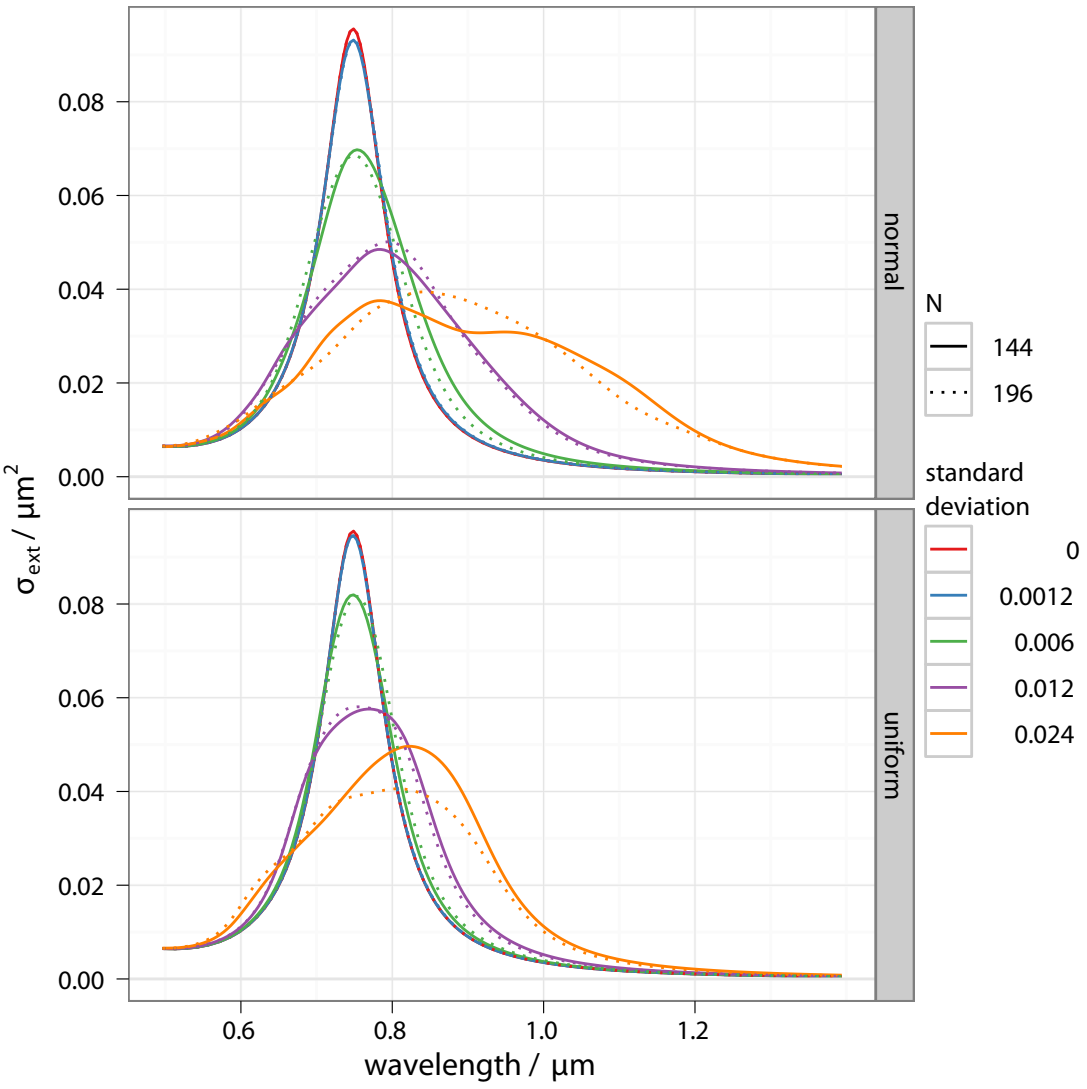

Figure 5.11: Inhomogeneous broadening in the dipole approximation. Calculated average spectra for several distributions of dipoles. The polarizability is described by the modified long-wavelength approximation for ellipsoids. The nominal axes of the ellipsoid were a=120nm, b=80nm, c=35nm, illuminated along the c-axis, with polarisation along the a-axis. The surrounding medium is air. The top panel presents the spectra for a normal distribution of long axes for 144 (solid lines) and 196 dipoles (dashed-lines). Five values of disorder in the long axis of the ellipsoids are considered (standard deviation indicated in the legend). The sizes are drawn from a normal distribution (top panel, standard deviation indicated in the legend) and uniform distribution (bottom panel, the deviation corresponds to the support of the distribution).

occurs because a symmetric distribution in particle sizes leads to a skewed distribution of resonance frequencies as the dependence of the LSPR on the aspect ratio is not linear, and also that the dispersion in the dielectric function gives more intense resonances at longer wavelengths. The spectral lineshape of an ensemble of particles is often described as a Voigt profile [28], which is the result of a convolution between the resonance curve of the LSPR associated with a single particle, and a distribution of resonance frequencies. This convolution should be weighted by a function

that describes the intensity of the LSPR as a function of particle size. Further, particles of different sizes can display a range of spectral linewidths (as seen in chapter 4). In view of those multiple parameters that affect the inhomogeneously broadened lineshape, the inverse scattering problem that consists in retrieving the individual particle response from a measurement of the ensemble response appears highly degenerate.

5.4 Particle interactions

In addition to inhomogeneous broadening — the measurement of an average spectrum from a sample of random particle sizes, the light scattered by a collection of particles can differ substantially from the response of a single particle due to electromagnetic interaction between neighbouring particles. Any such interaction is characteristic of a *multiple scattering* process: a particle in the cluster is excited by an electromagnetic field that differs from the light incident on the cluster. It should be noted, however, that the separation of the electromagnetic field exciting the structure in the sum of the incident field plus the contribution of partial waves is a purely mathematical construction. The view of multiple scattering as a step-by-step process where 'photons' are hitting particles two or more times in a chronological succession of events is misleading and should be avoided [29–31]. The response of a medium exhibiting multiple scattering is *non-local*, the susceptibility function involves a convolution of the electric field at neighbouring locations in space.

The situation of multiple scattering can be approached theoretically in several different ways, depending on the number of interacting elements and on their relative positions.

For clusters containing a small number of particles, there is the possibility of solving the scattering of light by the cluster with techniques such as `DDA`, `FEM` or `FDTD`, treating the cluster as a single scattering body (the fact that it is disjoint does not change the equations, only the shape specification). Another approach considers the scattering by individual elements using the Mie theory or a more general T-matrix scheme, and makes use of the translation theorem for vector spherical wave functions to express the partial waves scattered by each element in the coordinate system of the other particles. It is possible to cast the resulting system of equations in a simple form that requires only little computational overhead after the characterisation of the single particles.

When the scattering medium comprises a very large number of particles, and each of these particles is located in the far-field zone of its neighbours, the so-called *radiative transfer equation* can be used to describe the average diffusion of light through the medium [30]. Effective medium theories have also been employed to model the optical properties of a mixture of particles embedded in a matrix [32, 33]. Periodic systems in 1, 2, or 3 dimensions lead to another range of possible numerical and semi-analytical techniques based on the expansion of the fields in a basis of periodic functions (Fourier modal expansion).

In the next section I will discuss how the approximation of coupled dipoles can present a simple picture of the multiple scattering process that modifies substantially the optical properties of small gold nanoparticles.

5.4.1 Dipolar coupling

When two identical gold nanoparticles are widely separated (relative to their size and to the wavelength), they support unperturbed eigenmodes of the electromagnetic field that describe the interaction of light with the scatterers in isolation. When the separation is reduced, the field that is scattered by one particle can excite the other particle and conversely. This dynamical system describes a multiple scattering process. The optical properties of the ensemble are described by a combination of the two scatterers with a perturbation term that accounts for the relative interaction between the particles *via* their scattered field. The mathematical description of two such coupled oscillators is analogous to the interaction between two atomic orbitals in chemistry, where the coupling results in the formation of hybrid molecular orbitals. It is also the same description that is used to describe the mechanical system of two coupled pendulums. Each pendulum in isolation is characterised by a given eigen-frequency. When a link is made between the two oscillators, the compound system has a set of two *hybrid modes* with different eigen-frequencies that can be constructed as a linear combination of the modes of two isolated oscillators (symmetric and antisymmetric displacements). The stiffness of the link between the two oscillators dictates the splitting of frequencies between the isolated mode and the new hybrid modes (a stiffer link results in a stronger splitting). The beating between the two hybrid modes results in an alternating transfer of energy from one oscillator to the other.

Let us consider the case of two identical dipoles a and b of polarizability α, separated by a distance d. The dipole moments obey the coupled dipole equations,

$$\mathbf{P}_\mathrm{a} = \alpha\left(\mathbf{E}_0 + \bar{\mathrm{G}}\mathbf{P}_\mathrm{b}\right) \tag{5.1a}$$

$$\mathbf{P}_\mathrm{b} = \alpha\left(\mathbf{E}_0 + \bar{\mathrm{G}}\mathbf{P}_\mathrm{a}\right), \tag{5.1b}$$

where $\bar{\mathrm{G}}$ is the Green's dyadic that expresses the field radiated by a dipole (equation 3.40). Equations 5.1 can be cast in matrix form,

$$\begin{pmatrix}\mathbf{E}_0\\ \mathbf{E}_0\end{pmatrix} = \begin{pmatrix}\mathbb{I}/\alpha & -\bar{\mathrm{G}}\\ -\bar{\mathrm{G}} & \mathbb{I}/\alpha\end{pmatrix}\begin{pmatrix}\mathbf{P}_\mathrm{a}\\ \mathbf{P}_\mathrm{b}\end{pmatrix}, \tag{5.2}$$

where the interaction matrix on the right-hand side is formed of 3×3 blocks. The diagonal terms are the response of each dipole to the incident field, and the off-diagonal elements $\bar{\mathrm{G}}(d)$ describe the coupling between the two dipoles and can be seen as a perturbation of the uncoupled system of the two oscillators (when d is large). Equation 5.2 can be solved by diagonalising the interaction matrix. In the new system of normal coordinates, the dimer is described by a combination of two eigen-modes which are the symmetric configuration (two dipoles aligned) and antisymmetric configuration (two dipoles of opposite orientation). The two eigenmodes have a different effective polarizability,

$$\alpha^* = \frac{\alpha}{1 \pm \alpha g}, \tag{5.3}$$

where g is the relevant term from the Green' dyadic. The antisymmetric mode (+) has no net dipole moment and cannot be excited by a plane wave incident along the normal to the dimer axis (there needs to be a phase difference between the two particles). The symmetric configuration (−) corresponds to an effective dipole moment located at the centre of the dimer. The intensity of the total dipole moment depends on the coupling between the two dipoles, and this coupling is described by the components of the Green's dyadic that depend on the relative orientation of the dipoles and of their separation [34]. An illustration of the field scattered by a unit dipole is presented in figure 5.12.

The bottom panel presents the near-field component of the electric field for a unit vertical dipole (arbitrary intensity scale). The radial component peaks along the dipole axis, while the tangential component is maximum in the orthogonal direction. The maximum of the radial component is twice the value of the maximum for the tangential component: as a consequence the coupling between two particles will be stronger in the direction of the dipole moments when the particles are situated in this near-field zone. The near-field contribution of the dipolar field decays as $1/r^3$, and after a distance of about a wavelength the induction term in $1/r^2$ and radiation term in $1/r$ will dominate [34, 35]. The top panel presents the tangential component of the electric field in the radiation zone (distance $\gg \lambda$). In this region, the field forms a spherical wave-front. The radial component vanishes faster than $1/r$ and carries no energy in the far-field (not shown here). The tangential component is maximum in the direction orthogonal to the dipole moment, and vanishes along the dipole moment. The field that is scattered from the dipole is a wave that is modulated in space with the periodicity given by the wavelength of the light in the surrounding medium. In particular, this means that if the distance between the two dipoles is such that the field radiated by one dipole is in phase with the incident field at the other dipole's location, the effective polarizability is increased (and *vice versa*). This periodic modulation will be important in chapter 6 where I will present a study of the long-range radiative coupling between particles that are separated by an integer factor of the wavelength.

Due to the particular symmetry of the dipolar field, the coupling between two dipoles depends on their relative position. I will now illustrate this dependence by considering two particular configurations: (i) the dipoles are aligned along the dimer axis, (ii) the dipoles are orthogonal to the dimer axis. In 5.13 the coupled dipole approximation (equation 5.3) is used to model the influence of the radiative coupling between two gold nano-ellipsoids as a function of distance. The dimer is formed of two identical dipoles that characterise a gold ellipsoid of semi-axes a = 60 nm, b = 40 nm, c = 20 nm, for which the polarizability was obtained using the modified long wavelength approximation 3.28.

In the top panel the calculated extinction of the dimer is compared to the isolated dipole extinction (dashed curve) for different separations. For the larger separation (400 nm) little interaction is observed — the extinction is slightly blue-shifted from the isolated particle response, this blue-shift occurs because of the long-range components of the dipolar field. As the gap between the dipoles is made smaller, the resonance of the dimer broadens and red-shifts as a result of near field interactions. At small gap values (100 nm) the red-shift of the mode is substantial ($\sim$ 150 nm) and

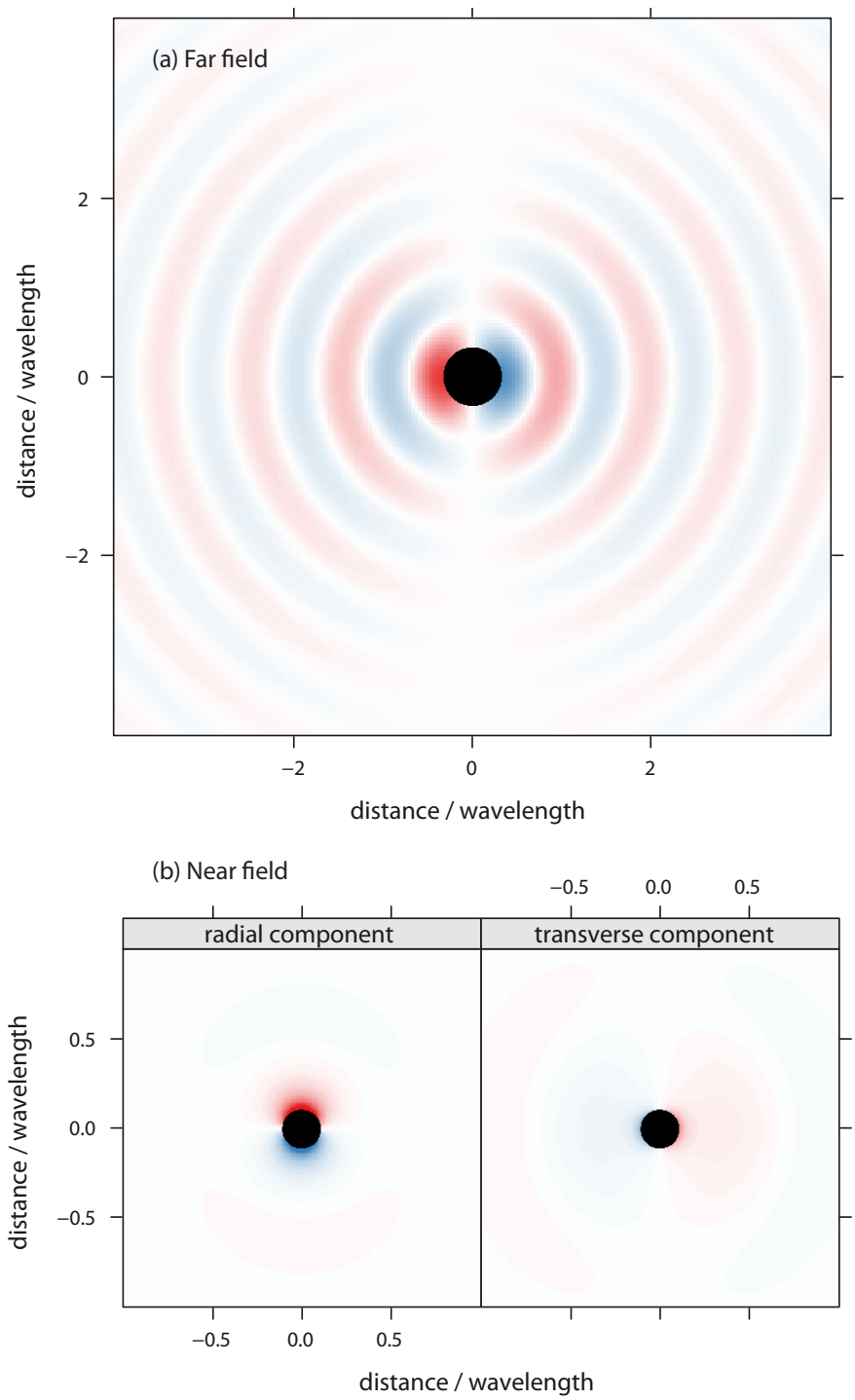

Figure 5.12: Calculated near-field and far-field radiation in the vicinity of a vertical point dipole (distance in units of the wavelength). (a) Instantaneous tangential component of the electric field. The black dot in the centre is an exclusion zone around the origin where the formula diverges. (b) Near-field distribution for the instantaneous radial component of the field (left) and tangential component (right). The colour scale is common to both panels.

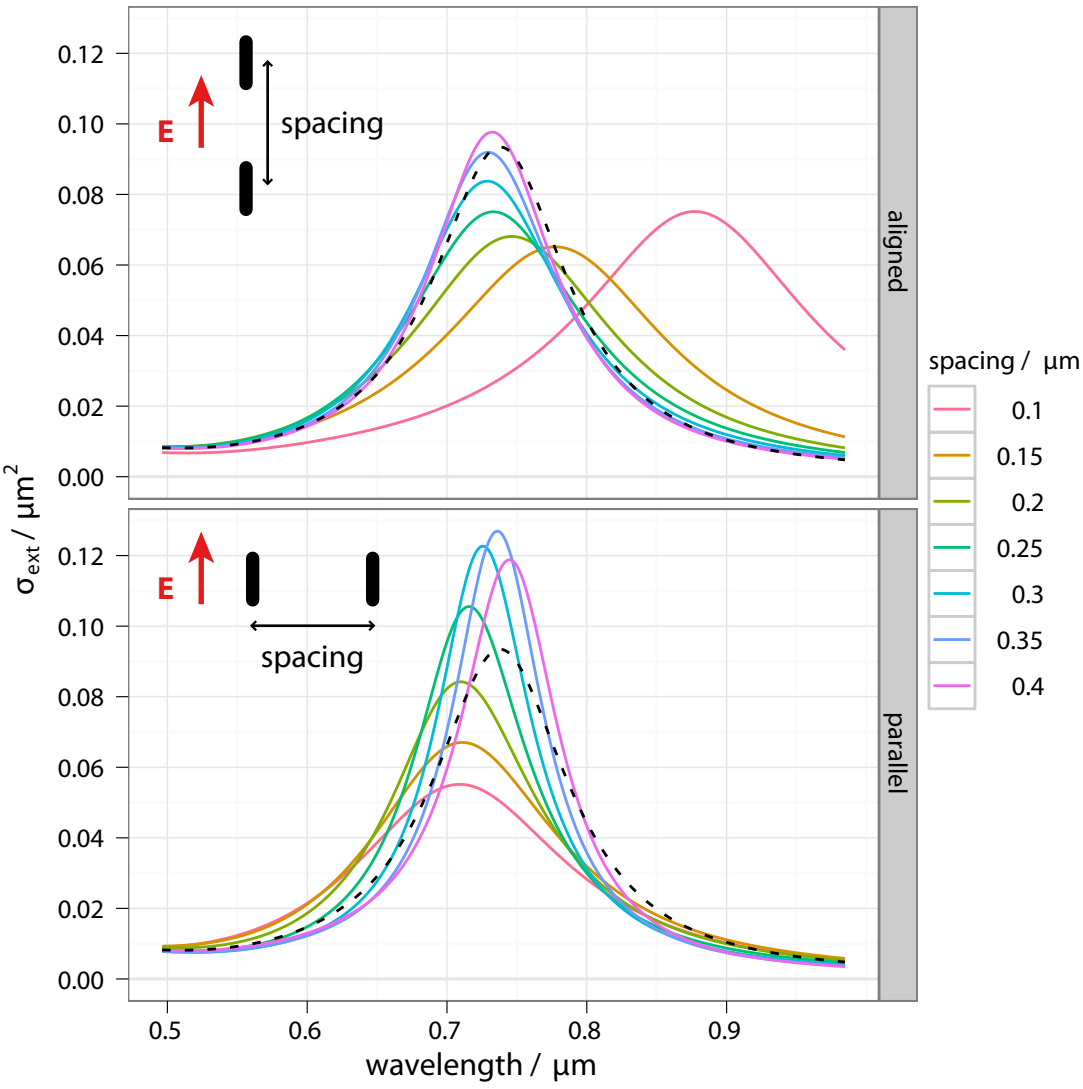

Figure 5.13: Coupled dipole model of the extinction spectrum of a dimer of identical gold nanoellipsoids. The dashed line is the extinction spectrum of a single particle (semi-axes a = 60 nm, b = 40 nm, c = 20 nm.) The light is incident along the c axis, and is polarised along the long axis a, in an homogeneous surrounding medium of index 1.5. The separation is varied from 100 nm to 400 nm by steps of 50 nm, for two orientations of the dimer as indicated in the insets.

arises from the decreased restoring force acting on the charges due to the Coulomb attraction of the charges on either side of the gap.

In the bottom panel of figure 5.13, a different behaviour is observed for the situation where the two dipole moments are not aligned but parallel. The smallest gap yields a blue-shift of the LSPR with respect to the isolated dipole response, and a broadening of the spectrum. As the separation is increased the blue-shift is reduced and the peak position tends towards that of the isolated dipole. The intensity is however higher than for the isolated dipole even with a separation of 400 nm. The blue-shift and increase in intensity occur because the field that is acting on each dipole is strengthened by the distribution of charges on the neighbouring particle.

For closely spaced particles, the interaction of the modes is mainly of electrostatic nature ($1/r^3$, no retardation). The shift in resonance frequency of the LSPR can be understood by the plasmon hybridization model [36, 37] described in figure 5.14.

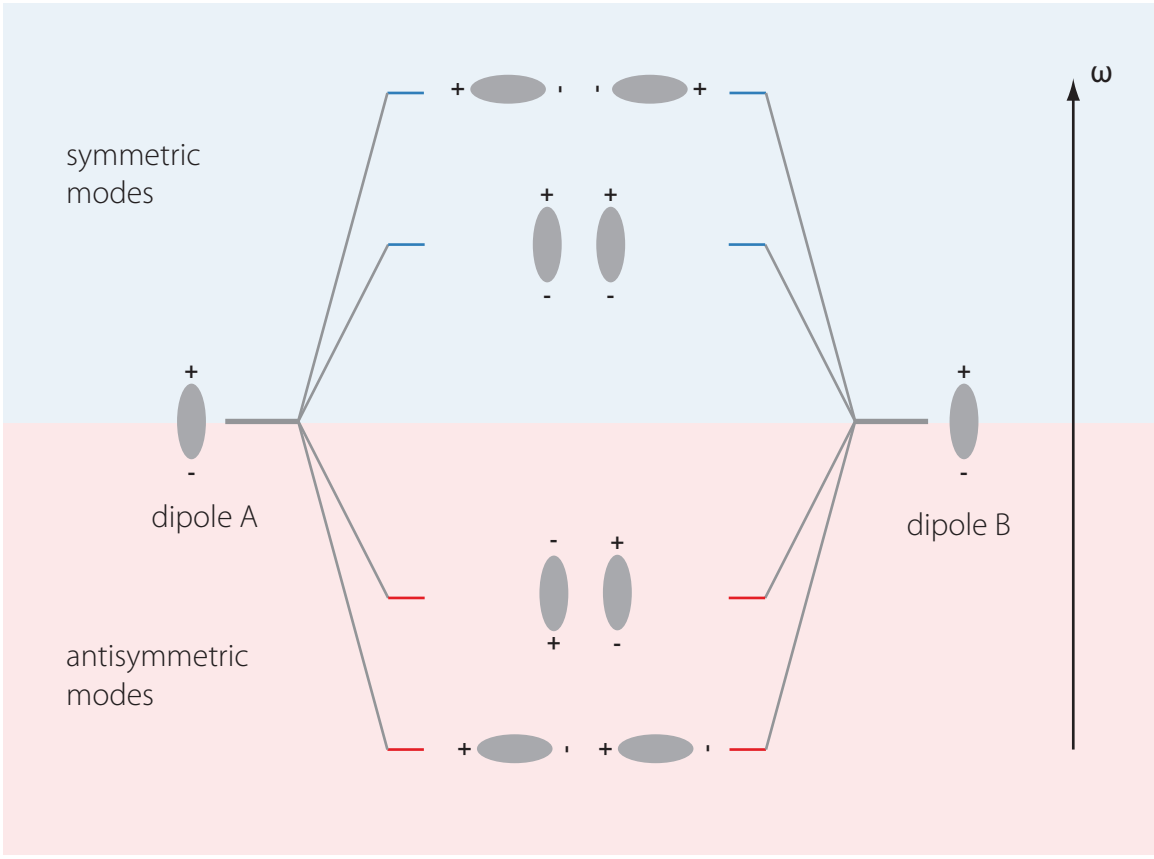

Figure 5.14: Schematic of the hybridization of two dipoles (after [37]). The diagram displays the energy levels of different combinations of two LSPRs (the reference energy is for the two dipoles in isolation).

In this schematic, the LSPR modes associated with two nanoparticles split in two hybrid modes with different energy levels (one blue-shifted, the other symmetrically red-shifted) when the dipoles are brought in proximity. The symmetric configuration yields a blue-shift of the resonance because the charges of the two particles acting in concert result in a stronger restoring force for the surface charge density associated with the LSPR (bottom panel of figure 5.13). The antisymmetric configuration, however, leads to a red-shift of the LSPR (top panel of figure 5.13). The two other configurations are not observed when the dimer is excited by a plane wave (dark modes). The possibility of excitation of dark-modes has however been demonstrated for larger nanoparticles [10, 38], and using a localized emitter [39].

The plasmon hybridization model discussed in this section describes accurately the coupling between two small nanoparticles that can be modelled as dipoles [36, 37]. The approximation however breaks down for very short particle-to-particle separations, or large particles where the electromagnetic interaction involves higher order multipoles [40, 41].

5.4.2 Coupling to higher order modes

In addition to the dipolar coupling between particles, the electromagnetic coupling of neighbouring particles can lead to an increased excitation of higher order modes. This effect arises because each particle is not only excited by a plane wave, but also by the inhomogeneous partial fields originating from neighbouring particles. For spheres, the orthogonality of the normal modes (spherical harmonics) is broken when the field scattered by one particle is translated to the location of another particle. The non-vanishing overlap between the modes means that a partial wave scattered by one sphere can excite a combination of modes on another sphere. In figure 5.15 the effect of particle separation and particle size on the scattering spectrum is studied by modelling a pair of gold spheres with different values of sphere radius.

This numerical simulation was performed for gold spheres of radii 50 nm, 80 nm and 120 nm in a surrounding medium of index 1.5. The response of an isolated sphere is shown in dashed line for comparison. The numerical scheme is described in [42], and is based on the rigourous solution of the Maxwell equations by the multipolar expansion of the fields at the location of each scatterer. The translation of the multipoles to the coordinates of each particle in the cluster leads to a system of coupled equations similar to equation 5.1a but for an arbitrary number of multipoles. In practice, the number of multipoles required in a simulation is truncated to a finite value that can be tuned to reach a required accuracy of the solution (such convergence was verified for each of the spectra presented in figure 5.15).

The top panel (smaller spheres) present results that are qualitatively similar to that of the coupled dipole model (figure 5.13), which is the expected result for particles much smaller than the wavelength (the case of very short gaps relative to the sphere radius is not investigated here, see for instance [40] for a study of the critical transition from short gaps to touching dimers). The resonance red-shifts for the parallel polarisation, and blue-shifts for orthogonal polarisation. The strong absorption edge of gold near the LSPR frequency however dampens the change in the resonance intensity in comparison to the situation of gold ellipsoids (figure 5.13).

The larger particles (bottom panels) depart from the coupled dipole model by the presence of multipolar resonances. When the incident polarisation is directed along the axis of the dimer (figure 5.15, left panels), we observe a strong excitation of a quadrupolar resonance. The spectral position of the quadrupolar mode is not affected by the separation between the two particles, but the intensity relative to the dipolar mode undergoes a large change. For short particle spacings, the dipolar mode is strongly red-shifted and of the same magnitude as the quadrupolar mode. As the separation increases, the dipolar mode blue-shifts and weakens considerably while the quadrupolar mode gains in intensity. For a separation of several times the sphere radius, one recovers the single scattering response (dashed line), where the dipolar mode regains its strength. This complicated behaviour would require further study. In particular, the field pattern associated with the quadrupolar mode has a different symmetry to that of a dipole [34, 43], which could provide some insight in the coupling mechanism between the two quadrupoles, and the possible mixing between dipoles and quadrupoles.

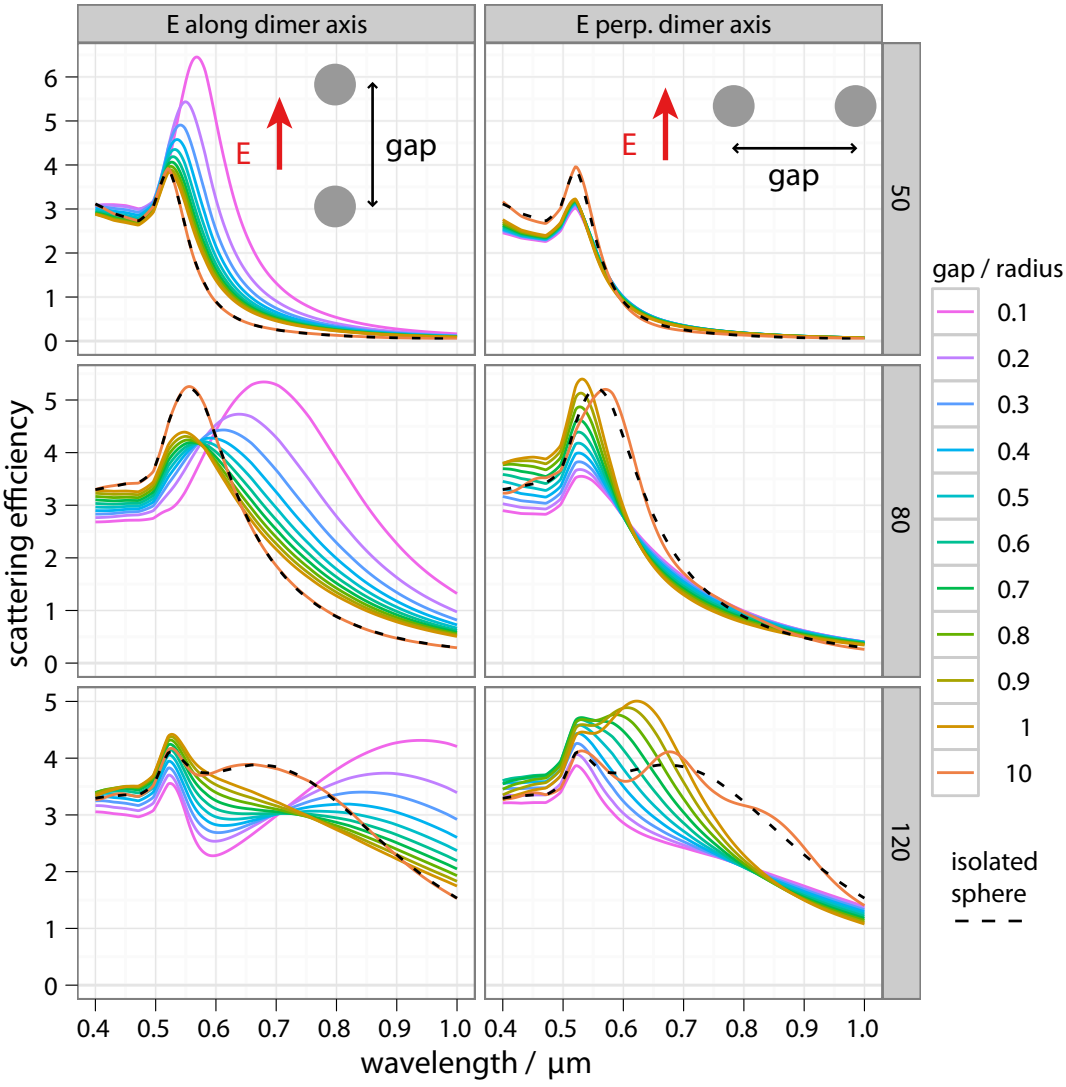

Figure 5.15: Modelled scattering efficiency spectra of a dimer of gold spheres as a function of sphere radius and separation, using a rigourous multiple scattering calculation for a cluster of spheres (code courtesy of J. García de Abajo [42]). The dimer consists of two identical spheres of radius 50 nm, 80 nm, 120 nm in a surrounding medium of index 1.5. The spheres are illuminated at normal incidence from the dimer axis, with two polarisations (left *vs* right panels). The separation between spheres is varied as a multiple of the sphere radius, as indicated by the colour legend. The dashed line is the scattering efficiency spectrum of a single sphere shown for comparison.

In the bottom-right panel, the dimer of large spheres is illuminated with a polarisation perpendicular to the dimer axis. We note that even at a separation of 10 times the sphere radius the extinction of the dimer differs from the response of an isolated sphere. An oscillation in the spectral lineshape indicates the interference between the incident light and the dipolar radiation from one particle acting on the other. This far-field radiation is maximum in this orientation, and vanishes for the case of parallel polarisation. As the gap between the spheres is reduced, the dipolar

mode blue-shifts and weakens. For small gaps, the quadrupolar mode is the dominant feature of the extinction spectrum.

5.4.3 Large clusters

The discussion of the modification of the optical response of a dimer as a function of the particle separation contains the essence of the effects that are observed in large collections of particles. The near-field interaction is of short-range nature, and is therefore limited to the nearest neighbours. A disordered collection of identical LSPR-supporting particles will typically present a broad extinction spectrum in comparison to the LSPR of an isolated particle because the interaction between neighbouring particles leads to a range of red-shifts and blue-shifts according to the distribution of particle separations and orientations. I will now present experimental measurements on such ensembles of gold nanorods with varying particle-to-particle separations.

5.5 Extinction measurements in dense arrays, sensitivity to bulk refractive index

A sample of scanning electron micrographs of six arrays of gold nanorods fabricated by electron-beam lithography is displayed in figure 5.16. The sample presents several levels of disorder in particle positions and particle orientation.

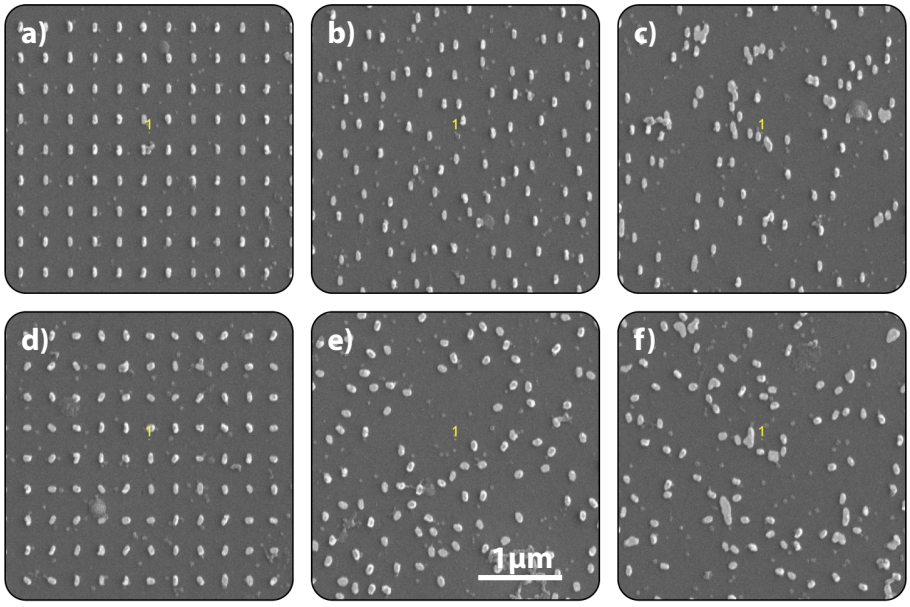

Figure 5.16: SEMs of dense arrays with positional disorder. (a–c) arrays of particles with fixed orientations and different levels of disorder (a: nominally regular, b: pseudo-random, c: random). (d–f) identical positions as in (a–d) but random orientation of the particles.

Because collections of particles typically offer a higher signal-to-noise ratio in optical measurements (compare figure 4.6 and figure 5.17), and can be produced with large-scale fabrication techniques (*e.g* nanosphere lithography), ensembles of particles are often more attractive in practical applications than single particles. If a collection of nanoparticles is a good candidate for the

design of a biosensor, for instance, it is important to assess the relative sensitivity of single particles and collections of particles with respect to a change in the surrounding medium. Because of particle interactions, two samples with a fabrication process leading to comparable inhomogeneous broadening can shown a resonance of very different quality depending on the geometrical arrangement of the particles. These effects are quantified experimentally in figure 5.17.

Arrays of particles with two different occupancy were investigated. The left panels correspond to an average separation of 300 nm between particles, and 200 nm for the right panels. The transmittance was obtained by measuring the transmission of the light through the sample and normalising by the light transmitted through a neighbouring part of the sample where no particles were present. The refractive index of the superstrate medium was varied from air to pure water (n=1.333) by using a flow cell adapted onto the substrate. The transmittance for both media is shown for comparison in each panel (solid curves: air, dashed curves: water). The six different geometrical arrangements of particles in the arrays are split into two categories: the top three panels are for nanorods aligned along one particular direction (that of the polarised light) and correspond to three degrees of disorder (top: regular array, middle: random array with an exclusion zone, bottom: random array). The three bottom panels correspond to the same geometrical arrangement of particles but with a random orientation of the nanorods.

It is clear that the regular array with a consistent orientation of the particles (top panels) provides the sharpest and most defined resonance curve. The density of 300 nm leads to a narrower and stronger transmittance dip than the array of spacing 200 nm. This is in agreement with the discussion of interparticle coupling (section 5.4.1).

As the disorder increases, the range of LSPR shifts due to particle interactions leads to a further broadening and weakening of the transmittance minimum associated with the LSPR. Further, the situation of a completely random arrangement of particles leads to a distribution of particle sizes (neighbouring particles can become connected, see figure 5.16(f)). The distribution of particles sizes causes an inhomogeneous broadening of the resonance. The effect of the random particle orientation on the transmittance is to further broaden the spectrum (compare (a) and (d), for instance), as a mixture of long-axis and short-axis resonances is excited with a strength that depends on the relative orientation of the incident (polarised light) and the axes of the particles. For the small aspect ratio considered in this sample, the two resonances overlap spectrally and the resulting spectrum shows only one broad spectral feature.

The sensitivity of these arrays to a change of refractive index of the superstrate medium from air to IPA is difficult to assess in the broader spectra. The spectral shift of the extinction peak is evaluated as $40 - 50$ nm for all the samples considered here. This value is however a poor indication of the relative performance of the arrays in a sensing perspective: arrays (a) are clearly more suitable than arrays (f) as a clean and well defined LSPR spectrum allows for an accurate and reproducible determination of the spectral shift due to a change of the surrounding environment. The width of the spectral feature is particularly important in this respect, as a broader resonance leads to a smaller change of intensity at a fixed probing wavelength for a given value of the spectral shift.

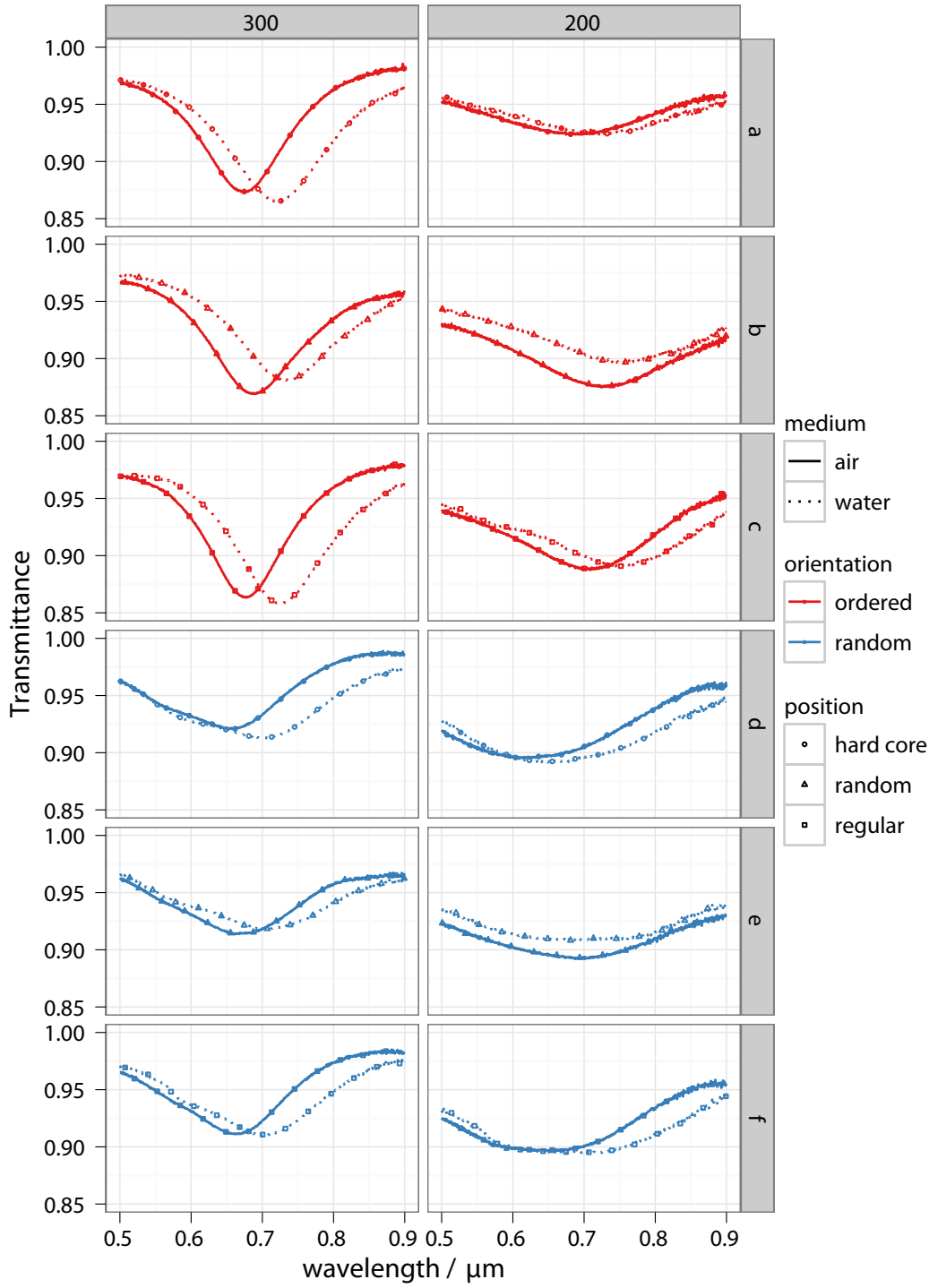

Figure 5.17: Experimental transmittance spectra from arrays of gold nanorods with different geometrical configurations. The particle sizes were 120 nm×80 nm×40 nm. The superstrate medium was air (solid curves) and water (dashed curves, $n = 1.333$). The left panels consider arrays with an average particle separation of 300 nm, while the right panels consider denser arrays with average separation 200 nm. For each density of particles, 6 geometrical arrangement of particles are considered (a—f). Panels (a)–(c) are for arrays where the nanorods are all aligned along one direction, while panels (d)–(f) are for arrays where the in-plane orientation of the nanorods was random. For each of these groups three different configurations are presented: regular arrays (a and d); random arrays with no overlapping particles (exclusion zone, arrays b and e); random arrays (c and f).

5.6 Conclusion

The subject of this chapter focussed on the response of a collection of gold nanoparticles in close proximity (average spacing $\sim 200\,\text{nm}$–$400\,\text{nm}$). Arrays of such particles were fabricated by electron beam lithography and nanosphere lithography, and characterised using bright-field transmission spectroscopy.

In this situation, the particles present a modified optical response that is due to the electromagnetic interaction between neighbouring particles. Each particle is excited by a combination of the incident field and a superposition of partial waves multiply scattered in the cluster of particles. The spectral response of such collections of particles was examined in bright field transmission spectroscopy and revealed the following conclusions. First, the observation of a large sample of particle responses affects the observed lineshape by inhomogeneous broadening. The resonance observed in extinction measurements on several particles leads to a much broader lineshape than in single particle measurements on isolated particles. This effect was verified using electron-beam lithography samples for which three particles were individually probed by dark-field spectroscopy, in comparison to the global scattering obtained from the three particles simultaneously. The spectral lineshape can be represented as a convolution of the individual particle spectra with the distribution of resonance frequencies. The optical response of a collection of particles may also differ from the individual particle response because of the electromagnetic coupling between particles. Using a dipole model, this coupling was shown to result in a broadening of the spectral shape for densely packed particles. Further, the proximity of neighbouring particles with a strong scattering response can result in the excitation of multipolar resonances that would not be observed for isolated particles illuminated by a single plane wave. This coupling to higher order resonances was modelled for a cluster of spheres using an extension of the Mie theory.

Transmission experiments were conducted on regular and irregular arrays with varying degree of disorder and density. It was found that the arrangement of the particles can substantially compromise the sensitivity of the arrays to a change in the bulk refractive index environment. The spectral shift is only weakly modified, but the resonance lineshape is strongly broadened and weakened by the combine effects of inhomogeneous broadening, mixture of resonances, and particle interactions.

"Si l'on pouvait se voir avec les yeux des autres, on disparaîtrait sur-le-champ."

Emile M. Cioran

6

Diffractive coupling in regular arrays

Collections of gold nanoparticles display interesting optical properties due to their strong interaction with light, an interaction that arises from the excitation of localised surface plasmon resonances (LSPR) [1, 2]. When the average particle separation is sufficiently small, light scattered by one such LSPR-supporting particle can significantly contribute to the excitation of its neighbours. Such coupling between particles can alter the single scattering response in a variety of ways depending on the distance between particles, as well as their geometrical arrangement.

In chapter 5, we observed the strong electromagnetic interaction between gold nanoparticles when their average separation was shorter than the wavelength of resonant excitation of a localised surface plasmon. This coupling regime exhibits a mixture of near-field dipolar coupling and excitation of multipolar resonances that leads to a general broadening of the resonance as observed in extinction measurements. This is especially clear when the experimental spectra are compared with the scattering measurements obtained for largely spaced (in effect, *isolated*) particles, chapter 4.

There exists an intermediate regime where the separation between particles and their arrangement are such that radiative coupling can occur between a large number of particles, leading to a very different modification to the LSPR. Of particular interest here is the regime where the particles are separated by an average distance that is approximately equal to the wavelength of the light that propagates in the surrounding medium. In 1- or 2-dimensional ordered arrays of such particles, a delocalised surface mode can develop that couples together particles over large distances. Applications in nanoscale waveguides [3, 4], sensing [5], and slow light [4, 6, 7] have been envisaged.

In this chapter, I will consider this regime of large-scale coupling in two-dimensional, regular square arrays of nanoparticles. A typical scanning electron micrograph of such a sample is shown in figure 6.1.

Light incident on such system is scattered by the particles in all directions. Of particular interest here is the light that is scattered so as to propagate in the plane of the particles. Such light will

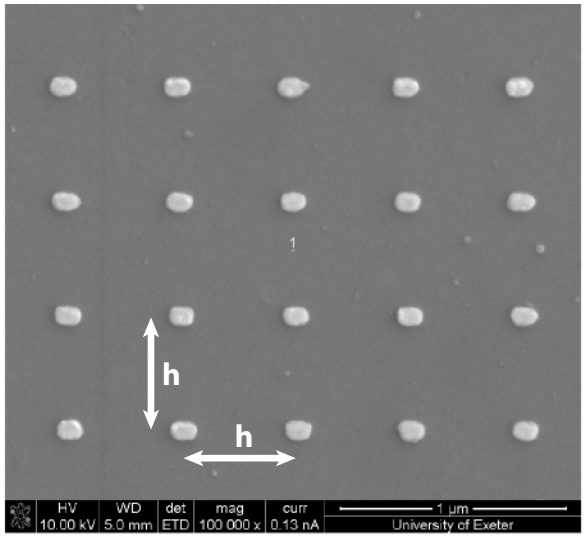

Figure 6.1: Scanning Electron Micrograph of the central region of a typical array. The pitch h of the array (in this case 500 nm) is indicated.

undergo multiple scattering by the regularly spaced particles. A geometric resonance can arise when the wavelength of the scattered light is commensurate with the periodicity of the array, which, when it occurs in the same spectral range as the LSPR, can lead to a dramatic modification of the measured optical extinction. This coupling regime is very different to the one discussed for a dimer of dipoles situated in the near-field zone. Here the interaction between particles occurs over large distances and couples a large number of particles. A particularly interesting consequence of this regime of particle interactions is the formation of a sharp spectral feature near the diffraction edge, in contrast to the broadening observed in the near-field coupling regime. It appears that this effect was first predicted by Wokaun and coworkers (see for example [8]) and Markel [9, 10] and more recently followed up by Schatz and co-workers [11]. Further theoretical/computational work by these groups has extended our understanding [3, 9, 10, 12–16], and a tutorial review linking these concepts to those associated with hole arrays has recently been given [17].

Previous experiments to confirm the existence of these sharp diffractive features in the optical response of metallic nanoparticle arrays met with only limited success. Haynes *et al.* [18], Hicks *et al.* [19], Sung *et al.* [20] and Lamprecht *et al.* [21] performed detailed studies of arrays of gold and silver nanoparticles, but the effect was not as pronounced as expected from the modelling. In each case, failure to observe the sharp spectral features appears to be due to one or more of the following factors: lack of an homogeneous environment, an angle spread of the illumination, an inappropriate choice of the particle volume and aspect ratio. Félidj *et al.* [22] reported sharp features in a system consisting of a regular array of gold nanorods supported on a thin indium tin oxide (ITO) layer. However the presence of the ITO layer complicates the analysis and makes the underlying physics harder to unravel: such a system leads to a rich physics when the ITO is thick enough to support waveguide modes that interact with the LSPR [23, 24]. In this chapter I report measurements from regular arrays of gold nanorods that exhibit the expected sharp peaks in extinction. I also explore the role of array period and surrounding index on the spectral lineshape.

6.1 Radiative coupling

The interaction of incident light with an array of particles as shown in figure 6.1 is depicted in the schematic view of figure 6.2. For simplicity light is considered incident on the array of particles at normal incidence. The probability of interaction of the light with each particle is described by the scattering cross-section of the nanorods, which is typically much larger than their geometrical occupancy when the wavelength is in the range of excitation of the LSPR. The remaining part of the incident light is transmitted through the substrate. The light that is scattered by the particles

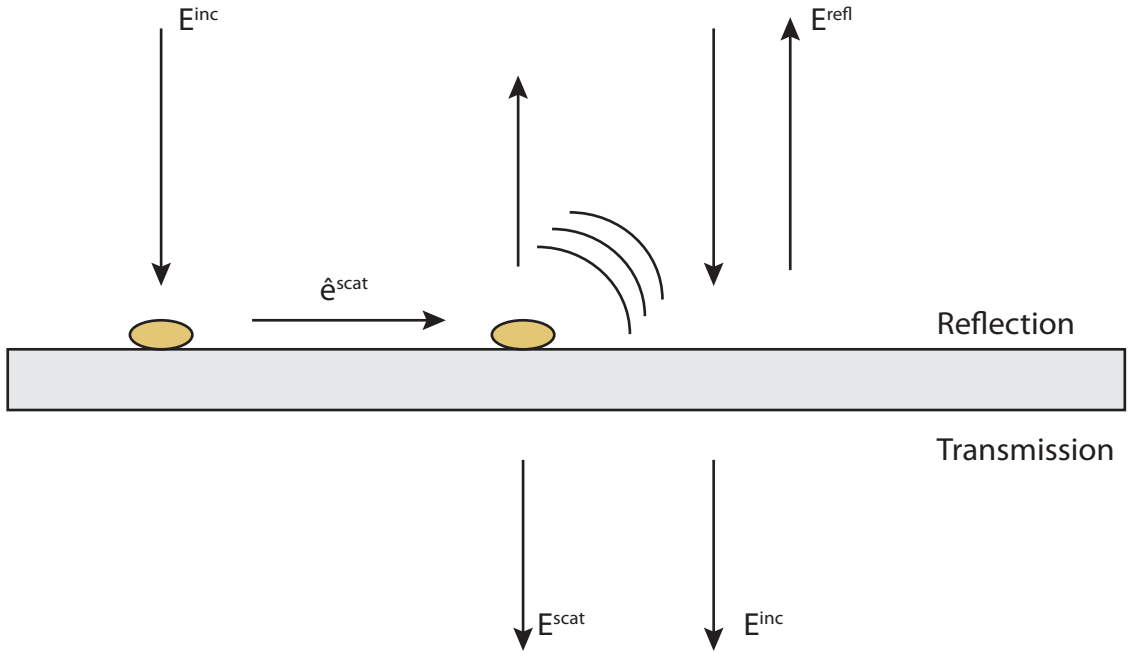

Figure 6.2: Schematic of the multiple scattering process.

arranged in a periodic structure will produce an interference pattern that is associated with diffraction. In fact, such a periodic structure can be described as a diffraction grating. For wavelengths of the light that are a multiple of the particle separation, the scattered light interferes constructively. The far-field radiation pattern is formed by a succession of fringes that correspond to the spatial Fourier components of the scattering sample [25]. In particular, for wavelengths shorter than the separation between particles a first order of diffraction emerges from the sample in the forward direction, and moves closer to the normal as the ratio separation / wavelength is increased.

In the first decade of the 20th century, Wood [26, 27] and Rayleigh [28] observed the peculiar response of such metallic gratings when this diffraction condition is occurring at a *grazing angle*. A succession of a bright and dark band was observed in the transmission of such structures which were referred to as *Wood's anomalies*. The explanation for this phenomenon was given by Fano [29] who described the excitation of a surface mode at the wavelength corresponding to the Rayleigh *cut-off* of the grating. This surface mode was recognised as a surface-plasmon propagating on the grating surface.

In the situation considered here, the grating is formed by nanoparticles that are isolated from each other by a non-conducting substrate, but the existence of a surface mode can be attributed to a

polarisation current that couples together the different scatterers and propagates into the dielectric medium. Light that is scattered so as to propagate at a grazing angle can undergo multiple scattering — instead of considering only individual scattering events from the particles in isolation, we need to consider a delocalised surface mode of the structure as a whole. This surface mode can re-couple to radiation on both sides of the interface. It is the interference between this scattered light and the direct transmission that is measured as extinction. Similarly, the reflection of light by the sample will contain the interference between this scattered light and the light that is reflected by the interface (with an additional π-phase shift upon reflection in a generally asymmetric (air/dielectric) configuration).

The resonance exhibited by such a sample involves an interplay between the excitation of plasmons localised on the particles, and diffraction resulting from the scattering by the periodic arrangement of these particles. A simple coupled dipole model can be used to obtain a semi-analytical description of the effect, revealing the origin of the main features in the observed spectral lineshape.

6.1.1 Coupled dipole model

In chapter 5, the coupled dipole approximation was introduced as a simple modelling tool to describe the optical response of a pair of interacting, well-separated, sub-wavelength particles. This procedure can be generalised to an arbitrary number of particles and is closely related to the Discrete Dipole Approximation (DDA), a numerical technique that is commonly employed to model the scattering properties of a single, connected scatterer. In the DDA, a 'dipole' corresponds to a mathematical construction and represents a virtual polarisable unit that is *part of* a larger scattering body. The prescription for the polarizability is obtained in the DDA from the Lorentz-Lorenz formula that describes the refractive index of the bulk medium. This simple prescription violates the conservation of energy as expressed in the optical theorem [30]. Several corrections have been suggested, the most widely used being the Lattice Dispersion Relation (LDR) which is obtained by considering the effective dielectric function of an infinite cubic lattice of dipoles [30].

In the coupled dipole approximation (CDA) for collections of subwavelength particles, however, a dipole has a more direct physical interpretation: it approximates the optical response of one scatterer. To be accurate, the CDA requires that the particles are sufficiently small compared to the wavelength, as discussed in chapter 3. A prescription for the polarizability of such dipoles needs to consider the influence of the size and shape of the particle, where the Lorentz-Lorenz polarizability only considered an isotropic unit cell. Further, to account for the dynamic depolarisation and radiative damping, corrections to the static polarizability need to be introduced to obtain a realistic approximation of the individual particle scattering properties in the dipolar approximation (see section 3.2.2). In this section I will show how the salient properties of diffractive coupling in arrays of nanorods can be understood by using a further simplification of the CDA, which assumes an infinite array of dipoles excited at normal incidence.

The nanorods studied in this chapter are described as ellipsoids (semi-axes a, b, and c, volume V), for which the static polarizability can be written as [31],

$$\alpha^{\text{static}} = abc\frac{\varepsilon_m - \varepsilon_d}{3\varepsilon_d + 3\mathrm{L}(\varepsilon_m - \varepsilon_d)}, \tag{6.1}$$

with ε_m and ε_d the relative permittivities of the metal and surrounding medium respectively, L is a shape factor given by equation 3.24.

When the particle size is of order 50 nm or more, this expression needs to be modified to account for dynamic depolarisation and radiative damping, a generalisation known as the modified long wavelength approximation (MLWA) [18]. This is done by introducing an effective polarizability α^{mlwa},

$$\alpha^{\text{mlwa}} = \frac{\alpha^{\text{static}}}{1 - \frac{2}{3} i k^3 \alpha^{\text{static}} - \frac{k^2}{a} \alpha^{\text{static}}}, \tag{6.2}$$

$k = n k_0$ being the wavenumber in the (homogeneous) surrounding medium which has refractive index n. When excited by an electromagnetic wave at frequency ω, a dipole re-radiates a scattered wave in proportion to its dipole moment. The net field on every dipole is therefore the sum of the incident field, plus the radiation from all other dipoles, which leads to a system of coupled equations to be solved self-consistently for the total field.

6.1.1.1 Semi-analytical formulation for normal incidence

Assuming an infinite array, the general solution can be expressed as an effective polarizability α^* for every (indistinguishable) particle,

$$\alpha^* = \frac{1}{1/\alpha - S}, \tag{6.3}$$

where the array factor S embraces the contribution from the other dipoles, and is only dependent on geometrical parameters. In the case of normal incidence, and for a square array of dipoles, this factor is

$$S = \sum_{\text{other dipoles}} \left[\frac{(1 - i k r)(3\cos^2\theta - 1)\exp(i k r)}{r^3} + \frac{k^2 \sin^2\theta \exp(i k r)}{r} \right], \tag{6.4}$$

θ being the in-plane angle between the dipole locations. The effective polarizability 6.3 is formally identical to the one obtained in chapter 5 for a pair of dipoles — we therefore understand the array factor S to be responsible for a splitting of the LSPR due to the interaction between multiple scatterers. The coupling between the dipoles results in a hybrid, delocalised surface mode.

The poles of the effective polarizability define the resonances of this hybrid mode [10], and result from an interplay between the particle properties and the geometrical array factor. The array factor is a complex number, and in appendix A a derivation is proposed for the introduction of an effective polarizability of the form 6.3 with the following conclusions,

- the real part of S induces a shift of the resonance frequency (blue shift for $\Re(S) < 0$, red-shift for $\Re(S) > 0$)
- the imaginary part of S modifies the resonance width ($\Im(S) < 0$ results in a broadening of the resonance, while $\Im(S) > 0$ reduces the width).

The possibility of partial cancellation of the radiative damping was soon recognised (see for example [13]), and triggered a renewed interest in the study of such periodic structures. The LSPR

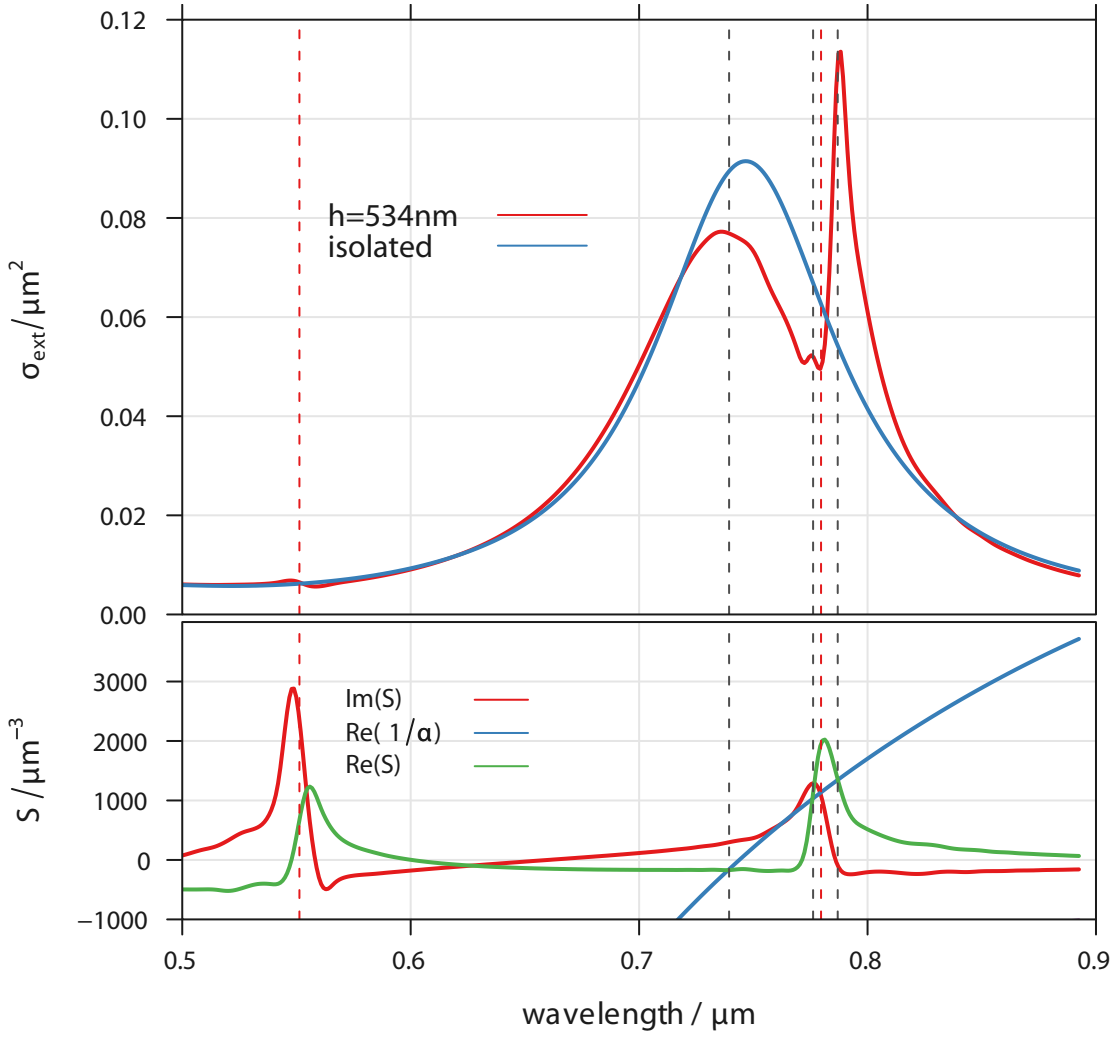

Figure 6.3: (Top graph) Blue curve: calculated isolated particle extinction cross section for an ellipsoidal particle (semi-axes: $a = 60\,\text{nm}$, $b = 40\,\text{nm}$, $c = 15\,\text{nm}$, surrounding medium: $n = 1.46$, incident light polarised along a). Red curve: same particle in an array. (Bottom graph) Corresponding calculated array factor (real and imaginary part). The finite number of dipoles (400×400) creates spurious fast oscillations in the array factor S, which were smoothed before insertion in equation 6.4 (continuous lines).

supported by isolated gold nanoparticles has a low quality factor ($Q \sim 10$, see chapter 4) and this limits the range of applicability in subwavelength plasmonic waveguides, surface-enhanced spectroscopies, *etc.* It is therefore of great interest to observe the reduction of the damping in plasmonic structures and try to overcome the limitations of the LSPR width that were discussed in chapter 4.

The optical extinction cross-section σ_{ext} is obtained from the polarizability using the optical theorem (equation 3.14) [12, 31],

$$\sigma_{\text{ext}} = k\Im(\alpha). \tag{6.5}$$

Using this simple approach will help us to understand the nature of the hybrid mode and predict qualitatively the spectral features observed in the experiments. Figure 6.3 presents an example of

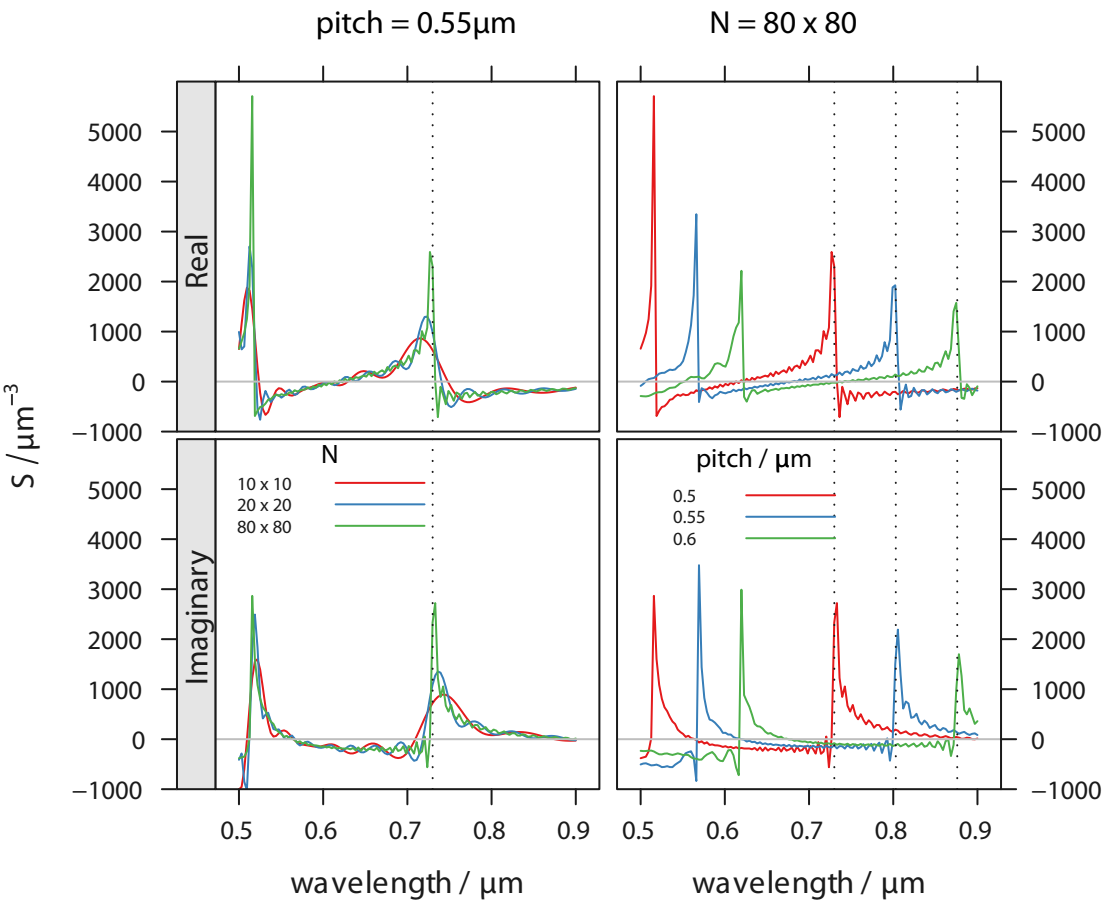

Figure 6.4: Numerical calculation of the real and imaginary parts of the S factor (equation 6.4). (Left) Varying the number of dipoles for a given dipole separation (0.55 µm); (Right) Varying the separation for a fixed number of dipoles (80×80).

this calculation for an isolated gold ellipsoid, and for the situation when the ellipsoid is part of a periodic square array.

Several features may be noted. i) A peak in the extinction curve (upper panel) is obtained when the real part of $(1/\alpha - S)$ vanishes in equation 6.3 [10]. These crossing points are shown by dashed grey lines. ii) The jumps in both the real and imaginary part of S (lower panel) are associated with diffraction: the two vertical dashed red lines indicate the position of the $< 1,0 >$ and $< 1,1 >$ diffraction edges for this square grating. iii) The intensity of the resulting extinction peaks (upper panel) depends on the imaginary part of S at this wavelength, and the width will also depend on the slope of both $1/\alpha$ and the real part of S [17]: a sharp crossing point indicates that the range of wavelengths for which the effective polarizability diverges is narrow. A set of array factors is shown in figure 6.4 for three different periodicities and an increasing number of dipoles in the numerical evaluation of equation 6.4. As the number of dipoles increases the divergence of the array factor at the wavelength corresponding to the diffraction condition is more pronounced and sharper.

It is interesting to note the influence of the particle size and shape on the radiative coupling as described by the array factor: for particles with small polarizability such as small dielectric spheres, $1/\alpha$ is large, therefore the crossing points with the array factor will occur for an narrow

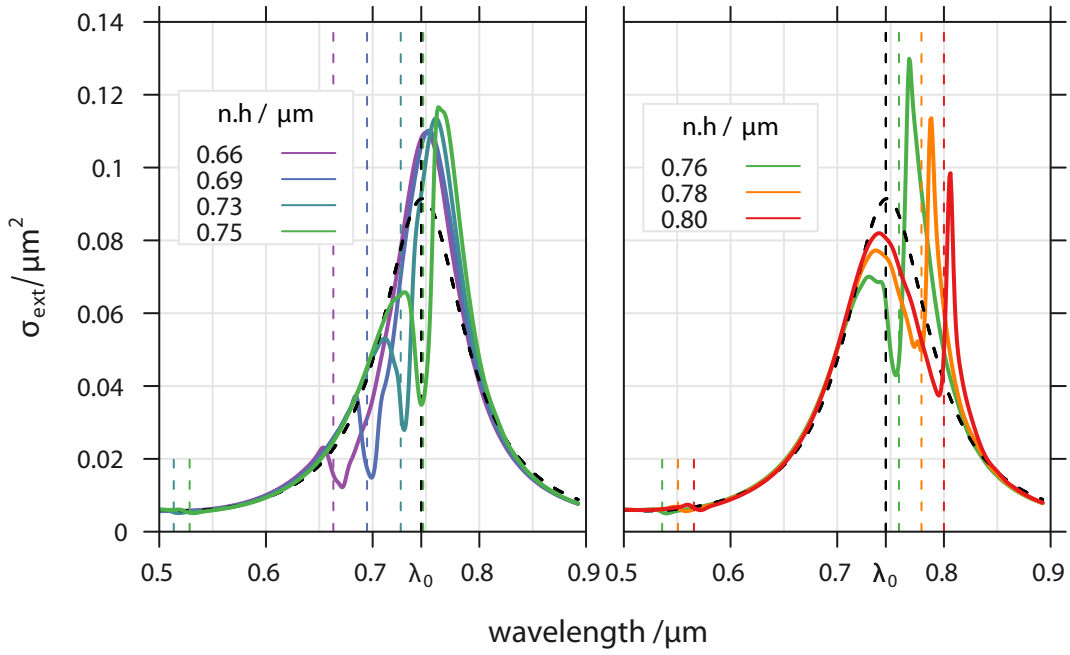

Figure 6.5: Calculated extinction spectra from a coupled dipole model, with varying dipole separation. The dipole represents an ellipsoid of semi-axes 60 nm×40 nm×15 nm in surrounding index 1.46. The pitch values, h, are 454 nm, 476 nm, 497 nm, and 512 nm for the curves in the left panel, and 519 nm, 534 nm, 548 nm for the curves in the right panel.

wavelength range (the peak in the S factor becomes extremely sharp), and may not be detectable. Markel [10] predicted this effect theoretically with an analytical study of the divergence properties of the coupled dipole model at the diffraction condition, the predicted resonance widths being as narrow as less than a nanometer.

Using gold particles of large volume and / or aspect ratio, the inverse polarizability can be scaled down to the regime where the S factor presents a less pronounced slope.

Figure 6.5 shows the effect of pitch variation on the resulting extinction spectra, and reveals two different regimes.

When the diffraction edge is on the high-energy side of the main localised surface plasmon resonance ($nh < \lambda_0$), little radiative coupling can occur as the allowed diffracted orders are all of higher energy than the plasmon resonance. The blue curves show the effect of pitch variation in this regime, the spectra show a Fano type shape resulting from interference between directly transmitted light and light scattered by the array. Notice also that the main resonance is sharpened, red-shifted, and enhanced with respect to the isolated LSPR. In the other regime, when the diffraction edge is on the low-energy side of the main resonance ($nh > \lambda_0$, red curves), a very sharp and intense peak is found in the long wavelength tail of the main resonance, its intensity and width decrease for peak positions further from the main resonance.

6.2 Extinction measurements

The samples were produced by electron beam lithography (EBL) on fused silica substrates ($n = 1.46$). A 100 nm thick layer of PMMA resist was spin coated on the substrates, with a 15 nm thick gold over-layer deposited by thermal evaporation to ensure the electrical conductivity required for the EBL exposure. The spatial extent of the arrays was limited to 35 µm × 35 µm to minimize the shape variation due to beam distortion at the edges of the available electron-beam write-field (50 µm × 50 µm). Particle sizes were in the range 50 nm to 120 nm with aspect ratios ranging from 1:1 to 2:1. This spread of sizes was dictated by three parameters: i) the spectral range of our acquisition system (400 nm — 900 nm), ii) the requirement that only the dipolar mode contributes substantially to the optical response of the particles, iii) smaller particles have resonances that suffer from strong absorption by the gold and consequently scatter little light. After developing the exposed resist mask, a 2 nm chromium adhesion layer was deposited by thermal evaporation, followed by a 35 nm thick gold layer (99.99 % purity, pressure 2×10^{-6} Torr). This very thin layer of chromium was found not to alter noticeably the LSPR. Finally, the resist layer is dissolved in acetone until only the nanoparticles in contact with the glass are left on the substrate.

The in-plane particle geometries were measured by scanning electron microscopy (SEM), and the particle height measured by a calibrated crystal monitor during the deposition, and cross-checked against a tilted SEM image.

The optical characterisation of the sample was undertaken using bright-field transmission spectroscopy at normal incidence (angular spread $< 0.1°$), using a 10x objective for the collection optics (figure 5.7). A polariser was used in the illumination path to selectively probe the short- and long-axis resonance of the nanoparticles.

6.2.1 Effect of pitch variation

The experimental data were processed as follows. First, the transmittance spectra for different particle separations were scaled to account for the fact that a different number of particles contribute to the extinction, the relevant factor is the occupancy (inverse pitch squared). Second, as the transmittance per particle has little physical meaning, it was converted into an extinction cross-section, related to the measured transmittance T by $\sigma_{\text{ext}} = h^2 \cdot (1 - T)$.

The results are plotted in figure 6.6, and show all the features expected from the coupled dipole model (compare with figure 6.5). As the periodicity is varied, an interference pattern sweeps through a broad resonance (the 'isolated localised plasmon resonance' with a typical width of ~ 100 nm, centred at ~ 710 nm). More specifically, we observe the existence of a sharp and intense extinction peak on the low energy side of the diffraction edge when the diffraction edge is on the red-wing of the LSPR. The spectral position of this peak exhibits a clear correlation with the array period, and I will therefore refer to it as a 'diffractive peak'. A drop in extinction is also noticeable around the diffraction edge with respect to the singe particle response, with a small secondary peak present near the diffraction edge (figure 6.6 (b)). Félidj *et al.* observed something similar [22], but for a sample where the particles were supported on a thin ITO layer. Our observation in the absence of index asymmetry suggests that the additional minimum cannot be explained by the ex-

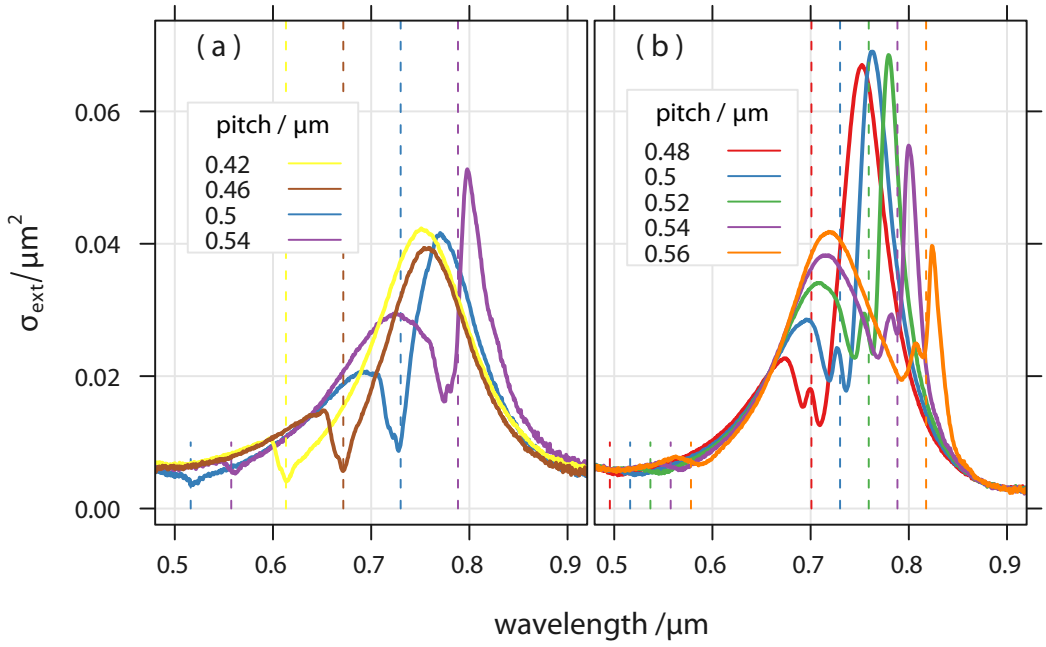

Figure 6.6: Extinction spectra (per particle) for several gold nanoparticle arrays. (a) Average particle size: 123 nm×85 nm×35 nm. (b) nominal particle size: 120 nm×90 nm× 35 nm. The particles are in a symmetric refractive index environment (oil immersion, $n = 1.46$).

istence of two different values of the surrounding refractive index, as suggested in [22]. To further support this argument, we note that the relationship between the two minima and the diffraction edge changes as the diffraction edge sweeps through the particle resonance. In chapter 7 further evidence is presented that this secondary peak is in fact due to the incident light being slightly off normal incidence.

Another interesting feature observed in figure 6.6 is the strong suppression of extinction when the diffraction edge is on the high energy side of the LSPR (figure 6.6 (a)), *i.e.* the array becomes almost transparent to the light.

Finally, the area under the normalised extinction curves appears to be almost constant for identical particle sizes but different particle separations. This finding will be further investigated in connection with a sum rule for extinction in chapter 7.

In the next section I will present the evolution of the extinction spectrum of such arrays of particles when the surrounding environment presents an asymmetry in refractive index.

6.2.2 Surrounding medium

The sharpness of the spectral feature promised from the modelling depicted above has attracted attention for applications such as biosensing and nonlinear spectroscopies. The relatively low quality factor exhibited by LSPRs is indeed a practical limitation to the applicability of gold nanoparticles in these and other applications. For a sensing application, two other key factors are to be considered: the relative shift of the resonance position with respect to a change of the bulk environment ; the relative shift of the resonance due to a thin (sub-wavelength) coating. In the remainder of this chapter

I will assess the influence of the refractive index of the superstrate medium in such diffractive arrays of nanoparticles.

6.2.2.1 Bulk change of refractive index environment

The response of such arrays in an asymmetric refractive index environment was investigated experimentally by using the setup of figure 5.7 with the particles being immersed in various fluids. Such data is presented in figure 6.7, where the extinction spectra are plotted for two different sets of arrays of varying particle separations.

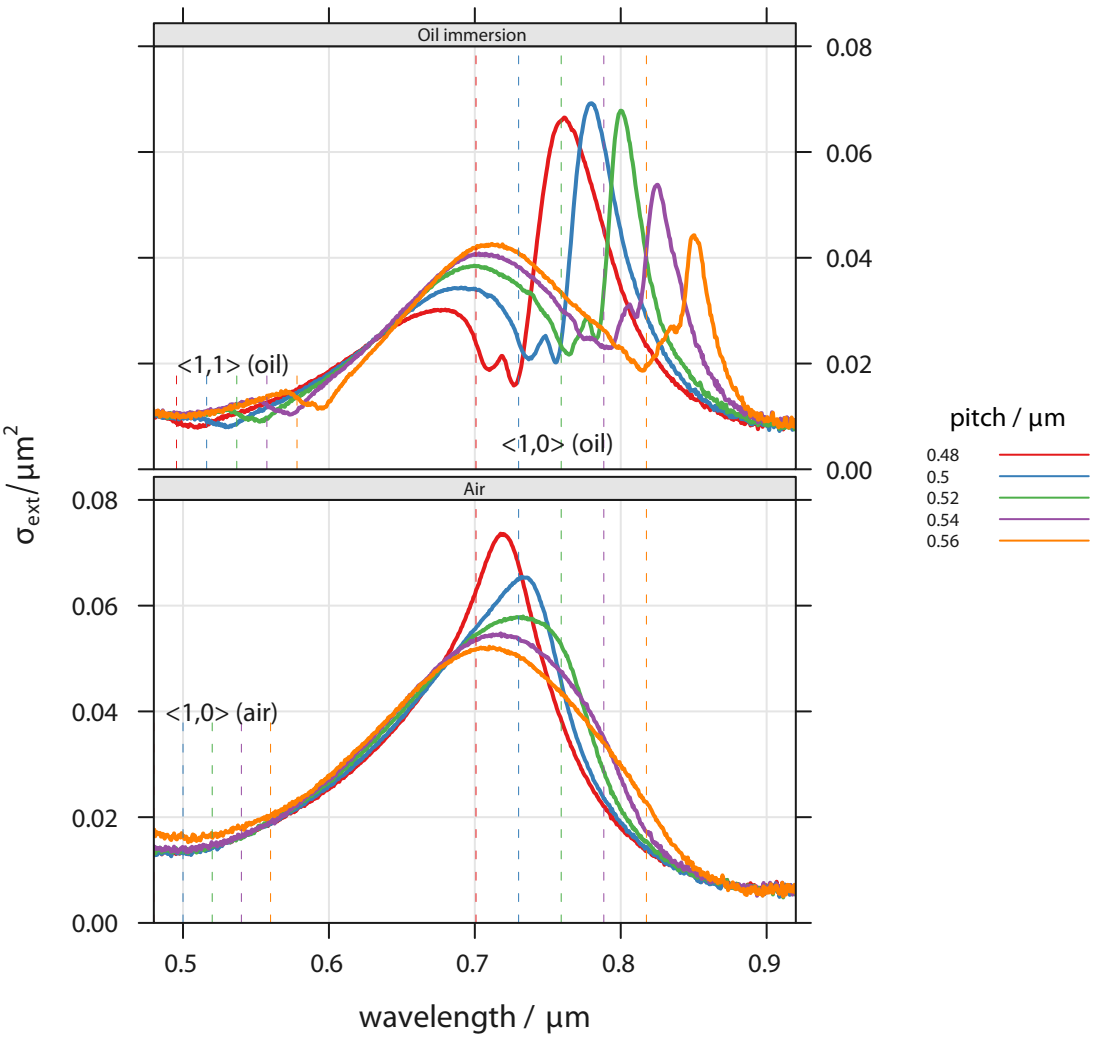

Figure 6.7: Extinction spectra for gold nanorod arrays in an homogeneous index environment (top, oil immersion n=1.46) and asymmetric refractive index configuration (bottom, incident light in air), for five particle separations. Nominal particle sizes: 100 nm×90 nm×35 nm (Top), 120 nm×90 nm×35 nm (Bottom). The vertical lines indicate the position of the $< 1,0 >$ and $< 1,1 >$ diffraction edges for the two refractive index environment configurations.

The particle sizes were chosen so as to provide similar LSPR spectral positions in air (bottom panel) and in the homogeneous index (top panel). The asymmetry between substrate and superstrate strongly hinders the radiative coupling effect between particles and the results we observe in the bottom panel are very similar to the results from previous experimental studies [21, 32]: a strong asymmetry in the spectral lineshape, but without the presence of a sharp spectral feature near the diffraction edge.

In figure 6.8 the superstrate medium is varied from air (red curves) to isopropanol (blue curves) (IPA, $n = 1.378$), to immersion oil (green curves) ($n = 1.46$) for 5 arrays of nominally identical particles but different separations. The substrate is fused silica ($n = 1.46$). Only the symmetric configuration leads to a strong, Fano-type modification of the LSPR lineshape with clear constructive and destructive interference on either side of the diffraction edge. In the asymmetric configurations, the lineshape is still modified from the LSPR response, but no sharp spectral feature is apparent. Of particular interest in these spectra is the modification of the resonance width occurring as a result of collective radiative coupling. The narrow resonance obtained for the array of 480 nm periodicity with either air or IPA superstrate medium is an interesting result in this regard.

The extinction spectrum for the array of 480 nm periodicity in IPA was fitted with a Lorentzian to estimate the width of the LSPR (54 nm). This resonance is considerably narrower than what would be expected from a non-interacting collection of such nanoparticles where inhomogeneous broadening is quite severe (see figure 5.11). In fact, the resonance width is found to be close to the value dictated by the gold permittivity alone at this frequency (intrinsic damping, discussed in chapter 4) as shown in figure 6.9. This narrowing of the LSPR in a collection of particles means that the effect of radiative damping and inhomogeneous broadening are largely suppressed. The interparticle coupling and its effect on the width of the LSPR was studied for dimers of gold particles by [34, 35], where it was found that the resonance width oscillates as a function of particle separation. This is due to the fact that the phase relationship between the incident field and the field that is scattered by the neighbouring particle presents an alternate of constructive and destructive interference as a function of particle separation. When the dipolar field scattered by one particle contradicts the incident field for the other particle, the radiation damping from that particle is reduced. Further, in the situation where an infinite number of particles participate in the field exciting each particle, there can be a situation where the field is completely suppressed in the particle — this is the situation of transparency observed at the diffraction edge where the extinction is largely suppressed (in theory, the extinction by an infinite array of dipoles vanishes at the Rayleigh condition).

6.2.2.2 Thin coating

A measure of the figure of merit of such nanostructures for a sensing application needs to take into account the high field confinement around the particles that stems from the excitation of localised surface plasmons. Therefore, it is necessary to try to differentiate between *bulk* effects and *local* effects in the spectral change observed in scattering or extinction measurements. Because the resonance that arises in these structures involves an interplay between the localised plasmon resonances and a purely geometrical diffractive coupling, it is not clear whether the sensitivity to a

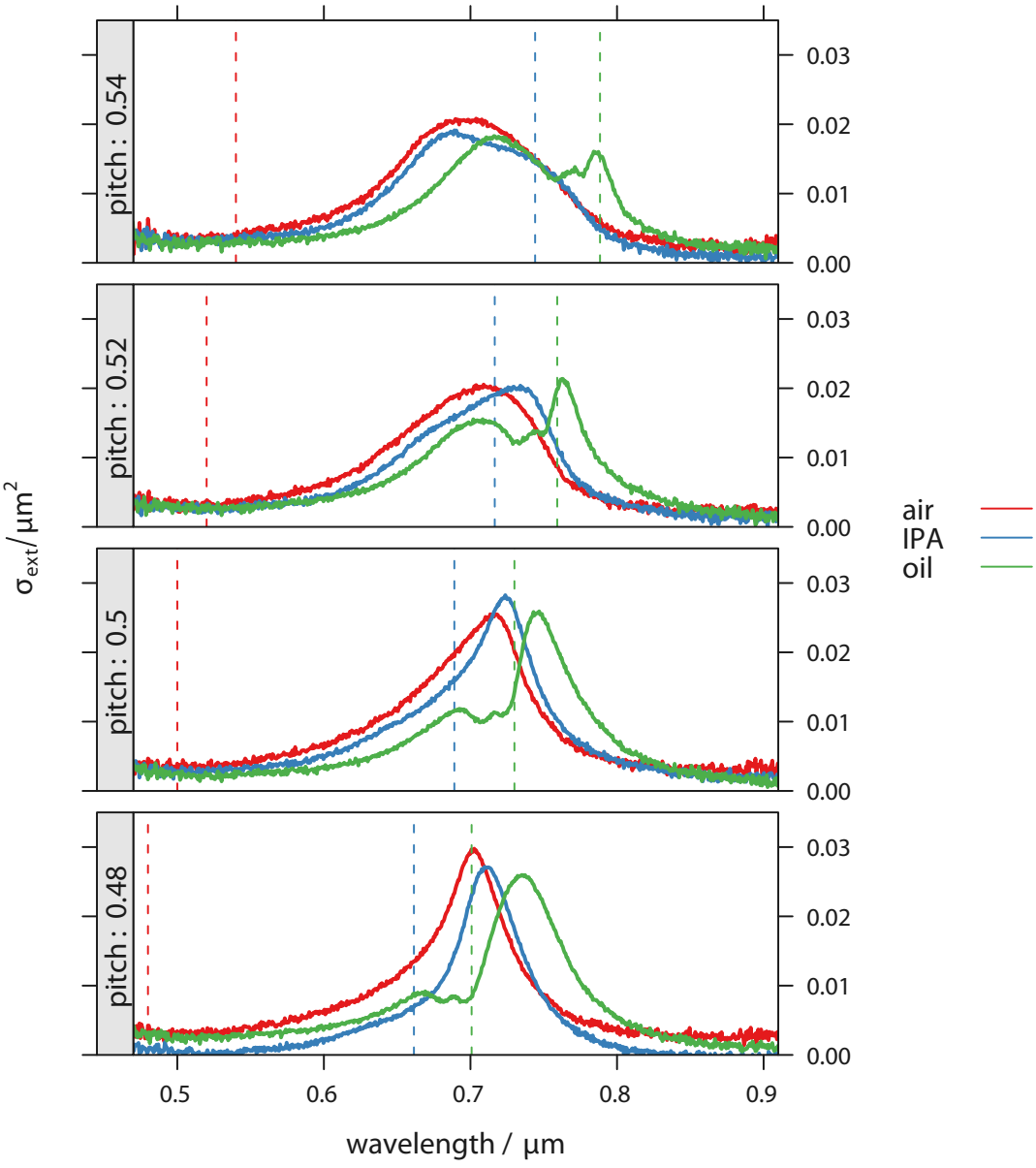

Figure 6.8: Effect of varying the superstrate index on the extinction spectra. The red, blue and green curves correspond to the case where the superstrate medium is respectively air, IPA ($n = 1.378$), immersion oil ($n = 1.46$). The different panels correspond to different particle separations (From top to bottom: 540 nm, 520 nm, 500 nm, 480 nm), and the vertical dashed lines indicate the diffraction condition in each medium.

local change will be more pronounced than for a single particle response, despite the considerable reduction in the spectral width previously discussed. To investigate this question I used the coupled dipole model as experiments aimed at assessing the sensitivity of the arrays to a thin coating have been hindered by the apparent requirement of a homogeneous surrounding medium. In order to describe the influence of a thin coating on the particle response in the coupled dipole model, I

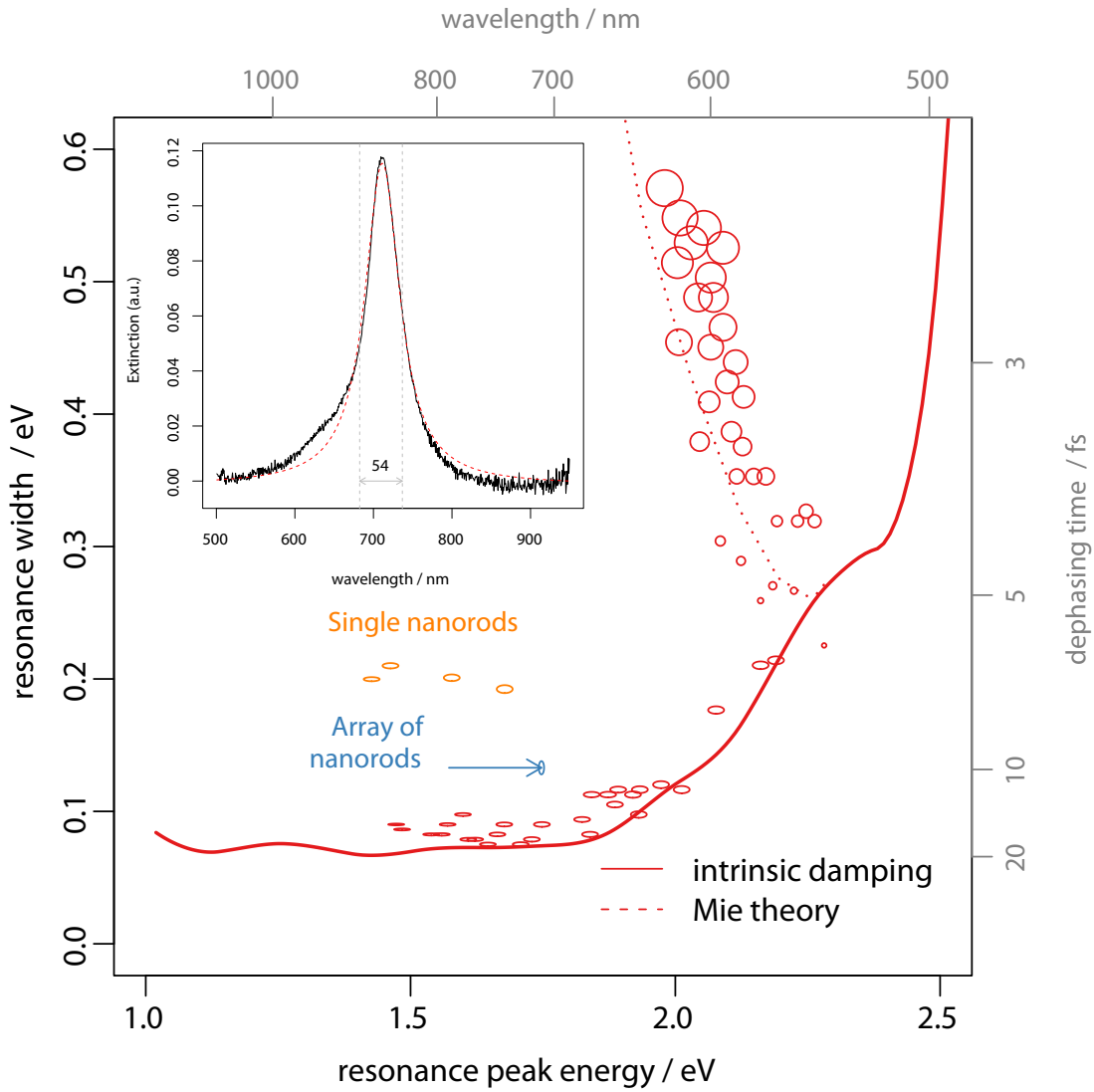

Figure 6.9: LSPR width in isolated particles and in ensembles. The solid line shows the calculated intrinsic damping (equation 4.3) for gold (permittivity values from Johnson and Christy). Note that the damping due to surface roughness is not taken into account. Red symbols are single particle measurements on colloidal nanorods and spheres from Sönnichsen *et al.* [33]. Orange ellipses are typical single particle dark-field scattering measurements from EBL-fabricated nanorods presented in chapter 4. The blue symbol is obtained from the extinction curve of the array of figure 6.8 (pitch 480 nm in IPA). Inset: Lorentzian fit of the resonance, the width is estimated as 54 nm.

used the polarizability as derived by Bohren and Huffman for a coated ellipsoid in the quasi-static approximation [31],

$$\alpha = V_2 \frac{(\varepsilon_c - \varepsilon_d)\left[\varepsilon_c + (\varepsilon_m - \varepsilon_c)(L_1 - fL_2)\right] + f\varepsilon_c(\varepsilon_m - \varepsilon_c)}{\left[\varepsilon_c + (\varepsilon_m - \varepsilon_c)(L_1 - fL_2)\right]\left[\varepsilon_d + L_2(\varepsilon_c - \varepsilon_d)\right] + fL_2\varepsilon_c(\varepsilon_m - \varepsilon_c)}, \tag{6.6}$$

where $\varepsilon_c, \varepsilon_d, \varepsilon_m$ are the permittivities of the coating, dielectric environment, and metal core respectively, $f = V_1/V_2$ is the ratio of the inner volume (V_1) and outer volume (V_2) of the two ellipsoids, L_1 and L_2 are their respective aspect ratio. The polarizability of equation 6.6 is modified

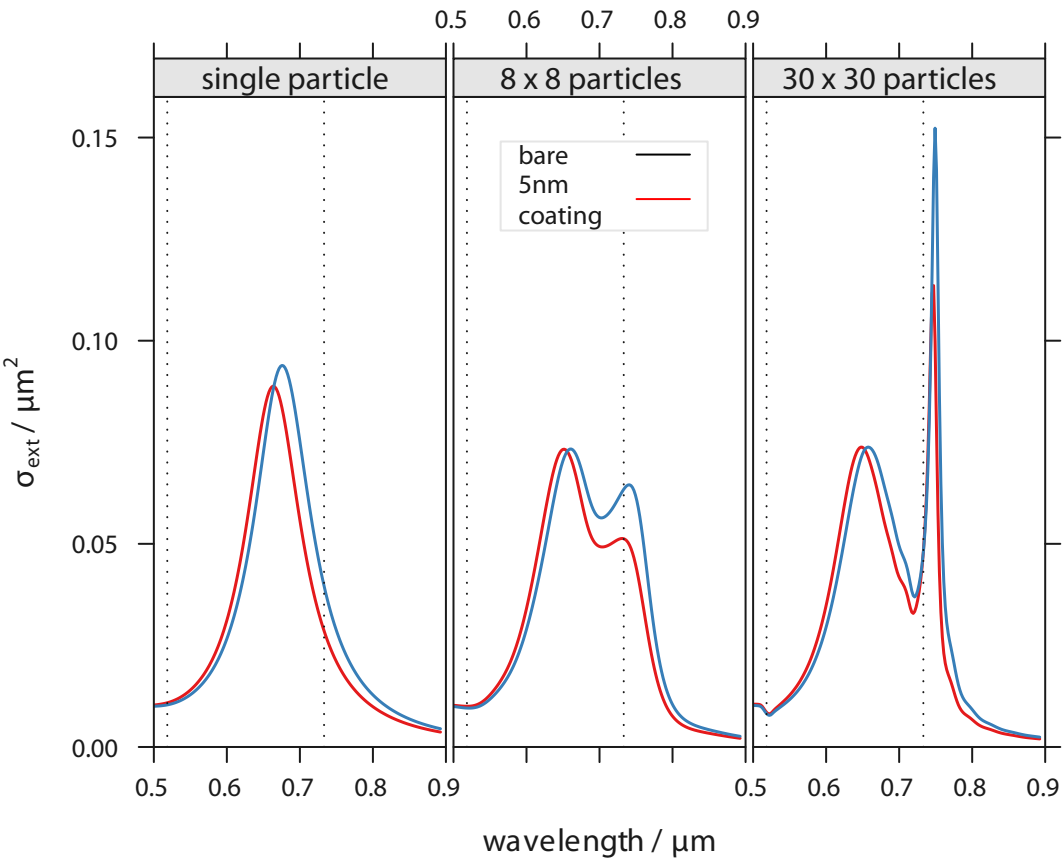

Figure 6.10: Coupled dipole model for the extinction spectra of particle arrays with particles coated with a thin overlayer. The surrounding environment is water, of refractive index 1.333. The left panel is for a single gold ellipsoid of semi-axes 60 nm×50 nm×20 nm. The middle and right panels are for regular, square arrays of respectively 8×8 and 30×30 dipoles, with a spacing between dipoles of 550 nm.

according to the long-wavelength approximation to take into account dynamic depolarisation and radiative damping (as discussed in section 3.2.1). Although less accurate than the prescription of Kuwata *et al.* [36], this expression for the polarizability allows us to approximate the effect of a thin coating on the particles whilst maintaining a reasonable agreement with more elaborate models (see figure 3.4).

Figure 6.10 presents extinction spectra calculated with this model for two different configurations: a bare gold ellipsoid in water (red), and the same particle with a 5 nm coating of refractive index 1.5 typical of biological samples [37] (blue curves). The three panels differ in the number of dipoles considered in the model: panel (a) is the result for a single dipole; panel (b) is the result for a regular array of 8×8 identical dipoles; panel (c) for 30×30 dipoles.

The left panel presents the red-shift of the LSPR when a thin overlayer is added to the bare gold particle. This red-shift is accompanied by an increase of scattering intensity as the scatterer gains in volume. The middle panel shows the modification of the resonance curve when the scattering sample consists of a regular square array of 8×8 particles separated by a distance of 550 nm. Here the interaction between dipoles results in a modification of the resonance spectrum near the diffraction edge associated with the periodicity of the scatterers. We note that the change of in-

tensity in the extinction curve upon addition of a thin coating is increased at the wavelength of the diffraction edge. The spectral shift is however not modified substantially. In the right panel the coupling is considered for and array of 30×30 dipoles. The diffractive peak is very intense (twice as intense as the extinction maximum for a single particle response), and narrow. The intensity change when adding a thin coating is appreciable, however the spectral shift of the diffractive peak is much smaller than the spectral shift of the main LSPR. From this calculation, it is apparent that the position of the diffraction edge with respect to the LSPR will have a strong influence on the intensity of the sharp extinction peak. This question is investigated in figure 6.11 by varying the dipole spacing, and observing the influence on the intensity and shift of the diffractive peak when adding successive overlayers.

As the diffraction edge is moved further from the LSPR, the spectral shift of the diffractive peak due to the presence of a thin layer is less and less important and the geometrical origin of the peak dominates (which is sensitive to a *bulk* refractive index change). The relative change of intensity of the peak seems mostly unaffected, although a more rigourous calculation should be performed to check the validity of the coupled dipole model in this regime. The absolute intensity of the diffractive peak is seen to vary in proportion to the single particle extinction at that wavelength, and is therefore weaker for wavelengths further from the main resonance. Inasmuch as the local sensitivity determines the performance of a sensor, we can conclude that a compromise should be found between the intensity of the diffractive peak, its width, and the shift in its spectral position due to the presence of a thin overlayer.

6.3 Conclusion and outlook of further investigations

In this chapter I presented experimental evidence for narrow spectral features in the optical response of periodic metal nanoparticle arrays, in contrast to the general broadening of the spectral response in dense ensembles of particles studied in chapter 5. In fact, the spectral width of the diffractive feature is found to be much narrower than the LSPR associated with a single, isolated nanoparticle (chapter 4). The periodic arrangement of nanorods introduces an interference feature close to the diffraction edge, and its position with respect to the localised plasmon resonance was varied by changing the particle separation. The technique of electron-beam lithography can be used with sufficient control over the particle positions and sizes for this long-range interaction between a large number of particles to be very pronounced. In chapter 8, I will present a study of the effect of disorder in particle positions and in particle sizes on the extinction properties of these diffractive arrays.

The influence of the refractive index of the environment of the nanoparticles was assessed by conducting experiments varying the bulk index of the superstrate. An asymmetric index configuration leads to a much less pronounced coupling between particles, which is in fact suppressed for moderate index contrast. The study of this transition behaviour should be the subject of further theoretical and experimental studies. In particular, the non-existence of a surface mode in the asymmetric configuration appears to be related to the Fresnel coefficient at the interface of the two media, for a grazing angle of incidence. Vecchi *et al.* [38] recently studied the dispersion properties

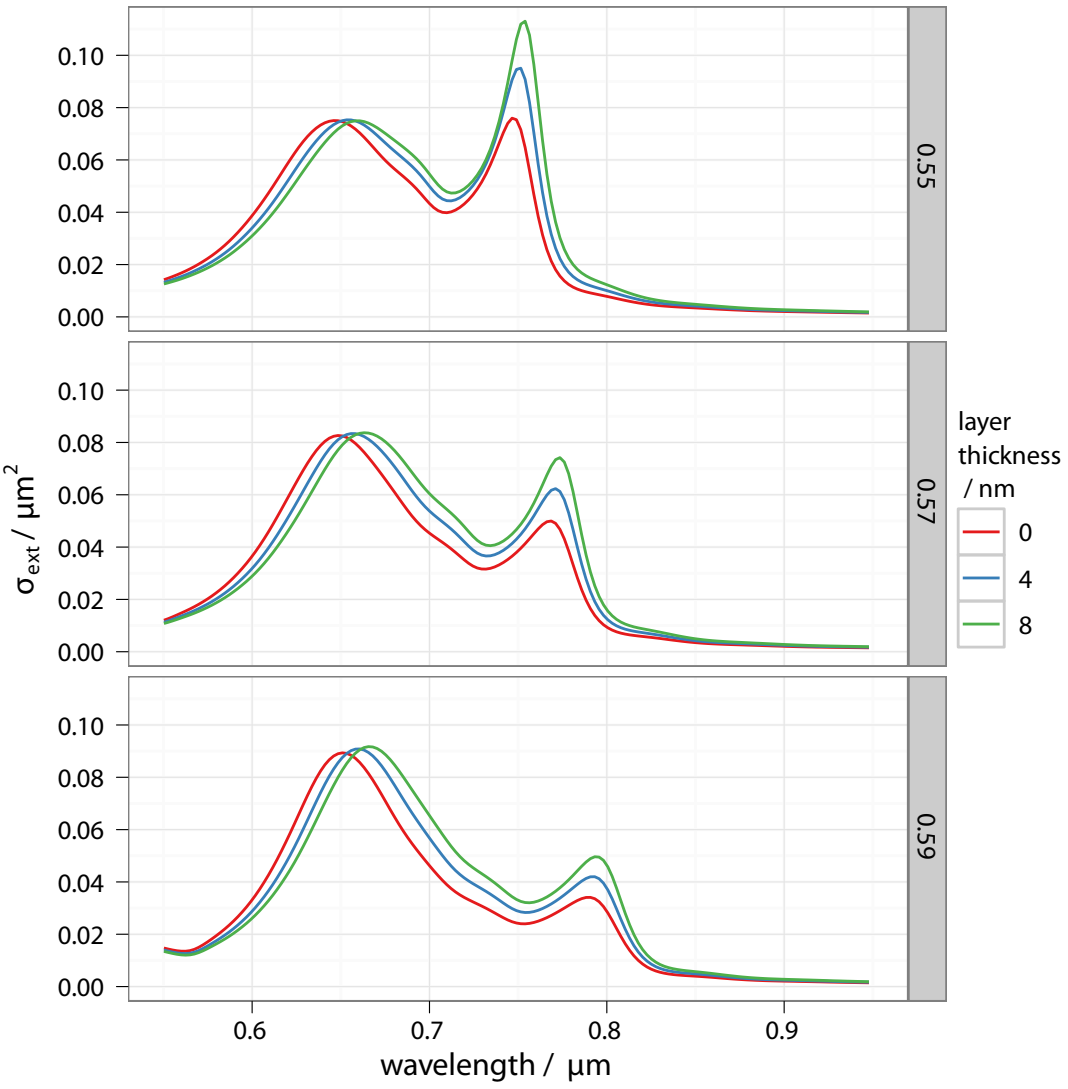

Figure 6.11: Coupled dipole model for the extinction spectra of particle arrays with particles coated with a thin overlayer. The arrays consist of 10×10 gold ellipsoids of semi-axes 60 nm×50 nm×20 nm immersed in water (index 1.333). Three periodicities are considered: 550 nm (top), 570 nm (middle), 590 nm (bottom). For each case, a coating of refractive index 1.5 is added to the particles with increasing thickness: bare particle (red curves), 4 nm (blue curves), 8 nm (green curves).

of the surface mode supported by such diffractive arrays, and found that the requirement of an homogeneous index configuration may not be as stringent as suggested by the experiments presented in this chapter, at least for a thin coating of the particles.

The sensitivity of the sample to a sub-wavelength coating was evaluated by numerical modelling. It was found that the diffractive arrays of gold nanoparticles may offer a general improvement over the single particle response in terms of signal-to-noise ratio, but at the expense of the spectral shift. It is however not yet demonstrated that such a sensing system can be realised within an asymmetric environment (a requirement for such supported particles). The discussion of the

optimal size of the nanoparticles for this diffractive coupling to be maximally efficient in terms of extinction intensity and sharpness of the observed spectral feature will be treated in chapter 7.

In this study we have developed a picture of the interaction between incident light and an array of particles that involves a multiple scattering process. In this view several questions would require further theoretical and experimental work. One of these questions relates to the coherence of the scattering process. The spatial and temporal coherence of the illumination should influence the coupling between particles since a collective coupling requires a coherent superposition of partial waves scattered from spatially separated sources. The phase relationship across the array should be maintained for the multiple scattering process to be efficient. In particular, for arrays of a very large extent, there may be a limitation of the long-range interaction due to a loss of coherence. The finite lifetime of the LSPR, and also the broadband illumination may both play a limiting role.

"But in space light is light and doesn't know where it came from."

Richard P. Feynman

7

Diffractive arrays of gold nanorods: a study of the spectral lineshape

The periodic arrangement of nanoparticles in a diffractive array was shown in chapter 6 to yield a dramatic modification of the optical response of gold nanorods when the periodicity is commensurate with the wavelength of excitation of localised plasmon resonances (LSPR). In the previous chapter, we observed the influence of the periodicity on this geometrical resonance, and how a sharp spectral feature can result from the coherent coupling of the particles. The intensity of this peak appeared to drop as the diffraction edge was moved away from the LSPR, for arrays of a given particle shape and size. It was also noted in chapter 6 that the area under the extinction curve (normalised by the occupancy) appears constant when changing the separation. An obvious question arises as to how the particle size and aspect ratio influence the integrated extinction, as well as the intensity and width of the sharp spectral feature.

In this chapter I will present further experiments and simulations on such regular arrays of nanoparticles that aim at a better understanding of the spectral lineshape. Experiments and simulations will be presented for particles of varying sizes that will clarify the role of the LSPR in the diffractive coupling. I will also investigate the dispersion of the modes by varying the angle of incidence, and show that the small secondary peak observed in chapter 6 was due to a slight misalignment of the optical setup. Finally, a sum rule for the integrated extinction of the particles will be discussed.

7.1 Influence of the particle shape and size

In studying the sharp spectral feature and its dependence on the different parameters, it is useful to de-correlate the effect of particle separation, particle volume, and particle aspect ratio. This study was performed using a wide spread of particle sizes.

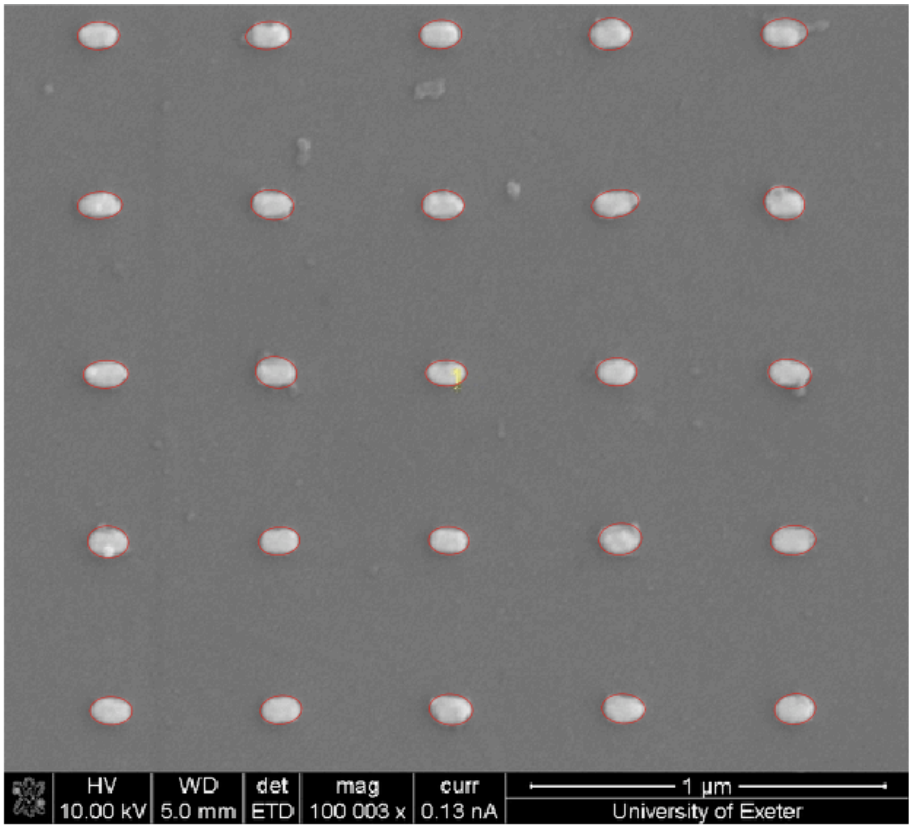

Figure 7.1: Scanning electron micrograph of an array. The particle separation for this particular array was 500 nm, the particle sizes measured for the 25 particles displayed here are 60 ± 3 nm$\times 40 \pm 3$ nm$\times 30 \pm 5$ nm.

The geometrical shapes were retrieved from scanning electron microscopy (SEM) measurements (figure 7.1). Twenty-five particles per array were scanned, and a shape recognition software, `imageJ`, was used to characterise their in-plane geometry with three parameters: the short and long axis of an ellipse, together with an estimate of the area. The height of the particles was estimated during the deposition process with a calibrated crystal monitor, and verified to be 30 ± 5 nm by a tilted SEM. This procedure allows us to describe each particle array with an ellipsoid of average axes a and b, together with an estimate of standard error on these parameters (typical fitted ellipses are shown in red in figure 7.1). The range of variation of the particle sizes is shown in figure 7.2. For this study, 60 arrays were characterised, with parameters the pitch varied from 480 nm to 560 nm, the short axis of the particles (four different nominal sizes from 60 nm to 120 nm), and the long axis of the particles (three different nominal sizes from 120 nm to 160 nm).

As shown in figure 7.2, the actual distribution of sizes vary considerably due to the sensitivity of the electron-beam lithography process. First, the particle shape and size differ from the nominal rectangular design, because of the limitations of resolution discussed in chapter 4 (sensitivity of the resist, exposure by secondary electrons, metal deposition, *etc.*). Second, we note that for a common value of the nominal size, the real size and shape differs for arrays of varying particle separations. This artefact of the fabrication process is attributed to the proximity effects in the exposure of the resist by the electron-beam (secondary electrons backscattered from the substrate contribute to

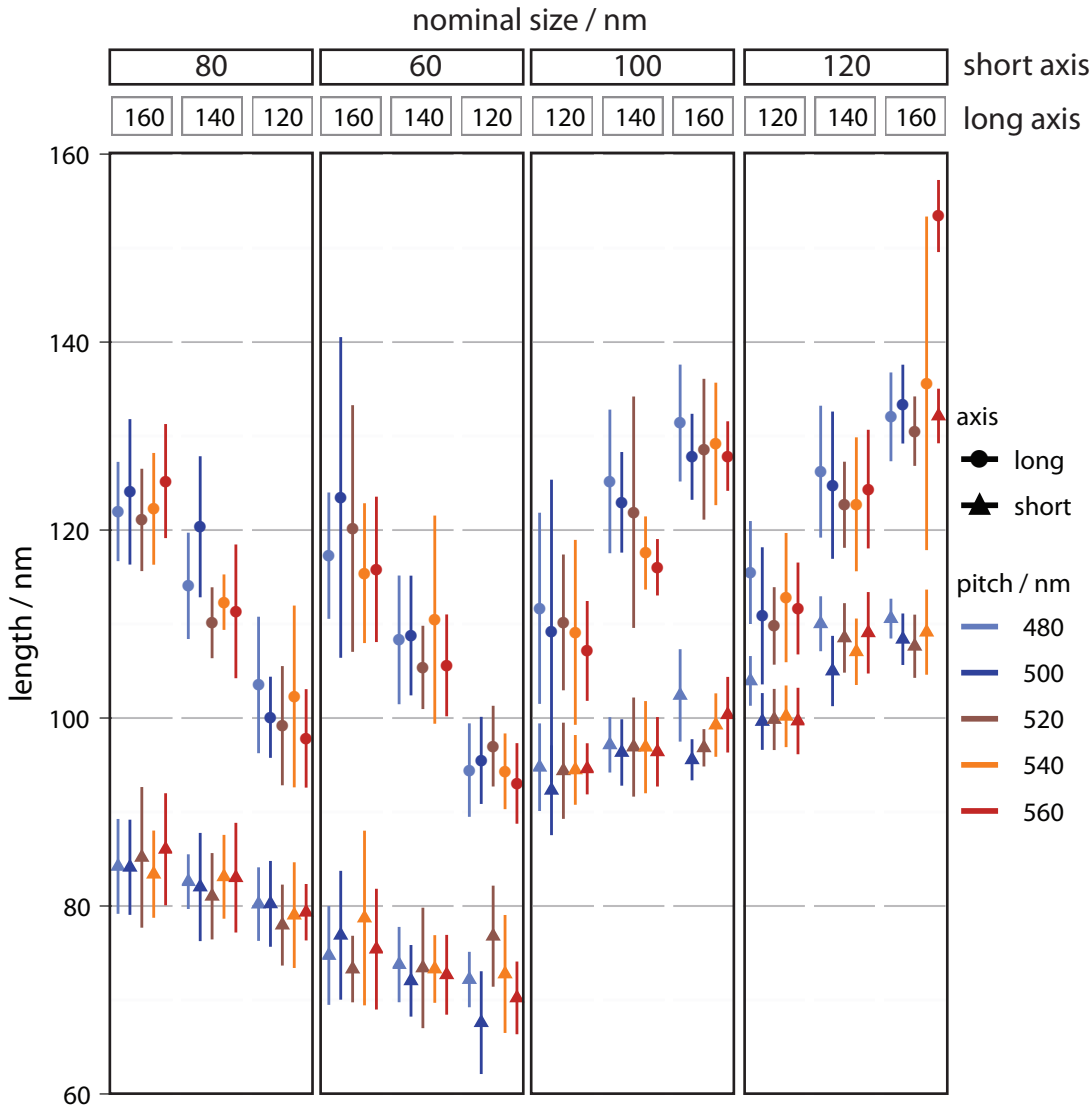

Figure 7.2: Average in-plane shape parameters retrieved from SEM measurements on 60 arrays, with error estimates considering the dispersion measured from 25 particles per array.

exposing the surrounding resist). Such effects can be partially corrected by a careful weighting of the exposure dose as a function of the array density. Finally, the dispersion of sizes within each array is considerable. Two major sources of such variation have been identified. (i) The electron-beam provides a non-uniform exposure across the write-field. This effect is limited by using a restricted part of the write-field (35 µm for a write-field of 50 µm). (ii) The granularity of the particles formed by thermal evaporation yields a variability of the shapes. By measuring 25 particles for each array I could estimate the average size of the particles and the distribution of the particles sizes for each array (this will prove especially useful for the experimental verification of the sum rule).

With such a range of particle sizes, I was able to compare the extinction spectra from two particles of different aspect ratio that had the same volume. The use of a polariser allows one to additionally compare the two in-plane axes for a given particle. The comparison is shown in figure

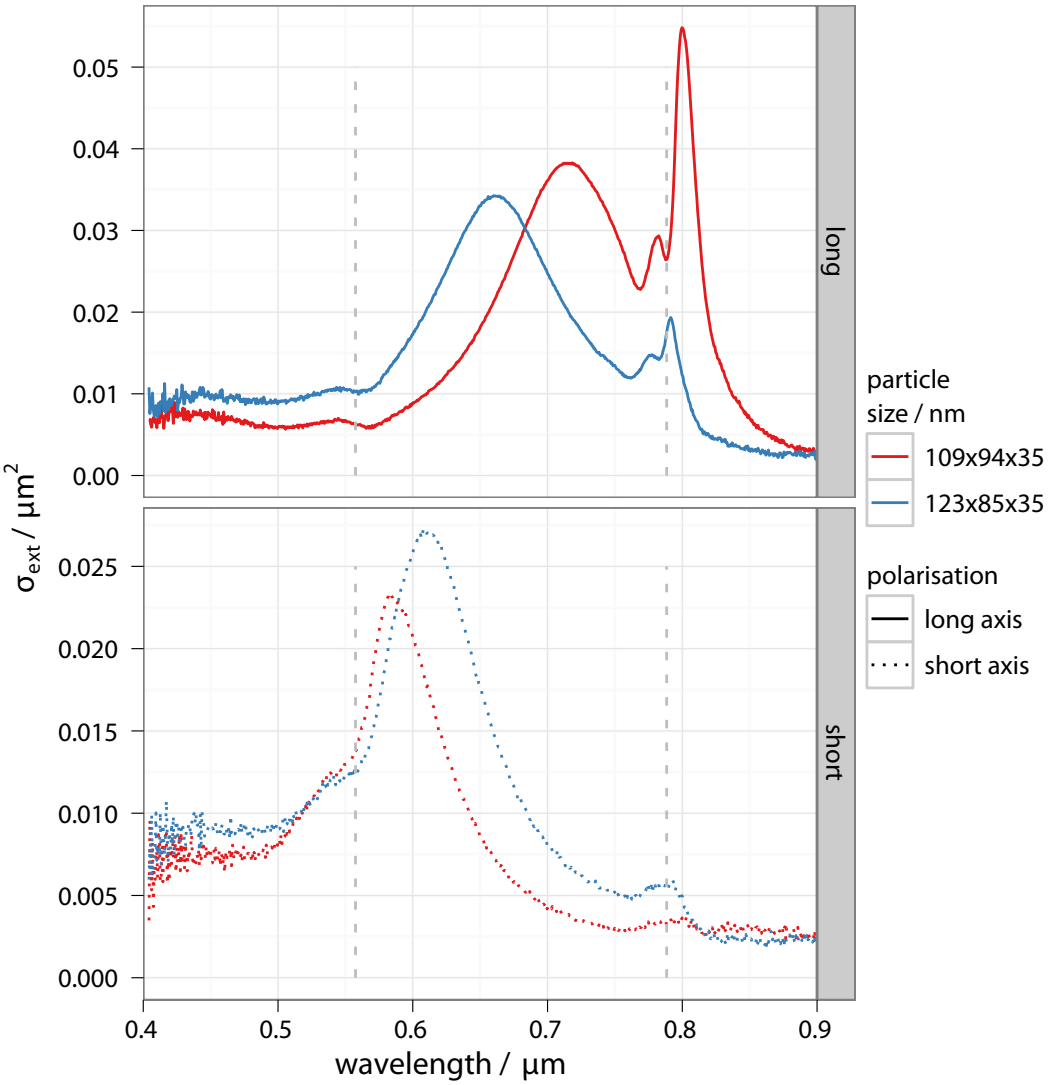

Figure 7.3: Extinction spectra, normalised by the occupancy for two polarisation states (long-axis: solid lines, short-axis: dashed lines). The colours refer to two arrays of particles both of pitch 540 nm for which the particle volume is approximately the same, but the particles have different aspect ratios.

7.3. The more elongated particles exhibit a red-shifted resonance along the long axis, the short axis being blue-shifted.

As expected the particle volume alone is not sufficient to uniquely determine the observed spectral features. In particular, the sharp peak near the diffraction edge is much more intense for the case of the higher aspect ratio particle, at a constant volume and constant particle separation.

In these measurements, the peak intensity is mainly dictated by the proximity of the diffraction edge to the LSP resonance, which in turn is determined by the particle polarizability, a function of both the volume and aspect ratio (equation 3.44). In fact, we expect that the radiative coupling between particles will depend on the overlap between the propagating field and the mode associated with the localised plasmon resonance. This coupling is the scattering cross-section of the particles,

which can also be thought of as a probability of interaction between a propagating photon and the LSPR.

Between the main LSPR and the diffractive peak lies a small secondary peak that was already observed in figure 6.6. This spectral feature was also noted by Félidj *et al.* [1], where it was attributed to an asymmetric configuration for the surrounding refractive index. Because this study only considers an homogeneous environment this cannot be the case here. In the simple semi-analytical coupled dipole model presented in figure 6.3, the peaks in the extinction spectrum were attributed to poles in the effective polarizability (equation 6.3). This situation occurs when the inverse polarizability intersects with the array factor, a situation that allows three solutions (the vertical lines in figure 6.3). The middle crossing point occurs when the imaginary part of the array factor is large, and the associated resonance is therefore strongly damped if at all observable. Markel developed a similar picture in a theoretical study of the divergence properties of the array factor [2]. The strength of this secondary peak can be artificially increased by scaling the imaginary part of the array factor — there is however no clear physical ground for doing so, and this explanation of our experimental observations remains highly speculative. To further evaluate the departure of the observed spectral lineshape to our theoretical predictions, I used an accurate multiple scattering code developed by J. García de Abajo, which can model the reflectance, transmittance and absorbance of an infinite periodic array of particles. A set of modelled spectra is shown in figure 7.4. The spectral lineshape is very similar in reflection, extinction and absorption, and presents the same characteristics features observed in experiments (figure 6.6), and discussed in the context of the coupled dipole approximation (figure 6.5). The more accurate modelling used here allows us to observe the fine behaviour of the divergence in the spectral lineshape near the Rayleigh diffraction condition. In particular, we observe that with sufficient resolution, the array exhibits *complete* transparency at the diffraction condition (vanishing reflection and absorption). This astonishing result implies that the electromagnetic field vanishes inside the particles at this particular frequency, although a single particle would present a strong absorption and scattering due to the excitation of the LSPR. The radiative coupling between particles conspires to annihilate the net field at each particle's location. This very interesting effect requires further studies, in particular for the near-field distribution in the frequencies close to the diffraction condition.

These numerical simulations also confirm the narrowing of the diffractive peak with increasing particle separation. A quantitative comparison of this trend with the experimental results will be shown in figure 7.9.

The inset of figure 7.4 presents the detail of an absorbance spectrum (pitch 620nm) near the diffraction edge. In addition to the very narrow minimum, a small spectral feature appears on the short-wavelength side of the diffraction edge. This peak is extremely weak in comparison to the diffractive peak (on the long-wavelength side of the diffraction edge), and cannot be identified with the secondary peak observed in the experiments.

These simulations were performed for infinite periodic arrays, illuminated at normal incidence. In the next section I will present experimental data and numerical results at small oblique incidence that provide a better interpretation for this secondary peak.

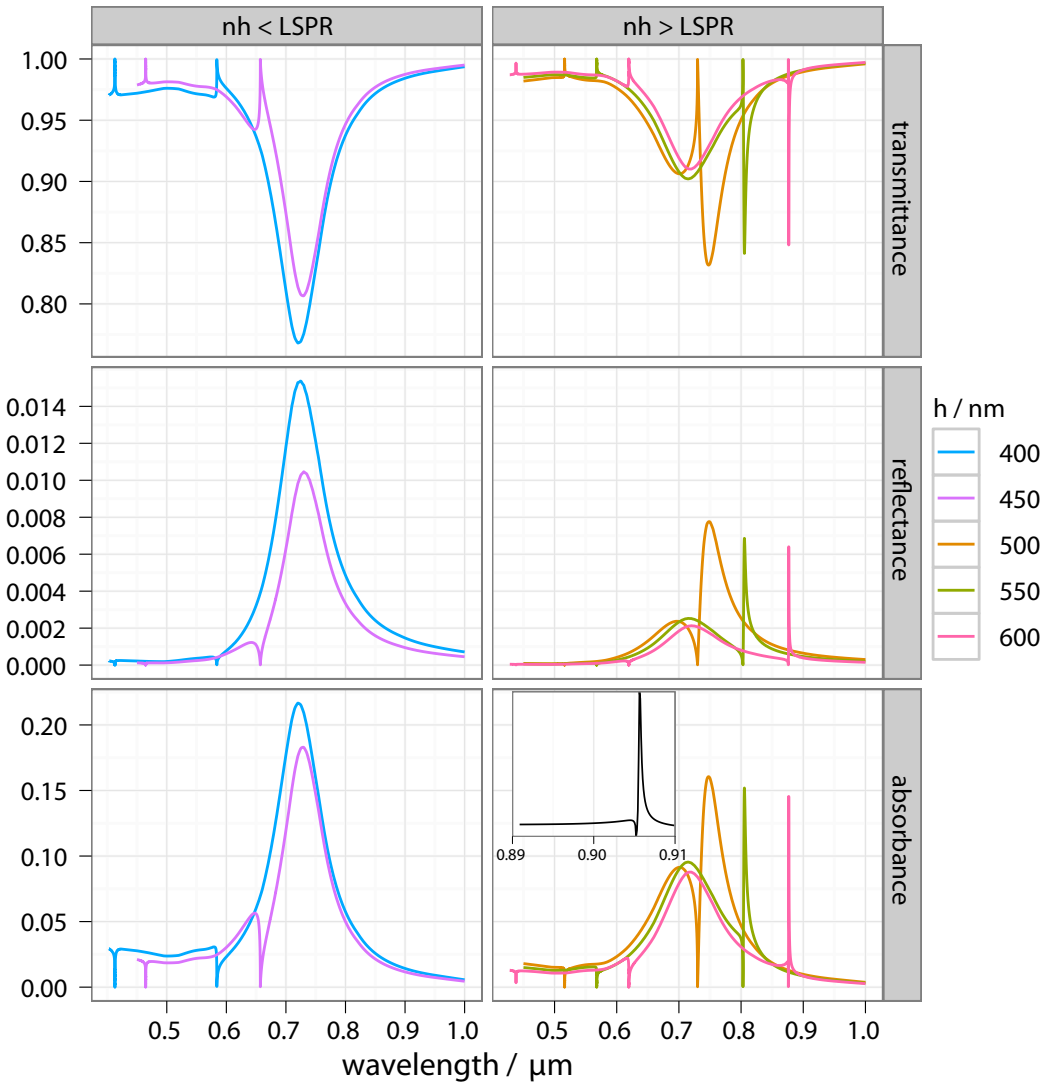

Figure 7.4: Simulated reflectance, transmittance, absorbance of a regular array of gold nanorods, using the program `pxtal` courtesy of J. García de Abajo. The dipole polarizability was obtained from a T-matrix calculation for a 120 nm×80 nm×50 nm gold nanorod with rounded corners (10 nm radius of curvature) in homogeneous refractive index 1.46. The multiple scattering program assumes an infinite square array of pitch h. The sharp spectral features are fully resolved with a supplementary fine wavelength sweep around the points of divergence of the array factor. The inset shows the absorbance of an array of periodicity 620 nm near the diffraction edge.

7.2 Angular response

The incident light that is scattered by the subwavelength particles can excite surface plasmons at the interface between the particles and the surrounding medium without the need for a phase-matching apparatus, as is the case with surface plasmons propagating on planar surfaces (figure 2.10). This convenient coupling of free radiation to the LSPR occurs because of the high curvature of the interface: as an incident plane wave is scattered by a subwavelength particle, the angular spectrum of the scattered field contains inhomogeneous waves with a range of k vectors that enables the coup-

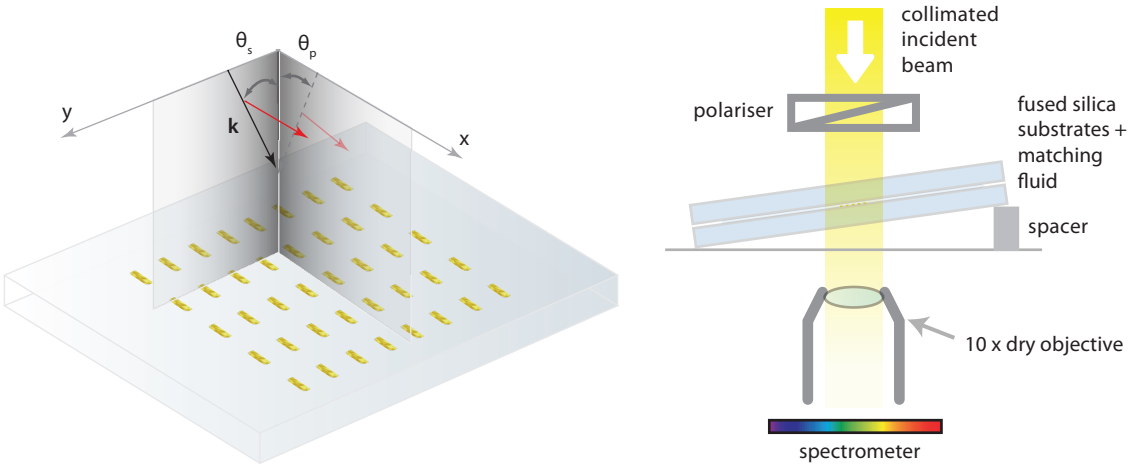

Figure 7.5: Schematic of the experimental setup. The incident light is polarised so as to excite the particles with an electric field along the long axis of the nanorods. The tilt angle (θ_s for s-polarisation and θ_p for p-polarisation) is varied by placing a spacer (substrate) on one side of the sample.

ling to the surface plasmon mode. Further, the surface plasmon dispersion is strongly modified by the curved geometry of the particle — in fact, the particle plasmon mode resembles a standing wave constrained by the edges of the particles [3–5]. The particle plasmon mode is therefore commonly considered to have a flat dispersion over a wide range of wave-vectors [6]. In the situation of a 2-dimensional array of particles, however, the electromagnetic eigenmode of the structure is delocalised and forms a surface mode [7]. It is therefore interesting to see the effect of varying the angle of incidence, *i.e* the in-plane component of the wave-vector. The coupling to the surface mode as a function of angle of incidence provides a map of the dispersion of the surface mode [8–10].

To perform these experiments I used the basic setup described in chapter 6 and reproduced in figure 7.5.

The angle of incidence is varied in discrete steps to assess the deviation away from normal incidence and in particular its repercussion in the spectral features near the diffraction edge. The incident light is polarised so that the projection of the electric field exciting the particles in the plane of the substrate is always aligned with the long-axis of the particles. A few transmission spectra for different angles of incidence are shown in figure 7.6.

The most pronounced variation is observed for s-polarisation. We observe the presence of three dips in transmission, and their spectral position is dependent upon the angle of incidence. The onset of the $+1$ and -1 diffracted orders is described by the following equation,

$$k = k_{\|} \pm \frac{2\pi}{h}, \tag{7.1}$$

where k is the wavenumber in the medium, $k_{\|}$ the in-plane component, and h the grating period. For a given incident angle, this condition dictates the pitch h for which the first order of diffraction emerges at a grazing angle.

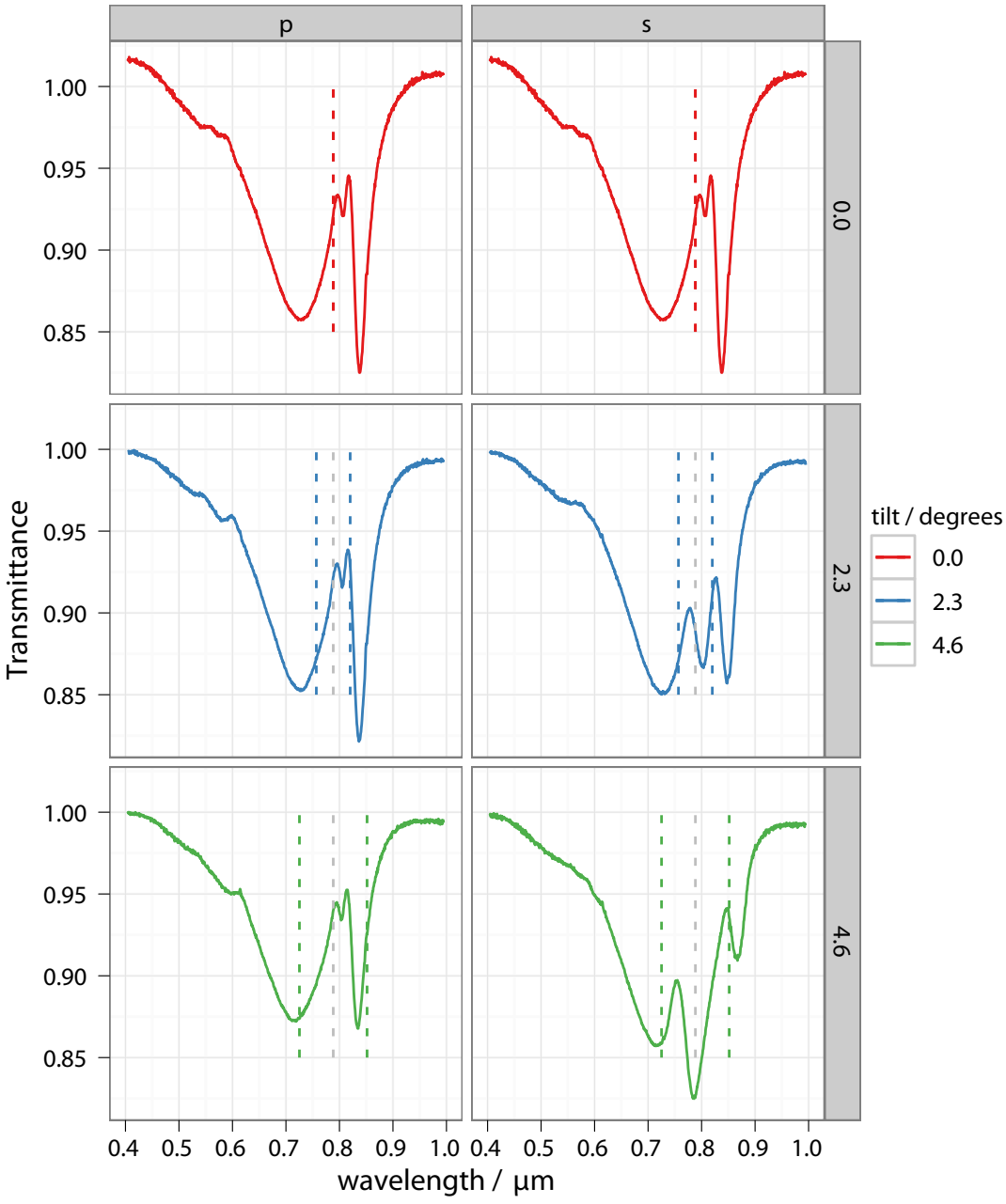

Figure 7.6: Experimental data on the influence of the tilt in s- and p-polarisation for a periodicity of 520 nm. The (approximate) first order diffraction edges for each angle of incidence are indicated by vertical coloured dashed lines. The diffraction edge at normal incidence is also shown in grey dashed lines.

The intensity of the three dips in transmission is also strongly modified and redistributed. At normal incidence, two minima merge and we can conclude that the small feature noted in figure 6.6 was in fact due to a slight off-normal incidence.

The case of p-polarisation reveals only a weak change in the overall intensity that could be attributed to a weakened excitation of the long-axis LSPR as the incident electric field has an out-of-plane component with respect to the substrate. We can understand the dispersion of the modes

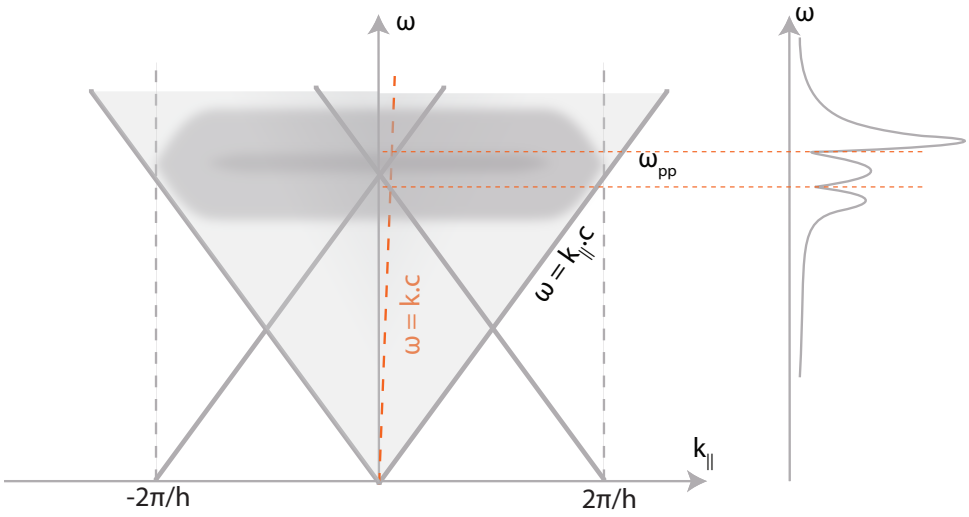

Figure 7.7: Schematic dispersion of the LSPR modified by a periodic grating. The unperturbed localised plasmon resonance spans the horizontal grey area. The light-line and the diffracted orders ±1 are represented by fine grey lines. The dashed red line corresponds to light near normal incidence. This light crosses the diffracted orders +1 and −1 at different energies. The spectral lineshape resulting from the interaction between the LSPR and the diffracted light-lines is shown schematically on the right.

by invoking a schematic dispersion diagram for the the LSPR in the presence of a periodic structure as depicted in figure 7.7. The LSPR mode is represented as a broad, flat mode on this diagram. The dispersion-less nature of this *localised* resonance can be understood as a characteristic standing-wave behaviour. The light cone $\omega = k_{\|}.c$ delimits the region for which free-propagating light can couple with the structure. The effect of the periodicity on the allowed electromagnetic modes of the structure is to provide an additional momentum to light with momentum greater than $2\pi/h$. In effect, this results in a back-folding of the light line at the boundary of the Brillouin zone ($k_{\|} = \frac{2\pi}{h}$). This results in two lines crossing the $y-$axis at $k_{\|} = 0$ (normal incidence). When the periodicity is such that the crossing of the diffracted light cone occurs in the spectral region of the LSPR, the modes of the structure are modified and this results in a dip followed by a maximum in the extinction curve (the *Wood anomalies*). We can now understand that a slight deviation from normal incidence results in two-crossing points: the degeneracy between the +1 and −1 diffracted orders is broken, and the incident light suffers two intercepts with the ±1 diffracted orders. This description is further supported by the coupled model dipole shown in figure 7.8 which reproduces the experimental results for a finite array of dipoles illuminated with s-polarised light for a range of incident angles. A tilt angle as small as 1° is sufficient to observe a secondary peak similar to that of the experimental results of chapter 6.

7.2.1 Width of the resonance

Of particular interest in the optical response of such diffractive arrays is the width of the sharp spectral feature that seems to contradict the limitations of the LSPR width discussed for single particles in chapter 4. Further, in chapter 5 we observed an appreciable *broadening* of the LSPR in

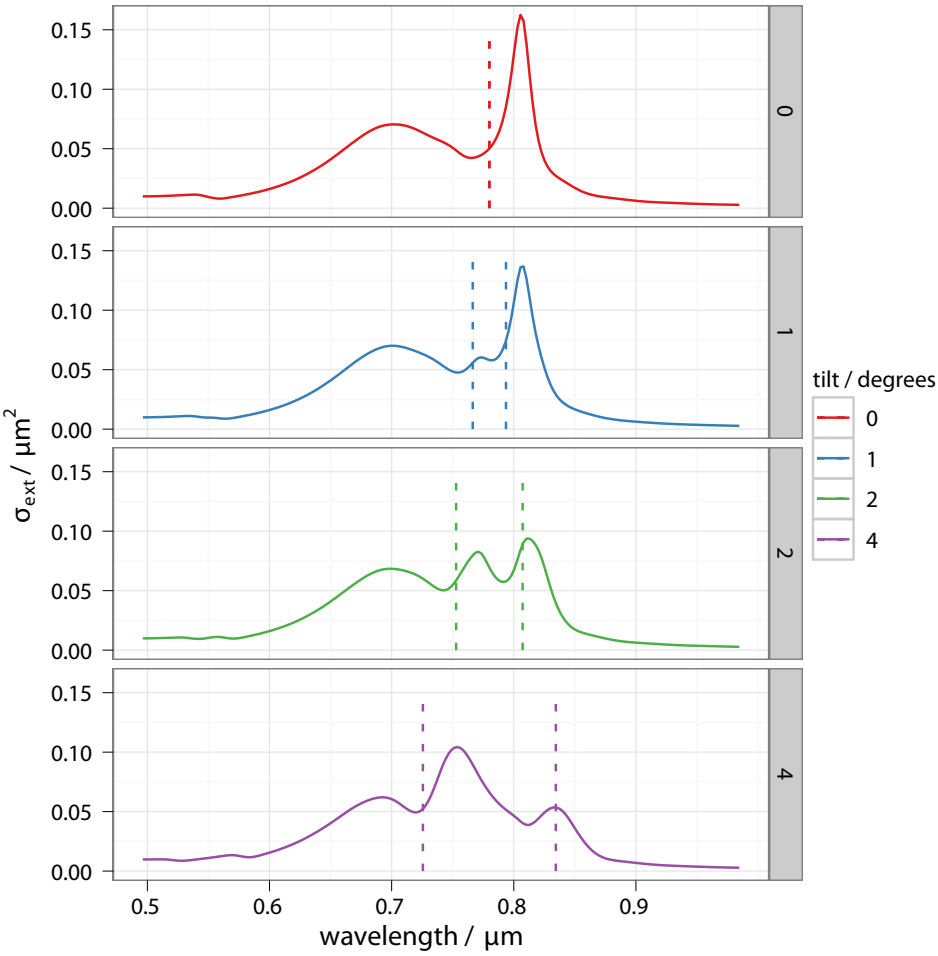

Figure 7.8: Modelled extinction spectra of an array of gold nanorods using a coupled dipole model. The tilt angle is varied from 0° to 4° for s-polarisation. The array (pitch 520 nm, surrounding medium 1.5) comprises 441 gold ellipsoids of semi-axes 60 nm×50 nm×20 nm. The dashed vertical lines indicate the position of the diffraction edge (orders ±1).

collections of particles due to the combination of inhomogeneous broadening and particle interactions. The possibility of *reducing* the LSPR width in a large array of particles is therefore particularly interesting.

The diffractive peak is generally quite asymmetric and resides on a varying background (LSPR). It is therefore difficult to unambiguously define its width. I chose to measure the distance between the peak maximum and the diffraction edge, which underestimates the width, but seems to provide a consistent measure for all samples. In figure 7.9 the evolution of the width is shown as a function of particle separation for 3 different particle sizes and two polarisations.

We note that the width (as defined above) decreases with increasing distance from the diffraction edge to the LSPR. A linear fit leads to a slope that depends on both the volume and the aspect ratio of the particles. Furthermore, we note that the trend is not linear. Markel suggested (for

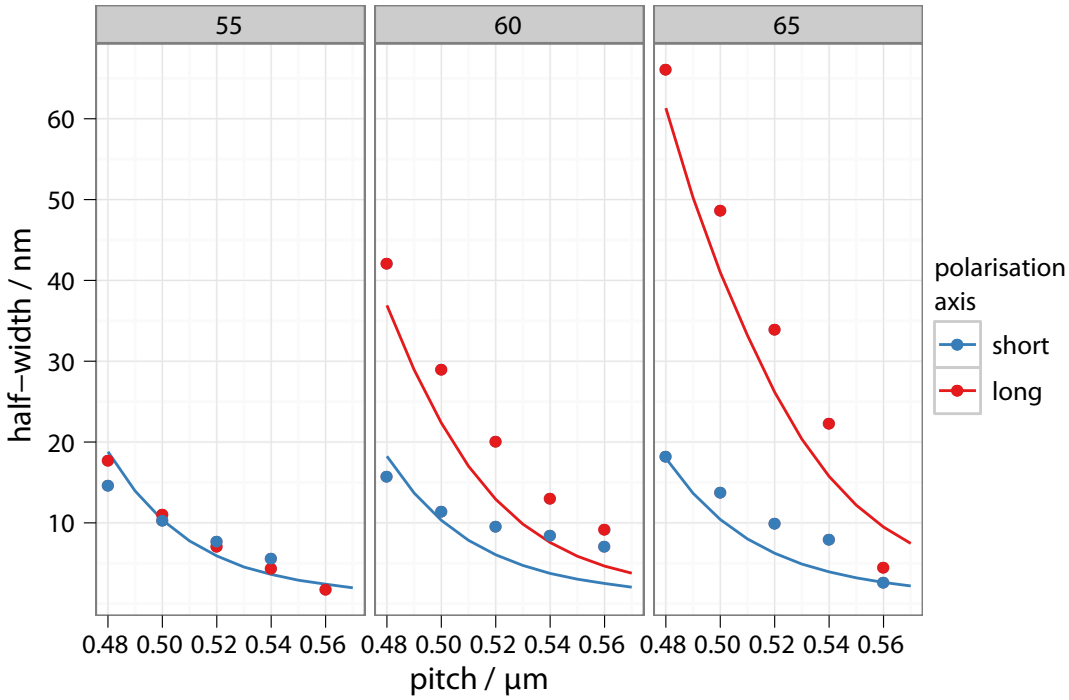

Figure 7.9: Measured half-width of the diffractive peak (points) for arrays of periodicities 480 nm to 560 nm in 1.46 surrounding index. Three different particle sizes are considered (semi-axes 55 nm×55 nm×20 nm, 60 nm×55 nm×20 nm, 65 nm×55 nm×20 nm). The incident light is polarised along the long axis (red) and short axis (blue). The solid lines are the numerical result from modelling arrays with the above parameters using the `pxtal` multiple scattering program [11].

linear, infinite chains of spheres [2]) an expression of the form,

$$\text{width} \sim h \exp\left(-C \frac{h^3}{\Re\left(\alpha_{\lambda=h}\right)}\right),$$

where h is the particle separation, C is a constant, and $\alpha_{\lambda=h}$ is the polarizability of the particle at the diffraction edge wavelength. The polarizability is however unknown from the experiment, I have not been able to verify the validity of this expression for 2-dimensional, finite structures. With the rigourous multiple scattering code used in figure 7.4, it was however possible to confirm the general trend of the width of this diffractive peak (solid lines in figure 7.9). An analytical expression should be readily obtained and will be the subject of future investigations.

7.3 A sum rule for metallic ellipsoids

In all the spectra obtained from arrays with a common particle size, we noted the interesting fact that the normalised extinction spectra present a constant area over the spectral range of interest. I will now discuss how this observation can be linked to a more general sum rule of extinction which relates the total extinction of light caused by metallic nanoparticles to their geometrical shape. In

the remainder of this chapter, I will test this interpretation both experimentally and with the help of numerical modelling.

Sum rules can provide powerful insight on the average behaviour of a complex optical or quantum system [12–14]. Perhaps the most well known optical sum rule is the one that relates the real part of the refractive index to the integrated absorption over all frequencies [13], also known as Kramers-Kronig (KK) relation. In the context of scattering by particles, Purcell [15] first derived the sum rule for the extinction of light caused by dust particles in an attempt to characterise the constitution of the interstellar medium. This is an example where sum rules can give some quantitative answers to a seemingly intractable problem: very few assumptions can be made on the constitution and shape of the particles, the only information on the scattering medium is taken from optical measurements at great distance.

In the samples fabricated for this thesis, we can test more directly a similar sum rule. The particles are produced with a control over the distribution of shapes and sizes using the fabrication technique of electron-beam lithography.

The usual derivation of the sum rule of extinction by particles was first given by Purcell [15], Bohren and Huffman [16], and recently given a more general form by Markel [17]. Although this sum rule relies only on very general properties of the dielectric function and of the scattering process, its derivation was recently re-envisaged by Mishchenko [18] who pointed out a basic logical flaw in the reasoning. Despite this severe warning, I will now review the usual derivation that provides the most plausible argument to date for this conjecture.

Let us consider the extinction of light by a single spheroidal particle of semi-axes a, b and c illuminated normally to its c axis. The scattering amplitude matrix $\mathbb{F}$ relates the far-field spherical wave scattered by the particle to an incoming plane wave [16, 19],

$$\mathbf{E}_{\text{scat}} = \frac{\exp(i\mathbf{k}\cdot\mathbf{r})}{r}\,[\mathbb{F}]\,\mathbf{E}_{\text{inc}}. \tag{7.2}$$

The components of this matrix depend on the frequency, refractive indices, polarisation, and on the angle between the incident and scattered beam. A consequence of the causality constraint on the optical response of a scattering system is the general relation that exists between the real and imaginary parts of the scattering amplitude [12, 16] which form a Hilbert transform pair,

$$\Im\left[f(\omega)/\omega^2\right] = \frac{-2\omega}{\pi}\mathscr{P}\int_0^\infty \mathrm{d}\Omega \frac{\Re\left[f(\Omega)/\Omega^2\right]}{\Omega^2-\omega^2}, \tag{7.3}$$

where f stands for the component of the scattering matrix relevant to the particular orientation and polarisation state of the incident field, and $\mathscr{P}$ denotes the principal value of the improper integral.

Mishchenko points out that such a causality relation cannot be directly stated within this frequency-domain formulation of the scattering process [18] where all monochromatic fields have infinite duration in time (past and future). In particular, the dichotomy of the total field into an incident field and a scattered field is a mathematical construction that does not imply any causal relationship. A rigourous derivation of the sum rule should therefore proceed from the time-dependent analogue of the volume integral equation but has not yet been proposed.

Pursuing the usual argument, we consider next the optical theorem, which relates the far-field extinction to the forward scattering amplitude $f(0°,\omega)$. It expresses the fact that extinction is the result of the interference between the incident and scattered wave in the exact same direction[16],

$$\sigma_{\text{ext}}(\omega) = \frac{4\pi}{k^2}\Re\left[f(0°,\omega)\right]. \tag{7.4}$$

Combining this expression with equation 7.3 leads to,

$$\Im\left[f(\omega)\right] = \frac{-\omega^3}{\pi^2 c^2}\mathscr{P}\int_0^\infty \mathrm{d}\Omega \frac{\sigma(\Omega)}{\Omega^2-\omega^2}. \tag{7.5}$$

The last step in the derivation is to relate the scattering amplitude to the shape of the particle. We wish to take the electrostatic limit of the left-hand side in equation 7.5, as the response of the scatterer can then be exactly described as a dipole of polarizability α_{static},

$$f(0°,\omega) = \frac{-i\omega^3}{c^3}\alpha_{\text{static}}, \tag{7.6}$$

where α_{static} is given by,

$$\alpha_{\text{static}} = \frac{V}{3}\frac{\varepsilon_m-\varepsilon_d}{\varepsilon_d+\mathrm{L}(\varepsilon_m-\varepsilon_d)}, \tag{7.7}$$

with V the particle volume, and L a shape-dependent depolarisation factor related to the semi-axes a, b, and c by the following formula,

$$\mathrm{L} = \frac{abc}{2}\int_0^\infty \frac{dq}{(l^2+q)\sqrt{(a^2+q)(b^2+q)(c^2+q)}}, \quad l=a,b,c. \tag{7.8}$$

Combining equations 7.5 and 7.6, and changing the integration variable to wavelength leads to the following sum rule,

$$\int_0^\infty \sigma(\lambda)\mathrm{d}\lambda \propto \alpha_{\text{static}}. \tag{7.9}$$

In the case of metallic particles, the static dielectric function is infinite due to the free surface charge perfectly screening any external DC field. This allows us to further simplify equation 7.9 by evaluating equation 7.7 in the limit $\varepsilon_m \to \infty$, which simply leaves $\alpha_{\text{static}} = V/\mathrm{L}$, remarkably irrespective of the metal and dielectric environment. Consequently, the sum rule we wish to consider reads,

$$\int_0^\infty \sigma(\lambda)\mathrm{d}\lambda \propto \frac{V}{\mathrm{L}}. \tag{7.10}$$

A similar sum rule was recently expressed in terms of radar cross-sections for meta-materials at micro-wave frequencies, and tested experimentally [20]. A promising study would be to test experimentally the validity of equation 7.10 over several orders of magnitude by using metallic nanoparticles at optical frequencies and metallic antennas at micro-wave frequencies with an identical shape.

7.3.1 Numerical verification of the sum rule for isolated prolate ellipsoids

Extinction spectra were calculated using an accurate T-matrix code [21] for a large number of single nanoparticles in the form of prolate ellipsoids. The prescription of the dielectric function of the scatterers and surrounding medium has proven very important. Because the sum rule equation 7.10 relies on the implicit assumption that the dielectric function obeys a Kramers-Kronig relation, one cannot use a dielectric function that is only valid in a limited range of wavelengths. For instance, most calculations presented in this work made the assumption of a non-dispersive and non-absorbing surrounding environment of index 1.5. This situation describes well the optical properties of glass and index-matching fluid in the optical and near-IR regimes, but cannot be a physical solution over a wider range of frequencies. From the KK relations, a refractive index different from unity at a given frequency must be accompanied by an absorption band at a higher energy. Further, the refractive index of a material must be a decreasing function of frequency (with the local exception of regions of anomalous dispersion near strong absorption bands). I therefore set the surrounding medium to vacuum.

The choice of the dielectric function of the scatterers faces further complications. The experimental values of the dielectric function of gold suffer two major problems in this regard: they span only a limited range of wavelengths; they have no *a priori* justification for satisfying the KK relations accurately. In fact, it is doubtful that the measurement of the real and imaginary parts of the dielectric function is subject to identical limitations, more probably the imaginary part is often overestimated due to experimental artefacts (for instance, surface roughness causes an increased loss channel [22]). A few simulations were performed using the permittivity from Johnson and Christy but the (relatively small) deviation from the sum rule could not be tested reliably.

I therefore used a simple Drude model of the form,

$$\epsilon = 1 - \frac{\omega_p^2}{\omega^2 + i\omega\gamma}, \tag{7.11}$$

with $\gamma = 1.0 \times 10^{14}$ rad/s the damping parameter, and $\omega_p = 1.5 \times 10^{16}$ rad/s the plasma frequency. Note that the absence of a low-frequency background permittivity makes this function unsuitable for a description of gold. This dielectric function is shown as an inset in figure 7.10. As compared to the Drude model for gold in the visible, the plasma frequency chosen here lies in the deep UV; consequently the expected Fröhlish frequency of a subwavelength particle occurs at shorter wavelengths (around 200 nm).

Figure 7.10 presents a small subset of the extinction spectra that were obtained in this numerical simulation. The range of particle sizes was dictated by three parameters. (i) The wavelength range of the simulation must span a wider range than the width of the LSPR so that the extinction curve is negligibly small on either side of the LSPR. (ii) For an accurate determination of the integrated extinction, a large number of wavelengths must be simulated (1000 points per spectrum in this case). The computer time required to run such a simulation restricts the number of particle sizes. (iii) More importantly, the convergence of the T-matrix method is known to deteriorate for highly elongated particles, and particles with a large permittivity [23]. I therefore restricted the

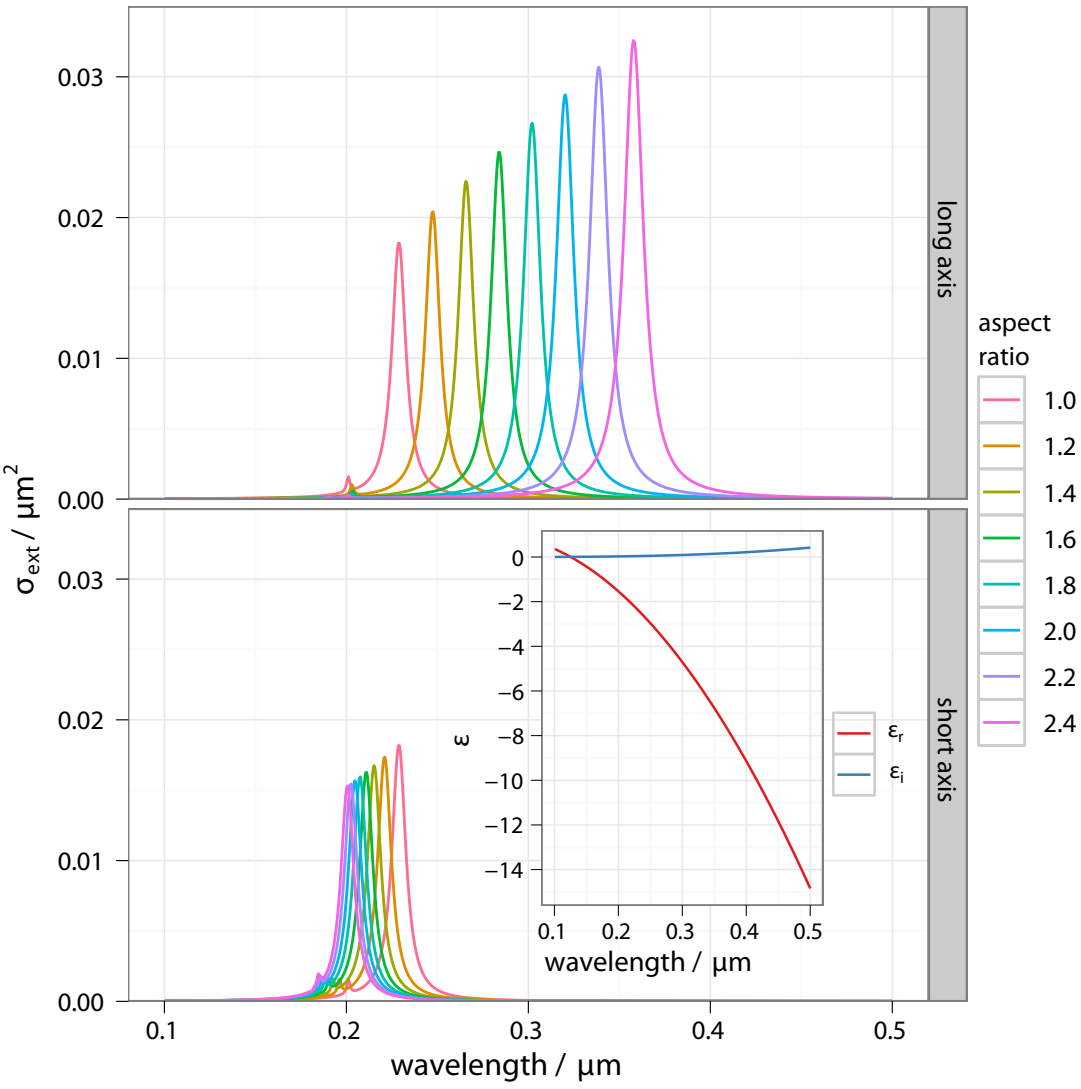

Figure 7.10: Calculated extinction spectra for 10 ellipsoids of constant volume and increasing aspect ratio. The top panel if for the incident polarisation along the long axis, the bottom panel is for the corresponding short axis. The inset presents the dielectric function of equation 7.11 with parameters $\gamma = 1.0 \times 10^{14}$ rad/s and $\omega_p = 1.5 \times 10^{16}$ rad/s.

study to small aspect ratios, similar to the ones presented in the experimental data. Other accurate modelling techniques such as the method of separation of variables in spheroidal coordinates [24] could be used to extend the range of simulated parameters.

Figure 7.11 presents the result of these simulations as a test for the sum rule of equation 7.10. In the x-axis the ratio volume over depolarisation factor is calculated for the various particles run in the simulation (equation 7.8). In the y-axis the numerical integration of the extinction spectra for each particle is plotted as a function of particle volume and aspect ratio (both x- and y- axes are on a logarithmic scale for clarity). A clear linear correlation suggests the validity of equation 7.10 for the range of parameters used in this simulation, with the notable restriction to small aspect ratios and a basic Drude model dielectric function.

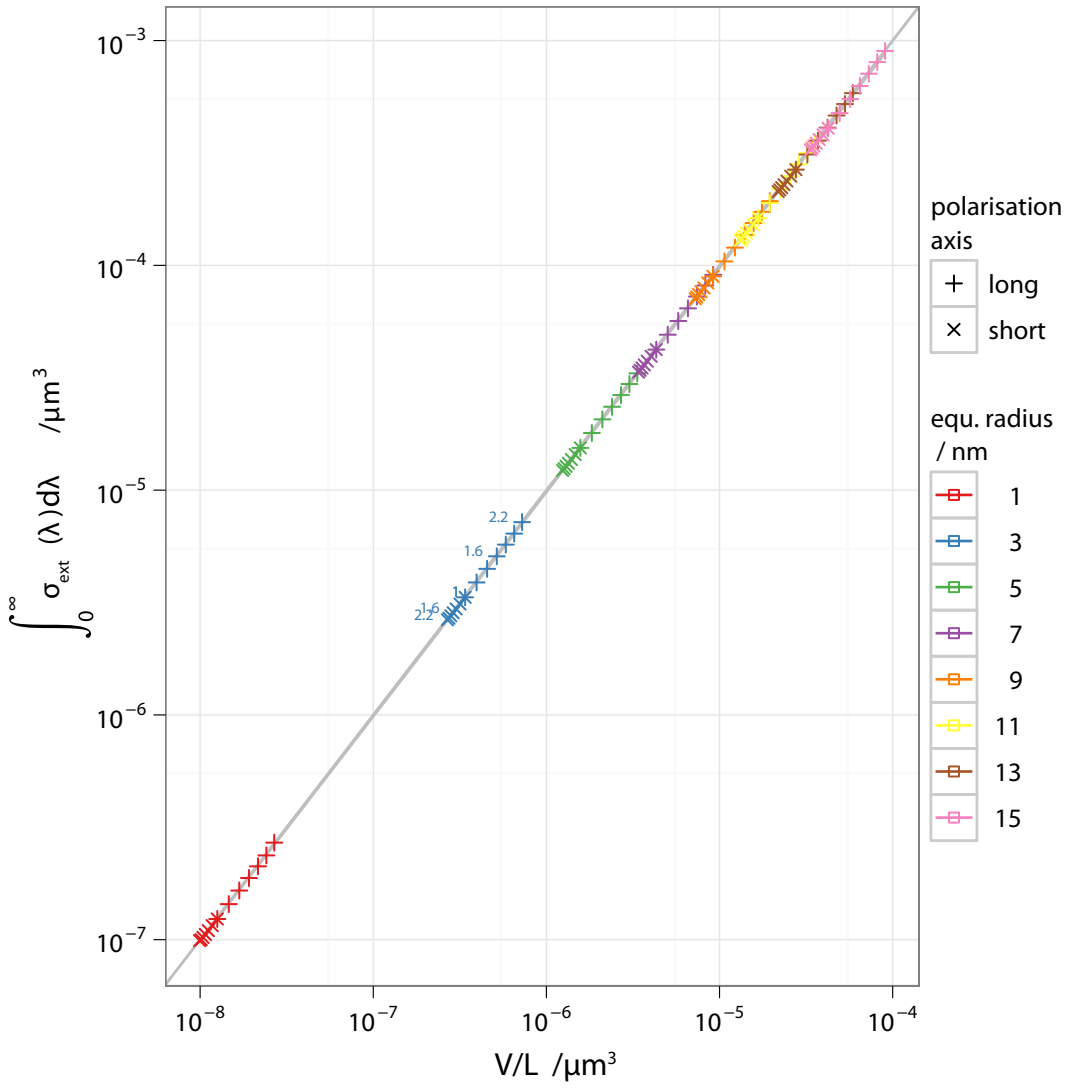

Figure 7.11: Testing of the sum rule from the results of T-matrix modelling on prolate ellipsoids of aspect ratio 1 to 2.2, for different volumes (indicated as an equivalent-volume sphere radius in the legend). The parameters are the same as for figure 7.10.

As a comparison, a similar simulation was performed with two different dielectric functions obtained from a best fit of the experimental data for gold and silver in the range 700 nm—1200 nm. Here the dielectric function is modelled by a Drude model with a background permittivity. In order to match a more physical situation, the surrounding medium was set to a permittivity equal to this background dielectric constant (as a result, the particle is invisible to radiation in the high-frequency regime).

The results for this simulation are shown in figure 7.12. We see that the linear relationship between the integrated extinction and the inverse depolarisation factor holds for particles of small volume. The larger volumes considered in this simulation depart from the linear trend as the aspect ratio is increased. Several possible causes for this discrepancy have been considered. First, it may be that a mechanism for extinction manifests itself outside the range of integration, how-

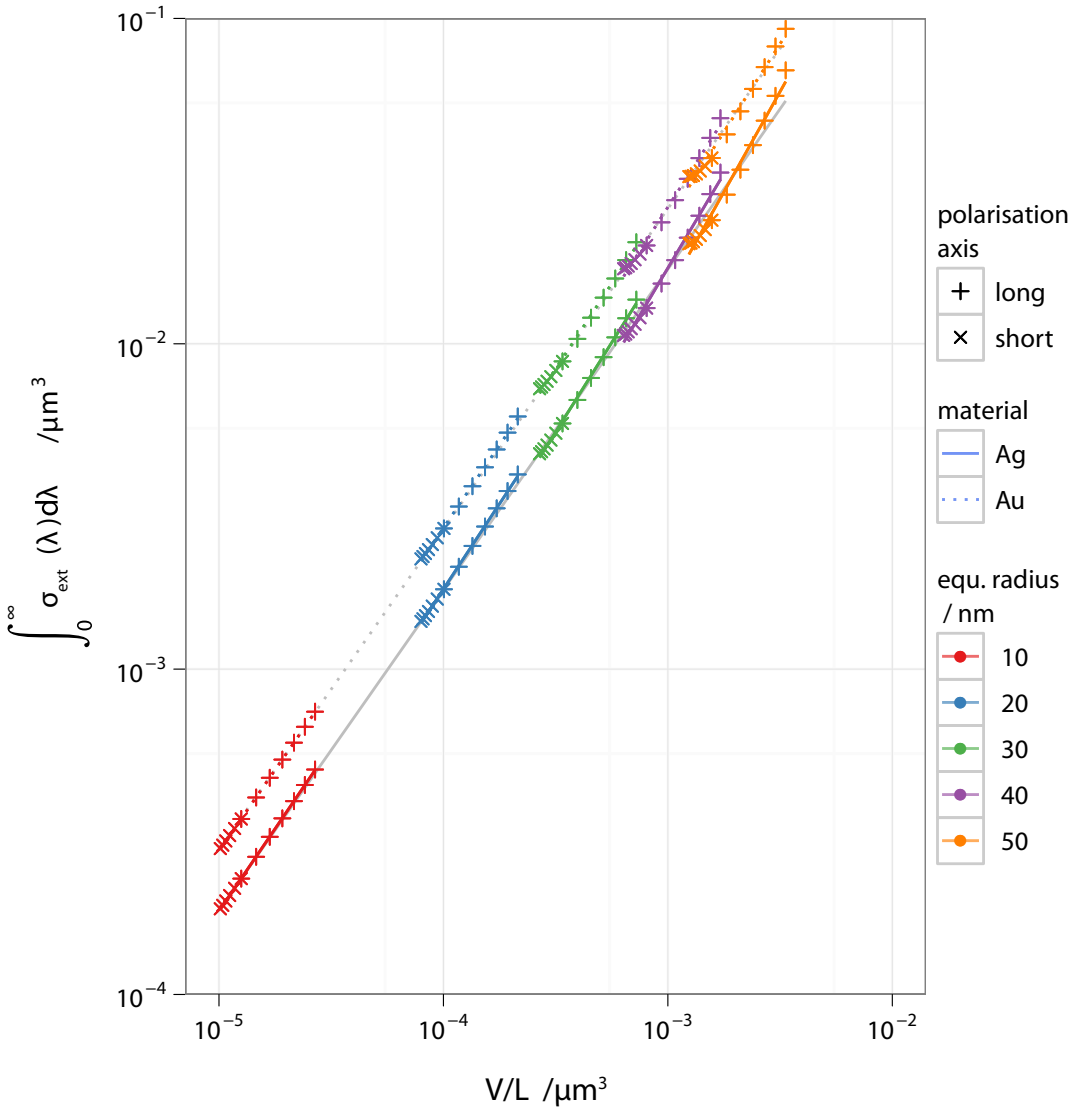

Figure 7.12: Testing of the sum rule from the results of T-matrix modelling on prolate ellipsoids. The dielectric functions were obtained from a best fit of the experimental data for gold ($\gamma = 1.128 \times 10^{14}$ rad/s, $\omega_p = 1.3355 \times 10^{16}$ rad/s, $\varepsilon_{DC} = 8.0933$) and silver ($\gamma = 1.0783 \times 10^{14}$ rad/s, $\omega_p = 1.3220 \times 10^{16}$ rad/s, $\varepsilon_{DC} = 3.4667$) in the range 700 nm—1200 nm. A linear fit to the data is shown for each subset with constant volume.

ever the Drude model should not yield any other response than the excitation of the LSPR in this frequency range as it describes the material as simply a collection of free electrons. The prescription of the surrounding medium having a permittivity equal to that of the background permittivity of the particles is very important to ensure that no index contrast at high-frequency yields spurious resonances (such as whispering gallery modes). A possible cause of departure from the linear relationship is the failure of the numerical model to accurately calculate the extinction of larger particles. This numerical code has however been thoroughly tested in this range of size parameters and aspect ratios, and cannot explain the large discrepancy in figure 7.12. We are left with the possibility of an invalid assumption in the derivation of the sum rule for this particular form of the

dielectric function. The presence of higher order resonances in the spectra of the larger ellipsoids modelled in this simulation should not affect the validity of the sum rule as the static limit is not used as an approximation for the extinction cross-section at high frequency but only for the exact static limit in the Kramers-Kronig relation.

7.3.2 Experimental results on 2-dimensional arrays

The experimental verification of this sum rule is difficult to achieve with a single particle as the extinction cross-section is much smaller than a diffraction-limited collimated beam. The very weak signal-to-noise ratio obtained in transmission measurements is only manageable when one probes the extinction by a collection of closely separated particles. When the particle separation is sufficient that no strong interaction and multiple scattering substantially contribute to the scattering, this simply leads to an inhomogeneous broadening of the extinction spectrum reflecting the distribution of scattering responses in the sample. With particles of noble metals such as gold and silver in the visible, however, the distance required for the particles not to interact is rather large, typically around one micrometer. This is due to the fact that these nanoparticles act as very efficient scatterers, they are in fact the nanoscale analogues of antennas. In this work, I considered the optical extinction by the particles arranged in square arrays of varying inter-particle spacing. As we saw in this chapter and in chapter 6, such configuration can produce remarkable spectral features that result from the interplay between the scattering properties of the individual particles, and the geometrical resonance arising from the periodical arrangement of scattering centres. It is therefore a challenging test for our sum rule, as the scattering medium displays strong radiative coupling between the particles that could be described as a non-local effective permittivity [25].

Using the formula 7.8 the mean depolarisation factor can be evaluated for each array of particles together with an estimate of the error, using the measurements of figure 7.2. The evaluation of the integral is more problematic: the sum rule is truly valid only if one considers all the frequencies from 0 to ∞. Here, I make the strong assumption that the main *difference* in the optical response of the different particle arrays is dictated by the contribution of the surface plasmon modes in the optical regime. Under this assumption, the extinction spectra of different arrays can be compared in the same spectral window provided they display a constant baseline trend. The numerical integration was performed over the range 500 nm–900 nm, limited by the spectral window of the spectrometer.

The correlation between the integrated area and the calculated depolarisation factors is shown in figure 7.13. A general offset between particles of different volumes and different particle separations is noticeable. The latter can be attributed to the normalisation procedure, that assumes a constant number of particles being sampled by the optical setup (spectrometer slit). A general offset between particle volumes should also be expected on the basis of the restriction of the sum rule to a limited spectral window. It is to be expected that other contributions to the overall extinction will depend on the particle volume. Within the dispersion of the measurements, a clear linear correlation can be observed that suggests the validity of this sum rule with arrays of metallic nanorods.

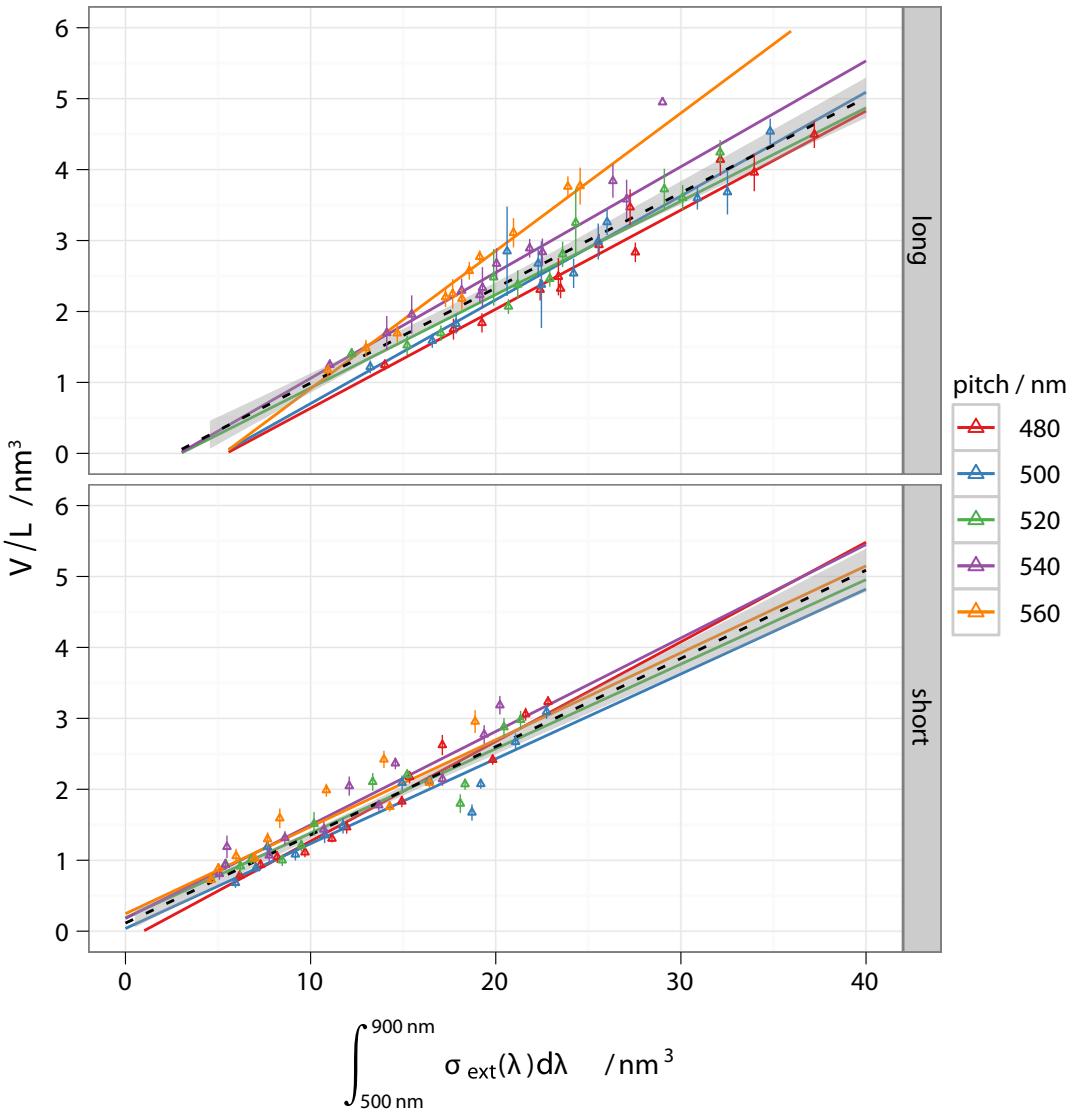

Figure 7.13: Experimental correlation between the integrated per-particle extinction and the depolarisation factors evaluated from the SEM. The lines are linear fits for each of the 5 particle separations Error bars are shown for the ratio volume over depolarisation factor calculated from the measurements shown in figure 7.2. Top panel shows the results for light polarised along the long axis of the particles, bottom panel for the short axis.

7.4 Conclusion

The spectral lineshape of the LSPR can be substantially modified by coherent radiative coupling between gold nanoparticles when they are arranged in a 2-dimensional array. In particular, the presence of grazing diffracted orders for wavelengths commensurate with the periodicity of the array results in a sharp dip followed by a peak of extinction. In chapter 6 experiments and simulations were presented that discussed the effect of the periodicity on the spectral lineshape, and how a geometrical resonance (diffraction) arises from the coherent interaction between scatterers.

A small deviation from normal incidence lifts the degeneracy between diffracted orders and results in a double peak near the diffraction condition at normal incidence. This results obtained for transmission measurements near normal incidence explains the presence of a secondary peak in the data presented in chapter 6. The dispersion map of the surface mode that interacts with the LSPR was recently further investigated by Vecchi *et al.* [7].

In this chapter I also presented experiments and simulations that elucidate the role played by the scattering properties of the particles. In particular, a comparison was presented for two arrays of particles that have an identical volume and an identical separation between particles. The extinction spectrum for both cases shows large differences that can be attributed to the influence of the aspect ratio of the particles. First, the main peak in extinction associated with the excitation of the LSPR is red-shifted for nano-rods with an increased aspect ratio. Second, the diffractive peak becomes more intense and broader as the spectral position of the LSPR approaches the diffraction edge. Third, the integrated extinction per particles is found to scale with the ratio volume over depolarisation factor. This sum rule was tested experimentally for several arrays of particles with varying sizes and particle separation. Further, numerical simulations were performed that suggest the validity of this sum rule for metallic particles using a simple Drude model for the dielectric function of the particles. The testing of this sum rule requires further investigation, in particular to verify its accuracy for more realistic prescriptions of the dielectric function and a wide range of particle sizes. Such experimental and numerical verifications should be complemented by a rigourous theoretical derivation of the sum rule.

"Quand les mystères sont très malins ils se cachent dans la lumière."

Jean Giono

8

The effect of disorder on the optical properties of diffractive arrays of gold nanorods

Two-dimensional arrays of gold nanoparticles with a periodicity commensurate with the wavelength of resonant excitation of localised plasmons have been shown in chapter 6 and chapter 7 to exhibit a strong, long-range interaction between particles. In this chapter I investigate experimentally the effect of varying the geometrical arrangement from a periodic to a disordered lattice with constant occupancy. The effect of disorder arising from variations in particle size is also studied for a regular lattice, and the effect this has on the broadening of the spectral lineshape is discussed. The coupled dipole model introduced in previous chapters is used to interpret the modifications in the extinction spectra with respect to the ordered situation considered before.

8.1 Experimental technique

I investigated the influence of disorder in such structures on their spectral response by conducting experiments with a controlled distribution of particle positions and particle sizes. The fabrication procedure is similar to that of chapter 5, only the particle separation is larger. Arrays were fabricated with several distributions of particle positions, as well as particle sizes, as illustrated in fig. 8.1. The spatial extent of the arrays was limited to 35 μm×35 μm to minimise the shape variation due to beam distortion at the edges of the available electron-beam write-field.

The particles (nominal size 120 nm×80 nm×35 nm) were deposited by thermal evaporation, with a thin (2 nm) chromium layer being used to improve the adhesion of the gold onto the sub-

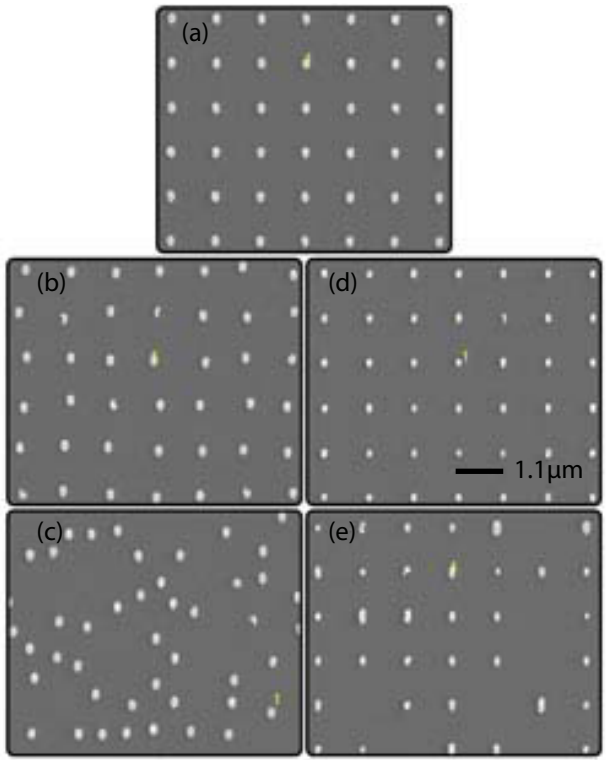

Figure 8.1: Scanning electron micrographs of particle arrays. (a) ordered array, *i.e.* no added disorder. (b) 10% disorder in particle positions. (c) pseudo-random positions. (d) 10% variation in the length of the long axis of the particles. (e) 100% variation in the length of the long axis of the particles.

strate. The particles were immersed in matching index fluid between two substrates so as to obtain an homogeneous refractive index environment ($n = 1.46$). The extinction spectra were obtained by measuring the transmittance at normal incidence with a collimated beam (divergence $< 0.1°$), using a `10x` objective for the collection optics. A polariser was used in the illumination path to selectively probe the LSPR associated with the long-axis of the nanoparticles (setup of figure 5.7).

8.2 Results and discussion

Figure 8.2 (a) presents the extinction spectra obtained from arrays that differed only in the degree of disorder of the particle positions. As was noted in chapter 6, the nominally ordered array presents a narrow extinction peak on the low-energy wing of the LSPR; this narrow feature occurs because of the coherent superposition of partial waves scattered from all the particles in the array. In addition, the extinction due to the excitation of the LSPR can be partially suppressed by the coherent scattering, which results in a dip in the extinction close to the diffraction edge.

The strict periodicity is broken by displacing the particles from their regular locations in a random manner. As this disorder increases the spectral shape evolves around the diffraction edge. In particular, the sharp peak weakens and blue-shifts in the disordered samples as the disorder increases, whilst the extinction due to the excitation of the LSPR regains its full strength. In the limit of spatially uncorrelated positions (labelled *pseudo-random* in the figure), we retrieve a smooth

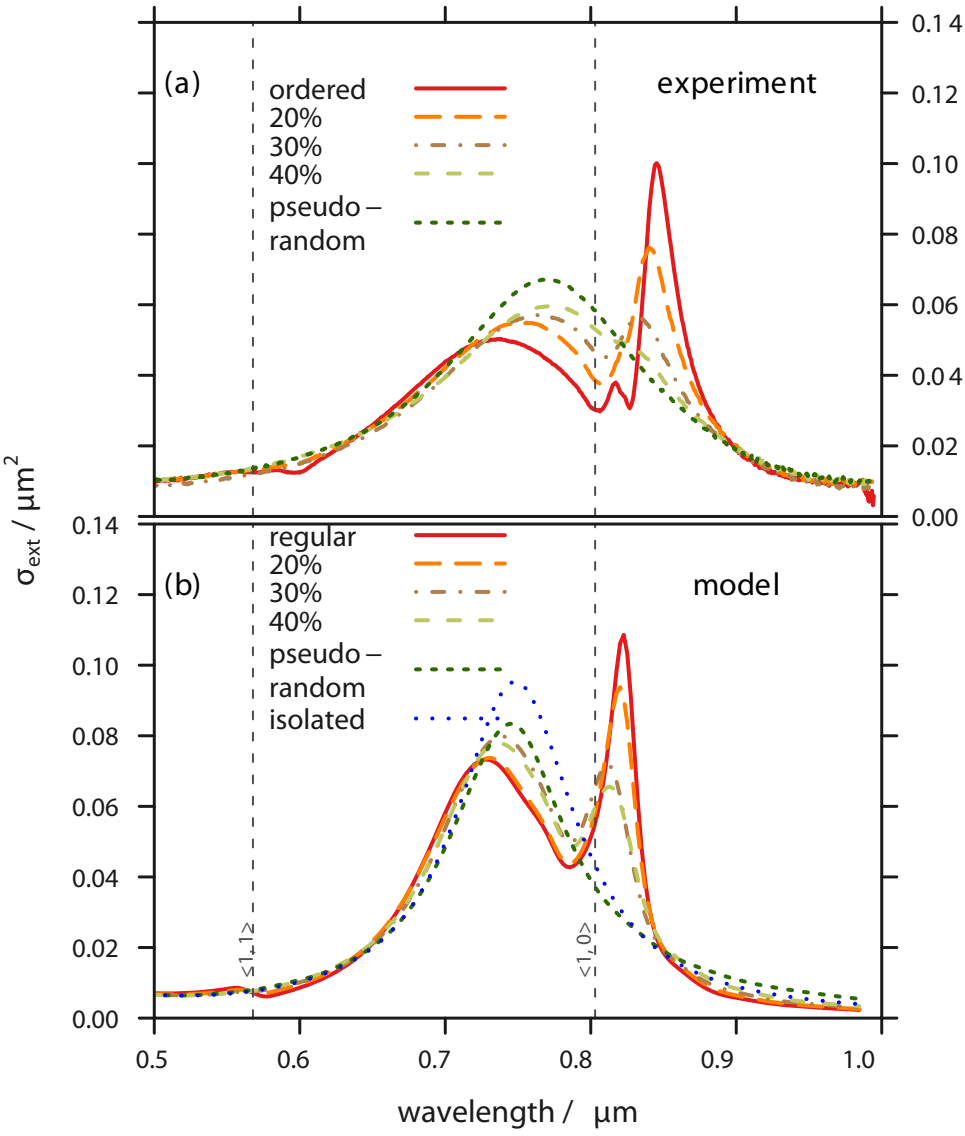

Figure 8.2: (a) Extinction spectra from five different arrays of nanoparticles of varying positional disorder but with constant average occupancy. The deviation from the ordered array is indicated in the legend as a percentage of the nominal regular particle separation (550 nm). The vertical dashed lines indicate the <1 , 0> and <1 , 1> diffraction edges for the periodic array in a homogeneous environment (refractive index 1.46). The nominal particle sizes were 120 nm× 80 nm×35 nm. (b) Calculated extinction spectra using a coupled dipole model with the same parameters.

spectrum characteristic of an inhomogeneously broadened LSPR response. These results are in good agreement with previous investigations on the effect of positional disorder in the optical response of metallic gratings (Nau *et al.* [1]). The design of each disordered configuration studied here was made so as to prevent overlap between particles, as this would introduce an additional, undesired distribution of particle sizes. The spatial pattern of the *pseudo-random* configuration was drawn from a Strauss point process [2, 3] which allows us to minimise the spatial correlation of the particles within the constraint of an exclusion zone around each particle.

Figure 8.2 (b) is the result of a coupled dipole model with 441 dipoles arranged in a 2-dimensional configuration to match that of the experiment. In this approximation, each particle is represented by a dipole of polarizability α, the expression for which was chosen according to the study of Kuwata *et al.* [4] to describe accurately the influence of the particle size and shape, and the relative permittivities of the metal and surrounding medium. This prescription includes terms to describe the dynamic depolarisation and radiative damping that affect particles larger than the Rayleigh limit ($<< \lambda$). The interaction between dipoles is described by the dipolar field that participates in the excitation of the other dipoles [5]. The resulting system of coupled linear equations between the incident field (E_{inc}) and the dipole moments (P) is solved numerically and the result is used to calculate the extinction cross section [5], $\sigma_{\text{ext}} \propto k\Im(E^*_{\text{inc}} \cdot P)$. A good qualitative agreement is found between the modelling and the experimental results (compare fig. 8.2 (a) and (b)), confirming the interpretation of the narrow spectral feature as a result of coherent coupling between the particles mediated by dipolar radiation. The difference in intensity and width of the LSPR between experiment and modelling can be explained by the approximations used in the model for the single particle response: additional damping mechanisms such as surface roughness and the presence of the chromium underlayer are not accounted for in the model. The small, secondary peak seen in the experimental spectra between the two main resonances can be reproduced by allowing a small deviation from normal incidence (numerical results not shown). Furthermore, this simple model allows us to gain information on the single particle extinction spectrum that cannot be obtained from experiment. This information is particularly useful in figure 8.3 where we consider an inhomogeneous distribution of particles.

In figure 8.3(a) I present the effect of a dispersion of particle sizes on the optical spectrum of ordered arrays. Here it is seen that in contrast with the case of positional disorder the dip in the extinction curve associated with the diffraction edge never disappears. In addition, all spectral features broaden with an increasing dispersion in particle sizes (as discussed in chapter 5). The LSPR peak is inhomogeneously broadened and red-shifted by the wide distribution of aspect ratios and volumes of the different particles in the array. Consequently, a measurement of the plasmon lifetime in a collection of particles is often limited by this additional inhomogeneous broadening [6]. The width of the diffractive peak has however a different origin [7], not dictated by the lifetime of the LSPR but rather by factors such as array size, angular spread of illumination, and dispersion in the particle LSPR frequencies. It is the latter factor that is altered here by introducing a distribution of particle sizes.

To illustrate this point, figure 8.3(c) presents the calculated extinction spectra for 5 normal distributions of disorder in particle sizes. Each curve is the average of 441 spectra obtained in the dipolar approximation with a range of long-axis lengths. No interaction between the particles is considered. The underlying distribution of the resonance frequencies of individual particles is displayed in figure 8.3(d). We see that a normal distribution of long-axis sizes results in a broadening of the overall spectrum, and also introduces a red-shift and skewness in the spectral shape. This can be understood by the non-linear dependence of the LSPR spectrum on the length of the long-axis of the ellipsoids, in addition to the dispersion of the material permittivity that strengthens the intensity of the red-shifted resonances. Figure 8.3(b) shows the calculated results for the same

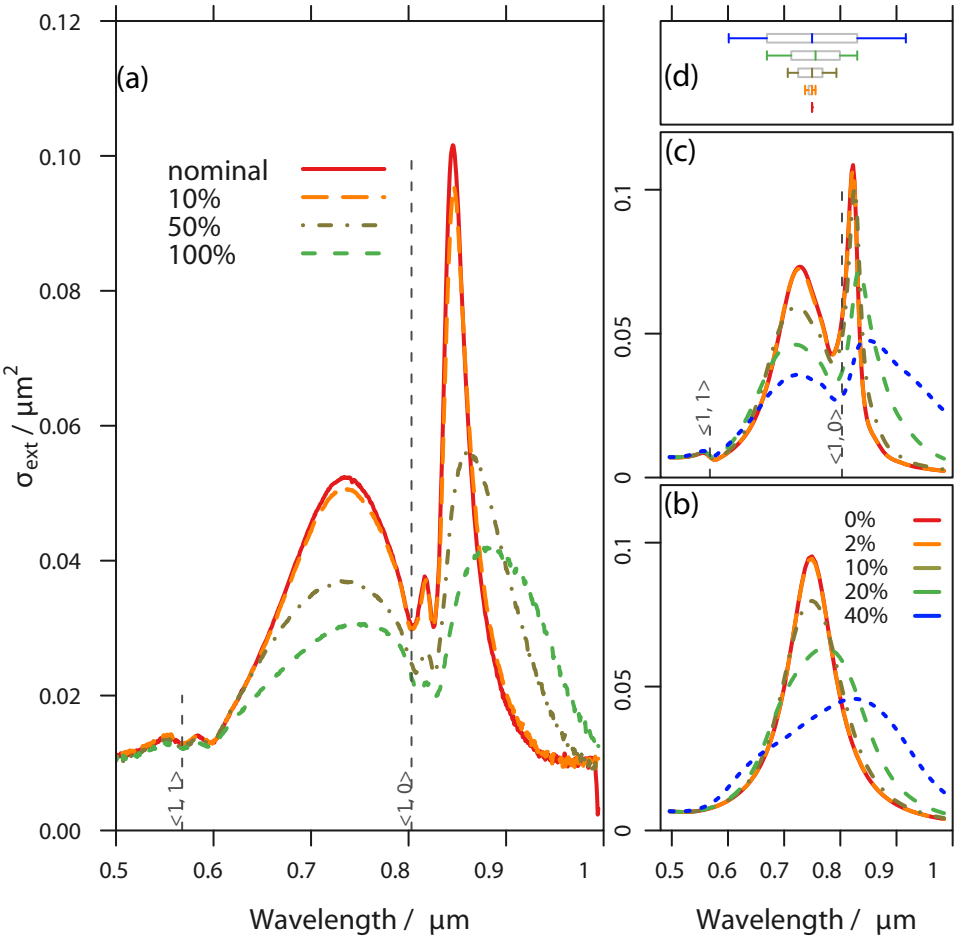

Figure 8.3: (a) Extinction spectra from arrays of nanoparticles with regular positions but variation in particle sizes. The legend indicates the level of disorder introduced in the length of the long axis of the nanorods. The vertical dashed lines indicate the <1,0> and <1,1> diffraction edges for the 550 nm periodic array in a 1.46 refractive index homogeneous environment. The nominal particle sizes were 120 nm×80 nm×35 nm. (b) Calculated average spectra for 5 distributions of 441 ellipsoids. (c) Calculated spectra for a regular array of dipoles (pitch 550 nm) using the distribution of individual LSPR frequencies shown in (d).

distributions of particle sizes, but with the dipoles being part of an array of periodicity 550 nm. The dipolar coupling results in a strong modification of the spectral lineshape that qualitatively reproduces the experimental results. Introducing a distribution of particle sizes means that some particles will have LSPRs that no longer match well with the period — they thus contribute less effectively to the coherent coupling, and so by varying the distribution of particle sizes, fewer particles support a LSPR that can contribute to the coherent coupling.

8.2.1 Array size

An important question to address is the number of particles participating to this coherent interaction in an array. Because the coupling occurs via dipolar radiation, the range of interaction can be very large. The simplified coupled dipole model used in chapter 6 was in fact making the assumption of an infinite array, and we saw that it was able to reproduce most of the features observed in

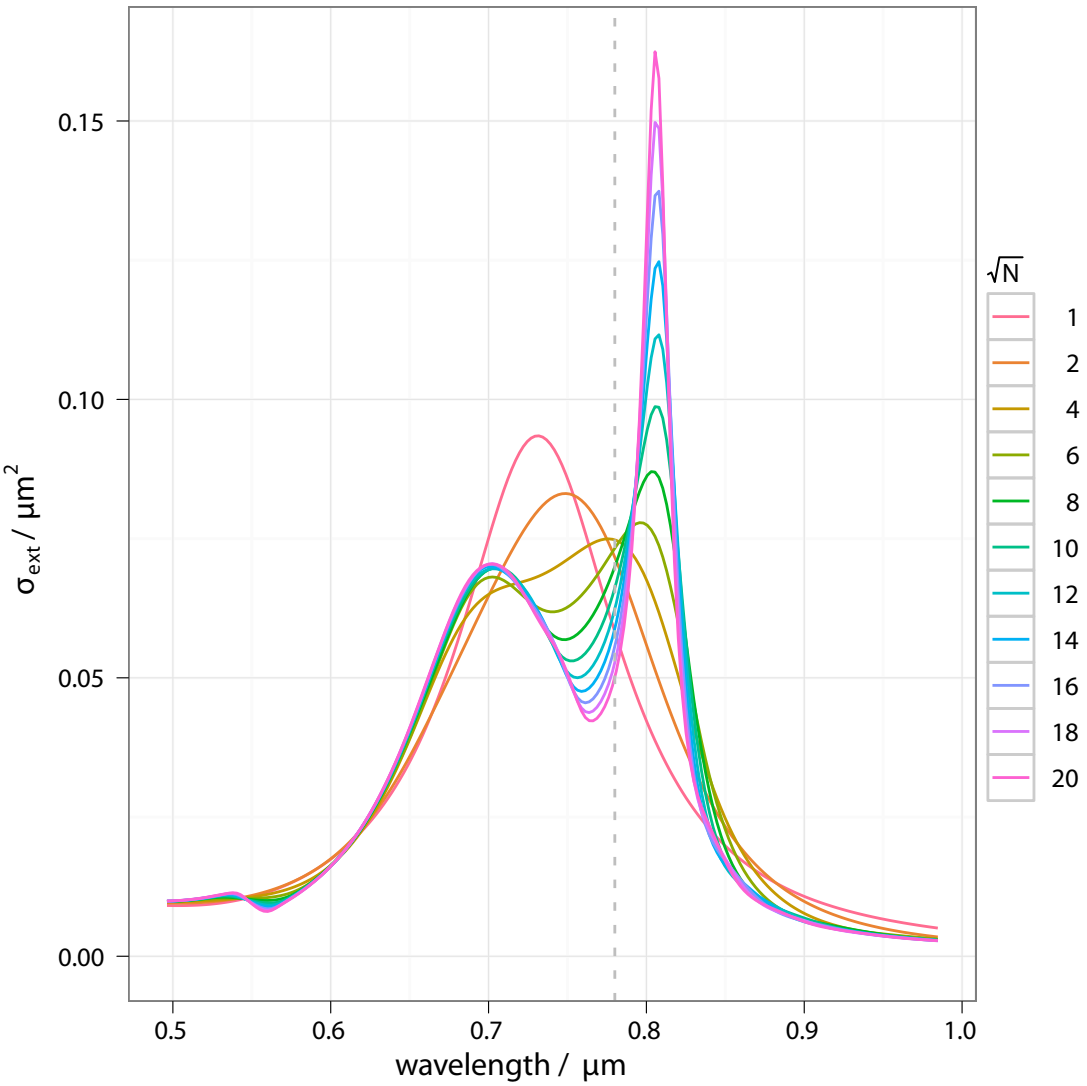

Figure 8.4: Coupled dipole model for the spectral response of particle arrays as a function of number of particles. The dipoles correspond to a gold ellipsoid of semi-axes 60 nm×40 nm×20 nm in surrounding medium 1.5. The periodicity is 520 nm.

the experiments. From an experimental point of view, the fabrication process makes it difficult to maintain a good resolution and order beyond the typical array size of 35×35 microns. A very interesting experiment would consist in constructing arrays of identical particles and identical spacing, but with varying dimensions. A technical difficulty was found in that the distribution of particle sizes is affected by the spatial extent of the array when no special care is taken to compensate for proximity effects in the electron-beam lithography procedure. This variation of particle sizes makes it more difficult to assess the influence of the array size on the strength of the extinction.

The coupled dipole model that was successfully adapted to model realistic array configurations can be used to predict the influence of the array size on the extinction spectra, in ideal conditions (no disorder, perfect coherence). In figure 8.4 a set of extinction spectra is presented for an increasing number of particles. It is seen how the coupling of the dipoles influences the isolated spectral

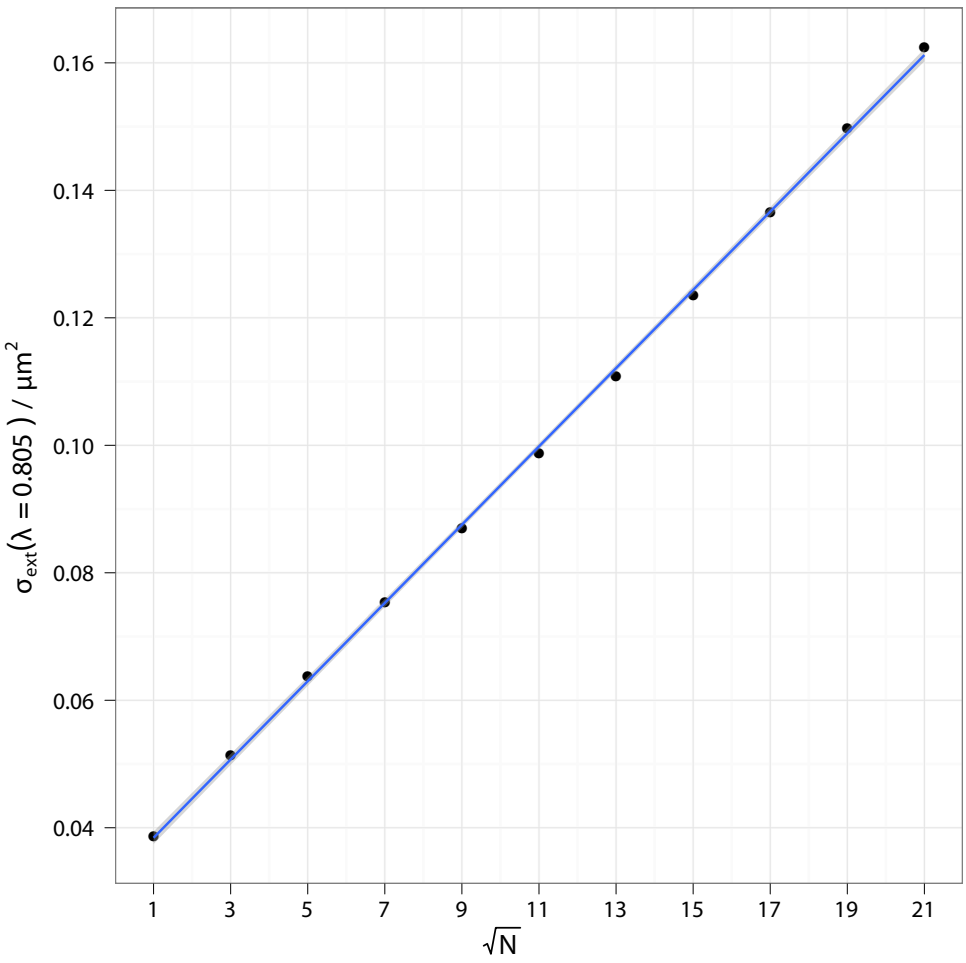

Figure 8.5: Coupled dipole model. Intensity of the diffractive peak as a function of number of particles.

response by splitting the LSPR in two distinct peaks. As the number of particles is increased, the diffractive peak is more and more intense, at the expense of the extinction in the broad resonance.

In figure 8.5 the peak intensity is plotted against the number of particles along one dimension of the array (the square root of the total number of particles). The trend is almost linear, and suggests that the coupling is occurring preferentially along one axis, in good agreement with the far-field expression of a dipole which is maximum along the axis orthogonal to the incident polarisation.

8.3 Conclusion

This study provides some insight into the coherent interaction between particles ordered in a periodic, two-dimensional array. In particular we have seen how the periodic arrangement results in a sharp spectral feature near the diffraction edge, and how this effect can be totally suppressed by altering the spatial correlation between the scattering centres. Of much importance for potential applications is the width of the diffractive peak, and I assessed the influence of a dispersion in particle sizes on the intensity and width of the spectral lineshape. A coupled dipole model was used to disentangle the effects of inhomogeneous broadening and coherent multiple scattering.

"And would it have been worth it, after all,
After the cups, the marmalade, the tea,
Among the porcelain, among some talk of you and me,
Would it have been worth while
To have bitten off the matter with a smile […]

And would it have been worth it, after all,
Would it have been worth while,
After the sunsets and the dooryards and the sprinkled streets,
After the novels, after the teacups,
after the skirts that trail along the floor–
And this, and so much more?–
It is impossible to say just what I mean!
But as if a magic lantern threw the nerves in patterns on a screen:
Would it have been worth while?
If one, settling a pillow or throwing off a shawl,
And turning toward the window, should say:
'That is not it at all,
That is not what I meant, at all' "

T.S. Eliot

9 Conclusions

The optical properties of gold nanoparticles have been investigated in this thesis with a series of experiments performed on single particles and on two-dimensional arrays of particles in different configurations.

A review of the current modelling techniques available to describe the interaction of light with gold nanoparticles was given in chapter 2 and chapter 3. Although there is a wide range of techniques available to describe the scattering response of gold nanoparticles, the research in this field is very active as the precise morphology and dielectric function of the particles has a very strong influence on the observed optical properties. A successful comparison between experiment and theory still suffers from the high computational cost of solving this particular scattering problem, and the limited description of the material in terms of a macroscopic dielectric function that is not necessarily adequate (*e.g.* non-local effects) or well characterised.

In chapter 4, the precise morphology of isolated gold nanorods was seen to offer a large tunability of the resonant excitation of localised plasmon resonances by incident light. The strong scattering response of gold nanorods of varying size and aspect ratio was probed by dark-field spectroscopy and revealed several trends. (i) The aspect ratio and size of the particle can be used to tune the resonance frequency (as with a radio-wave antenna). This behaviour was well accounted for by modelling the particles as dipolar scatterers. The finite size of the particles introduces retardation effects that need to be considered in the modelling to obtain a good agreement between the experimental observations and the dipolar approximation. However, it was observed that larger particles present a more complicated scattering response with a mixture of resonances in the scattering spectra. This experimental observation was attributed to the lack of symmetry of the granular particles obtained by thermal evaporation, and the uncertainty in the polarisation of the incident light with respect to the principal axes of the particles. A comparative study with mono-crystalline

nanorods could allow for a better characterisation of these effects. (ii) The width of the LSPR is the result of several contributions. First, the material properties (described by a complex permittivity ε) account for the *intrinsic* broadening the LSPR. This contribution can be modelled in good agreement with experimental data from small gold nanorods in the Rayleigh regime [1]. Second, nanoparticles of small size and/or large aspect ratio exhibit an additional damping mechanism that arises from the restricted mean free path of the electrons (surface scattering). This effect was seen to be important for the smaller particles characterised in this thesis, and improved the agreement between numerical modelling and experiments (figure 4.6). Last, the volume of the nanoparticles has a strong influence on the width of the LSPR through the mechanism of radiative damping. An experimental study of the relative influence of the radiative and intrinsic damping contributions would benefit from the possibility of creating a series of particles with a constant volume but a differing aspect ratio. Alternatively, Liu *et al.* [2] recently performed a series of experiments with a varying temperature that allowed them to decorrelate the effects of intrinsic damping from the radiative damping contribution.

The optical response of gold nanorods being well characterised in chapter 4, the subject of chapter 5 focussed on the response of a collection of such particles in close proximity (average spacing $\sim$ 200 nm–400 nm). In this situation, the particles present a modified optical response that is due to the electromagnetic interaction between neighbouring particles. Each particle is excited by a combination of the incident field and a superposition of partial waves multiply scattered in the cluster of particles. The spectral response of such collections of particles was examined in bright field transmission spectroscopy and revealed the following conclusions. First, the observation of a large sample of particle responses affects the observed lineshape by inhomogeneous broadening. The resonance observed in extinction measurements on several particles leads to a much broader lineshape than in single particle measurements on isolated particles. This effect was verified using samples prepared by electron-beam lithography for which three particles were individually probed by dark-field spectroscopy, in comparison to the global extinction obtained from the three particles simultaneously. The spectral lineshape can be represented as a convolution of the individual particle spectra with the distribution of resonance frequencies. The optical response of a collection of particles may also differ from the individual particle response because of the electromagnetic coupling between particles. In the dipole model, this coupling leads to a broadening of the spectral shape for dense arrangements of particles. Further, the proximity of neighbouring particles with a strong scattering response can result in the excitation of multipolar resonances that would not be observed for isolated particles illuminated by a single plane wave. This coupling to higher order resonances was modelled for a cluster of spheres using an extension of the Mie theory and revealed a complex interaction between particles. The predicted behaviour involves a balance between the dipolar response and the excitation of higher-order resonances. This interesting regime of interactions could only be explained by further experiments with large nanoparticles, and a theoretical description of the coupling between multipoles in adjacent particles. It is expected that the physics of such coupling can yield a rich variety of optical effects as does the dipolar coupling between neighbouring particles.

In order to maintain a sharp resonant feature in the optical response of arrays of nanoparticles with a dipolar response, a different regime was investigated in chapter 6— 8. The separation of the particles was chosen to be commensurate with the wavelength of resonant excitation of the localised plasmon supported by the individual particles. In this regime we observe the interplay of two resonant mechanisms. First, the isolated particles support a LSPR that leads to a strong scattering response. Second, the periodic arrangement of scatterers forms a diffraction grating that exhibits a *geometric resonance* when the light that is scattered by each particle is in phase with the light scattered by the other particles. This coherent multiple scattering process strongly modifies the LSPR and results in a sharp spectral feature near the diffraction condition. The experimental demonstration of this effect is presented in chapter 6. A simple coupled dipole model is used to describe the basic principle of this diffractive coupling. An index asymmetry of the surrounding environment of the particles was shown experimentally to strongly alter the radiative coupling between particles. Recent works [3] suggest that the diffractive coupling can survive a small index asymmetry. The study of the strength of the surface mode as a function of index asymmetry is the subject of current research in collaboration with the group of J. García de Abajo.

In chapter 7 the properties of such diffractive arrays of gold nanorods are further investigated in a symmetric environment by varying the particle size and periodicity. It is found that the integrated extinction per particle obeys a sum rule that related the shape factor and the volume of the particle to the integrated extinction at all frequencies. This sum rule is tested against the data and numerical modelling on gold ellipsoids. Further theoretical work seems to be needed in order to confirm the sum rule for particles with large aspect ratio and a realistic form of the dielectric function.

The influence of disorder on the diffractive coupling of gold nanoparticle arrays is studied in chapter 8 where the idealised periodic structure of chapter 6 is altered in two ways. First, the particles are displaced from their regular location by an increasing amount. It is seen that the sharp and intense spectral feature resulting from the coherent multiple scattering in the plane of the particles is progressively weakened. In the limit of uncorrelated positions, the extinction spectrum is the result of an inhomogeneously broadened collection of non-interacting single particles. A coupled dipole model is used to investigate this effect numerically and the results confirm the experimental observations. Second, the particles are placed on a regular array, with a distribution of particle sizes. Here the diffractive coupling is observed at the diffraction edge of the grating, but the main resonance features associated with the excitation of LSPRs on the particles is broadened and weakened by the distribution of localised resonances.

A

Poynting theorem and elastic scattering cross-sections

The rate of work done by the incident field on a system of charges is given by [1, 2],

$$W = \mathscr{J} \cdot \mathscr{E} \tag{A.1}$$

Conservation of energy requires the conversion of this incident electromagnetic power into mechanical energy and heat [3].

The total current $\mathscr{J}$ is given by the Maxwell equation $\mathscr{J} = \nabla \times \mathscr{H} - \partial_t \mathscr{D}$,

$$W = (\nabla \times \mathscr{H}) \cdot \mathscr{E} - (\partial_t \mathscr{D}) \cdot \mathscr{E}. \tag{A.2}$$

Let us consider the divergence of the Poynting vector defined as $\mathscr{S} = \mathscr{E} \times \mathscr{H}$,

$$\nabla \cdot \mathscr{S} = \mathscr{H} \cdot \nabla \times \mathscr{E} - \mathscr{E} \cdot \nabla \times \mathscr{H}. \tag{A.3}$$

Using the Maxwell equations, we substitute $\nabla \times \mathscr{E} = -\partial_t \mathscr{B}$, leading to the Poynting theorem,

$$-\mathscr{J} \cdot \mathscr{E} = \nabla \cdot \mathscr{S} + (\mathscr{H} \cdot \partial_t \mathscr{B} + \mathscr{E} \cdot \partial_t \mathscr{D}), \tag{A.4}$$

which expresses the conservation of energy: the power extracted from the applied field is equal to the divergence of the power radiated by the charges plus the rate of change of the energy density u defined as [2],

$$u = \mathscr{H} \cdot \partial_t \mathscr{B} + \mathscr{E} \cdot \partial_t \mathscr{D}. \tag{A.5}$$

Taking the time-average of equation A.4 gives the steady-state absorption of energy in the form of heat,

$$Q = < u > = \frac{1}{T} \int_0^T u(t) \mathrm{d}t. \tag{A.6}$$

It is convenient to express equation A.4 for a monochromatic field of frequency ω. The real fields in equation A.4 are expressed in terms of the complex fields in the frequency domain according to [2],

$$\begin{aligned} \mathscr{E} &\rightarrow (\mathbf{E} + \mathbf{E}^*)/2 \\ \partial_t \mathscr{D} &\rightarrow -i\omega(\varepsilon \mathbf{E} - \varepsilon^* \mathbf{E}^*)/2 \\ &\cdots \end{aligned}$$

Averaging the energy density with respect to time,

$$\left.\begin{array}{c} < \mathbf{E} \cdot \mathbf{E} > \\ < \mathbf{E}^* \cdot \mathbf{E}^* > \\ \cdots \end{array}\right\} \propto \int_0^T \exp(\pm 2 i \omega t) = 0.$$

Two non-zero terms remain,

$$Q = i\omega \left((\varepsilon^* - \varepsilon) \mathbf{E} \cdot \mathbf{E}^* + (\mu^* - \mu) \mathbf{H} \cdot \mathbf{H}^* \right),$$

which simplifies to,

$$Q = \omega \left(\varepsilon'' |\mathbf{E}|^2 + \mu'' |\mathbf{H}|^2 \right). \tag{A.7}$$

We note that if the conductivity is purely imaginary, $\varepsilon'' = 0$, and the material does not absorb energy. The absorption of energy (ohmic loss) is given by the in-phase component of the current times the incident field,

$$< u > = \frac{1}{T} \int_0^T J \sin(\omega t - \phi) \cdot E \sin(\omega t) \mathrm{d}t = \frac{EJ}{2} \cos(\phi), \tag{A.8}$$

which translates into $\Re(\mathbf{E} \cdot \mathbf{J}^*)$ in the Fourier domain.

The energy density requires a more careful treatment in the case of a dispersive medium (see [2]),

$$u = \partial_\omega (\varepsilon \omega) |\mathbf{E}|^2 + \partial_\omega (\mu \omega) |\mathbf{H}|^2. \tag{A.9}$$

A.1 Cross-sections

The time average of the energy density gives the rate of dissipation of energy in ohmic loss. Integrating over the particle volume and normalising by the incident power flux, we obtain the absorption cross-section [4],

$$\sigma_{\mathrm{abs}} = \frac{k}{|\mathbf{E}_{\mathrm{inc}}|^2} \int_{\mathrm{volume}} \varepsilon'' |\mathbf{E}|^2 \, d^3 r. \tag{A.10}$$

The scattering cross-section is obtained by integrating the real part of the complex Poynting vector $\mathbf{E} \times \mathbf{H}^*$ over the full solid angle around the scatterer,

$$\sigma_{\text{sca}} = \frac{k}{|\mathbf{E}_{\text{inc}}|^2} \int_{\text{sphere}} \Re(\mathbf{E} \times \mathbf{H}^*) \cdot \hat{\mathbf{n}} \, ds. \tag{A.11}$$

The work $\Re(\mathbf{E}_{\text{inc}} \cdot \mathbf{J}^*)$ done by the incident field on the charges of the scattering body results in both absorption and scattering [5]. Noting that the current $\mathbf{J}$ corresponds to a polarisation $\mathbf{J} = -i\omega\mathbf{P}$, we can write,

$$\sigma_{\text{ext}} = \frac{k}{|\mathbf{E}_{\text{inc}}|^2} \Im \left(\int_{\text{volume}} \mathbf{E}_{\text{inc}}^* \cdot \mathbf{P} \, d^3 r \right). \tag{A.12}$$

The polarisation $\mathbf{P}$ can be expressed in terms of the internal field $\mathbf{P} = (\varepsilon - 1)\mathbf{E}$, giving an alternative expression for the extinction cross-section [4],

$$\sigma_{\text{ext}} = \frac{k}{|\mathbf{E}_{\text{inc}}|^2} \Im \left(\int_{\text{volume}} (\varepsilon - 1)\mathbf{E}_{\text{inc}}^* \cdot \mathbf{E} \, d^3 r \right). \tag{A.13}$$

B

On the resonance of a radiating dipole perturbed by its environment and its relation to the effective polarizability

B.1 Lineshape of the LSPR

Let us consider a small spherical particle characterised by a static polarizability α,

$$\alpha = \frac{\varepsilon - 1}{\varepsilon + 2}. \tag{B.1}$$

The metal is described by the Drude permittivity

$$\varepsilon = 1 - \frac{\omega_p^2}{\omega^2 + i\gamma\omega}, \tag{B.2}$$

which, inserted in equation B.1 yields,

$$\alpha = \frac{\omega_0^2}{(\omega^2 - \omega_0^2) + i\gamma\omega}, \quad \omega_0 = \omega_p/\sqrt{3}. \tag{B.3}$$

The scattering is proportional to $|\alpha|^2$, leading to a lineshape of the form,

$$\sigma_{\text{sca}} \propto \frac{\omega_0^4}{(\omega^2 - \omega_0^2)^2 + \gamma^2\omega^2}. \tag{B.4}$$

Close to the resonance ($\omega \approx \omega_0$),

$$\omega^2 - \omega_0^2 = (\omega - \omega_0)(\omega + \omega_0) \approx 2\omega_0(\omega - \omega_0).$$

The lineshape can therefore be approximated by a Lorentzian (Cauchy distribution),

$$\sigma_{\text{sca}} \propto \frac{\omega_0^2}{(\omega - \omega_0)^2 + (\gamma/2)^2}. \tag{B.5}$$

B.2 Effective polarizability

The polarizability equation B.1 needs to be corrected to account for radiative damping and dynamic polarisation. This is done by considering the net field acting on each sub-element of the particle to be the sum of the incident field plus a contribution arising from the neighbouring polarisation. The result of this self-consistent equation for the net field yields a corrected polarizability of the form,

$$\alpha^* = \frac{1}{1/\alpha - c}, \tag{B.6}$$

where c is a complex number, $c = k^2/a - 2/3ik^3$.

Similarly, the electromagnetic interaction of two dipoles can be cast in a linear system of coupled equations that yields an effective polarizability for the dimer of the form equation B.6. Here c is a tensor with complex elements that describes the radiative coupling between two dipoles (the Green's dyadic).

This situation can be generalised to the interaction of dipoles in an infinite array illuminated at normal incidence. All dipoles are equivalent, and their response can be cast in the form equation B.6 where c is defined as the array factor (noted S in chapter 6). This is a complex number that describes the dipolar interaction of the array of dipoles. From a dimensionality argument, $[S] = [1/\alpha]$, therefore S can be thought of as the description of the field radiated by a Dirac comb of unit dipoles. The response of the array is then given by the convolution of the response of the real dipole with this Green's dyadic.

Assuming the form of α to be that of a Cauchy distribution (equation B.3), the effective polarizability α^* can be written as

$$\alpha^* = \frac{\omega_0^2}{(\omega^2 - \omega_0^2) + i\gamma\omega - \omega_0^2 c}. \tag{B.7}$$

The complex number c can be split into its real and imaginary part, leading to the following conclusion,

- $\Re(c)$ results in a shift of the resonance frequency from ω_0 to $\omega_0 - \Re(c)$
- $\Im(c)$ results in a modification of the resonance width from γ to $\gamma + \Im(c)$.

This result explains qualitatively the spectral shift and modification of width of the LSPR in three cases considered in this work. (i) The formulation of the modified long wavelength approximation. (ii) The response of a pair of dipoles. (iii) The radiative coupling in an infinite array of

identical dipoles illuminated at normal incidence. It should be noted, however, that c can be frequency dependent which results in a more complicated modification to the spectral lineshape than a frequency shift and change of resonance width.

C

Electron beam lithography: detailed procedure

In this section I will describe the details of the electron-beam lithography procedure.

C.1 Exposure

The substrate is placed on a conducting sample holder in the vacuum chamber of the EBL system. The process of EBL requires the following steps,

1. *Beam cross-over*
   After several weeks of use, the beam can show an offset that depends on the voltage and intensity settings. This misalignment needs to be adjusted manually by tuning the lens and beam offset parameters (figure C.1(c)).

2. *Specimen current*
   The 'Faraday cup' (figure C.1(a)) is used to determine the intensity of the current formed by the electron-beam from the source to the sample. By focussing the beam to the Faraday cup the maximum intensity is recorded and adjusted if necessary. Typical values were in the range $25 - 40$ pA.

3. *Alignment of the stage*
   The sample is placed on a XYZ-stage that can be moved in three directions and rotated. The sample is first rotated to be parallel to the axes of translation of the stage, and the height is carefully adjusted to a working distance of 5 mm. A focussing knob is adjusted to link the actual level of the stage to the monitoring program.

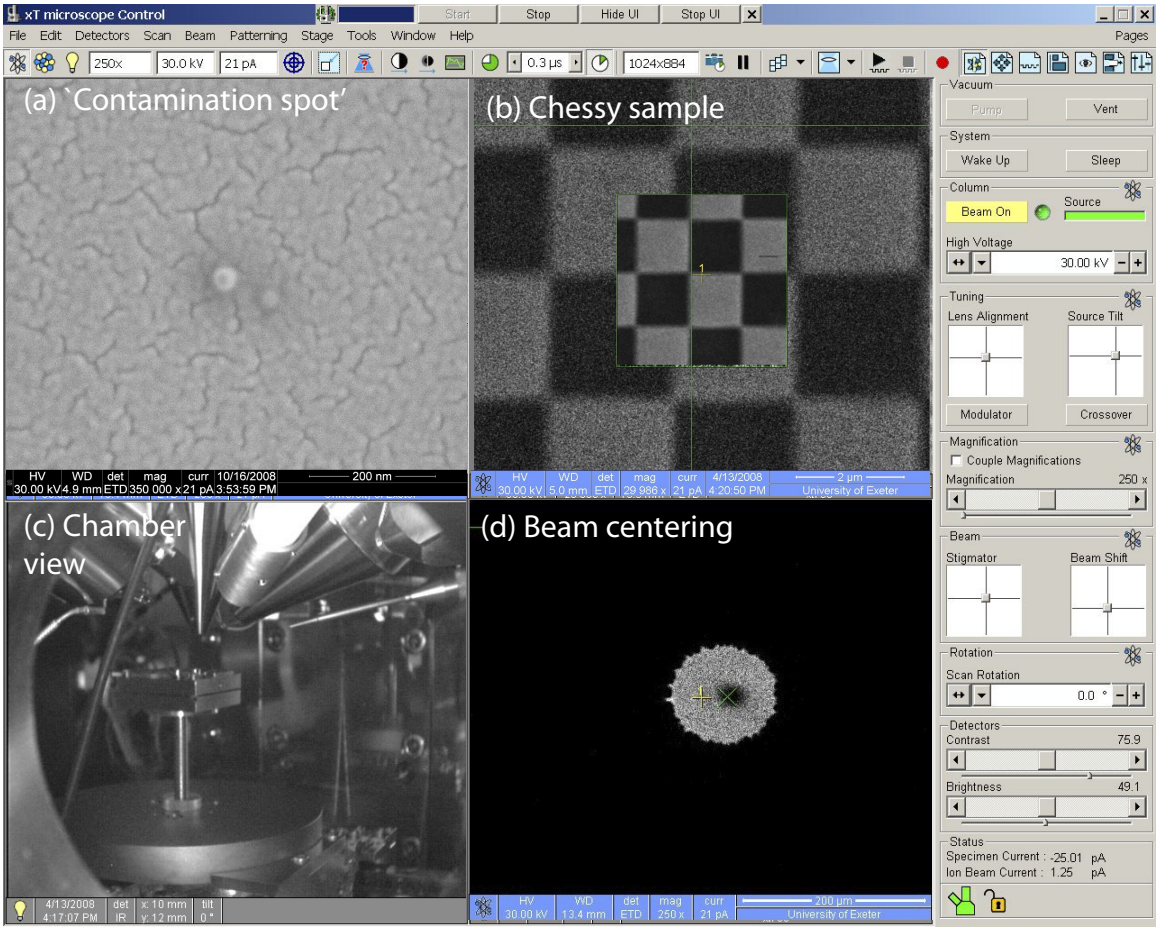

Figure C.1: Electron-beam lithography procedure (the figure is a montage from 3 individual screen-shots for illustration purposes).

4. *Write-field alignment*
   The stage is moved to the 'chessy sample' which is a metallic pattern designed for alignment procedures (figure C.1(b)). Square marks are separated by precise distances (1 µm, 10 µm…). A dedicated position list is used to set 3 specific markers aligned with the grid, and record the corresponding actual position of the beam measured by the sensors. This procedure needs to be performed at the write-field and magnification settings that will be used during the exposure.

5. *UV alignment*
   Similarly, the stage coordinates system needs to be aligned with the sample, and this is done by recording the position against 3 locations on the chessy sample.

6. *Focussing*
   The stage is moved so as to align the beam with the centre of the substrate. The beam needs to be blanked when passing near the region to be exposed. To adjust the focussing of the beam, a sacrificial area is chosen near the edge of the sample. The height of the stage is adjusted together with the focussing knob so as to recover the working distance of 5 mm

that was used for the beam alignment. The beam also needs to be precisely focussed on the surface of the substrate, and should not present a distortion (astigmatism). This important procedure is carried out by exposing a nanometre-sized point of the surface for a few seconds. The contamination of the chamber (small quantities of remaining gas) are deposited by the electron-beam on the surface and provide a cross-section of the beam shape at the surface. The 'contamination spot' should be a small (typically about 20 nm radius), round point. If the size of the spot is too large, the exposure will not be accurate. If the spot is distorted, the beam is astigmatic and this will also cause a loss of accuracy in the particle shapes. A typical 'contamination spot' is shown in figure C.2(a). The grain structure of the gold film used for electrical conductivity is well resolved and indicates a good focus.

7. *Exposure*
   The beam is blanked, the magnification is set to the value used in step 3 (1875×), and the origin of coordinates is set to the central part of the sample. The position list is loaded in the program and the exposure can start (with a duration of typically a few hours for the samples fabricated in this thesis).

C.2 Metal deposition

The triangular particles have a thin (~ 2 nm) chromium underlayer deposited before the ~ 40 nm thick layer of gold. Because of the necessity of not breaking the vacuum between the deposition of both metals, two boats are used to hold and melt the different metals. In this case, the separation between the boats was too large , resulting in a displacement of the layers deposited on the substrate through the PMMA mask. Such an effect can be minimized by adjusting the position of the boats closer to the vertical of the sample, and when possible using a higher deposition chamber.

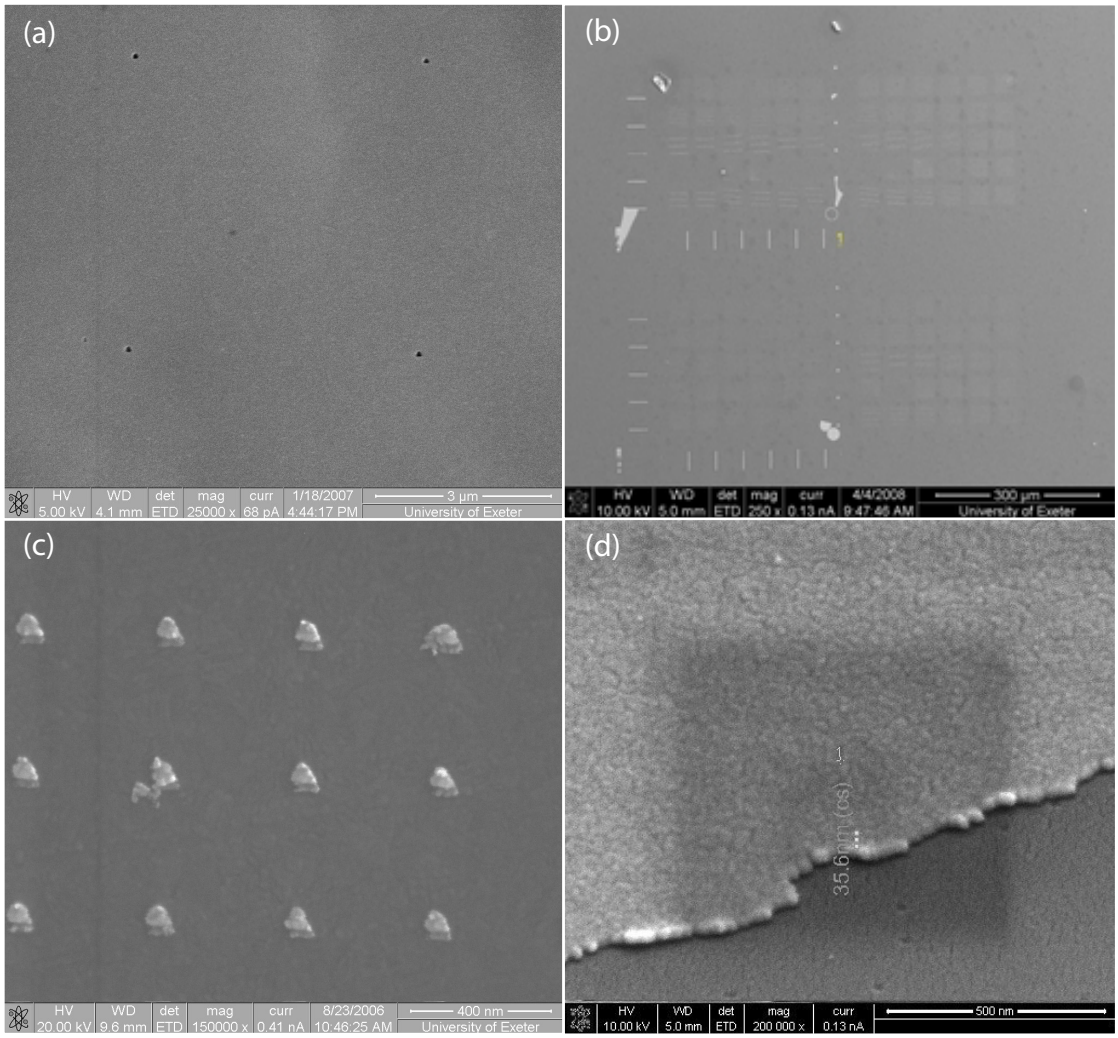

Figure C.2: SEMs illustrating the metal deposition after e-beam lithography. (a) Sample before the lift-off procedure. The 4 dark triangular holes correspond to the position of the particles where the resist was exposed and removed. (b) General overview of a typical EBL sample. Square arrays of particles and large labels (text and arrows) extend over an area of about half a millimetre squared. (c) Triangular gold particles after the lift-off, with a chromium underlayer. The offset is due to the excessive separation (about 5 cm) of the two boats in the chamber during the thermal evaporation. (d) Tilted SEM of a large gold label after the metal deposition. The thickness can be estimated from this measurement, with a correction for the tilt angle (52°).

References

Introduction

1. Barnes, W., Dereux, A. & Ebbesen, T. W. Surface plasmon subwavelength optics. *Nature* **424,** 824–830 (2003).
2. Novotny, L. & Hecht, B. *Principles of nano-optics* (Cambridge University Press, 2006).
3. Anker, J. *et al.* Biosensing with plasmonic nanosensors. *Nature Materials* **7,** 442–453 (2008).
4. Homola, J. *Surface Plasmon Resonance Based Sensors* 1st ed. (Springer, 2006).
5. Homola, Yee, S & Gauglitz Surface plasmon resonance sensors: review. *Sensors and Actuators B: Chemical* **54** (1999).
6. Whitney, A. Localized surface plasmon resonance nanosensor: A high-resolution distance-dependence study using atomic layer deposition. *Journal of Physical Chemistry B* **109,** 20522–20528 (2005).
7. Haes, A., Hall, W., Chang, S., Klein, W. & Van Duyne, R. P. A localized surface plasmon resonance biosensor: First steps toward an assay for Alzheimer's disease. *Nano Letters* **4,** 1029–1034 (2004).
8. Haes, A., Zou, S., Van Duyne, R. P. & Schatz, G. A nanoscale optical biosensor: The long range distance dependence of the localized surface plasmon resonance of noble metal nanoparticles. *Journal of Physical Chemistry B* **108,** 109–116 (2004).
9. Haes, A. & Van Duyne, R. P. A unified view of propagating and localized surface plasmon resonance biosensors. *Anal Bioanal Chem* (2004).
10. Haes, A. *Localized Surface Plasmon Resonance Spectroscopy for Fundamental Studies of Nanoparticle Optics and Applications to Biosensors* PhD thesis (Northwestern University, 2004).
11. Haes, A. & Van Duyne, R. P. Nanoscale optical biosensor: Short range distance dependence of the localized surface plasmon resonance of noble metal nanoparticles. *Journal of Physical Chemistry B* **108,** 6961–6968 (2004).
12. Haes, A. & Van Duyne, R. P. A Nanoscale Optical Biosensor: Sensitivity and Selectivity of an Approach Based on the Localized Surface Plasmon Resonance Spectroscopy of Triangular Silver Nanoparticles. *Journal of the American Chemical Society* **124** (2002).
13. Larsson, E., Alegret, J., Käll, M. & Sutherland, D. Sensing characteristics of NIR localized surface plasmon resonances in gold nanorings for application as ultrasensitive biosensors. *Nano Letters* **7,** 1256–63 (2007).
14. Miller, M. *Plasmonic Nanoparticles: Factors Controlling Refractive Index Sensitivity* PhD thesis (Duke University, 2007).
15. McFarland, A. & Van Duyne, R. P. Single silver nanoparticles as real-time optical sensors with zeptomole sensitivity. *Nano Letters* **3,** 1057–1062 (2003).
16. Raether, H. *Surface Plasmons on Smooth and Rough Surfaces and on Gratings* (Springer, 1988).

17. Zhou, Y Quantitative interpretation of gold nanoparticle-based bioassays designed for detection of immunocomplex formation. *Biointerphases* **2** (2007).

18. Kretschmann, E. & Raether, H. Radiative decay of non-radiative surface plasmons excited by light. *Z. Naturforsch* **23A,** 2135–2136 (1968).

19. Murray, W., Suckling, J. & Barnes, W. Overlayers on silver nanotriangles: Field confinement and spectral position of localized surface plasmon resonances. *Nano Letters* **6,** 1772–1777 (2006).

20. Yonzon, C. *et al.* A comparative analysis of localized and propagating surface plasmon resonance sensors: the binding of concanavalin a to a monosaccharide functionalized self-assembled monolayer. *Journal of the American Chemical Society* **126,** 12669–76 (2004).

21. Willets, K. A. & Duyne, R. P. V. Localized surface plasmon resonance spectroscopy and sensing. *Annu Rev Phys Chem* **58,** 267–297 (2007).

22. Vukušić, P. *Sensing thin layers using surface plasmon resonance* PhD thesis (University of Exeter, 1993).

23. Dahlin, A., Tegenfeldt, J. & Hook, F Improving the instrumental resolution of sensors based on localized surface plasmon resonance. *Analytical Chemistry* **78,** 4416–4423 (2006).

24. Schultz, S, Smith, D., Mock, J. & Schultz, D. Single-target molecule detection with nonbleaching multicolor optical immunolabels. *Proceedings of the National Academy of Sciences* **97,** 996–1001 (2000).

25. Raschke, G *et al.* Biomolecular recognition based on single gold nanoparticle light scattering. *Nano Letters* **3,** 935–938 (2003).

26. Novo, C., Funston, A. M., Pastoriza-Santos, I., Liz-Marzán, L. M. & Mulvaney, P. Influence of the medium refractive index on the optical properties of single gold triangular prisms on a substrate. *Journal of Physical Chemistry. C* **112,** 3–7 (2008).

27. Garcia-Parajo, M. F. *Optical antennas focus in on biology* (2008).

28. Gunnarsson, L. *Optical properties of silver nanostructures prepared by electron beam lithography* PhD thesis (Chalmers University of Technology, 2003).

29. Murray, W. *Optical properties of nanoscale silver structures fabricated by nanosphere lithography* PhD thesis (University of Exeter, 2005).

30. Sönnichsen, C. *Plasmons in metal nanostructures* PhD thesis (University of Munich, 2001).

31. Wood, R. On a remarkable case of uneven distribution of light in a diffraction grating spectrum. *Proceedings of the Physical Society of London* **18,** 269 (1902).

32. Rayleigh, L. On the Dynamical Theory of Gratings. *Proceedings of the Royal Society of London. Series A Containing Papers of a Mathematical and Physical Character* **79,** 399–416 (1907).

33. Fano, U. The theory of anomalous diffraction gratings and of quasi-stationary waves on metallic surfaces (Sommerfeld's waves). *Journal of the Optical Society of America* **31,** 213 (1941).

34. Ritchie, R. Plasma losses by fast electrons in thin films. *Physical Review* **106** (1957).

35. Stern, E. & Ferrell, T. Surface Plasma Oscillations of a Degenerate Electron Gas. *Physical Review* **120** (1960).

36. Turbadar, T. Complete Absorption of Light by Thin Metal Films. *Proceedings of the Physical Society* **73,** 40–44 (1959).

37. Otto, A. Excitation of nonradiative surface plasma waves in silver by the method of frustrated total reflection. *Zeitschrift für Physik A Hadrons and Nuclei* **216,** 398–410 (1968).

38. Lorenz, L. Sur la lumière réfléchie et réfractée par une sphère (surface) transparente. *Libraire Lehmann & Stage, Copenhague* (1898).

39. Garnett, M. Colours in Metal Glasses and in Metallic Films. *Royal Society of London Philosophical Transactions Series A* **203,** 385–420 (1904).

40. Mie, G Contributions to the optics of turbid media, particularly of colloidal metal solutions. *Annalen der physik* **25,** 377–445 (1908).

41. Debye, P. Der Lichtdruck auf Kugeln von beliebigem Material. *Annalen der physik* (1909).

42. Wood, R. A suspected case of the electrical resonance of minute metal particles for light-waves. a new type of absorption. *Proceedings of the Physical Society of London* **18,** 166 (1902).

43. Wood, R. On the electrical resonance of metal particles for light-waves - Second Communication. *Proceedings of the Physical Society of London* **18,** 276 (1902).

44. Kreibig, U. & Genzel, L Optical absorption of small metallic particles. *Surface Science* **156,** 678–700 (1985).

45. Bohren, C. & Huffman, D. *Absorption and Scattering of Light by Small Particles* (Wiley, 1998).

46. Pendry, J. Photonic band structures. *Journal of Modern Optics* **41,** 209–229 (1994).

47. Grigorenko, A., Geim, A., Gleeson, H., Zhang, Y & et al. Nanofabricated media with negative permeability at visible frequencies. *Nature Physics* **438** (2005).

48. Murray, W. & Barnes, W. Plasmonic materials. *Advanced Materials* **19,** 3771–3782 (2007).

Background physics

1. Jackson *Classical Electrodynamics* (Wiley, 1999).

2. Born, M. & Wolf, E *Principles of Optics* 7th ed. (Cambridge University Press, 2000).

3. Prescott, S. & Mulvaney, P. Gold nanorod extinction spectra. *Journal of Applied Physics* **103** (2006).

4. Kahnert, M Numerical methods in electromagnetic scattering theory. *Journal of Quantitative Spectroscopy & Radiative Transfer* **79,** 775 (2003).

5. Mishchenko, M. I., Travis, L. & Lacis, A. A. *Scattering, Absorption, and Emission of Light by Small Particles* (Cambridge University Press, 2002).

6. Bottcher, C & F. *Theory of electric polarisation* (Elsevier, 1952).

7. Bliokh, K, Freilikher, V, Savel'ev, S & Nori, F Colloquium: Unusual resonators: Plasmonics, metamaterials, and random media. *Reviews Of Modern Physics* **80,** 1201–1213 (2008).

8. Pattanayak, D. & Wolf, E General form and a new interpretation of the Ewald-Oseen extinction theorem. *Optics Communications* **6,** 217–220 (1972).

9. Mironov, F Extinction theorem for stratified medium. *Journal of Optics* **25** (1994).

10. James, M. & Griffiths, D. Why the speed of light is reduced in a transparent medium. *American Journal of Physics* **60** (1992).

11. Ballenegger, V & Weber, T The Ewald–Oseen extinction theorem and extinction lengths. *American Journal of Physics* **67** (1999).

12. Doyle, W. Scattering approach to Fresnel's equations and Brewster's law. *American Journal of Physics* **53,** 463–468 (1985).

13. Fearn, H, James, D. & Milonni, P. Microscopic approach to reflection, transmission, and the Ewald–Oseen extinction theorem. *American Journal of Physics* **64,** 986–995 (1996).
14. Wriedt, T. *Studies of light scattering by complex particles using the null-field method with discrete sources* (Springer, 2007).
15. Bohren, C. & Huffman, D. *Absorption and Scattering of Light by Small Particles* (Wiley, 1998).
16. Kittel, C. *Introduction to Solid State Physics* (Wiley, 2005).
17. Ritchie, R. Plasma losses by fast electrons in thin films. *Physical Review* **106** (1957).
18. Novotny, L. & Hecht, B. *Principles of nano-optics* (Cambridge University Press, 2006).
19. Johnson, P. & Christy, R. Optical Constants of the Noble Metals. *Physical Review B* **6** (1972).
20. Etchegoin, P., Ru, E. L. & Meyer, M An analytic model for the optical properties of gold. *The Journal of Chemical Physics* **125** (2005).
21. Feynman, R. *QED: The Strange Theory of Light and Matter* (Princeton University Press, 2006).
22. Hooper, I. R., Preist, T. W. & Sambles, J. R. Making Tunnel Barriers (Including Metals) Transparent. *Physical Review Letters* **97,** 053902 (2006).
23. Barnes, W. Surface plasmon–polariton length scales: a route to sub-wavelength optics. *Journal of Optics A: Pure and Applied Optics* **8,** S87–S93 (2006).
24. Raether, H. *Surface Plasmons on Smooth and Rough Surfaces and on Gratings* (Springer, 1988).
25. Herminghaus, S, Klopfleisch, M & Schmidt, H. J Attenuated total reflectance as a quantum interference phenomenon. *Optics Letters* **19,** 293 (1994).
26. Kreibig, U. & Vollmer, M. *Optical Properties of Metal Clusters* (1995).
27. Apell, S., Echenique, P. & Ritchie, R. Sum rules for surface plasmon frequencies. *Ultramicroscopy* **65,** 53–60 (1996).
28. Hohenester, U & Krenn, J. Surface plasmon resonances of single and coupled metallic nanoparticles: A boundary integral method approach. *Physical Review B* **72** (2005).
29. Nelayah, J *et al.* Mapping surface plasmons on a single metallic nanoparticle. *Nature Physics* **3,** 348–353 (2007).

Modelling techniques

1. Lorenz, L. Sur la lumière réfléchie et réfractée par une sphère (surface) transparente. *Libraire Lehmann & Stage, Copenhague* (1898).
2. Garnett, M. Colours in Metal Glasses and in Metallic Films. *Royal Society of London Philosophical Transactions Series A* **203,** 385–420 (1904).
3. Debye, P. Der Lichtdruck auf Kugeln von beliebigem Material. *Annalen der physik* (1909).
4. Mie, G Contributions to the optics of turbid media, particularly of colloidal metal solutions. *Annalen der physik* **25,** 377–445 (1908).
5. Mishchenko, M. I., Travis, L. & Lacis, A. A. *Scattering, Absorption, and Emission of Light by Small Particles* (Cambridge University Press, 2002).
6. Bohren, C. & Huffman, D. *Absorption and Scattering of Light by Small Particles* (Wiley, 1998).
7. Van de Hulst, H. C. *Light Scattering by Small Particles* 470 (Wiley, 1957).
8. Stratton, J. A. *Electromagnetic theory* (McGraw-Hill, 1941).

9. Born, M. & Wolf, E *Principles of Optics* 7th ed. (Cambridge University Press, 2000).
10. Draine, B. The discrete-dipole approximation and its application to interstellar graphite grains. *Astrophysical Journal* **333,** 848–872 (1988).
11. Pendry, J. Photonic band structures. *Journal of Modern Optics* **41,** 209–229 (1994).
12. García de Abajo, F. J. Multiple scattering of radiation in clusters of dielectrics. *Physical Review B (Condensed Matter and Materials Physics)* **60** (1999).
13. Stefanou, N, Karathanos, V & Modinos, A Scattering of electromagnetic waves by periodic structures. *Journal of Physics: Condensed Matter* **4,** 7389–7400 (1992).
14. Moroz, A Density-of-states calculations and multiple-scattering theory for photons. *Physical Review B* **51,** 2068–2081 (1995).
15. Newton, R. *Scattering Theory of Waves and Particles: Second Edition* (Dover, 2002).
16. Myroshnychenko, V. *et al.* Modelling the optical response of gold nanoparticles. *Chem Soc Rev* **37,** 1792–1805 (2008).
17. Schatz, G. Using theory and computation to model nanoscale properties. *Proceedings of the National Academy of Sciences of the United States of America* **104,** 6885–92 (2007).
18. Kahnert, M Numerical methods in electromagnetic scattering theory. *Journal of Quantitative Spectroscopy & Radiative Transfer* **79,** 775 (2003).
19. Mishchenko, M. I., Travis, L. & Lacis, A. A. *Multiple scattering of light by particles* (Cambridge University Press, 2006).
20. Barber, P & Massoudi, H Recent Advances in Light Scattering Calculations for Nonspherical Particles. *Aerosol Science and Technology* **1,** 303–315 (1982).
21. Jensen, L, Kelly, K., Lazarides, A & Schatz, G. Electrodynamics of Noble Metal Nanoparticles and Nanoparticle Clusters. *Journal of Cluster Science* **V10,** 295–317 (1999).
22. Kelly, K., Coronado, E., Zhao, L. & Schatz, G. The Optical Properties of Metal Nanoparticles: The Influence of Size, Shape, and Dielectric Environment. *Journal of Physical Chemistry B* **107,** 668–677 (2003).
23. Kelly, K. L., Lazarides, A. A. & Schatz, G. C. Computational Electromagnetics of Metal Nanoparticles and Their Aggregates. *Computing in Science and Engineering* **3,** 67–73 (2001).
24. Mishchenko, M. I. Far-field approximation in electromagnetic scattering. *Journal of Quantitative Spectroscopy & Radiative Transfer* **100** (2006).
25. Wolf, E. & Foley, J. T. Do evanescent waves contribute to the far field? *Opt. Lett.* **23,** 16–18 (1998).
26. Mishchenko, M. I. Multiple scattering, radiative transfer, and weak localization in discrete random media: Unified microphysical approach. *Reviews of Geophysics* **46** (2008).
27. Draine, B. T. & Flatau, P. J. Discrete-dipole approximation for periodic targets: theory and tests. *Journal Optical Society America A* **25,** 2693–2703 (2008).
28. Mishchenko, M. I. Maxwell's equations, radiative transfer, and coherent backscattering: A general perspective. *Journal of Quantitative Spectroscopy & Radiative Transfer* **101** (2006).
29. Martin, O. Accurate and efficient computation of the Green's tensor for stratified media. *Physical Review E* **62** (2000).
30. Jackson *Classical Electrodynamics* (Wiley, 1999).
31. Novotny, L. & Hecht, B. *Principles of nano-optics* (Cambridge University Press, 2006).

32. Essex, E. Hertz vector potentials of electromagnetic theory. *American Journal of Physics* **45,** 1099–1101 (1977).

33. Mishchenko, M. I. The electromagnetic optical theorem revisited. *Journal of Quantitative Spectroscopy & Radiative Transfer* **101,** 404–410 (2006).

34. Kreibig, U. Silver Nanowires as Surface Plasmon Resonators. *Physical Review Letters* **95** (2005).

35. Novotny, L. Effective Wavelength Scaling for Optical Antennas. *Physical Review Letters* **98,** 1–4 (2007).

36. Ghenuche, P, Cherukulappurath, S, Taminiau, T, Hulst, N. V. & Quidant, R Spectroscopic Mode Mapping of Resonant Plasmon Nanoantennas. *Physical Review Letters* **101** (2008).

37. Pendry, J. B Mimicking Surface Plasmons with Structured Surfaces. *Science* **305,** 847–848 (2004).

38. Venermo, J & Sihvola, A Dielectric polarizability of circular cylinder. *Journal of Electrostatics* **63,** 101–117 (2005).

39. Apell, S., Echenique, P. & Ritchie, R. Sum rules for surface plasmon frequencies. *Ultramicroscopy* **65,** 53–60 (1996).

40. Kreibig, U. & Vollmer, M. *Optical Properties of Metal Clusters* (1995).

41. Moroz, A Depolarization field of spheroidal particles. *Journal Optical Society America B* **26** (2009).

42. Meier, M & Wokaun, A Enhanced fields on large metal particles: dynamic depolarization. *Optics Letters* **8** (1983).

43. Feynman, R. P., Leighton, R. B. & Sands, M. *The Feynman Lectures on Physics* Commemorative Ed 592 (Addison Wesley, 1989).

44. Kuwata-Gonokami, H, Tamaru, H, Esumi, K & Miyano, K Resonant light scattering from metal nanoparticles: Practical analysis beyond Rayleigh approximation. *Applied Physics Letters* **83,** 4625–4627 (2003).

45. Voshchinnikov, N. & Farafonov, V. Optical properties of spheroidal particles. *Astrophysics and Space Science* **204** (1993).

46. Mishchenko, M. I., Hovenier, J. W. & Travis, L. D. *Light Scattering by Nonspherical Particles: Theory, Measurements, and Applications* (Academic Press, San Diego, 2000).

47. Lukʻyanchuk On the peculiarities of light scattering by nanoparticles and nanowires. *Journal of Physics Conference Series* **59** (2007).

48. Willets, K. A. & Duyne, R. P. V. Localized surface plasmon resonance spectroscopy and sensing. *Annu Rev Phys Chem* **58,** 267–297 (2007).

49. Voros, J The Density and Refractive Index of Adsorbing Protein Layers. *Biophysical Journal* **87,** 553–561 (2004).

50. Mishchenko, M. I., Videen, G, Babenko, V., Khlebtsov, N. & Wriedt, T T-matrix theory of electromagnetic scattering by particles and its applications: a comprehensive reference database. *Journal Of Quantitative Spectroscopy & Radiative Transfer* **88,** 357–406 (2004).

51. Agarwal, G. Relation between Waterman's extended boundary condition and the generalized extinction theorem. *Physical Review D* **14** (1976).

52. Nieminen, T., Rubinsztein-Dunlop, H & Heckenberg, N. Calculation of the T-matrix: general considerations and application of the point-matching method. *Journal Of Quantitative Spectroscopy & Radiative Transfer* **79,** 1019–1029 (2003).

53. Adrian Doicu, Y. E. Thomas Wriedt *Light Scattering by Systems of Particles: Null-field Method with Discrete Sources : Theory and Programs* (Springer, 2006).

54. Wriedt, T. *Studies of light scattering by complex particles using the null-field method with discrete sources* (Springer, 2007).

55. Schatz, G. & Van Duyne, R. P. Discrete dipole approximation for calculating extinction and Raman intensities for small particles with arbitrary shapes. *Journal of Chemical Physics* **103,** 869–875 (1995).

56. Goodman, J. & Draine, B. Application of fast-Fourier-transform techniques to the discrete-dipole approximation. *Optics Letters* **16** (2002).

57. Twersky, V Multiple scattering of waves and optical phenomena. *Journal of the Optical Society of America* **52** (1962).

58. Mishchenko, M. I., Liu, L & Videen, G Conditions of applicability of the single-scattering approximation. *Optics Express* **15,** 7522–7527 (2007).

59. Meier, M, Wokaun, A & Liao, P. Enhanced fields on rough surfaces - dipolar interactions among particles of sizes exceeding the Rayleigh limit. *Journal Of The Optical Society Of America B-Optical Physics* **2,** 931–949 (1985).

60. Markel, V. A. Coupled-dipole approach to scattering of light from a one-dimensional periodic dipole structure. *Journal of Modern Optics* **40,** 2281–2291 (1993).

61. Soller, B. & Hall, D. Dynamic modifications to the plasmon resonance of a metallic nanoparticle coupled to a planar waveguide: beyond the point-dipole limit. *Journal Optical Society America B* **19,** 1195–1203 (2002).

62. Zou, S. & Schatz, G. Extinction spectra of nanoparticle arrays: The influence of size, shape, and interparticle spacing. *Abstracts of Papers of the American Chemical Society* **227,** 266–266 (2004).

63. Markel, V. A. Divergence of dipole sums and the nature of non-Lorentzian exponentially narrow resonances in one-dimensional periodic arrays of nanospheres. *Journal Of Physics B-Atomic Molecular And Optical Physics* **38,** L115–L121 (2005).

64. Aspnes, D Optical properties of thin films. *Thin Solid Films* **89,** 249–262 (1982).

65. García de Abajo, F. J. & Sáenz, J. J Electromagnetic Surface Modes in Structured Perfect-Conductor Surfaces. *Physical Review Letters* **95,** 1–4 (2005).

66. García de Abajo, F. J. Nonlocal Effects in the Plasmons of Strongly Interacting Nanoparticles, Dimers, and Waveguides. *The Journal of Physical Chemistry C* **112,** 17983–17987 (2008).

67. García de Abajo, F. J. Interaction of Radiation and Fast Electrons with Clusters of Dielectrics: A Multiple Scattering Approach. *Physical Review Letters* **82** (1999).

68. Novo, C., Funston, A. M., Pastoriza-Santos, I., Liz-Marzán, L. M. & Mulvaney, P. Influence of the medium refractive index on the optical properties of single gold triangular prisms on a substrate. *Journal of Physical Chemistry. C* **112,** 3–7 (2008).

69. Eremina, E., Eremin, Y & Wriedt, T Analysis of the light scattering properties of a gold nanorod on a plane surface via discrete sources method. *Optics Communications* **273,** 278–285 (2007).

70. Johansson, P & Käll, M. Surface-enhanced Raman scattering and fluorescence near metal nanoparticles. *Physical Review B* **72** (2005).

71. Zeman, E. & Schatz, G. *Electromagnetic theory calculations for spheroids: an accurate study of the particle size dependence of SERS and hyper-Raman measurements* tech. rep. (Northwestern University, 1984).

72. Masiello, D & Schatz, G. Many-body theory of surface-enhanced Raman scattering. *Physical Review A* **78** (2008).

Experiments on single nanoparticles

1. Mishchenko, M. I. Gustav Mie and the fundamental concept of electromagnetic scattering by particles: A perspective. *Journal of Quantitative Spectroscopy & Radiative Transfer* 1–21 (2009).
2. Mishchenko, M. I. & Travis, L. Gustav Mie and the Evolving Discipline of Electromagnetic Scattering by Particles. *Bulletin of the American Meteorological Society* **89,** 1853–1861 (2008).
3. Freestone, I, Meeks, N, Sax, M & Higgitt, C The Lycurgus Cup A Roman Nanotechnology. *Gold Bulletin* **40,** 270–277 (2007).
4. Murray, W. & Barnes, W. Plasmonic materials. *Advanced Materials* **19,** 3771–3782 (2007).
5. Zsigmondy, R. A. *Properties of colloids* Nobel Lecture (1926).
6. Hu, M *et al.* Dark-field microscopy studies of single metal nanoparticles: understanding the factors that influence the linewidth of the localized surface plasmon resonance. *Journal of Materials Chemistry* **18,** 1949–1960 (2007).
7. Schultz, S Shape effects in plasmon resonance of individual colloidal silver nanoparticles. *Journal of Chemical Physics* **116** (2002).
8. Sönnichsen, C. *et al.* Drastic Reduction of Plasmon Damping in Gold Nanorods. *Physical Review Letters* **88,** 077402 (2002).
9. Wiederrecht, G. Near-field optical imaging of noble metal nanoparticles. *The European Physical Journal Applied Physics* **28,** 3–18 (2004).
10. Hamann, H Extinction near-field optical microscopy. *Optics Communications* **227,** 1–13 (2003).
11. Lindfors, K, Kalkbrenner, T, Stoller, P & Sandoghdar, V Detection and spectroscopy of gold nanoparticles using supercontinuum white light confocal microscopy. *Physical Review Letters* **93** (2004).
12. Zuechner, T, Failla, A., Hartschuh, A & Meixner, A. A novel approach to detect and characterize the scattering patterns of single Au nanoparticles using confocal microscopy. *Journal Of Microscopy-Oxford* **229,** 337–343 (2008).
13. Sönnichsen, C. *et al.* Spectroscopy of single metallic nanoparticles using total internal reflection microscopy. *Applied Physics Letters* **77,** 2949–2951 (2000).
14. Eremina, E., Eremin, Y & Wriedt, T Simulations of light scattering spectra of a nanoshell on plane interface based on the discrete sources method. *Optics Communications* **267,** 524–529 (2006).
15. Zoriniants, G. & Barnes, W. L. Fluorescence enhancement through modified dye molecule absorption associated with the localized surface plasmon resonances of metallic dimers. *New Journal of Physics* **10,** 105002 (2008).
16. Canfield, B. *et al.* Linear and nonlinear optical properties of gold nanoparticles with broken symmetry. *Journal Of Nonlinear Optical Physics & Materials* **15,** 43–53 (2006).
17. Johansson, P & Käll, M. Surface-enhanced Raman scattering and fluorescence near metal nanoparticles. *Physical Review B* **72** (2005).

18. Wriedt, T. *Studies of light scattering by complex particles using the null-field method with discrete sources* (Springer, 2007).
19. Johnson, P. & Christy, R. Optical Constants of the Noble Metals. *Physical Review B* **6** (1972).
20. Mulvaney, P. Contributions from radiation damping and surface scattering to the linewidth of the longitudinal plasmon band of gold nanorods: a single particle study. *Physical Chemistry Chemical Physics* **8,** 3540–3546 (2006).
21. Sherry, L., Jin, R, Mirkin, C., Schatz, G. & Van Duyne, R. P. Localized surface plasmon resonance spectroscopy of single silver triangular nanoprisms. *Nano Letters* **6,** 2060–5 (2006).
22. Willets, K. A. & Duyne, R. P. V. Localized surface plasmon resonance spectroscopy and sensing. *Annu Rev Phys Chem* **58,** 267–297 (2007).
23. Zou, S. & Schatz, G. Silver nanoparticle array structures that produce giant enhancements in electromagnetic fields. *Chemical Physics Letters* **403,** 62–67 (2005).
24. Bergman, D. & Stockman, M. Surface plasmon amplification by stimulated emission of radiation: Quantum generation of coherent surface plasmons in nanosystems. *Physical Review Letters* **90,** 027402 (2003).
25. Markel, V. A. & Sarychev, A. Propagation of surface plasmons in ordered and disordered chains of metal nanospheres. *Physical Review B* **75,** 85426 (2007).
26. Maier, S. *et al.* Local detection of electromagnetic energy transport below the diffraction limit in metal nanoparticle plasmon waveguides. *Nature Materials* **2,** 229–232 (2003).
27. Kreibig, U. & Vollmer, M. *Optical Properties of Metal Clusters* (1995).
28. Wang, X. & Shen, Y. General Properties of Local Plasmons in Metal Nanostructures. *Physical Review Letters* **97** (2006).
29. Valle, G. D., Sondergaard, T & Bozhevolnyi, S. I Plasmon-polariton nano-strip resonators: from visible to infra-red. *Optics Express* **16,** 6867–6876 (2008).
30. Valle, G. D., Sondergaard, T & Bozhevolnyi, S. I. Efficient suppression of radiation damping in resonant retardation-based plasmonic structures. *Physical Review B* **79,** 1–4 (2009).
31. Landau, L., Pitaevskii, L. & Lifshitz, E. *Electrodynamics of Continuous Media* (Butterworth-Heinemann, 1985).
32. Scalora & sibilia Pulse propagation, dispersion, and energy in magnetic materials. *Physical Review E* **72** (2005).
33. Liu, M. M. & Guyot-Sionnest, P. Reduced damping of surface plasmons at low temperatures. *Physical Review B (Condensed Matter and Materials Physics)* **79,** 035418–5 (2009).
34. Coronado, E. & Schatz, G. Surface plasmon broadening for arbitrary shape nanoparticles: A geometrical probability approach. *Journal of Chemical Physics* **119,** 3926–3934 (2003).
35. Etchegoin, P., Ru, E. L. & Meyer, M An analytic model for the optical properties of gold. *The Journal of Chemical Physics* **125** (2005).
36. Raschke, G. *et al.* Gold Nanoshells Improve Single Nanoparticle Molecular Sensors. *Nano Letters* **4,** 1853–1857 (2004).
37. Pecharromán, C, Pérez-Juste, J, Mata-Osoro, G, Liz-Marzán, L. M. & Mulvaney, P. Redshift of surface plasmon modes of small gold rods due to their atomic roughness and end-cap geometry. *Physical Review B* **77** (2008).
38. García de Abajo, F. J. Nonlocal Effects in the Plasmons of Strongly Interacting Nanoparticles, Dimers, and Waveguides. *The Journal of Physical Chemistry C* **112,** 17983–17987 (2008).

39. Nehl, C. L., Liao, H. & Hafner, J. H. Optical Properties of Star-Shaped Gold Nanoparticles. *Nano Letters* **6,** 683–688 (2006).

40. Larsson, E., Alegret, J., Käll, M. & Sutherland, D. Sensing characteristics of NIR localized surface plasmon resonances in gold nanorings for application as ultrasensitive biosensors. *Nano Letters* **7,** 1256–63 (2007).

Extinction measurements in a collection of particles

1. Prodan, E, Radloff, C, Halas, N. J. & Nordlander, P. A hybridization model for the plasmon response of complex nanostructures. *Science* **302,** 419–422 (2003).

2. Jain, P. K., Huang, W. & El-Sayed, M. A. On the universal scaling behavior of the distance decay of plasmon coupling in metal nanoparticle pairs: A plasmon ruler equation. *Nano Letters* **7,** 2080–2088 (2007).

3. Schmeits, M. & Dambly, L. Fast-electron scattering by bispherical surface-plasmon modes. *Physical Review B* **44** (1975).

4. Gunnarsson, L. *et al.* Confined plasmons in nanofabricated single silver particle pairs: Experimental observations of strong interparticle interactions. *Journal of Physical Chemistry B* **109,** 1079–1087 (2005).

5. Markel, V. A. & Sarychev, A. Propagation of surface plasmons in ordered and disordered chains of metal nanospheres. *Physical Review B* **75,** 85426 (2007).

6. Maier, S., Kik, P., Atwater, H., Meltzer, S & et al. Observation of coupled plasmon-polariton modes of plasmon waveguides for electromagnetic energy transport below the diffraction limit. *Proceedings of SPIE* **4810** (2002).

7. Maier, S. *et al.* Local detection of electromagnetic energy transport below the diffraction limit in metal nanoparticle plasmon waveguides. *Nature Materials* **2,** 229–232 (2003).

8. Vardeny, Z. & Nahata, A. Anderson localization of slow light. *Nature Photonics* **2,** 75–76 (2008).

9. Govyadinov, A & Markel, V. A. From slow to superluminal propagation: Dispersive properties of surface plasmon polaritons in linear chains of metallic nanospheroids. *Physical Review B* **78** (2008).

10. Grigorenko, A. *et al.* Antisymmetric plasmon resonance in coupled gold nanoparticles as a sensitive tool for detection of local index of refraction. *Applied Physics Letters* **88** (2006).

11. Enoch, S., Quidant, R. & Badenes, G. Optical sensing based on plasmon coupling in nanoparticle arrays. *Optics Express* **12,** 3422–3427 (2004).

12. Eversole, J. D. & Broida, H. P. Size and shape effects in light scattering from small silver, copper, and gold particles. *Physical Review B* **15,** 1644–1655 (1977).

13. Hulteen, J. & Van Duyne, R. P. Nanosphere lithography: A materials general fabrication process for periodic particle array surfaces. *Journal of Vacuum Science and Technology-Section A-Vacuum Surfaces and Films* **13,** 1553–1558 (1995).

14. Haes, A. & Van Duyne, R. P. Plasmonic materials for surface-enhanced sensing and spectroscopy. *MRS Bulletin* **30,** 368–375 (2005).

15. Link, S & El-Sayed, M. Shape and size dependence of radiative, non-radiative and photothermal properties of gold nanocrystals. *International Reviews In Physical Chemistry* **19,** 409–453 (2000).

16. Nikoobakht, B & El-Sayed, M. Preparation and growth mechanism of gold nanorods (NRs) using seed-mediated growth method. *Chemistry Of Materials* **15,** 1957–1962 (2003).

17. Prescott, S. & Mulvaney, P. Gold nanorod extinction spectra. *Journal of Applied Physics* **103** (2006).

18. Alekseeva, A. *et al.* Gold nanorods: Synthesis and optical properties. *Colloid Journal* **68** (2006).

19. Perez-Juste, L. J. & Mulvaney, P. Electric-Field-Directed Growth of Gold Nanorods in Aqueous Surfactant Solutions. *Advanced Functional Materials* **14** (2004).

20. McFarland, A. & Van Duyne, R. P. Single silver nanoparticles as real-time optical sensors with zeptomole sensitivity. *Nano Letters* **3,** 1057–1062 (2003).

21. Nau, D *et al.* Optical properties of disordered metallic photonic crystal slabs. *Physica Status Solidi A-Applications And Materials Science* **204,** 3848–3861 (2007).

22. Strauss, D. Model for clustering. *Biometrika* **62,** 467–475 (1975).

23. Baddeley, A & Turner, R Spatstat: an R package for analyzing spatial point patterns. *Journal of Statistical Software* **12,** 1–42 (2005).

24. Hanson, K. Quasi-Monte Carlo: halftoning in high dimensions. *Computational Imaging. Edited by Bouman* **5016** (2003).

25. Mishchenko, M. I. The electromagnetic optical theorem revisited. *Journal of Quantitative Spectroscopy & Radiative Transfer* **101,** 404–410 (2006).

26. Mishchenko, M. I., Berg, M. J., Sorensen, C. M. & van der Mee, C. V. M. On definition and measurement of extinction cross section. *Journal of Quantitative Spectroscopy & Radiative Transfer* 1–5 (2009).

27. Bohren, C. & Huffman, D. *Absorption and Scattering of Light by Small Particles* (Wiley, 1998).

28. Liu, M. M. & Guyot-Sionnest, P. Reduced damping of surface plasmons at low temperatures. *Physical Review B (Condensed Matter and Materials Physics)* **79,** 035418–5 (2009).

29. Lamb, W. Anti-photon. *Applied Physics B: Lasers and Optics* **60,** 77–84 (1995).

30. Mishchenko, M. I. Maxwell's equations, radiative transfer, and coherent backscattering: A general perspective. *Journal of Quantitative Spectroscopy & Radiative Transfer* **101** (2006).

31. Mishchenko, M. I., Travis, L. & Lacis, A. A. *Multiple scattering of light by particles* (Cambridge University Press, 2006).

32. Garnett, M. Colours in Metal Glasses and in Metallic Films. *Royal Society of London Philosophical Transactions Series A* **203,** 385–420 (1904).

33. Aspnes, D Optical properties of thin films. *Thin Solid Films* **89,** 249–262 (1982).

34. Born, M. & Wolf, E *Principles of Optics* 7th ed. (Cambridge University Press, 2000).

35. Pinchuk, A & Schatz, G Nanoparticle optical properties: Far- and near-field electrodynamic coupling in a chain of silver spherical nanoparticles. *Materials Science and Engineering: B* **149,** 251–258 (2008).

36. Rechberger, W *et al.* Optical properties of two interacting gold nanoparticles. *Opt. Commun* **220,** 137–141 (2003).

37. Myroshnychenko, V. *et al.* Modelling the optical response of gold nanoparticles. *Chem Soc Rev* **37,** 1792–1805 (2008).

38. Grigorenko, A., Geim, A., Gleeson, H., Zhang, Y & et al. Nanofabricated media with negative permeability at visible frequencies. *Nature Physics* **438** (2005).

39. Liu, M., Lee, T.-W., Gray, S. K., Guyot-Sionnest, P. & Pelton, M. Excitation of Dark Plasmons in Metal Nanoparticles by a Localized Emitter. *Physical Review Letters* **102,** 1–4 (2009).

40. Romero, I, Aizpurua, J & andF. Javier García de Abajo, G. B. Plasmons in nearly touching metallic nanoparticles: singular response in the limit of touching dimers. *Optics Express* **14,** 9988–9999 (2006).

41. Stefanou, N & Modinos, A Optical-properties of thin discontinuous metal-films. *J Phys-Condens Mat* **3,** 8149–8157 (1991).

42. García de Abajo, F. J. Interaction of Radiation and Fast Electrons with Clusters of Dielectrics: A Multiple Scattering Approach. *Physical Review Letters* **82** (1999).

43. Stratton, J. A. *Electromagnetic theory* (McGraw-Hill, 1941).

Diffractive coupling in regular arrays

1. Murray, W. & Barnes, W. Plasmonic materials. *Advanced Materials* **19,** 3771–3782 (2007).

2. Myroshnychenko, V. *et al.* Modelling the optical response of gold nanoparticles. *Chem Soc Rev* **37,** 1792–1805 (2008).

3. Markel, V. A. & Sarychev, A. Propagation of surface plasmons in ordered and disordered chains of metal nanospheres. *Physical Review B* **75,** 85426 (2007).

4. Maier, S. *et al.* Local detection of electromagnetic energy transport below the diffraction limit in metal nanoparticle plasmon waveguides. *Nature Materials* **2,** 229–232 (2003).

5. Kravets, V, Schedin, F & Grigorenko, A. Extremely Narrow Plasmon Resonances Based on Diffraction Coupling of Localized Plasmons in Arrays of Metallic Nanoparticles. *Physical Review Letters* **101** (2008).

6. Vardeny, Z. & Nahata, A. Anderson localization of slow light. *Nature Photonics* **2,** 75–76 (2008).

7. Govyadinov, A & Markel, V. A. From slow to superluminal propagation: Dispersive properties of surface plasmon polaritons in linear chains of metallic nanospheroids. *Physical Review B* **78** (2008).

8. Carron, K., Fluhr, W., Meier, M., Wokaun, A. & Lehmann, H. Resonances of two-dimensional particle gratings in surface-enhanced raman-scattering. *Journal Optical Society America B* **3,** 430–440 (1986).

9. Markel, V. A. Coupled-dipole approach to scattering of light from a one-dimensional periodic dipole structure. *Journal of Modern Optics* **40,** 2281–2291 (1993).

10. Markel, V. A. Divergence of dipole sums and the nature of non-Lorentzian exponentially narrow resonances in one-dimensional periodic arrays of nanospheres. *Journal Of Physics B-Atomic Molecular And Optical Physics* **38,** L115–L121 (2005).

11. Zou, S. & Schatz, G. Generating narrow plasmon resonances from silver nanoparticle arrays: influence of array pattern and particle spacing. *Physical Chemistry of Interfaces and Nanomaterial* **5513,** 22–29 (2004).

12. Zou, S. & Schatz, G. Narrow plasmonic/photonic extinction and scattering line shapes for one and two dimensional silver nanoparticle arrays. *Journal of Chemical Physics* **121,** 12606–12 (2004).

13. Zou, S. & Schatz, G. Silver nanoparticle array structures that produce giant enhancements in electromagnetic fields. *Chemical Physics Letters* **403,** 62–67 (2005).

14. Zou, S. & Schatz, G. Theoretical studies of plasmon resonances in one-dimensional nanoparticle chains: narrow lineshapes with tunable widths. *Nanotechnology* **17,** 2813–2820 (2006).

15. Markel, V. A. *et al.* Electromagnetic density of states and absorption of radiation by aggregates of nanospheres with multipole interactions. *Physical Review B* **70,** 54202 (2004).

16. Markel, V. A. Local anisotropy and giant enhancement of local electromagnetic fields in fractal aggregates of metal nanoparticles. *Physical Review B* **72** (2005).

17. García de Abajo, F. J. Colloquium: Light scattering by particle and hole arrays. *Reviews Of Modern Physics* **79** (2007).

18. Haynes, C. *et al.* Nanoparticle Optics: The Importance of Radiative Dipole Coupling in Two-Dimensional Nanoparticle Arrays. *Journal of Physical Chemistry B* **107,** 7337–7342 (2003).

19. Hicks, E. M. *et al.* Controlling plasmon line shapes through diffractive coupling in linear arrays of cylindrical nanoparticles fabricated by electron beam lithography. *Nano Letters* **5,** 1065–70 (2005).

20. Sung, J, Hicks, E., Van Duyne, R. P. & Spears, K. Nanoparticle Spectroscopy: Plasmon Coupling in Finite-Sized Two-Dimensional Arrays of Cylindrical Silver Nanoparticles. *Journal of Physical Chemistry C* **112,** 4091–4096 (2008).

21. Rechberger, W *et al.* Optical properties of two interacting gold nanoparticles. *Opt. Commun* **220,** 137–141 (2003).

22. Félidj, N *et al.* Grating-induced plasmon mode in gold nanoparticle arrays. *Journal of Chemical Physics* **123** (2005).

23. Linden, S, Kuhl, J & Giessen, H Controlling the interaction between light and gold nanoparticles: Selective suppression of extinction. *Physical Review Letters* **86,** 4688–4691 (2001).

24. Yannopapas, V & Stefanou, N Optical excitation of coupled waveguide-particle plasmon modes:A theoretical analysis. *Physical Review B* **69,** 1–4 (2004).

25. Hecht, E. *Optics* 4th ed. (Addison Wesley, 2001).

26. Wood, R. On a remarkable case of uneven distribution of light in a diffraction grating spectrum. *Proceedings of the Physical Society of London* **18,** 269 (1902).

27. Wood, R. Anomalous diffraction gratings. *Physical Review* **48,** 928–936 (1935).

28. Rayleigh, L. On the Dynamical Theory of Gratings. *Proceedings of the Royal Society of London. Series A Containing Papers of a Mathematical and Physical Character* **79,** 399–416 (1907).

29. Fano, U. The theory of anomalous diffraction gratings and of quasi-stationary waves on metallic surfaces (Sommerfeld's waves). *Journal of the Optical Society of America* **31,** 213 (1941).

30. Draine, B. & Flatau Discrete-dipole approximation for scattering calculations. *Journal Optical Society America A* **11** (1993).

31. Bohren, C. & Huffman, D. *Absorption and Scattering of Light by Small Particles* (Wiley, 1998).

32. Hohenau, A., Krenn, J., Rodrigo, S., Martín-Moreno, L. & Garcia-Vidal, F. Spectroscopy and nonlinear microscopy of Au nanoparticle arrays: Experiment and theory. *Physical Review B* **73,** 155404 (2006).

33. Sönnichsen, C. *et al.* Drastic Reduction of Plasmon Damping in Gold Nanorods. *Physical Review Letters* **88,** 077402 (2002).

34. Dahmen, C, Schmidt, H. J & von Plessen, G. Radiation damping in metal nanoparticle pairs. *Nano Letters* **7,** 318–322 (2007).

35. Fischer, H & Martin, O. Retardation-induced plasmonic blinking in coupled nanoparticles. *Optics Letters* **34,** 368–370 (2009).

36. Kuwata-Gonokami, H, Tamaru, H, Esumi, K & Miyano, K Resonant light scattering from metal nanoparticles: Practical analysis beyond Rayleigh approximation. *Applied Physics Letters* **83,** 4625–4627 (2003).

37. Voros, J The Density and Refractive Index of Adsorbing Protein Layers. *Biophysical Journal* **87,** 553–561 (2004).

38. Vecchi, G, Giannini, V & Rivas, J. G. Shaping the Fluorescent Emission by Lattice Resonances in Plasmonic Crystals of Nanoantennas. *Physical Review Letters* **102,** 1–4 (2009).

Diffractive arrays of gold nanorods: a study of the spectral lineshape

1. Félidj, N *et al.* Grating-induced plasmon mode in gold nanoparticle arrays. *Journal of Chemical Physics* **123** (2005).

2. Markel, V. A. Divergence of dipole sums and the nature of non-Lorentzian exponentially narrow resonances in one-dimensional periodic arrays of nanospheres. *Journal Of Physics B-Atomic Molecular And Optical Physics* **38,** L115–L121 (2005).

3. Allione, M., Temnov, V. V., Fedutik, Y., Woggon, U. & Artemyev, M. V. Surface plasmon mediated interference phenomena in low-Q silver nanowire cavities. *Nano Letters* **8,** 31–35 (2008).

4. Valle, G. D., Sondergaard, T & Bozhevolnyi, S. I Plasmon-polariton nano-strip resonators: from visible to infra-red. *Optics Express* **16,** 6867–6876 (2008).

5. Novotny, L. Effective Wavelength Scaling for Optical Antennas. *Physical Review Letters* **98,** 1–4 (2007).

6. Krenn, J. Plasmon dispersion relation of Au and Ag nanowires. *Physical Review B* **68** (2003).

7. Vecchi, G, Giannini, V & Rivas, J. G. Shaping the Fluorescent Emission by Lattice Resonances in Plasmonic Crystals of Nanoantennas. *Physical Review Letters* **102,** 1–4 (2009).

8. Schaich, W. L. *et al.* Optical Resonances in Periodic Surface Arrays of Metallic Patches. *Appl. Opt.* **42,** 5714–5721 (2003).

9. Kravets, V, Schedin, F & Grigorenko, A. Extremely Narrow Plasmon Resonances Based on Diffraction Coupling of Localized Plasmons in Arrays of Metallic Nanoparticles. *Physical Review Letters* **101** (2008).

10. Giannattasio, A. Direct observation of surface plasmon-polariton dispersion. *Optics Express* **13** (2005).

11. García de Abajo, F. J. Multiple scattering of radiation in clusters of dielectrics. *Physical Review B (Condensed Matter and Materials Physics)* **60** (1999).

12. Toll, J Causality and the Dispersion Relation: Logical Foundations. *Physical Review* **104** (1956).

13. Palik, E. D. *Handbook of Optical Constants of Solids* (Academic Press, 1985).

14. Apell, S., Echenique, P. & Ritchie, R. Sum rules for surface plasmon frequencies. *Ultramicroscopy* **65,** 53–60 (1996).

15. Purcell, E. On the Absorption and Emission of Light by Interstellar Grains. *The Astrophysical Journal* **158,** 433–40 (1969).

16. Bohren, C. & Huffman, D. *Absorption and Scattering of Light by Small Particles* (Wiley, 1998).

17. Markel, V. A. Local anisotropy and giant enhancement of local electromagnetic fields in fractal aggregates of metal nanoparticles. *Physical Review B* **72** (2005).

18. Mishchenko, M. I. Broadband electromagnetic scattering by particles. *Journal Optical Society America A* **25,** 2893–2895 (2008).

19. Mishchenko, M. I., Travis, L. & Lacis, A. A. *Scattering, Absorption, and Emission of Light by Small Particles* (Cambridge University Press, 2002).

20. Sohl, C., Larsson, C., Gustafsson, M. & Kristensson, G. A scattering and absorption identity for metamaterials: Experimental results and comparison with theory. *Journal of Applied Physics* **103,** 054906 (2008).

21. Adrian Doicu, Y. E. Thomas Wriedt *Light Scattering by Systems of Particles: Null-field Method with Discrete Sources : Theory and Programs* (Springer, 2006).

22. Innes, R & Sambles, J. Optical Characterisation of Gold Using Surface Plasmon–Polaritons. *Journal of Physics F* **17** (1987).

23. Moroz, A. Improvement of Mishchenko's T-matrix code for absorbing particles. *Appl. Opt.* **44,** 3604–3609 (2005).

24. Voshchinnikov, N. & Farafonov, V. Optical properties of spheroidal particles. *Astrophysics and Space Science* **204** (1993).

25. Yannopapas, V. Non-local optical response of two-dimensional arrays of metallic nanoparticles. *Journal of Physics: Condensed Matter* **20,** 325211 (2008).

The effect of disorder on the optical properties of diffractive arrays of gold nanorods

1. Nau, D *et al.* Optical properties of disordered metallic photonic crystal slabs. *Physica Status Solidi A-Applications And Materials Science* **204,** 3848–3861 (2007).

2. Baddeley, A & Turner, R Spatstat: an R package for analyzing spatial point patterns. *Journal of Statistical Software* **12,** 1–42 (2005).

3. Strauss, D. Model for clustering. *Biometrika* **62,** 467–475 (1975).

4. Kuwata-Gonokami, H, Tamaru, H, Esumi, K & Miyano, K Resonant light scattering from metal nanoparticles: Practical analysis beyond Rayleigh approximation. *Applied Physics Letters* **83,** 4625–4627 (2003).

5. Schatz, G. & Van Duyne, R. P. Discrete dipole approximation for calculating extinction and Raman intensities for small particles with arbitrary shapes. *Journal of Chemical Physics* **103,** 869–875 (1995).

6. Sönnichsen, C. *et al.* Drastic Reduction of Plasmon Damping in Gold Nanorods. *Physical Review Letters* **88,** 077402 (2002).

7. Markel, V. A. & Sarychev, A. Propagation of surface plasmons in ordered and disordered chains of metal nanospheres. *Physical Review B* **75,** 85426 (2007).

Conclusions

1. Sönnichsen, C. *et al.* Drastic Reduction of Plasmon Damping in Gold Nanorods. *Physical Review Letters* **88,** 077402 (2002).
2. Liu, M. M. & Guyot-Sionnest, P. Reduced damping of surface plasmons at low temperatures. *Physical Review B (Condensed Matter and Materials Physics)* **79,** 035418–5 (2009).
3. Vecchi, G, Giannini, V & Rivas, J. G. Shaping the Fluorescent Emission by Lattice Resonances in Plasmonic Crystals of Nanoantennas. *Physical Review Letters* **102,** 1–4 (2009).

Poynting theorem and elastic scattering cross-sections

1. Jackson *Classical Electrodynamics* (Wiley, 1999).
2. Landau, L., Pitaevskii, L. & Lifshitz, E. *Electrodynamics of Continuous Media* (Butterworth-Heinemann, 1985).
3. Mishchenko, M. I., Travis, L. & Lacis, A. A. *Multiple scattering of light by particles* (Cambridge University Press, 2006).
4. Mishchenko, M. I., Travis, L. & Lacis, A. A. *Scattering, Absorption, and Emission of Light by Small Particles* (Cambridge University Press, 2002).
5. Mishchenko, M. I. The electromagnetic optical theorem revisited. *Journal of Quantitative Spectroscopy & Radiative Transfer* **101,** 404–410 (2006).

List of conferences and publications

International conferences

Eleventh conference on electromagnetic and light scattering, (anniversary of Mie's 1908 paper), University of Hertfordshire, UK, *September 08*. (talk)

The push or pull of optical momentum, Rank Prize Symposium, Grasmere, UK, *July 08*. (talk)

EMRS conference, Strasbourg, France, *May 07*. (talk)

Discrete Dipole Approximation workshop, Bremen, Germany, *May 07*. (talk)

Attogram 2D surface plasmon imaging, Mid-term conference, Nottingham, UK, *March 08*. (poster)

From micro to nano: mind the gap, summer school, Cargese, Corsica, *July 06*. (poster)

Peer-reviewed publications

B. Auguié, W.L. Barnes. *Diffractive coupling in gold nanoparticle arrays and the effect of disorder.* Optics Letters, **34**, pp. 401–403 (2009).

B. Auguié, W.L. Barnes. *Collective resonances in gold nanoparticle arrays.* Physical Review Letters, **101**, p. 143902 (2008).

W.A.Murray, **B. Auguié**, W.L. Barnes. *Sensitivity of localized surface plasmon resonances to bulk and local changes in the optical environment.* J. Phys. Chem. C, **113**, pp. 5120–5125 (2009).

J. Parsons, E. Hendry, C. P. Burrows, **B. Auguié**, J. R. Sambles, and W. L. Barnes. *Localized surface-plasmon resonances in periodic non-diffracting metallic nanoparticle and nanohole arrays.* Physical Review B, **79**, p. 073412 (2009).